NASA/CR—2010-216794/VOL2

N+3 Aircraft Concept Designs and Trade Studies, Final Report

Volume 2: Appendices—Design Methodologies for Aerodynamics, Structures, Weight, and Thermodynamic Cycles

E.M. Greitzer, P.A. Bonnefoy, E. de la Rosa Blanco, C.S. Dorbian, M. Drela, D.K. Hall, R.J. Hansman, J.I. Hileman, R.H. Liebeck, J. Lovegren, P. Mody, J.A. Pertuze, S. Sato, Z.S. Spakovszky, and C.S. Tan
Massachusetts Institute of Technology, Cambridge, Massachusetts

J.S. Hollman, J.E. Duda, N. Fitzgerald, J. Houghton, J.L. Kerrebrock, G.F. Kiwada, D. Kordonowy, J.C. Parrish, J. Tylko, and E.A. Wen
Aurora Flight Sciences, Cambridge, Massachusetts

W.K. Lord
Pratt & Whitney, East Hartford, Connecticut

December 2010

NASA STI Program . . . in Profile

Since its founding, NASA has been dedicated to the advancement of aeronautics and space science. The NASA Scientific and Technical Information (STI) program plays a key part in helping NASA maintain this important role.

The NASA STI Program operates under the auspices of the Agency Chief Information Officer. It collects, organizes, provides for archiving, and disseminates NASA's STI. The NASA STI program provides access to the NASA Aeronautics and Space Database and its public interface, the NASA Technical Reports Server, thus providing one of the largest collections of aeronautical and space science STI in the world. Results are published in both non-NASA channels and by NASA in the NASA STI Report Series, which includes the following report types:

- TECHNICAL PUBLICATION. Reports of completed research or a major significant phase of research that present the results of NASA programs and include extensive data or theoretical analysis. Includes compilations of significant scientific and technical data and information deemed to be of continuing reference value. NASA counterpart of peer-reviewed formal professional papers but has less stringent limitations on manuscript length and extent of graphic presentations.

- TECHNICAL MEMORANDUM. Scientific and technical findings that are preliminary or of specialized interest, e.g., quick release reports, working papers, and bibliographies that contain minimal annotation. Does not contain extensive analysis.

- CONTRACTOR REPORT. Scientific and technical findings by NASA-sponsored contractors and grantees.

- CONFERENCE PUBLICATION. Collected papers from scientific and technical conferences, symposia, seminars, or other meetings sponsored or cosponsored by NASA.

- SPECIAL PUBLICATION. Scientific, technical, or historical information from NASA programs, projects, and missions, often concerned with subjects having substantial public interest.

- TECHNICAL TRANSLATION. English-language translations of foreign scientific and technical material pertinent to NASA's mission.

Specialized services also include creating custom thesauri, building customized databases, organizing and publishing research results.

For more information about the NASA STI program, see the following:

- Access the NASA STI program home page at *http://www.sti.nasa.gov*

- E-mail your question via the Internet to *help@sti.nasa.gov*

- Fax your question to the NASA STI Help Desk at 443–757–5803

- Telephone the NASA STI Help Desk at 443–757–5802

- Write to:
  NASA Center for AeroSpace Information (CASI)
  7115 Standard Drive
  Hanover, MD 21076–1320

NASA/CR—2010-216794/VOL2

N+3 Aircraft Concept Designs and Trade Studies, Final Report

Volume 2: Appendices—Design Methodologies for Aerodynamics, Structures, Weight, and Thermodynamic Cycles

E.M. Greitzer, P.A. Bonnefoy, E. de la Rosa Blanco, C.S. Dorbian, M. Drela, D.K. Hall, R.J. Hansman, J.I. Hileman, R.H. Liebeck, J. Lovegren, P. Mody, J.A. Pertuze, S. Sato, Z.S. Spakovszky, and C.S. Tan
Massachusetts Institute of Technology, Cambridge, Massachusetts

J.S. Hollman, J.E. Duda, N. Fitzgerald, J. Houghton, J.L. Kerrebrock, G.F. Kiwada, D. Kordonowy, J.C. Parrish, J. Tylko, and E.A. Wen
Aurora Flight Sciences, Cambridge, Massachusetts

W.K. Lord
Pratt & Whitney, East Hartford, Connecticut

Prepared under Cooperative Agreement NNX08AW63A

National Aeronautics and
Space Administration

Glenn Research Center
Cleveland, Ohio 44135

December 2010

This report contains preliminary findings,
subject to revision as analysis proceeds.

This work was sponsored by the Fundamental Aeronautics Program
at the NASA Glenn Research Center.

Level of Review: This material has been technically reviewed by NASA technical management.

Available from

NASA Center for Aerospace Information
7115 Standard Drive
Hanover, MD 21076–1320

National Technical Information Service
5301 Shawnee Road
Alexandria, VA 22312

Available electronically at http://gltrs.grc.nasa.gov

TASOPT 2.00
Transport Aircraft System OPTimization
Technical Description

Mark Drela
20 Mar 10

Appendices A–F present the theory behind the TASOPT methodology and code. Appendix A describes the bulk of the formulation, while Appendices B–F develop the major sub-models for the engine, fuselage drag, BLI accounting, etc.

Contents

Appendix A

TASOPT — Transport Aircraft System OPTimization

A.1 Introduction

A.1.1 Background

There is a vast body of work on conceptual and preliminary aircraft design. The more traditional approaches of e.g. Roskam [1], Torrenbeek [2], Raymer [3], have relied heavily on historical weight correlations, empirical drag build-ups, and established engine performance data for their design evaluations. The ACSYNT program [4],[5] likewise relies on such models, with a more detailed treatment of the geometry via its PDCYL [6] extension.

More recently, optimization-based approaches such as those of Knapp [7], the WINGOP code of Wakayama [8],[9], and in particular the PASS program of Kroo [10] perform tradeoffs in a much more detailed geometry parameter space, but still rely on simple drag and engine performance models.

The recent advent of turbofan engines with extremely high bypass ratios (Pratt geared turbofan), advanced composite materials (Boeing 787), and possibly less restrictive operational restrictions (Free-Flight ATC concept), make it of great interest to re-examine the overall aircraft/engine/operation system to maximize transportation efficiency. NASA's N+1,2,3 programs are examples of research efforts towards this goal. In addition, greater emphasis on limiting noise and emissions demands that such aircraft design examination be done under possibly stringent environmental constraints. Optimally exploiting these new factors and constraints on transport aircraft is a major motivation behind TASOPT's development.

A.1.2 Summary

Overall approach

To examine and evaluate future aircraft with potentially unprecedented airframe, engine, or operation parameters, it is desirable to dispense with as many of the historically-based

methods as possible, since these cannot be relied on outside of their data-fit ranges. The approach used by TASOPT is to base most of the weight, aerodynamic, and engine-performance prediction on low-order models which implement fundamental structural, aerodynamic, and thermodynamic theory and associated computational methods. Historical correlations will be used only where absolutely necessary, and in particular only for some of the secondary structure and for aircraft equipment. Modeling the bulk of the aircraft structure, aerodynamics, and propulsion by fundamentals gives considerable confidence that the resulting optimized design is realizable, and not some artifact of inappropriate extrapolated data fits.

Airframe structure and weight

The airframe structural and weight models used by TASOPT treat the primary structure elements as simple geometric shapes, with appropriate load distributions imposed at critical loading cases. The fuselage is assumed to be a pressure vessel with one or more "bubbles", with added bending loads, with material gauges sized to obtain a specified stress at specified load situations. The wing is assumed to be cantilevered or to have a single support strut, whose material gauges are also sized to obtain a specified stress. The resulting fuselage, wing, and tail material volumes, together with specified material density, then gives the primary structural weight. Only the secondary structural weights and non-structural and equipment weights are estimated via historical weight fractions.

Aerodynamic performance

The wing airfoil performance is represented by a parameterized transonic airfoil family spanning a range of thicknesses, whose performance is determined by 2D viscous/inviscid CFD calculation for a range of lift coefficients and Mach numbers. Together with suitable sweep corrections, this gives reliable profile+wave drag of the wing in cruise and high climb and high descent. The fuselage drag is likewise obtained from compressible viscous/inviscid CFD, suitably simplified with axisymmetric-based approximations. A side benefit is that detailed knowledge of the fuselage boundary layers makes it possibly for TASOPT to reliably predict the benefits of boundary layer ingestion in fuselage-mounted engines.

The drag of only the minor remaining components such as nacelles is obtained by traditional wetted area methods, but corrected for supervelocities estimated with vortex sheet models. Induced drag is predicted by fairly standard Trefftz-Plane analysis.

The primary use of CFD-level results in the present TASOPT method makes it more widely applicable than the previous more traditional approaches which have typically relied on wetted-area methods for major components of the configuration.

Engine performance

A fairly detailed component-based turbofan model, such as described by Kerrebrock [11], is used to both size the engines for cruise, and to determine their off-design performance at takeoff, climb, and descent. The model includes the effects of turbine cooling flows, allowing realistic simultaneous optimization of cycle pressure ratios and operating temperatures

together with the overall airframe and its operating parameters. The overall aircraft and engine system is actually formulated in terms of dissipation and power rather than drag and thrust [12], which allows a rigorous examination of advanced propulsion systems using boundary layer ingestion.

The use of component-based engine simulation in the present TASOPT method differs from previous approaches which typically have relied on simple historical regressions or established engine performance maps. The more detailed treatment is especially important for examining designs with extreme engines parameters which fall outside of historical databases.

Mission profiles

Integration of standard trajectory equations over a parameterized mission profile provides the required mission weight, which completes the overall sizing approach. The end result is a defined aircraft and engine combination which achieves the specified payload and range mission. Off-design missions are also addressed, allowing the possibility of minimizing fuel burn for a collection of fleet missions rather than for just the aircraft-sizing mission.

Takeoff and noise

A takeoff performance model is used to determine the normal takeoff distance and the balanced field length of any given design. The balanced field length can be included as a constraint in overall TASOPT optimization. Noise estimates are also calculated using a few published methods, e.g. [13], [14], [15]. These are used only for run-time rough estimates, and are not well suited for use as constraints. Much more detailed noise analyses can typically be performed as a post-processing step using the ANOPP method, for example.

Restriction to wing+tube aircraft

The description of the structural and aerodynamic models above explains why TASOPT is restricted to tube+wing configurations — most other configurations would be quite difficult or impossible to treat with these models. For example, a joined-wing configuration [16] has a relatively complex structure with out-of-plane deformations and the possibility of coupled twist/bend buckling in the presence of eccentricity from the airloads, which requires a greatly more complex structural analysis than straightforward beam theory. A blended-wing-body configuration [17] with non-circular cabin cross sections likewise has non-obvious critical load cases and load paths, and its transonic aerodynamics are dominated by 3D effects. For these reasons such non-traditional configurations are simply outside the scope of the present work.

A.2 Model Derivation

A.2.1 Weight Breakdown

The weight breakdown is summarized in Figure A.1, to serve as a convenient reference.

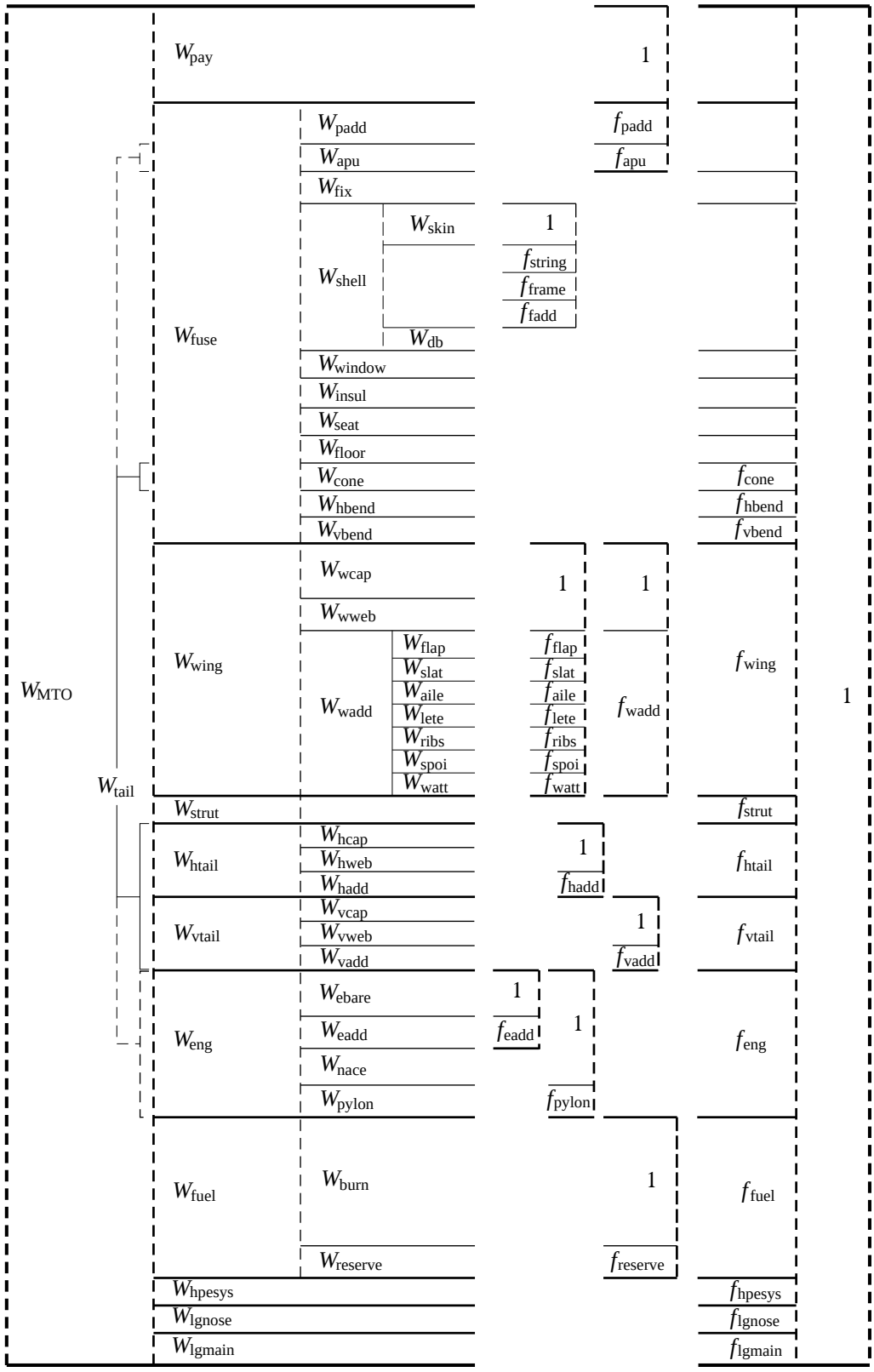

Figure A.1: Aircraft weights and weight fractions breakdown.

A.2.2 Fuselage pressure and torsion loads

The fuselage is modeled as a side-by-side "double-bubble" pressure vessel with an ellipsoidal nose endcap and a hemispherical tail endcap, which is subjected to pressurization, bending,

and torsion loads, as shown in Figures A.2 and A.3. The loaded cylindrical length of the pressure vessel shell is from $x_{\text{shell}\,1}$ to $x_{\text{shell}\,2}$.

$$l_{\text{shell}} \;=\; x_{\text{shell}\,2} \;-\; x_{\text{shell}\,1} \tag{A.1}$$

The horizontal-axis moment $\mathcal{M}_{\text{h}(x)}$ distributions on the front and back bending fuselage are assumed to match at location x_{wing}, as shown in Figure A.2. Theoretically this is the wing's net lift–weight centroid, which varies somewhat depending the fuel fraction in the wings, the wing's profile pitching moment and hence the flap setting, and on the aircraft C_L. For simplicity it will be approximated as the wing's area centroid. Note that for a swept wing the wing box location x_{wbox} will be centered somewhat ahead of x_{wing}, but it will then also impart a pitch-axis moment at its location, so that the front and back $\mathcal{M}_{\text{h}(x)}$ distributions must still match at x_{wing}.

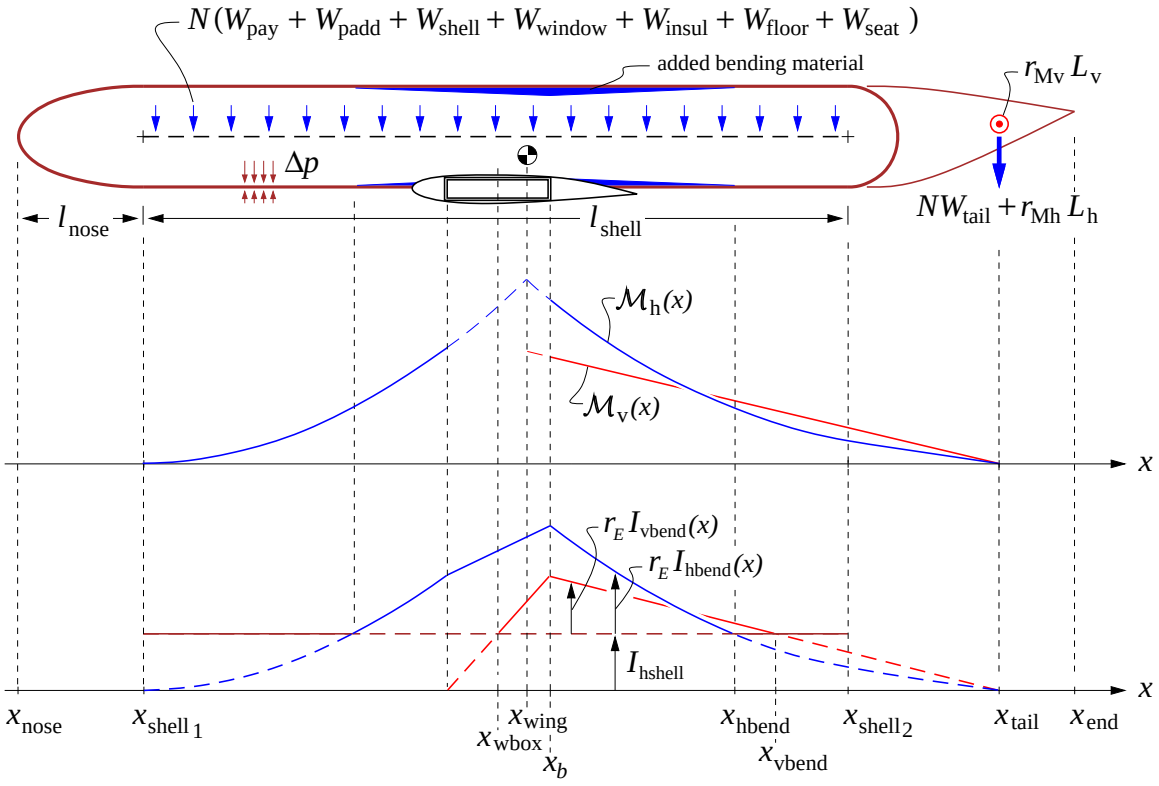

Figure A.2: Fuselage layout, loads, and bending moment and inertia distributions. Bending material and $r_E I_{\text{hbend}(x)}$ is added wherever the horizontal-axis bending moment $\mathcal{M}_{\text{h}(x)}$ exceeds the capability of the pressure vessel's bending inertia I_{hshell}, and likewise for the vertical-axis moment and inertia.

Figure A.3 shows the fuselage cross section. The pressure-vessel skin and endcaps have a uniform thickness t_{skin}, while the center tension web has an average thickness t_{db}. The cross-sectional area of the skin is A_{skin}, and has stiffening stringers which have a "smeared" average area $A_{\text{skin}} f_{\text{string}} \rho_{\text{skin}} / \rho_{\text{bend}}$, specified via the empirical stringer/skin weight fraction f_{string}. The enclosed area S_{skin} enters the torsional stiffness and strength calculations. The fuselage cross section also shows the possibility of added bottom bubbles or fairings, extended downward by the distance ΔR_{fuse}.

The skin and stringers constitute the "shell", which has bending inertias $I_{\text{hshell}}, I_{\text{vshell}}$ about the horizontal and vertical axes. Figure A.3 does not show any hoop-stiffening frames which are typically required, and whose weight is a specified fraction f_{frame} of the skin weight. These typically may be offset from the skin inside of the stringers, and hence are assumed to not contribute to the skin's circumferential tensile strength.

To address the weight and aerodynamic loads of the tail group on the fuselage, the horizontal and vertical tails, the tailcone, and any rear-mounted engines are treated as one lumped mass and aero force at location x_{tail}, shown in Figure A.2.

The bending loads on the shell may require the addition of vertical-bending material concentrated on top and bottom of the fuselage shell (typically as skin doublers or additional stringers). The total added cross sectional area is $A_{\text{hbend}(x)}$, and the associated added bending inertia is $I_{\text{hbend}(x)}$. Corresponding added material on the sides has $A_{\text{vbend}(x)}$ and $I_{\text{vbend}(x)}$. Because the wing box itself will contribute to the fuselage bending strength, these added areas and bending inertias do not match the $\mathcal{M}_{(x)}$ distribution there, but are made linear over the wing box extent, as shown in Figure A.2.

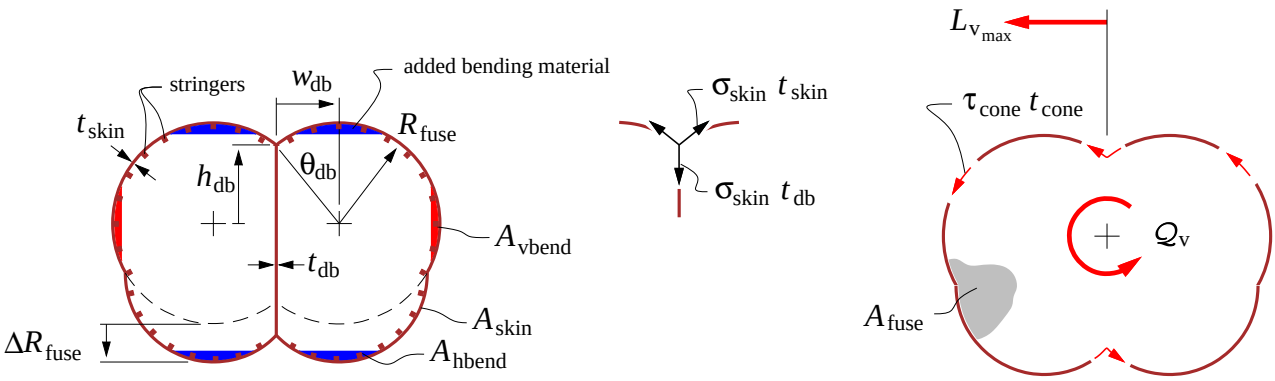

Figure A.3: Fuselage cross-section, shell/web junction tension flows, and torsion shear flow from vertical tail load. An optional bottom fairing extends down by the distance ΔR_{fuse}. Fuselage frames are not shown.

Cross-section relations

The fuselage pressure shell has the following geometric relations and beam quantities.

$$\theta_{\text{db}} = \arcsin(w_{\text{db}}/R_{\text{fuse}}) \tag{A.2}$$

$$h_{\text{db}} = \sqrt{R_{\text{fuse}}^2 - w_{\text{db}}^2} \tag{A.3}$$

$$A_{\text{skin}} = (2\pi + 4\theta_{\text{db}})\, R_{\text{fuse}}\, t_{\text{skin}} \ + \ 2\Delta R_{\text{fuse}}\, t_{\text{skin}} \tag{A.4}$$

$$A_{\text{db}} = (2h_{\text{db}} + \Delta R_{\text{fuse}})\, t_{\text{db}} \tag{A.5}$$

$$A_{\text{fuse}} = (\pi + 2\theta_{\text{db}} + \sin 2\theta_{\text{db}})\, R_{\text{fuse}}^2 \ + \ 2R_{\text{fuse}}\, \Delta R_{\text{fuse}} \tag{A.6}$$

The skin has some modulus and density $E_{\text{skin}}, \rho_{\text{skin}}$, while the stringers have some possibly different values $E_{\text{bend}}, \rho_{\text{bend}}$. The effective modulus-weighted "shell" thickness t_{shell} can then

be defined as follows, assuming that only the skin and stringers contribute to bending, but not the frames.

$$t_{\rm shell} \;=\; \frac{(Et)_{\rm skin}}{E_{\rm skin}} \;=\; t_{\rm skin}\left(1 + r_E\, f_{\rm string}\frac{\rho_{\rm skin}}{\rho_{\rm bend}}\right) \tag{A.7}$$

$$\text{where} \qquad r_E \;=\; \frac{E_{\rm bend}}{E_{\rm skin}} \tag{A.8}$$

This is then convenient for determining the modulus-weighted horizontal-axis and vertical-axis bending inertias. The center web, if any, is assumed to be made of the same material as the skin.

$$\begin{aligned}
I_{\rm hshell} &= \frac{(EI)_{\rm hshell}}{E_{\rm skin}} \\
&= 4\int_0^{\pi/2+\theta_{\rm db}} (R_{\rm fuse}\sin\theta + \Delta R_{\rm fuse}/2)^2\; R_{\rm fuse}\, t_{\rm shell}\, d\theta \;+\; \frac{2}{3}(h_{\rm db} + \Delta R_{\rm fuse}/2)^3 t_{\rm db} \\
&= \Big[\,(\pi + 2\theta_{\rm db} + \sin 2\theta_{\rm db})\, R_{\rm fuse}^2 \\
&\quad + 8\cos\theta_{\rm db}\;(\Delta R_{\rm fuse}/2)\, R_{\rm fuse} \\
&\quad + (2\pi + 4\theta_{\rm db})\,(\Delta R_{\rm fuse}/2)^2\,\Big]\, R_{\rm fuse}\, t_{\rm shell} \;+\; \frac{2}{3}(h_{\rm db} + \Delta R_{\rm fuse}/2)^3 t_{\rm db}
\end{aligned} \tag{A.9}$$

$$\begin{aligned}
I_{\rm vshell} &= \frac{(EI)_{\rm vshell}}{E_{\rm skin}} \\
&= 4\int_0^{\pi/2+\theta_{\rm db}} (R_{\rm fuse}\cos\theta + w_{\rm db})^2\; R_{\rm fuse}\, t_{\rm shell}\, d\theta \\
&= \Big[\,(\pi + 2\theta_{\rm db} - \sin 2\theta_{\rm db})\, R_{\rm fuse}^2 \\
&\quad + 8\cos\theta_{\rm db}\; w_{\rm db}\, R_{\rm fuse} \\
&\quad + (2\pi + 4\theta_{\rm db})\, w_{\rm db}^2\,\Big]\, R_{\rm fuse}\, t_{\rm shell}
\end{aligned} \tag{A.10}$$

It's useful to note that for the particular case of $w_{\rm db} = 0$ and $\Delta R_{\rm fuse} = 0$, the cross-section circles merge into one circle, and the tension and hence the thickness of the center web go to zero, $t_{\rm db} = 0$. The areas and bending inertias then reduce to those for a single circular cross-section.

$$A_{\rm skin} \;=\; 2\pi R_{\rm fuse}\, t_{\rm skin} \qquad (\text{if } w_{\rm db} = 0, \Delta R_{\rm fuse} = 0) \tag{A.11}$$

$$S_{\rm skin} \;=\; \pi R_{\rm fuse}^2 \qquad (\text{if } w_{\rm db} = 0, \Delta R_{\rm fuse} = 0) \tag{A.12}$$

$$I_{\rm hshell} \;=\; I_{\rm vshell} \;=\; \pi R_{\rm fuse}^3\, t_{\rm shell} \qquad (\text{if } w_{\rm db} = 0, \Delta R_{\rm fuse} = 0) \tag{A.13}$$

Hence, no generality is lost with this double-bubble cross-section model.

Pressure shell loads

The pressurization load from the Δp pressure difference produces the following axial and hoop stresses in the fuselage skin, with the assumption that the stringers share the axial loads, but the frames do not share the hoop loads. This assumes a typical aluminum fuselage structure, where the stringers are contiguous and solidly riveted to the skin, but the frames

are either offset from the skin or have clearance cutouts for the stringers which interrupt the frames' hoop loads.

$$\sigma_x = \frac{\Delta p}{2}\frac{R_{\rm fuse}}{t_{\rm shell}} \tag{A.14}$$

$$\sigma_\theta = \Delta p\,\frac{R_{\rm fuse}}{t_{\rm skin}} \tag{A.15}$$

An isotropic (metal) fuselage skin thickness $t_{\rm skin}$ and the web thickness $t_{\rm db}$ will therefore be sized by the larger σ_θ value in order to meet an allowable stress $\sigma_{\rm skin}$.

$$t_{\rm skin} = \frac{\Delta p\, R_{\rm fuse}}{\sigma_{\rm skin}} \tag{A.16}$$

$$t_{\rm db} = 2\,\frac{\Delta p\, w_{\rm db}}{\sigma_{\rm skin}} \tag{A.17}$$

This particular $t_{\rm db}$ value is obtained from the requirement of equal circumferential stress in the skin and the web, and tension equilibrium at the 3-point web/skin junction.

The volume of the skin material $\mathcal{V}_{\rm skin}$ is obtained from the cross-sectional skin area, plus the contribution of the ellipsoidal nose endcap and the spherical rear bulkhead. The nose uses Cantrell's approximation for the surface area of an ellipsoid.

$$S_{\rm nose} \simeq (2\pi{+}4\theta_{\rm db})R_{\rm fuse}^2\left[\frac{1}{3}+\frac{2}{3}\left(\frac{l_{\rm nose}}{R_{\rm fuse}}\right)^{8/5}\right]^{5/8} \tag{A.18}$$

$$S_{\rm bulk} \simeq (2\pi{+}4\theta_{\rm db})R_{\rm fuse}^2 \tag{A.19}$$

$$\mathcal{V}_{\rm cyl} = A_{\rm skin}\, l_{\rm shell} \tag{A.20}$$

$$\mathcal{V}_{\rm nose} = S_{\rm nose}\, t_{\rm skin} \tag{A.21}$$

$$\mathcal{V}_{\rm bulk} = S_{\rm bulk}\, t_{\rm skin} \tag{A.22}$$

$$\mathcal{V}_{\rm db} = A_{\rm db}\, l_{\rm shell} \tag{A.23}$$

$$x\mathcal{V}_{\rm cyl} = \tfrac{1}{2}(x_{{\rm shell}\,1}{+}x_{{\rm shell}\,2})\,\mathcal{V}_{\rm cyl} \tag{A.24}$$

$$x\mathcal{V}_{\rm nose} = \tfrac{1}{2}(x_{\rm nose}{+}x_{{\rm shell}\,1})\,\mathcal{V}_{\rm nose} \tag{A.25}$$

$$x\mathcal{V}_{\rm bulk} = (x_{{\rm shell}\,2}{+}\tfrac{1}{2}\Delta R_{\rm fuse})\,\mathcal{V}_{\rm bulk} \tag{A.26}$$

$$x\mathcal{V}_{\rm db} = \tfrac{1}{2}(x_{{\rm shell}\,1}{+}x_{{\rm shell}\,2})\,\mathcal{V}_{\rm db} \tag{A.27}$$

The total fuselage shell weight then follows by specifying a material density $\rho_{\rm skin}$ for the skin and web. The assumed skin-proportional added weights of local reinforcements, stiffeners, and fasteners are represented by the $f_{\rm fadd}$ fraction, and stringers and frames are represented by the $f_{\rm string}, f_{\rm frame}$ fractions.

$$W_{\rm skin} = \rho_{\rm skin}\, g\,(\mathcal{V}_{\rm cyl}+\mathcal{V}_{\rm nose}+\mathcal{V}_{\rm bulk}) \tag{A.28}$$

$$W_{\rm db} = \rho_{\rm skin}\, g\,\mathcal{V}_{\rm db} \tag{A.29}$$

$$x\!W_{\rm skin} = \rho_{\rm skin}\, g\,(x\mathcal{V}_{\rm cyl}+x\mathcal{V}_{\rm nose}+x\mathcal{V}_{\rm bulk}) \tag{A.30}$$

$$x\!W_{\rm db} = \rho_{\rm skin}\, g\, x\mathcal{V}_{\rm db} \tag{A.31}$$

$$W_{\rm shell} = W_{\rm skin}(1{+}f_{\rm string}{+}f_{\rm frame}{+}f_{\rm fadd}) \;+\; W_{\rm db} \tag{A.32}$$

$$x\!W_{\rm shell} = x\!W_{\rm skin}(1{+}f_{\rm string}{+}f_{\rm frame}{+}f_{\rm fadd}) \;+\; x\!W_{\rm db} \tag{A.33}$$

Cabin volume and Buoyancy weight

At this point it's convenient to calculate the pressurized cabin volume.

$$\mathcal{V}_{\rm cabin} \;=\; A_{\rm fuse}\,(l_{\rm shell} \,+\, 0.67\,l_{\rm nose} \,+\, 0.67\,R_{\rm fuse}) \tag{A.34}$$

The air in the cabin is pressurized to either the specified minimum cabin pressure $p_{\rm cabin}$, or the ambient pressure at altitude $p_{0(h)}$, whichever is greater. The resulting negative cabin buoyancy increases the effective instantaneous weight of the aircraft by the added buoyancy weight $W_{{\rm buoy}(h)}$ which varies with altitude.

$$\rho_{{\rm cabin}(h)} \;=\; \frac{1}{RT_{\rm cabin}}\,\max\left(\,p_{\rm cabin}\,,\;p_{0(h)}\,\right) \tag{A.35}$$

$$W_{\rm buoy} \;=\; (\rho_{{\rm cabin}(h)} \,-\, \rho_{0(h)})\,g\,\mathcal{V}_{\rm cabin} \tag{A.36}$$

This is then added to the physical weight to give the net effective aircraft weight used for cruise wing sizing and performance calculations.

$$\bar{W} \;=\; W \,+\, W_{\rm buoy} \tag{A.37}$$

Windows and Insulation

The window weight is specified by their assumed net weight/length density $W'_{\rm window}$, together with the cabin length $l_{\rm shell}$.

$$W_{\rm window} \;=\; W'_{\rm window}\,l_{\rm shell} \tag{A.38}$$

$$x\!W_{\rm window} \;=\; \tfrac{1}{2}(x_{{\rm shell}\,1}+x_{{\rm shell}\,2})W_{\rm window} \tag{A.39}$$

The $W'_{\rm window}$ value represents the actual window weight, minus the weight of the skin and insulation cutout which is eliminated by the window.

The fuselage insulation and padding weight is specified by its assumed weight/area density $W''_{\rm insul}$, together with the cabin+endcap shell surface area.

$$W_{\rm insul} \;=\; W''_{\rm insul}\,\left[\,(1.1\pi + 2\theta_{\rm db})R_{\rm fuse}\,l_{\rm shell} \,+\, 0.55\,(S_{\rm nose}+S_{\rm bulk})\,\right] \tag{A.40}$$

$$x\!W_{\rm insul} \;=\; \tfrac{1}{2}(x_{{\rm shell}\,1}+x_{{\rm shell}\,2})W_{\rm insul} \tag{A.41}$$

The 1.1 and 0.55 factors assume that 55% of the fuselage circle is over the cabin, and the remaining 45% is over the cargo hold which has no insulation.

Payload-proportional weights

The APU weight $W_{\rm apu}$ is assumed to be proportional to the payload weight, and is treated as a point weight at some specified location $x_{\rm apu}$.

$$W_{\rm apu} \;=\; W_{\rm pay}\,f_{\rm apu} \tag{A.42}$$

$$x\!W_{\rm apu} \;=\; x_{\rm apu}\,W_{\rm apu} \tag{A.43}$$

The seat weight is also assumed to be proportional to the payload weight, uniformly distributed along the cabin for a single-class aircraft.

$$W_{\text{seat}} = W_{\text{pay}}\, f_{\text{seat}} \tag{A.44}$$

$$x_{\text{seat}} W_{\text{seat}} = \tfrac{1}{2}(x_{\text{shell}\,1} + x_{\text{shell}\,2}) W_{\text{seat}} \tag{A.45}$$

Another payload-proportional weight W_{padd} is used to represent all remaining added weight: flight attendants, food, galleys, toilets, luggage compartments and furnishings, doors, lighting, air conditioning systems, in-flight entertainment systems, etc. These are also assumed to be uniformly distributed on average.

$$W_{\text{padd}} = W_{\text{pay}}\, f_{\text{padd}} \tag{A.46}$$

$$x_{\text{padd}} W_{\text{padd}} = \tfrac{1}{2}(x_{\text{shell}\,1} + x_{\text{shell}\,2}) W_{\text{padd}} \tag{A.47}$$

The proportionality factors $f_{\text{apu}}, f_{\text{seat}}, f_{\text{padd}}$ will depend on generator technology, seat technology, passenger class, and slightly on long-haul versus short-haul aircraft.

Fixed weight

A specified fixed weight contribution W_{fix} is assumed. This represents the pilots, cockpit windows, cockpit seats and control mechanisms, flight instrumentation, navigation and communication equipment, antennas, etc., which are expected to be roughly the same total weight for any transport aircraft. To get the associated weight moment, a specified weight centroid x_{fix} is also specified. Typically this will be located in the nose region.

$$W_{\text{fix}} = \ldots \text{ specified} \tag{A.48}$$

$$x_{\text{fix}} W_{\text{fix}} = x_{\text{fix}}\, W_{\text{fix}} \tag{A.49}$$

Floor

The weight of the transverse floor beams is estimated by assuming the payload weight is distributed uniformly over the floor, producing the shear and bending moment distributions shown in Figure A.4. The weight of the floor itself is typically much smaller than the payload and is neglected. The floor beams are assumed to by sized by some load factor N_{land}, which is typically the emergency landing case and greater than the usual in-flight load factor N_{lift} which sizes most of the airframe. This gives to following total distributed load on the floor.

$$\mathcal{P}_{\text{floor}} = N_{\text{land}}(W_{\text{pay}} + W_{\text{seat}}) \tag{A.50}$$

The floor/wall joints are assumed to be pinned, with the double-bubble fuselage having an additional center floor support. The single-bubble fuselage can of course also have center supports under the floor. The maximum shear and bending moment seen by all the floor beams put together are then readily obtained from simple beam theory.

$$\mathcal{S}_{\text{floor}} = \frac{1}{2}\mathcal{P}_{\text{floor}} \qquad \text{(w/o support)} \tag{A.51}$$

$$\mathcal{S}_{\text{floor}} = \frac{5}{16}\,\mathcal{P}_{\text{floor}} \qquad \text{(with support)} \tag{A.52}$$

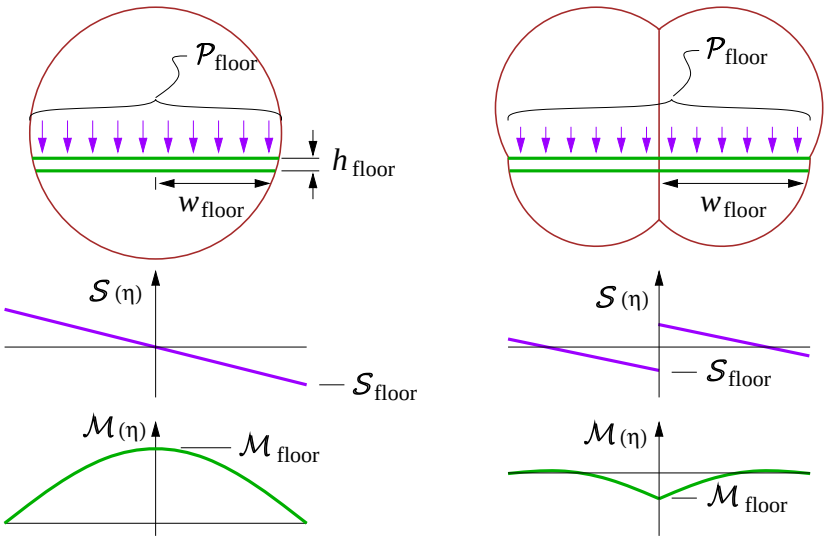

Figure A.4: Distributed floor load $\mathcal{P}_{\text{floor}}$, resulting in maximum shear $\mathcal{S}_{\text{floor}}$ and maximum bending moment $\mathcal{M}_{\text{floor}}$ in all the floor beams, without and with a center support.

$$\mathcal{M}_{\text{floor}} = \frac{1}{4}\,\mathcal{P}_{\text{floor}}\,w_{\text{floor}} \qquad \text{(w/o support)} \tag{A.53}$$

$$\mathcal{M}_{\text{floor}} = \frac{9}{256}\,\mathcal{P}_{\text{floor}}\,w_{\text{floor}} \qquad \text{(with support)} \tag{A.54}$$

$$w_{\text{floor}} \simeq w_{\text{db}} + R_{\text{fuse}} \tag{A.55}$$

Note that $w_{\text{db}} = 0$ for a single-bubble fuselage, so that the expression for the floor half-width w_{floor} above is valid in general.

For a given floor I-beam height h_{floor}, and max allowable cap stress σ_{floor} and shear-web stress τ_{floor}, the beams' total average cross-sectional area and corresponding weight are then determined. The added weight of the floor planking is determined from a specified weight/area density W''_{floor}.

$$A_{\text{floor}} = \frac{2.0\,\mathcal{M}_{\text{floor}}}{\sigma_{\text{floor}}\,h_{\text{floor}}} + \frac{1.5\,\mathcal{S}_{\text{floor}}}{\tau_{\text{floor}}} \tag{A.56}$$

$$\mathcal{V}_{\text{floor}} = 2\,w_{\text{floor}}\,A_{\text{floor}} \tag{A.57}$$

$$l_{\text{floor}} = x_{\text{shell}\,2} - x_{\text{shell}\,1} + 2R_{\text{fuse}} \tag{A.58}$$

$$W_{\text{floor}} = \rho_{\text{floor}}\,g\,\mathcal{V}_{\text{floor}} + 2\,w_{\text{floor}}\,l_{\text{floor}}\,W''_{\text{floor}} \tag{A.59}$$

$$x W_{\text{floor}} = \tfrac{1}{2}(x_{\text{shell}\,1} + x_{\text{shell}\,2})\,W_{\text{floor}} \tag{A.60}$$

Relation (A.56) assumes the beams are uniform in cross-section. Suitable taper of the cross section would reduce the 2.0 and 1.5 coefficients substantially, especially for the center-supported case for which the bending moment rapidly diminishes away from the center.

It's also important to recognize that if clamped ends rather than the assumed pinned end joints are used, and if the center support is present, then the hoop compliance of the fuselage frame cross-section shape will become important. Without doing the much more complicated deformation analysis of the entire fuselage frame + floor cross section, the conservative pinned-end and uniform beam assumptions are therefore deemed appropriate.

Tail cone

The tail cone average wall thickness is assumed to be sized by the torsion moment $\mathcal{Q}_{\rm v}$ imparted by the vertical tail, defined in terms of its maximum lift $L_{\rm vmax}$, span $b_{\rm v}$, and taper ratio $\lambda_{\rm v}$.

$$L_{\rm vmax} = q_{NE}\, S_{\rm v}\, C_{L{\rm vmax}} \tag{A.61}$$

$$\mathcal{Q}_{\rm v} = \frac{L_{\rm vmax}\, b_{\rm v}}{3}\frac{1+2\lambda_{\rm v}}{1+\lambda_{\rm v}} \tag{A.62}$$

Referring to Figure A.3, this $\mathcal{Q}_{\rm v}$ produces a shear flow $\tau_{\rm cone}\, t_{\rm cone}$ according to the torsion-shell relation

$$\mathcal{Q}_{\rm v} = 2A_{\rm cone}\, \tau_{\rm cone}\, t_{\rm cone} \tag{A.63}$$

where the cone's enclosed area $A_{\rm cone}$ is assumed to taper linearly with a taper ratio of $\lambda^2_{\rm cone}$. The cone radius $R_{\rm cone}$ then tapers to a ratio of $\lambda_{\rm cone}$, but nonlinearly. The taper extends from $x_{\rm shell\,2}$ to $x_{\rm conend}$, the latter being the endpoint of the cone's primary structure, roughly at the horizontal or vertical tail attachment.

$$A_{{\rm cone}(x)} = A_{\rm fuse}\left[1+(\lambda^2_{\rm cone}-1)\frac{x-x_{\rm shell\,2}}{x_{\rm conend}-x_{\rm shell\,2}}\right] \tag{A.64}$$

$$R_{{\rm cone}(x)} = R_{\rm fuse}\left[1+(\lambda^2_{\rm cone}-1)\frac{x-x_{\rm shell\,2}}{x_{\rm conend}-x_{\rm shell\,2}}\right]^{1/2} \tag{A.65}$$

Setting $\mathcal{Q}_{\rm v}$ to the moment imparted by the vertical tail lift gives the cone wall thickness $t_{\rm cone}$ and corresponding material volume and weight.

$$t_{{\rm cone}(x)} = \frac{\mathcal{Q}_{\rm v}}{2\tau_{\rm cone}A_{{\rm cone}(x)}} \tag{A.66}$$

$$\begin{aligned}\mathcal{V}_{\rm cone} &= \int_{x_{\rm shell\,2}}^{x_{\rm conend}} 2(\pi+2\theta_{\rm db})R_{\rm cone}\, t_{\rm cone}\, dx \\ &= \frac{\mathcal{Q}_{\rm v}}{\tau_{\rm cone}}\,\frac{\pi+2\theta_{\rm db}}{\pi+2\theta_{\rm db}+\sin 2\theta_{\rm db}}\,\frac{x_{\rm conend}-x_{\rm shell\,2}}{R_{\rm fuse}}\,\frac{2}{1+\lambda_{\rm cone}}\end{aligned} \tag{A.67}$$

$$W_{\rm cone} = \rho_{\rm cone}\, g\, \mathcal{V}_{\rm cone}(1+f_{\rm string}+f_{\rm frame}+f_{\rm fadd}) \tag{A.68}$$

$$x W_{\rm cone} = \tfrac{1}{2}(x_{\rm shell\,2}+x_{\rm conend})\, W_{\rm cone} \tag{A.69}$$

A.2.3 Fuselage Bending Loads

In addition to the pressurization and torsion loads, the fuselage also sees bending loads from its distributed weight load plus the tail weight and airloads. In the case where the pressurization-sized shell is not sufficient to withstand this, additional bending material area is assumed to be added at the top and bottom (total of $A_{{\rm hbend}(x)}$), and also sides of the shell (total of $A_{{\rm vbend}(x)}$), as shown in Figure A.3. If the shell is sufficiently strong, then these areas will be zero.

Lumped tail weight and location for fuselage stresses

For simplicity in the fuselage bending stress analysis to be considered next, both the horizontal and vertical tails, the tailcone, and any APU or rear-engine weight loads (if present) are lumped into their summed weight $W_{\rm tail}$, which is assumed to be located at the corresponding mass centroid location $x_{\rm tail}$. The tail aero loads are also assumed to act at this point.

$$W_{\rm tail} = W_{\rm htail} + W_{\rm vtail} + W_{\rm cone} \ [\ + W_{\rm apu} + W_{\rm eng}] \tag{A.70}$$

$$x_{\rm tail} = \frac{x_{\rm htail} W_{\rm htail} + x_{\rm vtail} W_{\rm vtail} + \frac{1}{2}(x_{\rm shell\,2} + x_{\rm conend}) W_{\rm cone} \ [\ + x_{\rm apu} W_{\rm apu} + x_{\rm eng} W_{\rm eng}]}{W_{\rm tail}} \tag{A.71}$$

For the overall aircraft pitch balance and pitch stability analyses to be presented later, this lumping simplification will not be invoked.

Tail aero loads

An impulsive load on the horizontal or vertical tail will produce a direct static bending load on the aft fuselage. It will also result in an overall angular acceleration of the aircraft, whose distributed inertial-reaction loads will tend to alleviate the tail's static bending loads. These effects are captured by the inertial-relief factor $r_{\rm M}$ evaluated just to the right of the wingbox, which takes on the two different values $r_{\rm Mh}$ and $r_{\rm Mv}$ due to the different wing inertias about the horizontal and vertical axes. Typical values are $r_{\rm Mh} \simeq 0.4$ and $r_{\rm Mv} \simeq 0.7$, with the latter applied only over the rear fuselage. The resulting net bending moment distributions are shown in Figure A.5, where the static case is the limit for an infinitely massive wing.

The maximum tail loads are set at a specified never-exceed dynamic pressure q_{NE}, and some assumed max-achievable lift coefficient for each surface.

$$L_{\rm h_{max}} = q_{NE}\, S_{\rm h}\, C_{L{\rm h_{max}}} \tag{A.72}$$

$$L_{\rm v_{max}} = q_{NE}\, S_{\rm v}\, C_{L{\rm v_{max}}} \tag{A.73}$$

$$(\mathcal{M}_{\rm h})_{\rm aero} = \begin{cases} r_{\rm Mh}\, L_{\rm h_{max}}\, (x_{\rm tail} - x) & , \quad x > x_{\rm wing} \\ r_{\rm Mh}\, L_{\rm h_{max}}\, (x + x_{\rm tail} - 2x_{\rm wing}) & , \quad x < x_{\rm wing} \end{cases} \tag{A.74}$$

$$(\mathcal{M}_{\rm v})_{\rm aero} = \begin{cases} r_{\rm Mv}\, L_{\rm v_{max}}\, (x_{\rm tail} - x) & , \quad x > x_{\rm wing} \\ 0.0 & , \quad x < x_{\rm wing} \end{cases} \tag{A.75}$$

$$r_{\rm M} = 1 - \frac{I_{\rm fuse}/2}{I_{\rm fuse} + I_{\rm wing}} - \frac{m_{\rm fuse}/4}{m_{\rm fuse} + m_{\rm wing}} \tag{A.76}$$

$$r_{\rm Mh} \simeq 0.4 \tag{A.77}$$

$$r_{\rm Mv} \simeq 0.7 \tag{A.78}$$

Landing gear loads

The maximum vertical load on the landing gear typically occurs in the emergency landing case, and subjects the fuselage to some vertical acceleration $N = N_{\rm land}$ which is specified. The fuselage distributed mass will then subject the fuselage to a bending load shown in Figure A.2.

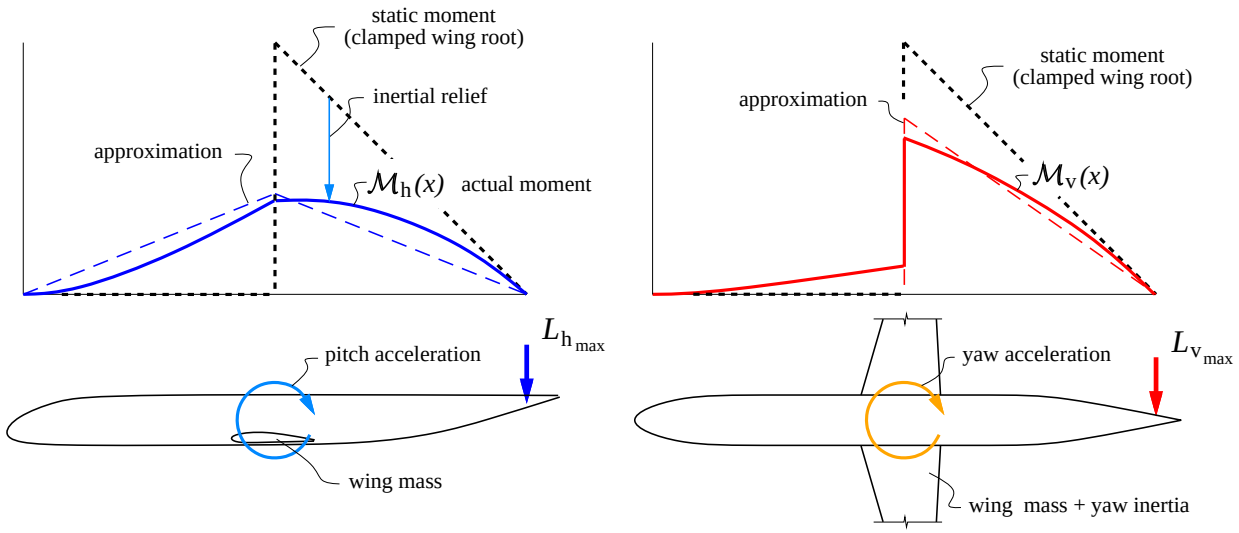

Figure A.5: Fuselage bending moments due to unbalanced horizontal and vertical tail aero loads. The static bending moment (dashed lines) is partly relieved by reaction loads from the overall angular acceleration.

Distributed and point weight loads

The fuselage is loaded by the payload weight W_{pay}, plus its own component weights W_{padd}, W_{shell} ... etc. which are all assumed to be uniformly distributed over the fuselage shell length l_{shell}. The overall tail weight W_{tail} is assumed to be a point load at x_{tail}. With all weights scaled up by a load factor N, plus the impulsive horizontal-tail aero load moment (A.74), gives the following quadratic+linear horizontal-axis fuselage bending moment distribution, also sketched in Figure A.2.

$$\begin{aligned} \mathcal{M}_{h(x)} &= N \frac{W_{\text{pay}}+W_{\text{padd}}+W_{\text{shell}}+W_{\text{window}}+W_{\text{insul}}+W_{\text{floor}}+W_{\text{seat}}}{2\, l_{\text{shell}}} (x_{\text{shell}\,2} - x)^2 \\ &+ (NW_{\text{tail}} + r_{\text{Mh}} L_h)(x_{\text{tail}} - x) \end{aligned} \tag{A.79}$$

Expression (A.79) has been constructed to represent the bending moment over the rear fuselage. Since the wing's inertial-reaction pitching moments are small compared to those of the tail and fuselage, the horizontal-axis bending moment is assumed to be roughly symmetric about the wing's center of lift at x_{wing}, as sketched in Figure A.2, so that (A.79) if reflected about x_{wing} also gives the bending moment over the front fuselage. For the same reason, the fixed weight W_{fix} is assumed to be concentrated near the aircraft nose, and hence it does not impose either a distributed load or a point load on the rear fuselage, and hence does not appear in (A.79).

Added horizontal-axis bending material

The total bending moment $\mathcal{M}_{h(x)}$ defined by (A.79) is used to size the added horizontal-axis bending area $A_{\text{hbend}(x)}$. Two loading scenarios are considered:

1. Maximum load factor at V_{NE}

$$N = N_{\text{lift}} \tag{A.80}$$
$$L_{\text{h}} = L_{\text{h}_{\text{max}}} \tag{A.81}$$

2. Emergency landing impact

$$N = N_{\text{land}} \tag{A.82}$$
$$L_{\text{h}} = 0 \tag{A.83}$$

The scenario which gives the larger added structural weight will be selected.

The maximum axial stress, which is related to the sum of the bending and pressurization strains, is limited everywhere to some maximum allowable value σ_{bend}.

$$E_{\text{bend}}\epsilon_{x(x)} = E_{\text{bend}}\left(\epsilon_{\text{bend}(x)} + \epsilon_{\text{press}}\right) \leq \sigma_{\text{bend}} \tag{A.84}$$
$$r_{_E}\left(\frac{\mathcal{M}_{\text{h}(x)}\, h_{\text{fuse}}}{I_{\text{hshell}} + r_{_E}\, I_{\text{hbend}(x)}} + \frac{\Delta p}{2}\frac{R_{\text{fuse}}}{t_{\text{shell}}}\right) \leq \sigma_{\text{bend}} \tag{A.85}$$
$$\text{where} \qquad h_{\text{fuse}} = R_{\text{fuse}} + \tfrac{1}{2}\Delta R_{\text{fuse}} \tag{A.86}$$

Relation (A.85) can then be solved for the required $I_{\text{hbend}(x)}$ and the associated $A_{\text{hbend}(x)}$.

$$I_{\text{hbend}(x)} = \max\left(\frac{\mathcal{M}_{(x)}\, h_{\text{fuse}}}{\sigma_{\text{Mh}}} - \frac{I_{\text{hshell}}}{r_{_E}}\ ,\ 0\right) \tag{A.87}$$
$$\text{where} \qquad \sigma_{\text{Mh}} = \sigma_{\text{bend}} - r_{_E}\frac{\Delta p}{2}\frac{R_{\text{fuse}}}{t_{\text{shell}}} \tag{A.88}$$
$$A_{\text{hbend}(x)} = \frac{I_{\text{hbend}(x)}}{h_{\text{fuse}}^2} = A_2(x_{\text{shell}_2} - x)^2 + A_1(x_{\text{tail}} - x) + A_0 \tag{A.89}$$
$$\text{where} \qquad A_2 = \frac{N(W_{\text{pay}} + W_{\text{padd}} + W_{\text{shell}} + W_{\text{window}} + W_{\text{insul}} + W_{\text{floor}} + W_{\text{seat}})}{2\, l_{\text{shell}}\, h_{\text{fuse}}\, \sigma_{\text{Mh}}} \tag{A.90}$$
$$A_1 = \frac{NW_{\text{tail}} + r_{\text{Mh}} L_{\text{h}}}{h_{\text{fuse}}\, \sigma_{\text{Mh}}} \tag{A.91}$$
$$A_0 = -\frac{I_{\text{hshell}}}{r_{_E}\, h_{\text{fuse}}^2} \tag{A.92}$$

The volume and weight of the added bending material is defined by integration of A_{hbend}, from the wing box to the location $x = x_{\text{hbend}}$ where $A_{\text{hbend}} = 0$ in the quadratic definition (A.89). If this quadratic has no real solution, then the inequality (A.79) holds for $\mathcal{M}_{\text{h}(x)} = 0$ everywhere, and no added bending material is needed.

Two separate integration limits are used for the front and back fuselage, to account for the shifted wing box for a swept wing. The integral for $\mathcal{V}_{\text{hbend}_f}$ for the front fuselage is actually computed over the back, by exploiting the assumed symmetry of $\mathcal{M}_{\text{h}(x)}$ and $A_{\text{hbend}(x)}$ about $x = x_{\text{wing}}$. The wing box offset Δx_{wing} is computed later in the wing-sizing section, so here it is taken from the previous iteration.

$$x_f = x_{\text{wing}} + \Delta x_{\text{wing}} + \tfrac{1}{2} c_o \bar{w} \tag{A.93}$$

$$
\begin{aligned}
x_b &= x_{\text{wing}} - \Delta x_{\text{wing}} + \tfrac{1}{2} c_o \bar{w} && \text{(A.94)} \\
\mathcal{V}_{\text{hbend}_f} &= \int_{x_f}^{x_{\text{hbend}}} A_{\text{hbend}(x)}\, dx \\
&= A_2 \frac{1}{3}\left[(x_{\text{shell}_2} - x_f)^3 - (x_{\text{shell}_2} - x_{\text{hbend}})^3\right] \\
&+ A_1 \frac{1}{2}\left[(x_{\text{tail}} - x_f)^2 - (x_{\text{tail}} - x_{\text{hbend}})^2\right] \\
&+ A_0 (x_{\text{hbend}} - x_f) && \text{(A.95)} \\
\mathcal{V}_{\text{hbend}_b} &= \int_{x_b}^{x_{\text{hbend}}} A_{\text{hbend}(x)}\, dx \\
&= A_2 \frac{1}{3}\left[(x_{\text{shell}_2} - x_b)^3 - (x_{\text{shell}_2} - x_{\text{hbend}})^3\right] \\
&+ A_1 \frac{1}{2}\left[(x_{\text{tail}} - x_b)^2 - (x_{\text{tail}} - x_{\text{hbend}})^2\right] \\
&+ A_0 (x_{\text{hbend}} - x_b) && \text{(A.96)} \\
\mathcal{V}_{\text{hbend}_c} &= \frac{1}{2}\left[A_{\text{hbend}(x_b)} + A_{\text{hbend}(x_f)}\right] c_o \bar{w} && \text{(A.97)} \\
\mathcal{V}_{\text{hbend}} &= \mathcal{V}_{\text{hbend}_f} + \mathcal{V}_{\text{hbend}_c} + \mathcal{V}_{\text{hbend}_b} && \text{(A.98)} \\
W_{\text{hbend}} &= \rho_{\text{bend}}\, g\, \mathcal{V}_{\text{hbend}} && \text{(A.99)} \\
x W_{\text{hbend}} &= x_{\text{wing}} W_{\text{hbend}} && \text{(A.100)}
\end{aligned}
$$

Added vertical-axis bending material

The vertical-axis bending moment on the rear fuselage is entirely due to the airload on the vertical tail (A.75), reduced by the r_{Mv} factor to account for inertial relief.

$$
\mathcal{M}_{\text{v}(x)} = r_{\text{Mv}}\, L_{\text{v}_{\text{max}}} (x_{\text{tail}} - x) \qquad \text{(A.101)}
$$

Since the wing is assumed to react the local $\mathcal{M}_{\text{v}}$ via its large yaw inertia, as sketched in Figure A.5, the moment distribution (A.101) is imposed only on the rear fuselage. The required bending inertia $I_{\text{vbend}(x)}$ and area $A_{\text{vbend}(x)}$ are then sized to keep the axial stress constant. The defining relations follow the ones for the horizontal-axis case above.

$$
E_{\text{bend}} \epsilon_{x(x)} = r_E \left(\frac{\mathcal{M}_{\text{v}(x)}\, w_{\text{fuse}}}{I_{\text{vshell}} + r_E\, I_{\text{vbend}(x)}} + \frac{\Delta p}{2} \frac{R_{\text{fuse}}}{t_{\text{shell}}} \right) \le \sigma_{\text{bend}} \qquad \text{(A.102)}
$$

$$
\text{where} \qquad w_{\text{fuse}} = R_{\text{fuse}} + w_{\text{db}} \qquad \text{(A.103)}
$$

$$
I_{\text{vbend}(x)} = \max\left(\frac{\mathcal{M}_{\text{v}(x)}\, w_{\text{fuse}}}{\sigma_{\text{Mv}}} - \frac{I_{\text{vshell}}}{r_E} \;,\; 0 \right) \qquad \text{(A.104)}
$$

$$
\text{where} \qquad \sigma_{\text{Mv}} = \sigma_{\text{bend}} - r_E \frac{\Delta p}{2} \frac{R_{\text{fuse}}}{t_{\text{shell}}} \qquad \text{(A.105)}
$$

$$
A_{\text{vbend}(x)} = \frac{I_{\text{vbend}(x)}}{w_{\text{fuse}}^2} = B_1 (x_{\text{tail}} - x) + B_0 \qquad \text{(A.106)}
$$

$$
\text{where} \qquad B_1 = \frac{r_{\text{Mv}} L_{\text{v}}}{w_{\text{fuse}}\, \sigma_{\text{Mv}}} \qquad \text{(A.107)}
$$

$$B_0 \;=\; -\frac{I_{\text{vshell}}}{r_E\, w_{\text{fuse}}^2} \tag{A.108}$$

The volume and weight of the added bending material is defined by integration of $A_{\text{vbend}(x)}$ over the rear fuselage, from the rear of the wing box x_b, up to the point $x = x_{\text{vbend}}$ where $A_{\text{vbend}} = 0$ in definition (A.106).

$$\begin{aligned}
\mathcal{V}_{\text{vbend}_b} &= \int_{x_b}^{x_{\text{vbend}}} A_{\text{vbend}(x)}\, dx \\
&= B_1 \frac{1}{2}\left[(x_{\text{tail}} - x_b)^2 - (x_{\text{tail}} - x_{\text{vbend}})^2\right] \;+\; B_0\,(x_{\text{vbend}} - x_b) && \text{(A.109)} \\
\mathcal{V}_{\text{vbend}_c} &= \frac{1}{2} A_{\text{vbend}(x_b)}\, c_o \bar{w} && \text{(A.110)} \\
\mathcal{V}_{\text{vbend}} &= \mathcal{V}_{\text{vbend}_c} \;+\; \mathcal{V}_{\text{vbend}_b} && \text{(A.111)} \\
W_{\text{vbend}} &= \rho_{\text{bend}}\, g \mathcal{V}_{\text{vbend}} && \text{(A.112)} \\
x\!W_{\text{vbend}} &= \tfrac{1}{3}(2x_{\text{wing}} + x_{\text{vbend}}) W_{\text{vbend}} && \text{(A.113)}
\end{aligned}$$

For simplicity, the $W_{\text{hbend}}, W_{\text{vbend}}$ weights' contributions to $\mathcal{M}_{\text{h}}$ are excluded from (A.79) and the subsequent calculations. A practical reason is that the added material does not have a simple distribution, and hence would greatly complicate the $\mathcal{M}_{\text{h}(x)}$ function, thus preventing the analytic integration of the added material's weight. Fortunately, the added bending material is localized close to the wing centroid and hence its contribution to the overall bending moment is very small in any case, so neglecting its weight on the loading is well justified at this level of approximation.

A.2.4 Total Fuselage Weight

The total fuselage weight includes the shell with stiffeners, tailcone, floor beams, fixed weight, payload-proportional equipment and material, seats, and the added horizontal and vertical-axis bending material.

$$\begin{aligned}
W_{\text{fuse}} &= W_{\text{fix}} \;+\; W_{\text{apu}} \;+\; W_{\text{padd}} \;+\; W_{\text{seat}} \\
&\quad + W_{\text{shell}} \;+\; W_{\text{cone}} \;+\; W_{\text{window}} \;+\; W_{\text{insul}} \;+\; W_{\text{floor}} \\
&\quad + W_{\text{hbend}} \;+\; W_{\text{vbend}} && \text{(A.114)} \\
x\!W_{\text{fuse}} &= x\!W_{\text{fix}} + x\!W_{\text{apu}} + x\!W_{\text{padd}} + x\!W_{\text{seat}} \\
&\quad + x\!W_{\text{shell}} + x\!W_{\text{cone}} + x\!W_{\text{window}} + x\!W_{\text{insul}} + x\!W_{\text{floor}} \\
&\quad + x\!W_{\text{hbend}} + x\!W_{\text{vbend}} && \text{(A.115)}
\end{aligned}$$

A.2.5 Wing or Tail Planform

The surface geometry relations derived below correspond to the wing. Most of these apply equally to the tails if the wing parameters are simply replaced with the tail counterparts. The exceptions which pertail to only the wing will be indicated with "(Wing only)" in the subsection title.

Chord distribution

The wing or tail surface is assumed to have a two-piece linear planform with constant sweep Λ, shown in Figure A.6. The inner and outer surface planforms are defined in terms of the center chord c_o and the inner and outer taper ratios.

$$\lambda_s = c_s/c_o \tag{A.116}$$
$$\lambda_t = c_t/c_o \tag{A.117}$$

Similarly, the spanwise dimensions are defined in terms of the span b and the normalized spanwise coordinate η.

$$\eta = 2y/b \tag{A.118}$$
$$\eta_o = b_o/b \tag{A.119}$$
$$\eta_s = b_s/b \tag{A.120}$$

For generality, the wing center box width b_o is assumed to be different from the fuselage width to allow possibly strongly non-circular fuselage cross-sections. It will also be different for the tail surfaces. A planform break inner span b_s is defined, where possibly also a strut or engine is attached. Setting $b_s = b_o$ and $c_s = c_o$ will recover a single-taper surface.

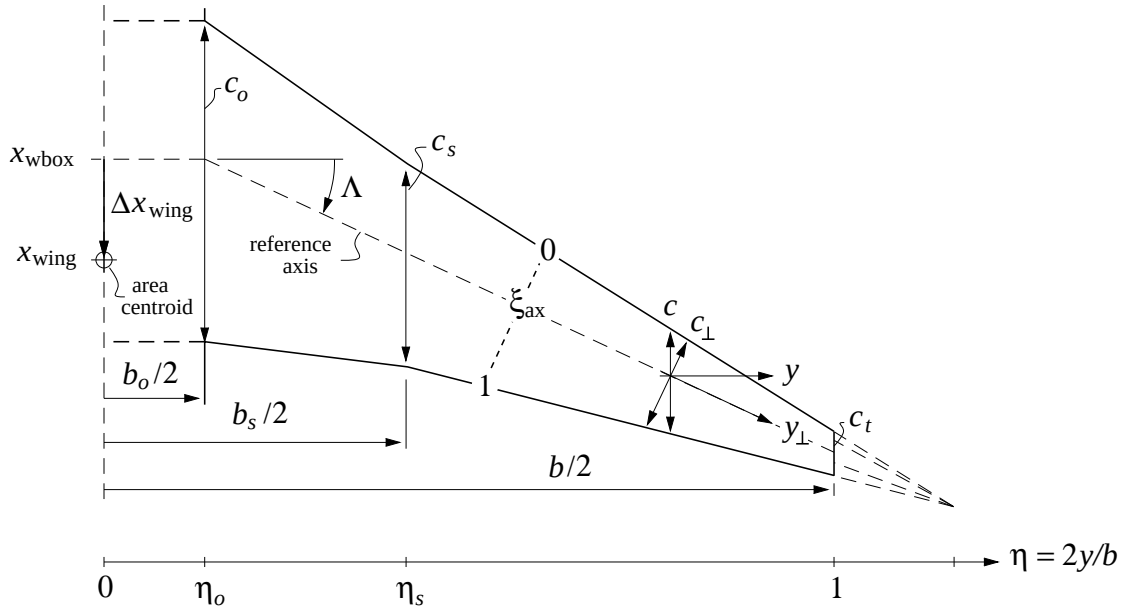

Figure A.6: Piecewise-linear wing or tail surface planform, with break at η_s.

It's convenient to define the piecewise-linear normalized chord function $C_{(\eta)}$.

$$\frac{c_{(\eta)}}{c_o} \equiv C_{(\eta\,;\eta_o,\eta_s,\lambda_s,\lambda_t)} = \begin{cases} 1 & , \quad 0 < \eta < \eta_o \\ 1 + (\lambda_s - 1)\dfrac{\eta-\eta_o}{\eta_s-\eta_o} & , \quad \eta_o < \eta < \eta_s \\ \lambda_s + (\lambda_t - \lambda_s)\dfrac{\eta-\eta_s}{1-\eta_s} & , \quad \eta_s < \eta < 1 \end{cases} \tag{A.121}$$

The following integrals will be useful for area, volume, shear, and moment calculations.

$$\int_0^{\eta_o} C\,d\eta = \eta_o \tag{A.122}$$

$$\int_{\eta_o}^{\eta_s} C\,d\eta = \frac{1}{2}(1+\lambda_s)(\eta_s-\eta_o) \tag{A.123}$$

$$\int_{\eta_s}^{1} C\,d\eta = \frac{1}{2}(\lambda_s+\lambda_t)(1-\eta_s) \tag{A.124}$$

$$\int_0^{\eta_o} C^2\,d\eta = \eta_o \tag{A.125}$$

$$\int_{\eta_o}^{\eta_s} C^2\,d\eta = \frac{1}{3}(1+\lambda_s+\lambda_s^2)(\eta_s-\eta_o) \tag{A.126}$$

$$\int_{\eta_s}^{1} C^2\,d\eta = \frac{1}{3}(\lambda_s^2+\lambda_s\lambda_t+\lambda_t^2)(1-\eta_s) \tag{A.127}$$

$$\int_{\eta_o}^{\eta_s} C\,(\eta-\eta_o)\,d\eta = \frac{1}{6}(1+2\lambda_s)(\eta_s-\eta_o)^2 \tag{A.128}$$

$$\int_{\eta_s}^{1} C\,(\eta-\eta_s)\,d\eta = \frac{1}{6}(\lambda_s+2\lambda_t)(1-\eta_s)^2 \tag{A.129}$$

$$\int_{\eta_o}^{\eta_s} C^2\,(\eta-\eta_o)\,d\eta = \frac{1}{12}(1+2\lambda_s+3\lambda_s^2)(\eta_s-\eta_o)^2 \tag{A.130}$$

$$\int_{\eta_s}^{1} C^2\,(\eta-\eta_s)\,d\eta = \frac{1}{12}(\lambda_s^2+2\lambda_s\lambda_t+3\lambda_t^2)(1-\eta_s)^2 \tag{A.131}$$

Surface area and aspect ratio

The surface area S is defined as the exposed surface area plus the fuselage carryover area.

$$S = 2\int_0^{b/2} c\,dy = c_o\,b\,K_c \tag{A.132}$$

$$\text{where} \qquad K_c = \int_0^1 C\,d\eta = \eta_o + \tfrac{1}{2}(1+\lambda_s)(\eta_s-\eta_o) + \tfrac{1}{2}(\lambda_s+\lambda_t)(1-\eta_s) \tag{A.133}$$

The aspect ratio is then defined in the usual way. This will also allow relating the root chord to the span and the taper ratios.

$$AR = \frac{b^2}{S} \tag{A.134}$$

It is also useful to define the wing's mean aerodynamic chord c_{ma} and area-centroid offset Δx_{wing} from the center axis.

$$\frac{c_{\text{ma}}}{c_o} = \frac{2}{S}\int_0^{b/2} c^2\,dy = \frac{K_{cc}}{K_c} \tag{A.135}$$

$$\Delta x_{\text{wing}} = \frac{2}{S}\int_{b_o/2}^{b/2} c\,(y-y_o)\tan\Lambda\,dy = \frac{K_{cx}}{K_c}\,b\,\tan\Lambda \tag{A.136}$$

$$x_{\text{wing}} = x_{\text{wbox}} + \Delta x_{\text{wing}} \tag{A.137}$$

$$\text{where} \quad K_{cc} = \int_0^1 C^2\,d\eta$$

$$= \eta_o + \frac{1}{3}(1+\lambda_s+\lambda_s^2)(\eta_s-\eta_o) + \frac{1}{3}(\lambda_s^2+\lambda_s\lambda_t+\lambda_t^2)(1-\eta_s) \quad \text{(A.138)}$$

$$K_{cx} = \int_{\eta_o}^{1} C\,(\eta-\eta_o)\,d\eta$$

$$= \frac{1}{12}(1+2\lambda_s)(\eta_s-\eta_o)^2 + \frac{1}{12}(\lambda_s+2\lambda_t)(1-\eta_s)^2 + \frac{1}{4}(\lambda_s+\lambda_t)(1-\eta_s)(\eta_s-\eta_o) \quad \text{(A.139)}$$

The wing area centroid is used in the fuselage bending load calculations as described earlier.

Reference quantities

The aircraft reference quantities are chosen to be simply the values for the wing.

$$b_{\text{ref}} = (b)_{\text{wing}} \quad \text{(A.140)}$$

$$S_{\text{ref}} = (S)_{\text{wing}} \quad \text{(A.141)}$$

$$AR_{\text{ref}} = (AR)_{\text{wing}} \quad \text{(A.142)}$$

For normalizing pitching moments the mean aerodynamic chord is traditionally used.

$$c_{\text{ref}} = c_{MA} \quad \text{(A.143)}$$

$$c_{MA} \equiv \frac{2}{S_{\text{ref}}}\int_0^{b/2} c^2\,dy = \frac{c_o^2\,b}{S_{\text{ref}}}\int_0^1 C^2\,d\eta$$

$$= \frac{c_o^2\,b}{S_{\text{ref}}}\left[\,\eta_o + \frac{1}{3}(1+\lambda_s+\lambda_s^2)(\eta_s-\eta_o) + \frac{1}{3}(\lambda_s^2+\lambda_s\lambda_t+\lambda_t^2)(1-\eta_s)\,\right] \quad \text{(A.144)}$$

A.2.6 Surface Airloads

Lift distribution

The surface lift distribution $\tilde{p}$ is defined in terms of a baseline piecewise-linear distribution $p_{(\eta)}$ defined like the chord planform, but with its own taper ratios γ_s and γ_t. These are actually defined using local section c_ℓ factors $r_{c_{\ell s}}$ and $r_{c_{\ell t}}$.

$$\gamma_s = r_{c_{\ell s}}\,\lambda_s \quad \text{(A.145)}$$

$$\gamma_t = r_{c_{\ell t}}\,\lambda_t \quad \text{(A.146)}$$

$$\frac{p_{(\eta)}}{p_o} \equiv P_{(\eta\,;\,\eta_o,\eta_s,\gamma_s,\gamma_t)} = \begin{cases} 1 & , \quad 0<\eta<\eta_o \\ 1+(\gamma_s-1)\dfrac{\eta-\eta_o}{\eta_s-\eta_o} & , \quad \eta_o<\eta<\eta_s \\ \gamma_s+(\gamma_t-\gamma_s)\dfrac{\eta-\eta_s}{1-\eta_s} & , \quad \eta_s<\eta<1 \end{cases} \quad \text{(A.147)}$$

To get the actual aerodynamic load $\tilde{p}$, lift corrections ΔL_o and ΔL_t are applied to account for the fuselage carryover and tip lift rolloff, as sketched in Figure A.7. The detailed shapes of these modifications are not specified, but instead only their integrated loads are defined by the following integral relation.

$$\frac{L_{\text{wing}}}{2} = \int_0^{b/2}\tilde{p}\,dy = \int_0^{b/2} p\,dy + \Delta L_o + \Delta L_t \quad \text{(A.148)}$$

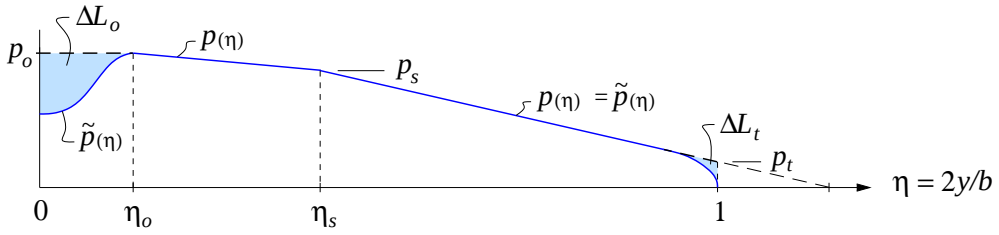

Figure A.7: Piecewise-linear aerodynamic load $\tilde{p}_{(\eta)}$, with modifications at center and tip.

The corrections are specified in terms of the center load magnitude p_o and the f_{L_o}, f_{L_t} adjustment factors.

$$\Delta L_o \;=\; f_{L_o}\, p_o\, \frac{b_o}{2} \;=\; f_{L_o}\, p_o\, \frac{b}{2}\, \eta_o \tag{A.149}$$

$$\Delta L_t \;=\; f_{L_t}\, p_t\, c_t \;=\; f_{L_t}\, p_o\, c_o\, \gamma_t\, \lambda_t \tag{A.150}$$

$$f_{L_o} \;\simeq\; -0.5 \tag{A.151}$$

$$f_{L_t} \;\simeq\; -0.05 \tag{A.152}$$

Lift load magnitude (Wing only)

The wing's p_o center loading magnitude is determined by requiring that the aerodynamic loading integrated over the whole span is equal to the total weight times the load factor, minus the tail lift.

$$2\int_0^{b/2} \tilde{p}_{(\eta)}\, dy \;=\; p_o\, b \int_0^1 P_{(\eta)}\, d\eta \;+\; 2\Delta L_o \;+\; 2\Delta L_t \;=\; NW \;-\; (L_{\text{htail}})_N \tag{A.153}$$

For structural sizing calculations $N = N_{\text{lift}}$ is chosen, and the appropriate value of $(L_{\text{htail}})_N$ is the worst-case (most negative) tail lift expected in the critical sizing case. One possible choice is the trimmed tail load at dive speed, where N_{lift} is most likely to occur.

The wing area (A.132) and aspect ratio (A.134) definitions allow the root chord and the tip lift drop (A.150) to be expressed as

$$c_o \;=\; b\, K_o \tag{A.154}$$

$$\Delta L_t \;=\; f_{L_t}\, p_o\, b\, K_o\, \gamma_t\, \lambda_t \tag{A.155}$$

$$\text{where} \qquad K_o \;=\; \frac{1}{K_c\, AR} \tag{A.156}$$

so that (A.153) can be evaluated to the following. The $P_{(\eta)}$ integrals have the form as for $C_{(\eta)}$, given by (A.122)–(A.131), but with the λ's replaced by γ's.

$$p_o\, b\, K_p \;=\; NW - (L_{\text{htail}})_N \tag{A.157}$$

$$\text{where} \qquad K_p \;=\; \eta_o + \tfrac{1}{2}(1{+}\gamma_s)(\eta_s{-}\eta_o) + \tfrac{1}{2}(\gamma_s{+}\gamma_t)(1{-}\eta_s) \;+\; f_{L_o}\eta_o \;+\; 2 f_{L_t} K_o \gamma_t \lambda_t \tag{A.158}$$

The root and planform-break loadings can then be explicitly determined.

$$p_o = \frac{NW - (L_{\text{htail}})_N}{K_p\, b} \tag{A.159}$$

$$p_s = p_o\, \gamma_s \tag{A.160}$$

$$p_t = p_o\, \gamma_t \tag{A.161}$$

Surface pitching moment

The surface's reference axis is at some specified chordwise fractional location ξ_{ax}, as shown in Figure A.6. The profile pitching moment acts along the span-axis coordinate $y_\perp$, and scales with the normal-plane chord $c_\perp$. These are shown in Figure A.6, and related to the spanwise and streamwise quantities via the sweep angle.

$$y_\perp = y/\cos\Lambda \tag{A.162}$$

$$c_\perp = c\, \cos\Lambda \tag{A.163}$$

$$V_\perp = V_\infty\, \cos\Lambda \tag{A.164}$$

The airfoil's pitching moment contribution shown in Figure A.8 is

$$dM_{y_\perp} = \frac{1}{2}\rho V_\perp^2\, c_\perp^2\, c_m\, dy_\perp \tag{A.165}$$

$$c_{m(\eta)} = \begin{cases} c_{m_o} & , \quad 0 < \eta < \eta_o \\ c_{m_o} + (c_{m_s} - c_{m_o})\dfrac{\eta-\eta_o}{\eta_s-\eta_o} & , \quad \eta_o < \eta < \eta_s \\ c_{m_s} + (c_{m_t} - c_{m_s})\dfrac{\eta-\eta_s}{1-\eta_s} & , \quad \eta_s < \eta < 1 \end{cases} \tag{A.166}$$

and including the contribution of the lift load $\tilde{p}$ with its moment arm gives the following overall wing pitching moment ΔM_{wing} increment about the axis center location.

$$d\Delta M_{\text{wing}} = \tilde{p}\left[c_\perp\left(\xi_{\text{ax}} - \tfrac{1}{4}\right)\cos\Lambda - (y - y_o)\tan\Lambda\right] dy + dM_{y_\perp}\cos\Lambda \tag{A.167}$$

Integrating this along the whole span then gives the total surface pitching moment about its root axis.

$$\begin{aligned} \Delta M_{\text{wing}} &= (p_o\, b_o + 2\Delta L_o)\, c_o\left(\xi_{\text{ax}} - \tfrac{1}{4}\right) \\ &+ \cos^2\Lambda\, b \int_{\eta_o}^{1} p_{(\eta)}\, c_{(\eta)} \left(\xi_{\text{ax}} - \tfrac{1}{4}\right) d\eta \\ &- \frac{b}{2}\tan\Lambda\, b \int_{\eta_o}^{1} p_{(\eta)}(\eta - \eta_o)\, d\eta \\ &+ 2\Delta L_t \left[c_o \lambda_t \left(\xi_{\text{ax}} - \tfrac{1}{4}\right)\cos^2\Lambda - \frac{b}{2}(1-\eta_o)\tan\Lambda\right] \\ &+ \frac{1}{2}\rho V_\infty^2\, \cos^4\Lambda\, b \int_{\eta_o}^{1} c_{m(\eta)}\, c_{(\eta)}{}^2\, d\eta \end{aligned} \tag{A.168}$$

$$\Delta M_{\text{wing}} = p_o\, b\, c_o\, \eta_o\, (1 + f_{Lo})\left(\xi_{\text{ax}} - \tfrac{1}{4}\right)$$

$$
\begin{aligned}
&+\ p_o\, b\, c_o \left(\xi_{\rm ax}-\tfrac{1}{4}\right)\cos^2\Lambda\ \frac{1}{3}\Big[\ \Big(1+\tfrac{1}{2}\,(\lambda_s+\gamma_s)+\lambda_s\gamma_s\Big)\,(\eta_s-\eta_o) \\
&\qquad\qquad +\ \Big(\lambda_s\gamma_s+\tfrac{1}{2}\,(\lambda_s\gamma_t+\gamma_s\lambda_t)+\lambda_t\gamma_t\Big)\,(1-\eta_s)\ \Big] \\
&-\ p_o\, b\, c_o\ \frac{\tan\Lambda}{K_o}\ \frac{1}{12}\Big[\ (1+2\gamma_s)\,(\eta_s-\eta_o)^2\ +\ (\gamma_s+2\gamma_t)\,(1-\eta_s)^2\ +\ 3\,(\gamma_s+\gamma_t)\,(\eta_s-\eta_o)(1-\eta_s)\ \Big] \\
&+\ 2\,p_o\, b\, c_o\, f_{L_t}\,\lambda_t\,\gamma_t\left[K_o\lambda_t\left(\xi_{\rm ax}-\tfrac{1}{4}\right)\cos^2\Lambda\ -\ \tfrac{1}{2}(1-\eta_o)\ \tan\Lambda\right] \\
&+\ \frac{1}{2}\rho V_\infty^2\, S\, c_o\ \frac{\cos^4\Lambda}{K_c}\frac{1}{12}\Big[\Big(c_{m_o}(3+2\lambda_s+\lambda_s^2)+c_{m_s}(3\lambda_s^2+2\lambda_s+1)\Big)\,(\eta_s-\eta_o) \\
&\qquad\qquad +\Big(c_{m_s}(3\lambda_s^2+2\lambda_s\lambda_t+\lambda_t^2)+c_{m_t}(3\lambda_t^2+2\lambda_s\lambda_t+\lambda_s^2)\Big)\,(1-\eta_s)\Big] \qquad \text{(A.169)}
\end{aligned}
$$

By using the relation

$$
p_o\, b\ \ =\ \ \frac{1}{2}\rho V_\infty^2\, S\ \frac{1}{K_p}\left(C_L-\frac{S_{\rm h}}{S}C_{L_{\rm h}}\right) \qquad \text{(A.170)}
$$

equation (A.169) gives the equivalent pitching moment coefficient constant and C_L derivative.

$$
\Delta C_{M_{\rm wing}}\ \equiv\ \frac{\Delta M_{\rm wing}}{\frac{1}{2}\rho V_\infty^2 S c_o}\ =\ \Delta C_{M_0}\ +\ \frac{dC_M}{dC_L}\left(C_L-\frac{S_{\rm h}}{S}C_{L_{\rm h}}\right) \qquad \text{(A.171)}
$$

$$
\begin{aligned}
\frac{dC_M}{dC_L}\ &=\ \frac{1}{K_p}\Bigg\{\eta_o\,(1+f_{Lo})\Big(\xi_{\rm ax}-\tfrac{1}{4}\Big) \\
&\quad +\ \Big(\xi_{\rm ax}-\tfrac{1}{4}\Big)\cos^2\Lambda\ \frac{1}{3}\Big[\ \Big(1+\tfrac{1}{2}\,(\lambda_s+\gamma_s)+\lambda_s\gamma_s\Big)\,(\eta_s-\eta_o) \\
&\qquad\qquad +\ \Big(\lambda_s\gamma_s+\tfrac{1}{2}\,(\lambda_s\gamma_t+\gamma_s\lambda_t)+\lambda_t\gamma_t\Big)\,(1-\eta_s)\ \Big] \\
&\quad -\ \frac{\tan\Lambda}{K_o}\ \frac{1}{12}\Big[\ (1+2\gamma_s)\,(\eta_s-\eta_o)^2\ +\ (\gamma_s+2\gamma_t)\,(1-\eta_s)^2 \\
&\qquad\qquad +3\,(\gamma_s+\gamma_t)\,(\eta_s-\eta_o)(1-\eta_s)\ \Big] \\
&\quad +\ 2\,f_{L_t}\,\lambda_t\,\gamma_t\left[K_o\lambda_t\left(\xi_{\rm ax}-\tfrac{1}{4}\right)\cos^2\Lambda\ -\ \tfrac{1}{2}(1-\eta_o)\ \tan\Lambda\right]\Bigg\} \qquad \text{(A.172)}
\end{aligned}
$$

$$
\begin{aligned}
\Delta C_{M_0}\ &=\ \frac{\cos^4\Lambda}{K_c}\ \frac{1}{12}\Big[\Big(c_{m_o}(3+2\lambda_s+\lambda_s^2)+c_{m_s}(3\lambda_s^2+2\lambda_s+1)\Big)\,(\eta_s-\eta_o) \\
&\quad +\Big(c_{m_s}(3\lambda_s^2+2\lambda_s\lambda_t+\lambda_t^2)+c_{m_t}(3\lambda_t^2+2\lambda_s\lambda_t+\lambda_s^2)\Big)\,(1-\eta_s)\Big] \qquad \text{(A.173)}
\end{aligned}
$$

A.2.7 Wing or Tail Structural Loads

Figure A.9 shows the airload $\tilde{p}$ again, partly offset by weight load distributions of the structure and fuel, producing shear and bending moment distributions.

Shear and bending moment magnitudes

The $\mathcal{S}_s$, $\mathcal{M}_s$ magnitudes at η_s are set by integration of the assumed $p_{(\eta)}$ defined by (A.147), with the tip lift drop ΔL_t is included as a point load at the tip station. The weight loading

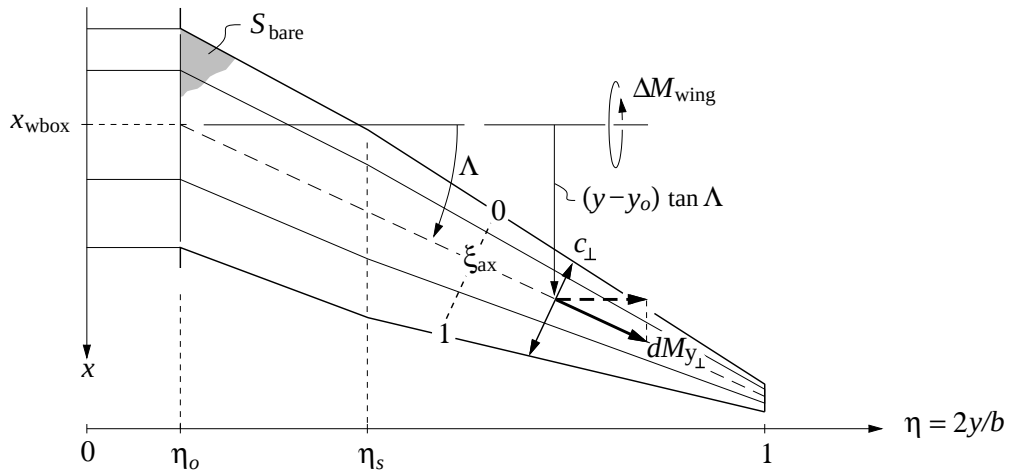

Figure A.8: Wing pitching moment quantities.

$w_{(\eta)}$ is also included via its overall outer panel weight W_{out} and weight moment $\Delta y W_{\text{out}}$, which are typically taken from a previous weight iteration.

$$\begin{aligned}
\mathcal{S}_s &= \frac{b}{2}\int_{\eta_s}^{1} p_{(\eta)}\, d\eta \;+\; \Delta L_t \;-\; N W_{\text{out}} \\
&= \frac{p_o\, b}{4}\,(\gamma_s{+}\gamma_t)(1{-}\eta_s) \;+\; \Delta L_t \;-\; N W_{\text{out}} \qquad \text{(A.174)} \\
\mathcal{M}_s &= \frac{b^2}{4}\int_{\eta_s}^{1} p_{(\eta)}\,(\eta{-}\eta_s)\, d\eta \;+\; \Delta L_t \frac{b}{2}(1{-}\eta_s) \;-\; N\,\Delta y W_{\text{out}} \\
&= \frac{p_o\, b^2}{24}(\gamma_s{+}2\gamma_t)(1{-}\eta_s)^2 \;+\; \Delta L_t \frac{b}{2}(1{-}\eta_s) \;-\; N\,\Delta y W_{\text{out}} \qquad \text{(A.175)}
\end{aligned}$$

Similarly, the $\mathcal{S}_o$ and $\mathcal{M}_o$ magnitudes at η_o are obtained by integrating the inner loading $p_{(\eta)}$, and adding the contributions of the strut load vertical component $\mathcal{R}$ and the spar compression component $\mathcal{P}$. The latter is applied at the strut attachment point, at a normal-offset distance n_s, as shown in Figure A.9.

$$\begin{aligned}
\mathcal{S}_o &= \mathcal{S}_s \;-\; \mathcal{R} \;+\; \frac{b}{2}\int_{\eta_o}^{\eta_s} p_{(\eta)}\; d\eta \;-\; N W_{\text{inn}} \\
&= \mathcal{S}_s \;-\; \mathcal{R} \;+\; \frac{p_o\, b}{4}\,(1{+}\gamma_s)(\eta_s{-}\eta_o) \;-\; N W_{\text{inn}} \qquad \text{(A.176)} \\
\mathcal{M}_o &= \mathcal{M}_s - \mathcal{P} n_s + (\mathcal{S}_s{-}\mathcal{R})\frac{b}{2}(\eta_s{-}\eta_o) \;+\; \frac{b^2}{4}\int_{\eta_o}^{\eta_s} p_{(\eta)}\,(\eta{-}\eta_o)\, d\eta \;-\; N\,\Delta y W_{\text{inn}} \\
&= \mathcal{M}_s - \mathcal{P} n_s + (\mathcal{S}_s{-}\mathcal{R})\frac{b}{2}(\eta_s{-}\eta_o) \;+\; \frac{p_o\, b^2}{24}(1{+}2\gamma_s)(\eta_s{-}\eta_o)^2 \;-\; N\,\Delta y W_{\text{inn}} \qquad \text{(A.177)}
\end{aligned}$$

Outer surface shear and bending moment distributions

Rather than obtain the exact $\mathcal{S}_{(\eta)}$ and $\mathcal{M}_{(\eta)}$ distributions by integration of the assumed $p_{(\eta)}$, $\mathcal{S}_s$ and $\mathcal{M}_s$ are simply scaled with the appropriate power of the local chord.

$$\mathcal{S}_{(\eta)} \;=\; \mathcal{S}_s \left(\frac{c}{c_s}\right)^2 \qquad , \qquad (\eta_s \le \eta \le 1) \qquad \text{(A.178)}$$

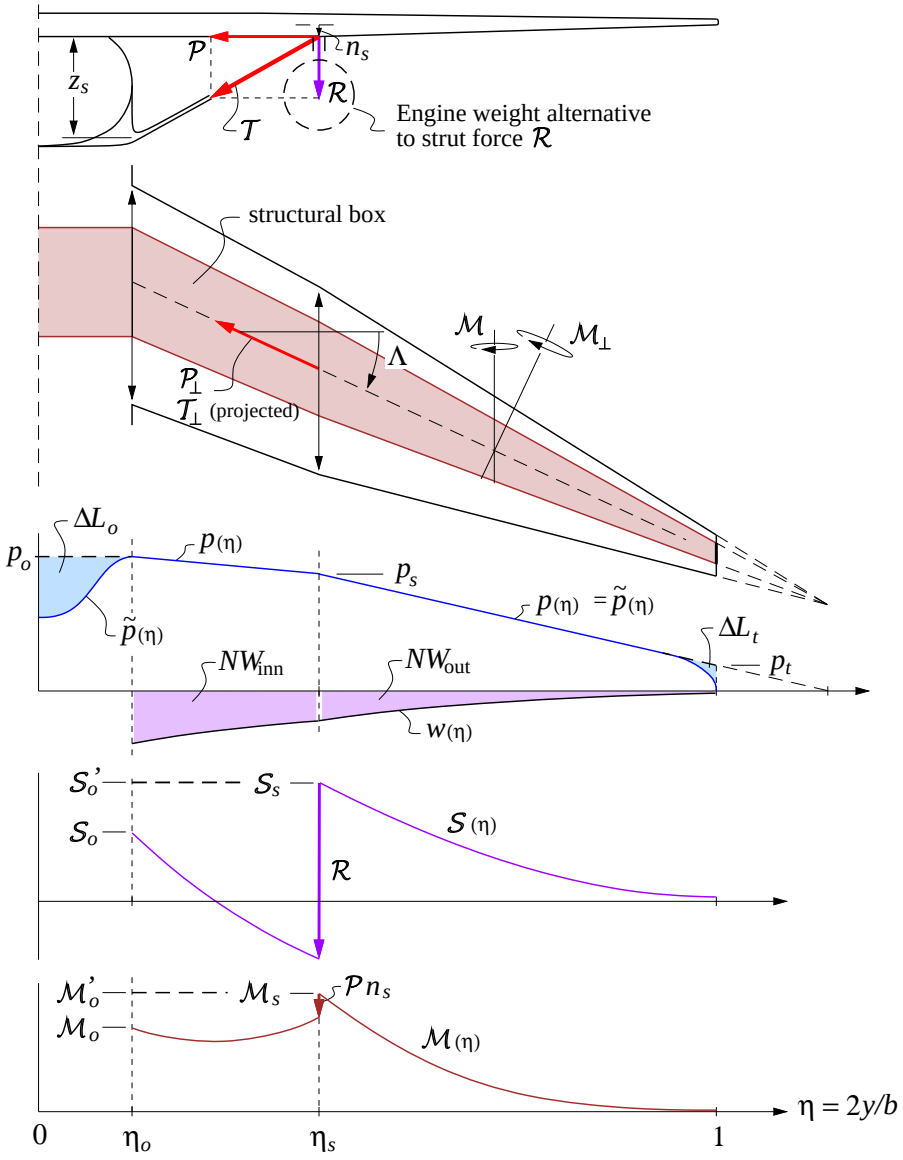

Figure A.9: Aerodynamic load $\tilde{p}_{(\eta)}$ and weight load $w_{(\eta)}$, with resulting shear and bending moments. An optional strut modifies the shear and bending moment as indicated.

$$\mathcal{M}_{(\eta)} \;=\; \mathcal{M}_s \left(\frac{c}{c_s}\right)^3 \quad , \qquad (\eta_s \le \eta \le 1) \tag{A.179}$$

These approximations are exact in the sharp-taper limit $\lambda_t, \gamma_t \to 0$, and are quite accurate for the small λ_t values typical of transport aircraft. Their main error is to slightly overpredict the loads near the tip where minimum-gauge constraints are most likely be needed anyway, so the approximation is deemed to be justified. Their great benefit is that they give a self-similar structural cross section for the entire cantilevered surface portion, and thus give simple explicit relations for the cross-section dimensions and the surface weight.

Strut or engine loads

The vertical load $\mathcal{R}$ applied at location η_s can represent either a strut load, or an engine weight. The two cases are described separately below.

Inner surface shear and moment — strut load case

In principle, both the strut anchor position η_s and the vertical strut load $\mathcal{R}$ can be optimized so as to achieve some best overall aircraft performance objective. A complication here is that multiple load conditions would need to be considered during the optimization, since a strut-braced wing optimized for a straight pullup case may not be able to withstand significant downloads, or may be too flexible in torsion and be susceptible to flutter. To avoid these great complications, it is assumed here that the strut is prestressed so as to give equal bending moments at the ends of the inner panel in level flight. The particular $\mathcal{R}$ which is then required in level flight is determined from (A.177).

$$\mathcal{M}_o = \mathcal{M}_s - \mathcal{P} n_s \qquad \text{(assumed)} \tag{A.180}$$

$$\mathcal{R} = \frac{p_o\, b}{12}(1+2\gamma_s)(\eta_s-\eta_o) + \mathcal{S}_s \tag{A.181}$$

Referring to Figure A.9, this required $\mathcal{R}$ then gives the projected strut tension $\mathcal{T}$ and the inner-wing projected compression $\mathcal{P}$ loads from the strut front-view geometry.

$$\ell_s = \sqrt{z_s^2 + \frac{b^2}{4}(\eta_s-\eta_o)^2} \tag{A.182}$$

$$\mathcal{T} = \mathcal{R}\,\frac{\ell_s}{z_s} \tag{A.183}$$

$$\mathcal{P} = \mathcal{R}\,\frac{b/2}{z_s}(\eta_s-\eta_o) \tag{A.184}$$

The applied vertical load (A.181) implicitly contains the strut's own weight, although this is immaterial in the present formulation. The associated strut tension force (A.183) which will be used to size the strut cross-section will still correctly give the maximum strut tension at the wing strut-attach location.

Although the inner shear and moment distributions can be obtained by integrating the inner loading $p_{(\eta)}$ and including the contribution of the strut tension, these inner $\mathcal{S}_{(\eta)}$ and $\mathcal{M}_{(\eta)}$ are not appropriate for sizing the inner wing structure at each spanwise location, since buckling, torsional stiffness, etc. typically come into play here. Instead, the inner wing structure will be sized to match the $\mathcal{S}_s$ and $\mathcal{M}_s$ values.

Inner surface shear and moment — engine load case

For the case of an engine attached at location η_s, the vertical load $\mathcal{R}$ is simply the engine weight times the load factor N. The new inner wing compression load is zero in this case.

$$\mathcal{R} = N\, W_{\text{eng}}/n_{\text{eng}} \tag{A.185}$$

$$\mathcal{T} = 0 \tag{A.186}$$

$$\mathcal{P} = 0 \tag{A.187}$$

The wing root shear and bending moment $\mathcal{S}_o$ and $\mathcal{M}_o$ are then obtained immediately from (A.176) and (A.177). Unlike in the strut case, these root loads will in general be greater than $\mathcal{S}_s$ and $\mathcal{M}_s$, so the inner wing panel structural elements need to be sized accordingly.

A.2.8 Wing or Tail Stresses

Normal-plane quantities

The wing and tail surface stress and weight analyses are performed in the cross-sectional plane, normal to the spanwise axis $y_\perp$ running along the wing box sketched in Figures A.6 and A.9. Together with the normal-plane coordinate and chord relations (A.162) and (A.163), the shear and bending moment are related to the corresponding airplane-axes quantities and to the sweep angle Λ as follows.

$$\mathcal{S}_\perp = \mathcal{S} \tag{A.188}$$

$$\mathcal{M}_\perp = \mathcal{M}/\cos\Lambda \tag{A.189}$$

Wing or tail section

The assumed wing or tail airfoil and structural box cross-section is shown in Figure A.10. The box is assumed to be the only structurally-significant element, with the slats, flaps, and spoilers (if any), represented only by added weight. It is convenient to define all dimensions as ratios with the local normal-plane chord $c_\perp$.

$$\bar{h} = \frac{h_{\text{wbox}}}{c_\perp} \tag{A.190}$$

$$\bar{w} = \frac{w_{\text{wbox}}}{c_\perp} \tag{A.191}$$

$$\bar{t}_{\text{cap}} = \frac{t_{\text{cap}}}{c_\perp} \tag{A.192}$$

$$\bar{t}_{\text{web}} = \frac{t_{\text{web}}}{c_\perp} \tag{A.193}$$

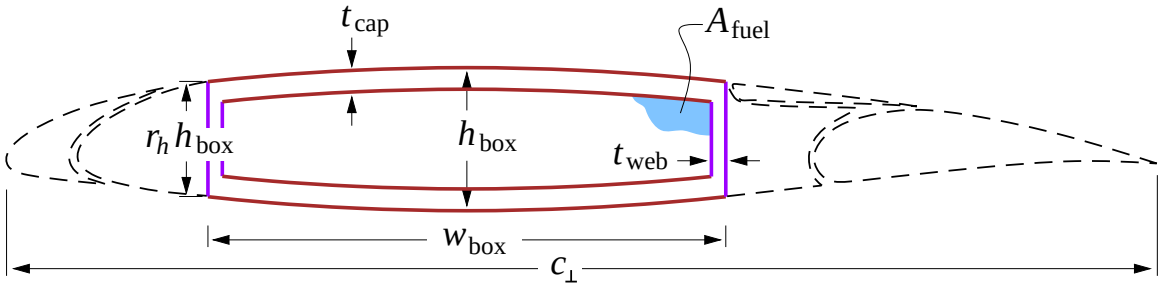

Figure A.10: Wing or tail airfoil and structure cross-section, shown perpendicular to spar axis. Leading edges, fairings, slats, flaps, and spoilers contribute to weight but not to the primary structure.

The maximum height $h_{\rm wbox}$ at the box center corresponds to the airfoil thickness, so that $\bar{h}$ is the usual "t/c" airfoil thickness ratio. The height is assumed to taper off quadratically to a fraction r_h at the webs, so that the local height $h_{(\xi)}$ is

$$h_{(\xi)} \;=\; h_{\rm wbox}\left[\,1-(1-r_h)\xi^2\,\right] \tag{A.194}$$

where $\xi = -1\ldots 1$ runs chordwise over the sparbox extent. Typical metal wings and airfoils have $\bar{w}\simeq 0.5$, $r_h \simeq 0.75$, although these are left as input parameters. For evaluating areas and approximating the bending inertia, it's useful to define the simple average and r.m.s. average normalized box heights.

$$\bar{h}_{\rm avg} \;=\; \frac{1}{c_\perp}\int_0^1 h_{(\xi)}\,d\xi \;=\; \bar{h}\left[\,1-\frac{1}{3}(1-r_h)\,\right] \tag{A.195}$$

$$\bar{h}^2_{\rm rms} \;=\; \frac{1}{c_\perp^2}\int_0^1 h^2_{(\xi)}\,d\xi \;=\; \bar{h}^2\left[\,1-\frac{2}{3}(1-r_h)+\frac{1}{5}(1-r_h)^2\,\right] \tag{A.196}$$

The areas and the bending and torsion inertias, all normalized by the normal chord, can now be determined.

$$\bar{A}_{\rm fuel} \;=\; \frac{A_{\rm fuel}}{c_\perp^2} \;=\; (\bar{w}-2\bar{t}_{\rm web})(\bar{h}_{\rm avg}-2\bar{t}_{\rm cap}) \tag{A.197}$$

$$\bar{A}_{\rm cap} \;=\; \frac{A_{\rm cap}}{c_\perp^2} \;=\; 2\,\bar{t}_{\rm cap}\bar{w} \tag{A.198}$$

$$\bar{A}_{\rm web} \;=\; \frac{A_{\rm web}}{c_\perp^2} \;=\; 2\,\bar{t}_{\rm web}\,r_h\,\bar{h} \tag{A.199}$$

$$\bar{I}_{\rm cap} \;\simeq\; \frac{I_{\rm cap}}{c_\perp^4} \;=\; \frac{\bar{w}}{12}\left[\bar{h}^3_{\rm rms}-(\bar{h}_{\rm rms}-2\bar{t}_{\rm cap})^3\right] \tag{A.200}$$

$$\bar{I}_{\rm web} \;=\; \frac{I_{\rm web}}{c_\perp^4} \;=\; \frac{\bar{t}_{\rm web}\,r_h^3\,\bar{h}^3}{6} \;\ll\; \bar{I}_{\rm cap} \qquad \text{(typically)} \tag{A.201}$$

$$G\bar{J} \;=\; \frac{4(\bar{w}-\bar{t}_{\rm web})^2(\bar{h}_{\rm avg}-\bar{t}_{\rm cap})^2}{2\dfrac{r_h\bar{h}-\bar{t}_{\rm cap}}{G_{\rm web}\bar{t}_{\rm web}} \;+\; 2\dfrac{\bar{w}-\bar{t}_{\rm web}}{G_{\rm cap}\bar{t}_{\rm cap}}} \tag{A.202}$$

Outboard surface stresses

The wing or tail surface outboard of the strut-attach location η_s is a simple cantilever, whose local shear and bending stresses can be obtained explicitly.

$$\tau_{\rm web} \;=\; \frac{\mathcal{S}_\perp}{A_{\rm web}} \;=\; \frac{\mathcal{S}_\perp}{c_\perp^2}\,\frac{1}{2\,\bar{t}_{{\rm web}_s}\bar{h}} \tag{A.203}$$

$$\sigma_{\rm cap} \;=\; \frac{\mathcal{M}_\perp h_{\rm wbox}/2}{I_{\rm cap}+r_E I_{\rm web}} \;\simeq\; \frac{\mathcal{M}_\perp h_{\rm wbox}/2}{I_{\rm cap}} \;=\; \frac{\mathcal{M}_\perp}{c_\perp^3}\,\frac{6\bar{h}}{\bar{w}}\,\frac{1}{\bar{h}^3_{\rm rms}-(\bar{h}_{\rm rms}-2\bar{t}_{{\rm cap}_s})^3} \tag{A.204}$$

$$r_E \;=\; \frac{E_{\rm web}}{E_{\rm cap}} \tag{A.205}$$

With the assumed triangular chord distribution (A.121), and the simplified shear and bending moment distributions (A.178) and (A.179), the shear and bending stresses become

$$\tau_{\rm web} = \frac{\mathcal{S}_s}{c_s^2} \frac{1}{2\,\bar{t}_{{\rm web}_s}\, r_h\, \bar{h}} \frac{1}{\cos^2\Lambda} \tag{A.206}$$

$$\sigma_{\rm cap} = \frac{\mathcal{M}_s}{c_s^3} \frac{6\bar{h}}{\bar{w}} \frac{1}{\bar{h}_{\rm rms}^3 - (\bar{h}_{\rm rms} - 2\bar{t}_{{\rm cap}_s})^3} \frac{1}{\cos^4\Lambda} \tag{A.207}$$

which are spanwise constant across the outer wing. This great simplification was the major motivator behind assuming the simple triangular planform and loading and the chord-scaled shear and moment (A.178), (A.179) for the outer wing. The optimally-sized wing sections at all spanwise locations then become geometrically self-similar, and only one convenient characteristic cross-section, e.g. at the strut-attach location η_s, needs to be sized to fully define the outer wing's structural and weight characteristics.

For a wing or tail surface without a strut, the outer surface constitutes the entire surface. In this case, the strut and inner-surface sizing below is omitted.

Inboard surface — strut case

The inboard surface structure is defined by its two end locations η_o and η_s, with linear material-gauge variation in between. The shear webs of the inner surface are assumed to be dominated by torsional requirements rather than bending-related shear requirements. Hence the inner panel is sized for the shear distribution shown dashed in Figure A.9, defined by the strut-attach value $\mathcal{S}_s$.

$$\mathcal{S}'_o = \mathcal{S}_s \tag{A.208}$$

$$\tau_{\rm web} = \frac{\mathcal{S}'_o}{c_o^2} \frac{1}{2\,\bar{t}_{{\rm web}_o}\, r_h\, \bar{h}} \frac{1}{\cos^2\Lambda} \tag{A.209}$$

Similarly, the inner panel bending stiffness must not only withstand the normal-flight bending loads, but also landing downloads and buckling loads from the strut compression. Hence, the sparcaps are sized to the linear bending moment shown dashed in Figure A.9, and defined by the end values $\mathcal{M}_s$ and $\mathcal{M}'_o$.

With the strut assumed to be attached to the bottom sparcap at $n_s = h/2$, the strut's compression load $\mathcal{P}$ cannot influence the compression stress on the top sparcap. An equivalent alternative view is that the offset-load bending moment reduction $-\mathcal{P}n_s$ is cancelled by $\mathcal{P}$'s own added compression stress. In any case, $\mathcal{P}$ does not explicitly enter into the sparcap sizing, provided $\mathcal{M}$ is positive everywhere on the inner panel, which is a reasonable assumption for a structurally-efficient wing. Hence, the strut-attach outer moment $\mathcal{M}_s$ is used for sizing the bending structure of the inner panel.

$$\mathcal{M}'_o = \mathcal{M}_s \tag{A.210}$$

$$\sigma_{\rm cap} = \frac{\mathcal{M}'_o}{c_o^3} \frac{6\bar{h}}{\bar{w}} \frac{1}{\bar{h}_{\rm rms}^3 - (\bar{h}_{\rm rms} - 2\bar{t}_{{\rm cap}_o})^3} \frac{1}{\cos^4\Lambda} \tag{A.211}$$

Inboard surface — engine case

In the case of an engine mounted at η_s, the root shear is simply offset by the single-engine weight, as shown in Figure A.11.

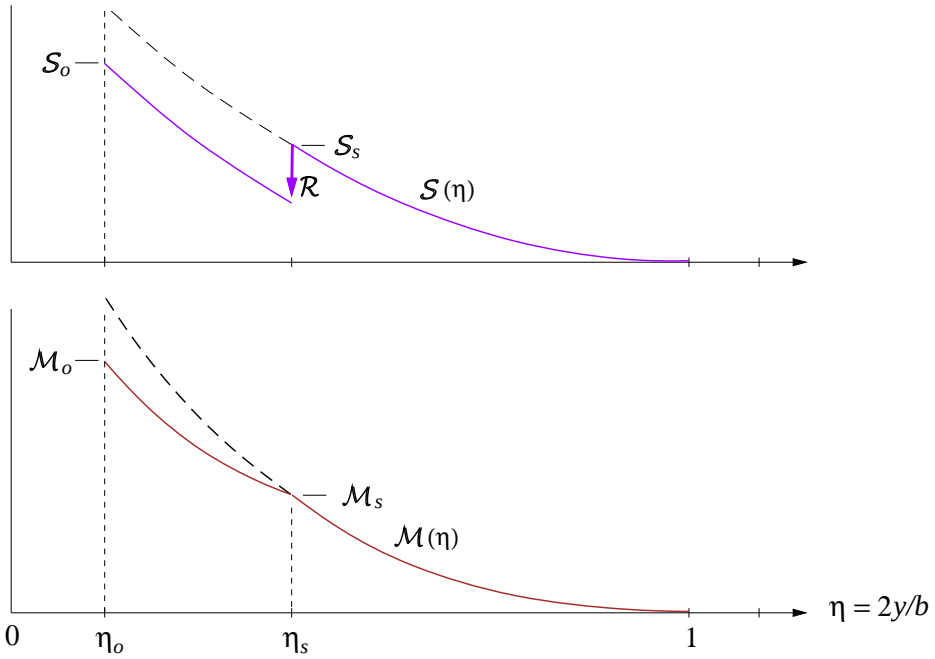

Figure A.11: Surface loads modified by load $\mathcal{R}$ equal to engine weight attached at η_s.

$$\mathcal{R} = NW_{\rm eng}/n_{\rm eng} \tag{A.212}$$

$$\mathcal{P} = 0 \tag{A.213}$$

The root shear and moment $\mathcal{S}_o$ and $\mathcal{M}_o$ are then given immediately by (A.176) and (A.177). The root web and cap stresses are then obtained with the same relations (A.206) and (A.207) used for station η_s.

$$\tau_{\rm web} = \frac{\mathcal{S}_o}{c_o^2}\,\frac{1}{2\,\bar{t}_{{\rm web}_o}\,r_h\,\bar{h}}\,\frac{1}{\cos^2\Lambda} \tag{A.214}$$

$$\sigma_{\rm cap} = \frac{\mathcal{M}_o}{c_o^3}\,\frac{6\bar{h}}{\bar{w}}\,\frac{1}{\bar{h}_{\rm rms}^3 - (\bar{h}_{\rm rms} - 2\bar{t}_{{\rm cap}_o})^3}\,\frac{1}{\cos^4\Lambda} \tag{A.215}$$

The $r_{\tau_{\rm web}}$ and $r_{\sigma_{\rm cap}}$ factors are estimated or known max/average stress ratios, and account for the fact that the material in a realistic structure is never all at the same stress, due to approximate detailed design or analysis, or from manufacturing or cost considerations.

Strut

The full strut length $\ell_{s_\perp}$ and full tension $\mathcal{T}_\perp$ are determined from the strut geometry.

$$\ell_{s_\perp} = \sqrt{z_s^2 + \frac{b^2}{4}\frac{(\eta_s - \eta_o)^2}{\cos^2\Lambda}} \tag{A.216}$$

$$\mathcal{T}_\perp \;=\; \mathcal{T}\,\frac{\ell_{s_\perp}}{\ell_s} \tag{A.217}$$

The strut stress is then simply related to $\mathcal{T}_\perp$ and the strut cross-sectional area $A_{\rm strut}$.

$$\sigma_{\rm strut} \;=\; \frac{\mathcal{T}_\perp}{A_{\rm strut}} \tag{A.218}$$

A.2.9 Surface Weights

Surface material volumes and volume moments

The surface structural weight is obtained directly from the total volume of the caps and webs, and the corresponding material densities. The volume $\mathcal{V}$ of any element of the swept surface is computed using the element's normalized cross sectional area $\bar{A}$, and the local streamwise chord $c_{(\eta)}$. The volume x-moment offsets $\Delta x\mathcal{V}$ from the center box are also computed for mass-centroid calculations. The volume y-moment offsets $\Delta y\mathcal{V}$ from y_o or y_s are computed for their contributions to the structural shear bending moment (A.174) and (A.175).

$$dy_\perp \;=\; \frac{dy}{\cos\Lambda} \;=\; \frac{b}{2}\,\frac{d\eta}{\cos\Lambda} \tag{A.219}$$

$$A \;=\; \bar{A}\,c_\perp^2 \;=\; \bar{A}\,c^2\,\cos^2\Lambda \tag{A.220}$$

$$\mathcal{V} \;=\; \int A\,dy_\perp \;=\; \frac{b}{2}\int \bar{A}c^2\,\cos\Lambda\,d\eta \tag{A.221}$$

$$\Delta x\mathcal{V} \;=\; \int A\,(x-x_{\rm wbox})\,dy_\perp \;=\; \frac{b^2}{4}\int \bar{A}c^2\,(\eta-\eta_o)\,\sin\Lambda\,d\eta \tag{A.222}$$

$$\Delta y\mathcal{V} \;=\; \int A\,(y-y_o)\,dy_\perp \;=\; \frac{b^2}{4}\int \bar{A}c^2\,(\eta-\eta_o)\,\cos\Lambda\,d\eta \tag{A.223}$$

Using the assumed three-panel chord distribution (A.121), the unit-area ($\bar{A}=1$) volume and volume moments evaluate to the following for each of the three panels of one wing half.

$$\mathcal{V}_{\rm cen} \;=\; \frac{b}{2}\int_0^{\eta_o} c^2\,d\eta \;=\; c_o^2\,\frac{b}{2}\,\eta_o \tag{A.224}$$

$$\mathcal{V}_{\rm inn} \;=\; \frac{b}{2}\int_{\eta_o}^{\eta_s} c^2\,\cos\Lambda\,d\eta \;=\; c_o^2\,\frac{b}{6}\,(1+\lambda_s+\lambda_s^2)(\eta_s-\eta_o)\,\cos\Lambda \tag{A.225}$$

$$\mathcal{V}_{\rm out} \;=\; \frac{b}{2}\int_{\eta_s}^{1} c^2\,\cos\Lambda\,d\eta \;=\; c_o^2\,\frac{b}{6}\,(\lambda_s^2+\lambda_s\lambda_t+\lambda_t^2)(1-\eta_s)\,\cos\Lambda \tag{A.226}$$

$$\Delta x\mathcal{V}_{\rm inn} \;=\; \frac{b^2}{4}\int_{\eta_o}^{\eta_s} c^2\,(\eta-\eta_o)\,\sin\Lambda\,d\eta \;=\; c_o^2\,\frac{b^2}{48}\,(1+2\lambda_s+3\lambda_s^2)(\eta_s-\eta_o)^2\,\sin\Lambda \tag{A.227}$$

$$\begin{aligned}\Delta x\mathcal{V}_{\rm out} \;=\; \frac{b^2}{4}\int_{\eta_s}^{1} c^2\,(\eta-\eta_o)\,\sin\Lambda\,d\eta \;&=\; c_o^2\,\frac{b^2}{48}\,(\lambda_s^2+2\lambda_s\lambda_t+3\lambda_t^2)(1-\eta_s)^2\,\sin\Lambda \\ &\quad + c_o^2\,\frac{b^2}{12}\,(\lambda_s^2+\lambda_s\lambda_t+\lambda_t^2)(\eta_s-\eta_o)(1-\eta_s)\,\sin\Lambda\end{aligned} \tag{A.228}$$

$$\Delta y\mathcal{V}_{\rm inn} \;=\; \frac{b^2}{4}\int_{\eta_o}^{\eta_s} c^2\,(\eta-\eta_o)\,\sin\Lambda\,d\eta \;=\; c_o^2\,\frac{b^2}{48}\,(1+2\lambda_s+3\lambda_s^2)(\eta_s-\eta_o)^2\,\cos\Lambda \tag{A.229}$$

$$\Delta y\mathcal{V}_{\rm out} \;=\; \frac{b^2}{4}\int_{\eta_s}^{1} c^2\,(\eta-\eta_s)\,\sin\Lambda\,d\eta \;=\; c_o^2\,\frac{b^2}{48}\,(\lambda_s^2+2\lambda_s\lambda_t+3\lambda_t^2)(1-\eta_s)^2\,\cos\Lambda \tag{A.230}$$

Surface weights and weight moments

For the structural sizing calculations it's necessary to determine the contributions of the structure and fuel separately for the inner and outer panels. These are calculated by applying the material densities and actual area ratios to the unit-area volumes calculated previously.

$$\bar{A}_{\mathrm{cap_{inn}}} = \frac{\bar{A}_{\mathrm{cap}_o} + \bar{A}_{\mathrm{cap}_s}\lambda_s^2}{1+\lambda_s^2} \tag{A.231}$$

$$\bar{A}_{\mathrm{web_{inn}}} = \frac{\bar{A}_{\mathrm{web}_o} + \bar{A}_{\mathrm{web}_s}\lambda_s^2}{1+\lambda_s^2} \tag{A.232}$$

$$W_{\mathrm{scen}} = \left[\rho_{\mathrm{cap}}\,\bar{A}_{\mathrm{cap}_o} + \rho_{\mathrm{web}}\,\bar{A}_{\mathrm{web}_o}\right] g\,\mathcal{V}_{\mathrm{cen}} \tag{A.233}$$

$$W_{\mathrm{sinn}} = \left[\rho_{\mathrm{cap}}\,\bar{A}_{\mathrm{cap_{inn}}} + \rho_{\mathrm{web}}\,\bar{A}_{\mathrm{web_{inn}}}\right] g\,\mathcal{V}_{\mathrm{inn}} \tag{A.234}$$

$$\Delta x W_{\mathrm{sinn}} = \left[\rho_{\mathrm{cap}}\,\bar{A}_{\mathrm{cap_{inn}}} + \rho_{\mathrm{web}}\,\bar{A}_{\mathrm{web_{inn}}}\right] g\,\Delta x\mathcal{V}_{\mathrm{inn}} \tag{A.235}$$

$$\Delta y W_{\mathrm{sinn}} = \left[\rho_{\mathrm{cap}}\,\bar{A}_{\mathrm{cap_{inn}}} + \rho_{\mathrm{web}}\,\bar{A}_{\mathrm{web_{inn}}}\right] g\,\Delta y\mathcal{V}_{\mathrm{inn}} \tag{A.236}$$

$$W_{\mathrm{sout}} = \left[\rho_{\mathrm{cap}}\,\bar{A}_{\mathrm{cap}_s} + \rho_{\mathrm{web}}\,\bar{A}_{\mathrm{web}_s}\right] g\,\mathcal{V}_{\mathrm{out}} \tag{A.237}$$

$$\Delta x W_{\mathrm{sout}} = \left[\rho_{\mathrm{cap}}\,\bar{A}_{\mathrm{cap}_s} + \rho_{\mathrm{web}}\,\bar{A}_{\mathrm{web}_s}\right] g\,\Delta x\mathcal{V}_{\mathrm{out}} \tag{A.238}$$

$$\Delta y W_{\mathrm{sout}} = \left[\rho_{\mathrm{cap}}\,\bar{A}_{\mathrm{cap}_s} + \rho_{\mathrm{web}}\,\bar{A}_{\mathrm{web}_s}\right] g\,\Delta y\mathcal{V}_{\mathrm{out}} \tag{A.239}$$

$$W_{\mathrm{fcen}} = \rho_{\mathrm{fuel}}\,\bar{A}_{\mathrm{fuel}_o}\,g\,\mathcal{V}_{\mathrm{inn}} \tag{A.240}$$

$$\bar{A}_{\mathrm{fuel_{inn}}} = \frac{\bar{A}_{\mathrm{fuel}_o} + \bar{A}_{\mathrm{fuel}_s}\lambda_s^2}{1+\lambda_s^2} \tag{A.241}$$

$$W_{\mathrm{finn}} = \rho_{\mathrm{fuel}}\,\bar{A}_{\mathrm{fuel_{inn}}}\,g\,\mathcal{V}_{\mathrm{inn}} \tag{A.242}$$

$$\Delta x W_{\mathrm{finn}} = \rho_{\mathrm{fuel}}\,\bar{A}_{\mathrm{fuel_{inn}}}\,g\,\Delta x\mathcal{V}_{\mathrm{inn}} \tag{A.243}$$

$$\Delta y W_{\mathrm{finn}} = \rho_{\mathrm{fuel}}\,\bar{A}_{\mathrm{fuel_{inn}}}\,g\,\Delta y\mathcal{V}_{\mathrm{inn}} \tag{A.244}$$

$$W_{\mathrm{fout}} = \rho_{\mathrm{fuel}}\,\bar{A}_{\mathrm{fuel}_s}\,g\,\mathcal{V}_{\mathrm{out}} \tag{A.245}$$

$$\Delta x W_{\mathrm{fout}} = \rho_{\mathrm{fuel}}\,\bar{A}_{\mathrm{fuel}_s}\,g\,\Delta x\mathcal{V}_{\mathrm{out}} \tag{A.246}$$

$$\Delta y W_{\mathrm{fout}} = \rho_{\mathrm{fuel}}\,\bar{A}_{\mathrm{fuel}_s}\,g\,\Delta y\mathcal{V}_{\mathrm{out}} \tag{A.247}$$

Assuming chord^2-weighted average areas $\bar{A}_{\mathrm{inn}}$ over the inner panel is deemed to be adequate for approximating the material and fuel volumes, since $\bar{A}_o$ and $\bar{A}_s$ will be very similar for any reasonable wing/strut configuration, and in fact are equal for the small taper ratio cantilevered wing case like for the outer panel.

The total structural wing weight and x-moment is obtained by summing the weights for all the panels for the two wing halves, with added wing weight accounted for by the f_{wadd} fraction components.

$$f_{\mathrm{wadd}} = f_{\mathrm{flap}} + f_{\mathrm{slat}} + f_{\mathrm{aile}} + f_{\mathrm{lete}} + f_{\mathrm{ribs}} + f_{\mathrm{spoi}} + f_{\mathrm{watt}} \tag{A.248}$$

$$W_{\mathrm{wing}} = 2\left(W_{\mathrm{scen}} + W_{\mathrm{sinn}} + W_{\mathrm{sout}}\right)\left(1+f_{\mathrm{wadd}}\right) \tag{A.249}$$

$$\Delta x W_{\mathrm{wing}} = 2\left(\Delta x W_{\mathrm{sinn}} + \Delta x W_{\mathrm{sout}}\right)\left(1+f_{\mathrm{wadd}}\right) \tag{A.250}$$

The maximum (volume-limited) wing fuel weight and x-moment is computed the same way.

$$W_{\rm fmax} = 2\,(W_{\rm fcen} + W_{\rm finn} + W_{\rm fout}) \tag{A.251}$$
$$\Delta xW_{\rm fmax} = 2\,(\Delta xW_{\rm finn} + \Delta xW_{\rm fout}) \tag{A.252}$$

This can be modified if only some of the wingbox volume is chosen to hold fuel.

Total panel weights

The wing structural shear and bending moment relations (A.174) – (A.177) require the weights and weight y-moments of the individual wing panels. These are assembled by summing the structure's and maximum fuel's weight contributions derived previously, with the latter simply scaled by the max-fuel usage fraction $r_{\rm fmax}$.

$$r_{\rm fmax} = \frac{W_{\rm fuel}}{W_{\rm fmax}} \tag{A.253}$$
$$W_{\rm inn} = W_{\rm sinn}(1+f_{\rm wadd}) + r_{\rm fmax}\,W_{\rm finn} \tag{A.254}$$
$$W_{\rm out} = W_{\rm sout}(1+f_{\rm wadd}) + r_{\rm fmax}\,W_{\rm fout} \tag{A.255}$$
$$\Delta yW_{\rm inn} = \Delta yW_{\rm sinn}(1+f_{\rm wadd}) + r_{\rm fmax}\,\Delta yW_{\rm finn} \tag{A.256}$$
$$\Delta yW_{\rm out} = \Delta yW_{\rm sout}(1+f_{\rm wadd}) + r_{\rm fmax}\,\Delta yW_{\rm fout} \tag{A.257}$$

Using a single $r_{\rm fmax}$ value assumes the partial fuel load is uniformly distributed percentage-wise in all the available volume. Of course, $r_{\rm fmax}$ could be varied between the panels to reflect other fuel distributions.

Strut weight

The weight of the strut is computed directly from its cross-sectional area and total length for the two sides.

$$W_{\rm strut} = \rho_{\rm strut}\,g A_{\rm strut}\,2\ell_{s_\perp} \tag{A.258}$$
$$\Delta xW_{\rm strut} = \frac{b}{4}\,(\eta_s - \eta_o)\,\tan\Lambda\,W_{\rm strut} \tag{A.259}$$

Wingbox component weights

The overall sparcap and web weights for the entire wing can also be determined, although these are merely informative and are not needed for any other calculations.

$$W_{\rm cap} = 2\rho_{\rm cap}\,g\left[\bar{A}_{{\rm cap}_o}\mathcal{V}_{\rm cen} + \tfrac{1}{2}\left(\bar{A}_{{\rm cap}_o} + \bar{A}_{{\rm cap}_s}\right)\mathcal{V}_{\rm inn} + \bar{A}_{{\rm cap}_s}\mathcal{V}_{\rm out}\right] \tag{A.260}$$
$$W_{\rm web} = 2\rho_{\rm web}\,g\left[\bar{A}_{{\rm web}_o}\mathcal{V}_{\rm cen} + \tfrac{1}{2}\left(\bar{A}_{{\rm web}_o} + \bar{A}_{{\rm web}_s}\right)\mathcal{V}_{\rm inn} + \bar{A}_{{\rm web}_s}\mathcal{V}_{\rm out}\right] \tag{A.261}$$

Tail surface weight

All the wing wing stress and weight analyses above apply equally to the vertical and horizontal tail surfaces, with the appropriate span and load definitions. It is assumed that no strut is used, so that

$$c_{s_{\rm h}} = c_{o_{\rm h}} \tag{A.262}$$
$$b_{s_{\rm h}} = b_{o_{\rm h}} \tag{A.263}$$

and likewise for the vertical tail. The main difference is the derivation of the root loading magnitude p_o, which is set by the maximum design loads at q_{NE}, defined by (A.72) and (A.74). Specifically, we have

$$p_{o_{\rm h}} = \frac{L_{\rm h_{max}}}{b_{\rm h}} \frac{2}{1+\lambda_{\rm h}} \tag{A.264}$$

where the $()_{\rm h}$ subscript denotes the horizontal tail/ The same relation is used for the vertical tail. Gravity and inertial loads are neglected here, since for tails they are typically much smaller than the airloads at q_{NE}. Of course, they could be included as was done for the wing. With the tail p_o values defined, the structural-box sizing and weight estimation proceeds using the same relations as for the wing, starting with $\mathcal{S}_o$. The vertical tail is treated by assuming its mirror image exists, so that the b value in (A.174) and (A.175) is actually twice the actual vertical tail span. No other adjustments need to be made. The net result is the overall horizontal and vertical tail weights, and tail weight moments.

$$\rightarrow W_{\rm htail} \tag{A.265}$$
$$\rightarrow W_{\rm vtail} \tag{A.266}$$
$$\rightarrow \Delta x W_{\rm htail} \tag{A.267}$$
$$\rightarrow \Delta x W_{\rm vtail} \tag{A.268}$$

A.2.10 Engine System Weight

The bare engine weight $W_{\rm ebare}$ is calculated using an assumed dependence on the engine design core mass flow $\dot{m}_{\rm D}$, overall design pressure ratio $OPR_{\rm D}$, and the design bypass ratio $BPR_{\rm D}$. The model's constants have been calibrated with listed weights for existing turbofans. The added weight $W_{\rm eadd}$, specified via the empirical fraction $f_{\rm eadd}$, accounts for the fuel system and miscellaneous related equipment.

$$W_{\rm ebare} = n_{\rm eng}\, W_{e_1}(\dot{m}_{\rm D}, OPR_{\rm D}, BPR_{\rm D}) \tag{A.269}$$
$$W_{\rm eadd} = W_{\rm ebare}\, f_{\rm eadd} \tag{A.270}$$

The nacelle plus thrust reverser weight is calculated using an assumed dependence on the engine fan diameter $d_{\rm f}$ and the nacelle surface area, the latter being specified by the empirical area ratio $r_{\rm Snace}$ relative to the fan area.

$$S_{\rm nace_1} = r_{\rm Snace}\, \frac{\pi}{4}\, d_{\rm f}^2 \tag{A.271}$$
$$W_{\rm nace} = n_{\rm eng}\, W_{n_1}\,(d_{\rm f}, S_{\rm nace_1}) \tag{A.272}$$

The pylon weight W_{pylon}, specified via the empirical fraction f_{pylon}, accounts for the pylon and other mounting structure.

$$W_{\text{ebare}} = n_{\text{eng}}\, W_{e_1}(\dot{m}_{\text{D}}, OPR_{\text{D}}, BPR_{\text{D}}) \quad \text{(A.273)}$$

$$W_{\text{pylon}} = (W_{\text{ebare}} + W_{\text{eadd}} + W_{\text{nace}})\, f_{\text{pylon}} \quad \text{(A.274)}$$

The total engine system weight and weight moment is then defined as follows. The engine weight fraction is also defined, and is used in the overall weight iteration procedure.

$$W_{\text{eng}} = W_{\text{ebare}} + W_{\text{eadd}} + W_{\text{nace}} + W_{\text{pylon}} \quad \text{(A.275)}$$

$$xW_{\text{eng}} = x_{\text{eng}}\, W_{\text{eng}} \quad \text{(A.276)}$$

$$f_{\text{eng}} = \frac{W_{\text{eng}}}{W_{\text{MTO}}} \quad \text{(A.277)}$$

A.2.11 Moments and Balance

Weight moment and aerodynamic moment calculations are used to size the horizontal tail to meet stability or trim-limit requirements, to determine allowable CG limits, and to determine the required pitch-trim tail lift.

Overall weight moment

The overall flying weight is summed as follows. Partial payload and partial fuel are specified with the arbitrary r_{pay} and r_{fuel} ratios relative to maximum design values.

$$\begin{aligned} W &= r_{\text{pay}} W_{\text{pay}} + r_{\text{fuel}} W_{\text{fuel}} \\ &+ W_{\text{fuse}} + W_{\text{wing}} + W_{\text{strut}} + W_{\text{htail}} + W_{\text{vtail}} \\ &+ W_{\text{eng}} + W_{\text{hpesys}} + W_{\text{lgnose}} + W_{\text{lgmain}} \end{aligned} \quad \text{(A.278)}$$

The partial passenger payload distribution in the cabin is specified by the parameter ξ_{pay} which can take on any value $0 \ldots 1$. Specific instances are

$$\xi_{\text{pay}} = \begin{cases} 0.0 & , \text{ passengers packed towards the front} \\ 0.5 & , \text{ passengers centered in cabin} \\ 1.0 & , \text{ passengers packed towards the back} \end{cases} \quad \text{(A.279)}$$

This then determines the passenger payload weight centroid x_{pay}.

$$x_{\text{cabin}} = \tfrac{1}{2}(x_{\text{shell}\,1} + x_{\text{shell}\,2}) \quad \text{(A.280)}$$

$$l_{\text{cabin}} = x_{\text{shell}\,2} - x_{\text{shell}\,1} \quad \text{(A.281)}$$

$$x_{\text{pay}} = x_{\text{cabin}} + l_{\text{cabin}} \left(\xi_{\text{pay}} - \tfrac{1}{2}\right)(1 - r_{\text{pay}}) \quad \text{(A.282)}$$

Note that with a full passenger load, $r_{\text{pay}} = 1$, the mass centroid is always at the center point x_{cabin}, regardless of ξ_{pay}. The overall aircraft weight moment is then computed as follows.

$$xW = r_{\text{pay}}\, x_{\text{pay}} W_{\text{pay}}$$

$$
\begin{aligned}
&+ \quad r_{\text{fuel}}\left(x_{\text{wbox}} W_{\text{fuel}} + \Delta x W_{\text{fuel}}\right) \\
&+ \quad x W_{\text{fuse}} \\
&+ \quad x_{\text{wbox}} W_{\text{wing}} \; + \; \Delta x W_{\text{wing}} \\
&+ \quad x_{\text{wbox}} W_{\text{strut}} \; + \; \Delta x W_{\text{strut}} \\
&+ \quad x_{\text{htail}} W_{\text{htail}} \; + \; \Delta x W_{\text{htail}} \\
&+ \quad x_{\text{vtail}} W_{\text{vtail}} \; + \; \Delta x W_{\text{vtail}} \\
&+ \quad x W_{\text{eng}} \\
&+ \quad x_{\text{hpesys}} W_{\text{hpesys}} \\
&+ \quad x_{\text{lgnose}} W_{\text{lgnose}} \\
&+ \quad x_{\text{lgmain}} W_{\text{lgmain}}
\end{aligned}
\tag{A.283}
$$

The aircraft CG location then follows.

$$
x_{CG} \;=\; \frac{x W}{W} \tag{A.284}
$$

Overall aerodynamic moment

The overall aerodynamic pitching moment about the origin comes from the wing, the horizontal tail, and the fuselage. For simplicity, the wing root chord c_o is used as the reference moment arm rather than the more traditional m.a.c.

$$
\begin{aligned}
C_M \;\equiv\; \frac{M}{\frac{1}{2}\rho V_\infty^2 S c_o} \;&=\; C_{M\text{w}_0} \;+\; \left(C_{M\text{w}_1} \;-\; \frac{x_{\text{wbox}}}{c_o}\right)\left(C_L \;-\; \frac{S_{\text{h}}}{S} C_{L_{\text{h}}}\right) \\
&+\; \frac{S_{\text{h}}\, c_{o\text{h}}}{S\, c_o}\, C_{M\text{h}_0} \;+\; \left(\frac{c_{o\text{h}}}{c_o}\, C_{M\text{h}_1} \;-\; \frac{x_{\text{hbox}}}{c_o}\right)\frac{S_{\text{h}}}{S}\, C_{L_{\text{h}}} \\
&+\; \frac{CMV_{\text{f}_1}}{S c_o}\, (C_L - C_{L_{Mf\,0}})
\end{aligned}
\tag{A.285}
$$

and CMV_{f_1} and $C_{L_{Mf\,0}}$ give the fuselage's pitching moment volume dependence on aicraft C_L.

$$
\frac{M_{\text{fuse}}}{\frac{1}{2}\rho V_\infty^2} \;\equiv\; CMV_{\text{f}} \;=\; CMV_{\text{f}_1}\,(C_L - C_{L_{Mf\,0}}) \tag{A.286}
$$

From slender body theory, a fuselage of volume $\mathcal{V}_{\text{f}}$ isolated from the wing has

$$
CMV_{\text{f}} \;\simeq\; 2\mathcal{V}_{\text{f}}\,(\alpha - \alpha_{Mf\,0}) \tag{A.287}
$$

$$
CMV_{\text{f}_1} \;\simeq\; \frac{2\mathcal{V}_{\text{f}}}{dC_L/d\alpha} \tag{A.288}
$$

but this will typically be considerably modified by the interaction with the wing. Ragardless, the aircraft center of pressure (or lift centroid) is given as follows.

$$
x_{CP} \;=\; -\frac{c_o\, C_M}{C_L} \tag{A.289}
$$

Neutral point

The neutral point is estimated by first translating the aerodynamic pitching moment (A.285) to some arbitrary reference x location.

$$C_M(x) \;=\; C_M \;+\; \frac{x}{c_o}\, C_L \tag{A.290}$$

The neutral point is the x location which makes (A.290) stationary with respect to C_L, or

$$\frac{\partial C_M(x_{NP})}{\partial C_L} \;=\; \frac{\partial C_M}{\partial C_L} \;+\; \frac{x_{NP}}{c_o} \;=\; 0 \tag{A.291}$$

$$x_{NP} \;=\; -c_o\, \frac{\partial C_M}{\partial C_L} \tag{A.292}$$

$$\begin{aligned} \text{where} \qquad c_o\, \frac{\partial C_M}{\partial C_L} \;&=\; (c_o C_{M\mathrm{w_1}} \;-\; x_{\mathrm{wbox}}) \left(1 \;-\; \frac{S_\mathrm{h}}{S} \frac{\partial C_{L_\mathrm{h}}}{\partial C_L}\right) \\ &+\; (c_{o\mathrm{h}} C_{M\mathrm{h_1}} \;-\; x_{\mathrm{hbox}})\, \frac{S_\mathrm{h}}{S}\, \frac{\partial C_{L_\mathrm{h}}}{\partial C_L} \\ &+\; \frac{C M V_{\mathrm{f_1}}}{S} \end{aligned} \tag{A.293}$$

Pitch trim requirement

Every operating point must meet the requirement of pitch trim, which is equivalent to the centers of weight and pressure cooinciding. This is enforced by requiring that the following total-moment residual is zero.

$$\mathcal{R}_M(x_{\mathrm{wbox}}, S_\mathrm{h}, C_{L\mathrm{h}}, C_L, r_{\mathrm{fuel}}, r_{\mathrm{pay}}, \xi_{\mathrm{pay}}) \;\equiv\; x_{CG} \;-\; x_{CP} \;=\; \frac{x_W}{W} + \frac{c_o\, C_M}{C_L} \;=\; 0 \tag{A.294}$$

The argument list of the residual indicates the variables which have the strongest influence on pitch trim.

Pitch stability requirement

An aircraft must also have some minimum amount of static pitch stability, which means that the rearmost center of gravity must be ahead of the neutral point by the static margin fraction f_{SM} of the mean aerodynamic chord. This is met when the following stability residual is zero.

$$\mathcal{R}_S(x_{\mathrm{wbox}}, S_\mathrm{h}, r_{\mathrm{fuel}}, r_{\mathrm{pay}}, \xi_{\mathrm{pay}}) \;\equiv\; x_{CG} \;-\; x_{NP} \;+\; f_{SM}\, c_{MA} \;=\; 0 \tag{A.295}$$

The argument list indicates the variables which have the strongest influence on pitch stability.

A.2.12 Tail Sizing

The tail areas can be sized by a number of alternative requirements. The most common approaches are outlined here.

Specified tail volumes

This is the simplest approach. The stability margin or damping requirements are assumed to be quantified by the horizontal and vertical tail volumes,

$$l_{\rm h} = x_{\rm htail} - x_{\rm wing} \tag{A.296}$$

$$l_{\rm v} = x_{\rm vtail} - x_{\rm wing} \tag{A.297}$$

$$V_{\rm h} = \frac{S_{\rm h}}{S}\,\frac{l_{\rm h}}{c_{\rm mac}} \tag{A.298}$$

$$V_{\rm v} = \frac{S_{\rm v}}{S}\,\frac{l_{\rm v}}{b} \tag{A.299}$$

which when specified give the necessary $S_{\rm h}$ or $S_{\rm v}$. Defining the tail arms from the center of wing centroid rather than from the CG or the wing's aerodynamic center is reasonable for these rather simple sizing relations.

Design-case: Horizontal tail sizing and wing positioning

For the design case, both $S_{\rm h}$ and $x_{\rm wbox}$ are determined so as to drive the pitch trim and stability residuals (A.294) and (A.295) to zero simultaneously. Their remaining arguments are set for the appropriate worst-case situations:

$$\mathcal{R}_{\!M} = \mathcal{R}_{\!M}(x_{\rm wbox}, S_{\rm h}\,;\,(C_{L\rm h})_{\rm min}, (C_L)_{\rm max}, (r_{\rm fuel})_{\rm fwd}, (r_{\rm pay})_{\rm fwd}, 0) \;=\; 0 \tag{A.300}$$

$$\mathcal{R}_{\!S} = \mathcal{R}_{\!S}(x_{\rm wbox}, S_{\rm h}\,;\,(r_{\rm fuel})_{\rm aft}, (r_{\rm pay})_{\rm aft}, 1) \;=\; 0 \tag{A.301}$$

Specifically, for pitch trim the most-forward CG and most-negative flaps-down wing airfoil c_m, at maximum flight C_L are assumed. For stability the most-aft CG is assumed. The $r_{\rm pay}$ values which give the extreme forward and aft CG locations are obtained by solving the extremizing relation

$$\frac{\partial \mathcal{R}_{\!M}}{\partial r_{\rm pay}} = 0 \tag{A.302}$$

which is a quadratic for $r_{\rm pay}$. It is solved twice, with $\xi_{\rm pay} = 0$ chosen to give $(r_{\rm pay})_{\rm fwd}$, and then $\xi_{\rm pay} = 1$ chosen to give $(r_{\rm pay})_{\rm aft}$. Zero fuel, or $r_{\rm fuel} = 0$ is assumed for both cases, as this typically gives the most extreme CG locations together with the worst-case payload distributions.

The two residuals (A.300) and (A.301) are simultaneously driven to zero by varying the wing position $x_{\rm wbox}$ and the horizontal tail area $S_{\rm h}$, by solving the 2×2 Newton system. The four Jacobian elements are readily calculated.

$$\begin{bmatrix} \frac{\partial \mathcal{R}_{\!M}}{\partial S_{\rm h}} & \frac{\partial \mathcal{R}_{\!M}}{\partial x_{\rm wbox}} \\ \frac{\partial \mathcal{R}_{\!S}}{\partial S_{\rm h}} & \frac{\partial \mathcal{R}_{\!S}}{\partial x_{\rm wbox}} \end{bmatrix} \begin{Bmatrix} \delta S_{\rm h} \\ \delta x_{\rm wbox} \end{Bmatrix} = -\begin{Bmatrix} \mathcal{R}_{\!M} \\ \mathcal{R}_{\!S} \end{Bmatrix} \tag{A.303}$$

Off-design case: Tail lift setting

For off-design calculations where the wing location and horizontal tail area is set, pitch trim is achieved by adjusting C_{L_h}. The pitch-trim residual (A.294) is therefore driven to zero with a Newton step on C_{L_h}.

$$\frac{\partial \mathcal{R}_M}{\partial C_{L_\mathrm{h}}} = \frac{1}{C_L}\left[-(c_o C_{M_1} - x_{\mathrm{wbox}})\frac{S_\mathrm{h}}{S} + (c_{o\mathrm{h}} C_{M\mathrm{h}_1} - x_{\mathrm{hbox}})\frac{S_\mathrm{h}}{S}\right] \tag{A.304}$$

$$(C_{L_\mathrm{h}})_{\mathrm{new}} = C_{L_\mathrm{h}} - \frac{\mathcal{R}_M}{\partial \mathcal{R}_M / \partial C_{L_\mathrm{h}}} \tag{A.305}$$

Vertical tail sizing via engine-out yaw power

An alternative to the specified vertical tail volume (A.299) is to size the vertical tail so that it can achieve yaw trim with one engine out. The requirement is

$$q_{\min} C_{L\mathrm{v}_{\mathrm{yaw}}} S_\mathrm{v}\, l_\mathrm{v} = (F_{\mathrm{eng}} + q_{\min} C_{D\mathrm{eng}} A_{\mathrm{eng}})\, y_{\mathrm{eng}} \tag{A.306}$$

where $q_{\min}$ is the minimum takeoff dynamic pressure, $C_{L\mathrm{v}_{\mathrm{yaw}}}$ is the maximum lift coefficient of the vertical tail with some yaw control margin, F_{eng} is the thrust of one engine, $C_{D\mathrm{eng}}$ is the drag coefficient of a windmilling engine with reference area A_{eng}, and y_{eng} is the lateral distance of the outermost engine from the centerline.

A.2.13 Dissipation (Drag) Calculation

Power-based formulation

The performance calculations used here are based on the power balance and dissipation analysis of Drela [12]. In brief, the usual streamwise force balance equation in constant-velocity flight is replaced with the power balance relation

$$F' V_\infty = D' V_\infty + W\dot{h} \tag{A.307}$$

where $\dot{h}$ is the climb rate, F' is an effective thrust, and D' is an effective drag. These two effective forces are actually defined in terms of the net propulsive power and the net dissipation and vortex kinetic energy loss rate.

$$F' V_\infty \equiv P_{K_{\mathrm{inl}}} + P_V + P_{K_{\mathrm{out}}} - \Phi_{\mathrm{jet}} \tag{A.308}$$

$$D' V_\infty \equiv \Phi_{\mathrm{surf}} + \Phi_{\mathrm{wake}} + \dot{E}_{\mathrm{vortex}} \tag{A.309}$$

The advantage of this power-balance approach is that it naturally handles the presence of boundary layer ingestion (BLI) without the ambiguities or complications which arise with a force-balance approach. If no BLI is present then the two approaches become entirely equivalent, and F', D' become the conventional thrust and drag F, D. The BLI accounting is described in more detail in the separate document "Power Accounting with Boundary Layer Ingestion". Only the relevant results will be used here.

The disspation and power loss terms in the above power equations are used to define the following convenient coefficients.

$$C'_{D_p} \equiv \frac{\Phi_{\text{surf}} + \Phi_{\text{wake}}}{\frac{1}{2}\rho V_\infty^3 S} \tag{A.310}$$

$$C'_{D_i} \equiv \frac{\dot{E}_{\text{vortex}}}{\frac{1}{2}\rho V_\infty^3 S} = C_{D_i} \tag{A.311}$$

$$C'_D \equiv \frac{D' V_\infty}{\frac{1}{2}\rho V_\infty^3 S} = C'_{D_p} + C_{D_i} \tag{A.312}$$

As with "F" and "D", the "C_D" notation is used as a reminder that if there is no BLI, the above definitions reduce to the conventional drag coefficients and the primes can be simply dropped in that case.

In the following subsections, the various contributions to the overall power-loss coefficient C'_D will be computed. Most of these rely on traditional drag models and terminology, hence the "Drag" label will be used in the sections titles, mostly out of habit. As a useful indicator, the prime $()'$ will be retained only for those contributions which are potentially influenced by BLI. Unprimed contributions will thus also correspond to the conventional drag coefficients.

Fuselage Profile Drag

The fuselage profile drag is determined by an pseudo-axisymmetric viscous/inviscid calculation method, which is described in the separate document "Simplified Viscous/Inviscid Calculation for Nearly-Axisymmetric Bodies". This gives reliable viscous flow and fuselage drag predictions for any reasonable fuselage shape, without the need to rely on effective wetted area or fineness-ratio correlations.

The method requires the geometry to be specified in the form of a cross-sectional area distribution $A_{(x)}$ and also a perimeter distribution $b_{0(x)}$, shown in Figure A.12. For a round cross-section these are of course related, but to allow treating more general fuselage cross-sections, they are assumed to be specified separately. The cross section sizes and shapes can vary along the body, provided the variation is reasonably smooth.

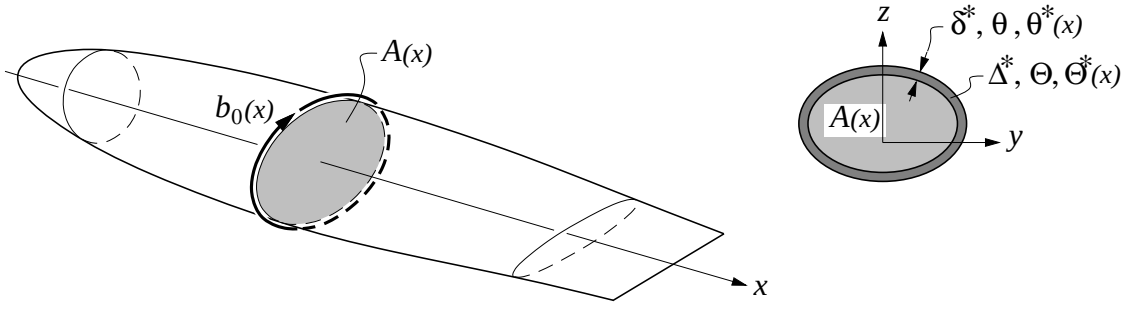

Figure A.12: Fuselage defined by cross-sectional area $A_{(x)}$ and perimeter $b_{0(x)}$ distributions. Viscous calculation produces displacement, momentum, and kinetic energy areas $\Delta^*, \Theta, \Theta^*{}_{(x)}$.

The cross-sectional area over the center cylindrical portion is $A_{\rm fuse}$, which has already been defined by (A.6). This also defines the radius of the equivalent round cylinder.

$$R_{\rm cyl} \;=\; \sqrt{\frac{A_{\rm fuse}}{\pi}} \tag{A.313}$$

The equivalent radii over the tapering nose and radius are then defined via the following convenient functions.

$$R_{(x)} \;=\; \begin{cases} R_{\rm cyl}\left[\,1-\left(\dfrac{x_{\rm blend_1}-x}{x_{\rm blend_1}-x_{\rm nose}}\right)^a\,\right]^{1/a} & , \quad x_{\rm nose} < x < x_{\rm blend_1} \\ R_{\rm cyl} & , \quad x_{\rm blend_1} < x < x_{\rm blend\,2} \\ R_{\rm cyl}\left[\,1-\left(\dfrac{x-x_{\rm blend\,2}}{x_{\rm end}-x_{\rm blend\,2}}\right)^b\,\right] & , \quad x_{\rm blend\,2} < x < x_{\rm tail} \end{cases} \tag{A.314}$$

$$a \;\simeq\; 1.6 \tag{A.315}$$

$$b \;\simeq\; 2.0 \tag{A.316}$$

The $x_{\rm blend_1}$ and $x_{\rm blend\,2}$ locations are the nose and tailcone blend points, and do not necessarily have to be exactly the same as the $x_{\rm shell_1}$ and $x_{\rm shell\,2}$ locations which define the loaded pressure shell. Likewise, $x_{\rm end}$ is the aerodynamic endpoint of the tailcone, and is distinct from its structural endpoint $x_{\rm conend}$. The a and b constant values above give reasonable typical fuselage shapes.

If the fuselage is nearly round, the necessary area and perimeter distributions follow immediately.

$$A_{(x)} \;=\; \pi\, R_{(x)}{}^2 \tag{A.317}$$

$$b_{0(x)} \;=\; 2\pi R_{(x)} \tag{A.318}$$

This would be suitably modified for non-circular cross-sections.

With this geometry definition, the viscous/inviscid calculation procedure provides the momentum and kinetic energy area distributions along the body and wake,

$$\{\Theta_{(s)}\,,\; \Theta^*{}_{(s)}\} \;=\; f_{\rm f_{excr}}\, \mathcal{F}(M_\infty, Re_\ell\,;\, A_{(x)}, b_{0(x)}) \tag{A.319}$$

where $\mathcal{F}$ denotes the overall viscous/inviscid calculation procedure, and $f_{\rm f_{excr}} \geq 1$ is an empirical factor to allow for fuselage excrescence drag sources.

Specific values of interest are the far-downstream momentum area $\Theta_{\rm wake}$ at the wake endpoint, and the kinetic energy area Θ_{TE} at the body endpoint or trailing edge.

$$\Theta_{\rm wake} \;=\; \Theta(s_{\rm wake}) \tag{A.320}$$

$$\Theta^*_{TE} \;=\; \Theta^*(s_{TE}) \tag{A.321}$$

The fuselage surface + wake dissipated power in the absence of BLI is then evaluated as follows, consistent with the usual wake momentum defect relations.

$$C_{D_{\rm fuse}} \;\equiv\; \frac{\Phi_{\rm fuse}}{\frac{1}{2}\rho V_\infty^3 S} \;=\; \frac{\Phi_{\rm surf}+\Phi_{\rm wake}}{\frac{1}{2}\rho V_\infty^3 S} \qquad \text{(without BLI)} \tag{A.322}$$

$$C_{D_{\rm fuse}} \;=\; \frac{D_{\rm fuse}}{\frac{1}{2}\rho V^2 S} \;=\; \frac{2\Theta_{\rm wake}}{S} \qquad \text{(without BLI)} \tag{A.323}$$

If BLI is present at or near the trailing edge, the upstream boundary layer and corresponding surface dissipation $\Phi_{\rm surf}$ will be mostly unaffected. But the viscous fluid flowing into the wake is now reduced by the ingestion fraction $f_{\rm BLI\,f}$, so that the wake dissipation $\Phi_{\rm wake}$ will be reduced by the same fraction. This then gives the following overall fuselage dissipation coefficient for the BLI case.

$$C'_{D_{\rm fuse}} \equiv \frac{\Phi_{\rm fuse}}{\frac{1}{2}\rho V_\infty^3 S} = \frac{\Phi_{\rm surf} + \Phi_{\rm wake}(1-f_{\rm BLI\,f})}{\frac{1}{2}\rho V_\infty^3 S} \qquad \text{(with BLI)} \qquad \text{(A.324)}$$

$$C'_{D_{\rm fuse}} = C_{\Phi_{\rm surf}} + C_{\Phi_{\rm wake}}(1-f_{\rm BLI\,f}) = C_{D_{\rm fuse}} - C_{\Phi_{\rm wake}} f_{\rm BLI\,f} \qquad \text{(with BLI)} \qquad \text{(A.325)}$$

where
$$C_{\Phi_{\rm surf}} = \frac{\Theta^*_{TE}}{S} \qquad \text{(A.326)}$$

$$C_{\Phi_{\rm wake}} = \frac{2\Theta_{\rm wake}}{S} - \frac{\Theta^*_{TE}}{S} \qquad \text{(A.327)}$$

Wing Profile Drag

The power dissipated in the wing's surface and wake for the non-ingesting case defines the wing's profile drag coefficient.

$$C_{D_{\rm wing}} \equiv \frac{\Phi_{\rm wing}}{\frac{1}{2}\rho V_\infty^3 S} = \frac{\Phi_{\rm surf} + \Phi_{\rm wake}}{\frac{1}{2}\rho V_\infty^3 S} \qquad \text{(without BLI)} \qquad \text{(A.328)}$$

Any ingestion of the wing boundary layer is captured by the ingestion fraction $f_{\rm BLI\,w}$, in the same manner as for the fuselage.

$$C'_{D_{\rm wing}} \equiv \frac{\Phi_{\rm wing}}{\frac{1}{2}\rho V_\infty^3 S} = \frac{\Phi_{\rm surf} + \Phi_{\rm wake}(1-f_{\rm BLI\,w})}{\frac{1}{2}\rho V_\infty^3 S} \qquad \text{(with BLI)} \qquad \text{(A.329)}$$

$$C'_{D_{\rm wing}} = C_{D_{\rm wing}} - C_{\Phi_{\rm wake}} f_{\rm BLI\,w} \qquad \text{(with BLI)} \qquad \text{(A.330)}$$

where
$$C_{\Phi_{\rm wake}} \simeq r_{\Phi_{\rm wake}}\, C_{D_{\rm wing}} \qquad \text{(A.331)}$$

$$r_{\Phi_{\rm wake}} \simeq 0.15 \qquad \text{(A.332)}$$

The wake dissipation is assumed here to be $r_{\Phi_{\rm wake}} = 15\%$ of the total airfoil dissipation, which is typical of optimized modern transonic airfoils.

The actual calculation of $C_{D_{\rm wing}}$ is via the drag using infinite swept wing theory, which also gives the lift in term of the perpendicular-plane velocity $V_\perp$ and lift coefficient $c_{\ell_\perp}$. Figure A.13 shows the relations. These quantities are related to the local loading via

$$V_\perp = V_\infty \cos\Lambda \qquad \text{(A.333)}$$

$$dL = \tilde{p}\, dy = \tfrac{1}{2}\rho V_\perp^2\, c_\perp\, c_{\ell_\perp}\, dy_\perp \qquad \text{(A.334)}$$

$$p_o\, P_{(\eta)} = \tfrac{1}{2}\rho V_\infty^2\, c_o\, C_{(\eta)}\, c_{\ell_\perp(\eta)}\, \cos^2\Lambda \qquad \text{(A.335)}$$

excluding the wing center and extreme tip where the lift adjustements ΔL_o and ΔL_t are located. The loading scale p_o in level flight is obtained from (A.159) with $N=1$ as follows.

$$W = L = \tfrac{1}{2}\rho V_\infty^2\, S\, C_L \qquad \text{(A.336)}$$

$$L_{\rm htail} = \tfrac{1}{2}\rho V_\infty^2\, S_{\rm h}\, C_{L_{\rm h}} \qquad \text{(A.337)}$$

$$p_o = \frac{1}{K_p\, b}\,(L - L_{\rm htail}) \qquad \text{(A.338)}$$

Using (A.338) to substitute for p_o in (A.335) and rearranging gives an explicit expression for the local section lift coefficient.

$$C_{L_{\text{htail}}} = \frac{S_{\text{h}}}{S} C_{L_{\text{h}}} \tag{A.339}$$

$$c_{\ell_\perp}(\eta) = \frac{C_L - C_{L_{\text{htail}}}}{\cos^2\Lambda} \frac{S}{K_p\, b\, c_o} \frac{P_{(\eta)}}{C_{(\eta)}} \tag{A.340}$$

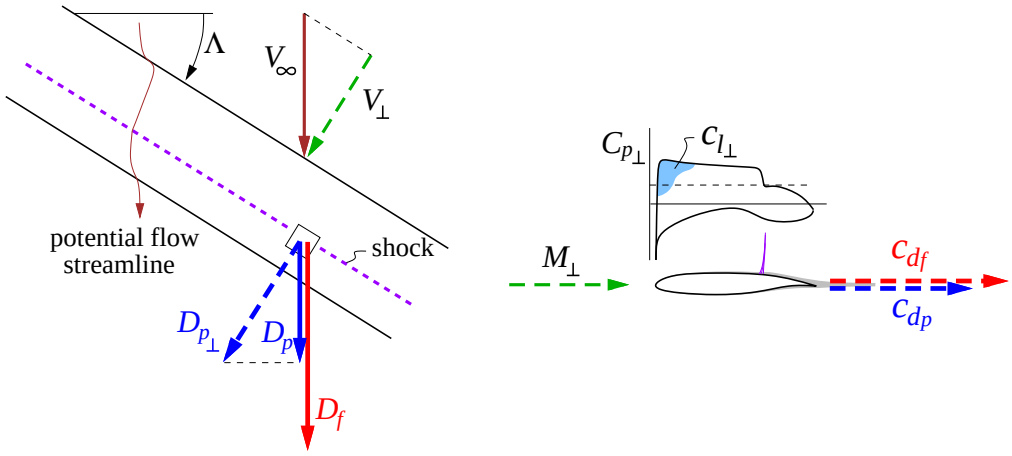

Figure A.13: Friction and pressure drag forces on infinite swept wing

Using this $c_{\ell_\perp}$ and also $M_\perp$, the perpendicular-plane friction and pressure drag coefficients are then obtained from a 2D airfoil drag database having the form

$$c_{d_f} = f_{\text{wexcr}}\, \bar{c}_{d_f}(c_{\ell_\perp}, M_\perp, \tfrac{t}{c}) \left(\frac{Re_c}{Re_{\text{ref}}}\right)^{a_{Re}} \tag{A.341}$$

$$c_{d_p} = f_{\text{wexcr}}\, \bar{c}_{d_p}(c_{\ell_\perp}, M_\perp, \tfrac{t}{c}) \left(\frac{Re_c}{Re_{\text{ref}}}\right)^{a_{Re}} \tag{A.342}$$

where

$$M_\perp = M_\infty \cos\Lambda \tag{A.343}$$

$$\tfrac{t}{c} = \bar{h} \tag{A.344}$$

$$Re_c = \frac{\rho_\infty V_\infty\, c}{\mu_\infty} \tag{A.345}$$

$$a_{Re} \simeq -0.15 \tag{A.346}$$

and $f_{\text{wexcr}} \geq 1$ is an empirical specified factor to account for wing excrescence drag sources, and Re_{ref} is a reference Reynolds number at which the database functions $\bar{c}_{d_f}, \bar{c}_{d_p}$ were computed. The chord Reynolds number Re_c could of course be treated as an additional parameter in the database, but at a considerable increase in the size of the database and the computational effort needed to construct it. The value of the Re-scaling exponent $a_{Re} \simeq -0.15$ is appropriate for fully-turbulent flow.

Note that the database includes the airfoil thickness/chord ratio $\frac{t}{c} = \bar{h}$, which is crucial for obtaining a realistic wing thickness/sweep/C_L/Mach tradeoff. The thickness dependence is determined by viscous MSES [18] calculations on a number of transonic airfoils or varying thickness, such as the ones shown in Figure A.14. Each airfoil has been designed independently for a well-behaved transonic drag rise, so that the database returns c_{d_f} and c_{d_p} values

representative of the best transonic airfoil technology. A piecewise-linear airfoil thickness distribution is assumed, defined by the three values $\bar{h}_o, \bar{h}_s, \bar{h}_t$.

$$\bar{h}_{(\eta)} \;=\; \begin{cases} \bar{h}_o & , \quad 0<\eta<\eta_o \\ \bar{h}_o \;+\; (\bar{h}_s - \bar{h}_o)\dfrac{\eta-\eta_o}{\eta_s-\eta_o} & , \quad \eta_o<\eta<\eta_s \\ \bar{h}_s \;+\; (\bar{h}_t - \bar{h}_s)\dfrac{\eta-\eta_s}{1\;-\eta_s} & , \quad \eta_o<\eta<\eta_s \end{cases} \tag{A.347}$$

On typical transport wings most of the thickness/chord variation occurs inboard, so in that case, only $\bar{h}_o$ and $\bar{h}_s$ would be considered as design variables, and $\bar{h}_t = \bar{h}_s$ would be assumed.

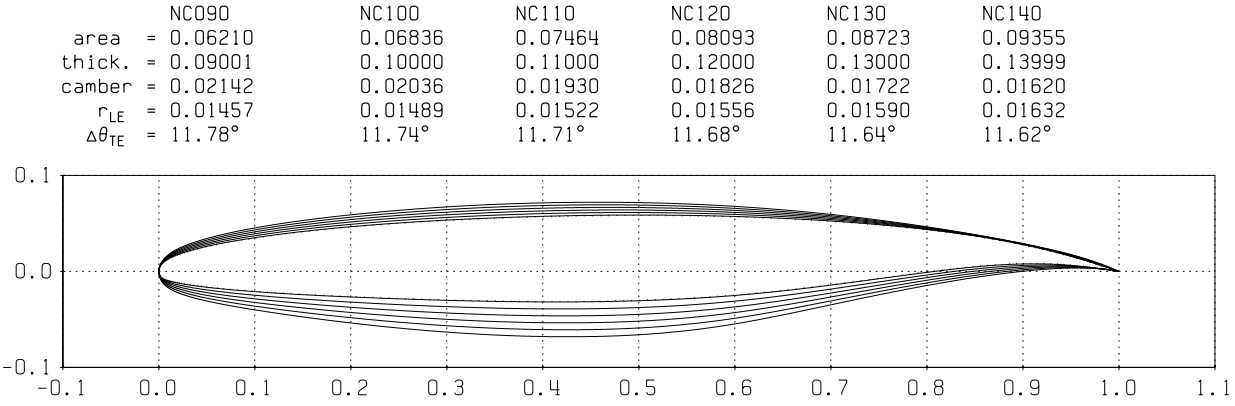

Figure A.14: Airfoil family used to generate airfoil-performance database.

The 2D profile drag coefficients are applied to the swept wing using infinite swept-wing theory, illustrated in Figure A.13. This treatment is exact for laminar flow on untapered wings, and quite accurate for turbulent flow. The friction drag is assumed to scale with freestream dynamic pressure and to act mostly along the freestream flow direction, while the pressure drag from the shock and viscous diplacement is assumed to scale with the wing-normal dynamic pressure and to act normal to the wing-spanwise axis. The total local streamwise drag element is then given as follows.

$$\begin{aligned} dD_{\text{wing}} \;&=\; dD_f \;+\; dD_p \;=\; dD_f \;+\; dD_{p_\perp}\cos\Lambda \\ &=\; \tfrac{1}{2}\rho V_\infty^2\, c\, c_d\, dy \end{aligned} \tag{A.348}$$

$$c_d \;=\; c_{d_f} + c_{d_p}\cos^3\Lambda \qquad \text{(infinite swept wing)} \tag{A.349}$$

However, this relation is not realistic near the fuselage. Here the potential flow is forced parallel to the freestream direction which causes the wing shock to become locally unswept, as shown in Figure A.15. Also, the full streamwise dynamic pressure (as opposed to the wing-normal dynamic pressure) acts at the trailing edge where most of the displacement-effect pressure drag occurs. Hence, the sweep correction is dropped off towards the fuselage via the heuristic "unsweep" function $f_{\text{Suns}(\eta)}$.

$$c_{d(\eta)} \;=\; \Big\{ c_{d_f} \;+\; c_{d_p}\Big[f_{\text{Suns}} + (1-f_{\text{Suns}})\cos^2\Lambda \Big]\cos\Lambda \Big\} \qquad \text{(actual swept wing)} \tag{A.350}$$

$$f_{\text{Suns}(\eta)} \;=\; \exp\!\left(-\frac{1}{k_{\text{Suns}}}\frac{y-y_o}{c}\right) \;=\; \exp\!\left(-\frac{1}{k_{\text{Suns}}}\frac{\eta-\eta_o}{C_{(\eta)}}\frac{b}{2c_o}\right) \tag{A.351}$$

$$k_{\text{Suns}} \;\simeq\; 0.5 \tag{A.352}$$

The k_{Suns} decay constant controls the area of the wing most influenced by the shock unsweep correction, as shown in Figure A.15.

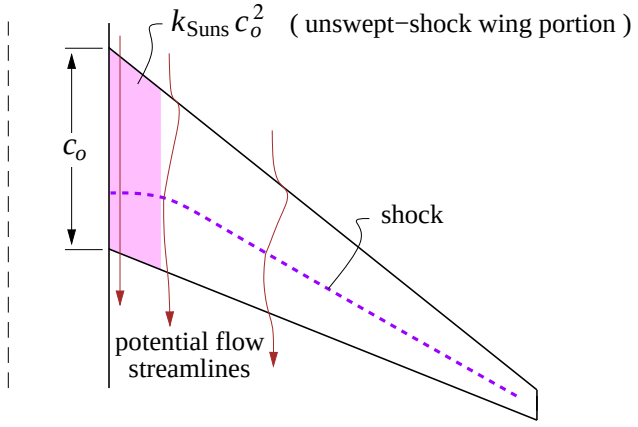

Figure A.15: Wing shock unsweeps near the fuselage, roughly over the area $k_{\text{uns}} c_o^2$.

The overall wing profile drag is then obtained by numerical integration of (A.348), using (A.350) for the $c_{d(\eta)}$ function and (A.121) for the chord $c_{(\eta)}$ function.

$$C_{D_{\text{wing}}} \equiv \frac{D_{\text{wing}}}{\frac{1}{2}\rho V_\infty^2 S} = \frac{b c_o}{S} \int_{\eta_o}^{1} c_{d(\eta)}\, C_{(\eta)}\, d\eta \tag{A.353}$$

Tail Profile Drag

The viscous dissipation of the tail surfaces is computed using the same relations as for the wing, giving the equivalent tail drag coefficients $C_{D_{\text{htail}}}$ and $C_{D_{\text{vtail}}}$. No BLI is assumed, but could be included in the same manner as for the wing. Because tail surfaces typically do not have significant shock waves, the shock-unsweep correction (A.350) is inappropriate. Instead, the 2D friction and pressure drag coefficients c_{d_f} and c_{d_p} are specified directly and are used in the infinite-wing relation (A.349), and are assumed constant over the surface so that numerical spanwise integration is unnecessary.

$$C_{D_{\text{htail}}} = c_{d_{f\text{h}}} + c_{d_{p\text{h}}} \cos^3\Lambda_{\text{h}} \tag{A.354}$$

$$C_{D_{\text{vtail}}} = c_{d_{f\text{v}}} + c_{d_{p\text{v}}} \cos^3\Lambda_{\text{v}} \tag{A.355}$$

Strut Profile Drag

In the absence of any BLI on the strut, its dissipation is fully captured by its conventional drag coefficient, scaled by the local mean-cube-average velocity ratio $r_{V_{\text{strut}}}$ to allow for the fact that a strut is typically in the decreased flow velocity below a lifting wing. Simple sweep corrections are also used as for the wing.

$$c_{\text{strut}} = \sqrt{\frac{A_{\text{strut}}}{k_A\, \bar{h}_{\text{strut}}}} \quad , \qquad k_A \simeq 0.65 \tag{A.356}$$

$$S_{\text{strut}} = 2 c_{\text{strut}}\, \ell_{s_\perp} \tag{A.357}$$

$$\cos\Lambda_s = \frac{\ell_s}{\ell_{s_\perp}} \tag{A.358}$$

$$C_{D_{\rm strut}} = \frac{S_{\rm strut}}{S}\left(c_{d_{f\rm s}} + c_{d_{p\rm s}}\cos^3\Lambda_{\rm s}\right) r^3_{V_{\rm strut}} \tag{A.359}$$

Picking a strut thickness/chord ratio $\bar{h}_{\rm strut} \simeq 0.15 \ldots 0.20$ typically gives the minimum overall drag for a given strut cross-sectional area $A_{\rm strut}$. The k_A area factor of 0.65 is typical of most symmetric airfoils.

Engine Nacelle Profile Drag

The nacelle viscous dissipation accounts for the external nacelle flow only, since the internal flow is represented by the engine diffuser and nozzle losses. The external wetted area and corresponding area fraction is determined as an assumed fraction $r_{\rm Snace}$ of the engine fan area.

$$S_{\rm nace} = n_{\rm eng}\, r_{\rm Snace}\, \frac{\pi}{4}\, d^2_{\rm fan} \tag{A.360}$$

$$f_{\rm Snace} = \frac{S_{\rm nace}}{S} \tag{A.361}$$

The skin friction coefficient can also be calculated based on the nacelle-length Reynolds number and a standard turbulent skin-friction law, with an excrescence factor $f_{\rm n_{excr}} \geq 1$ included as for the fuselage and wing.

$$\ell_{\rm nace} = 0.15\, r_{\rm Snace}\, d_{\rm fan} \tag{A.362}$$

$$Re_{\rm nace} = \frac{\rho_\infty V_\infty \ell_{\rm nace}}{\mu_\infty} \tag{A.363}$$

$$C_{f_{\rm nace}} = f_{\rm n_{excr}}\, C_{f_{\rm turb}}(Re_{\rm nace}) \tag{A.364}$$

The nacelle is assumed to be immersed in the potential nearfield of a nearby wing or fuselage, with a local effective freestream $V_{\rm nace}$ which differs somewhat from the true freestream V_∞, and is specified via the ratio $V_{\rm nace}/V_\infty$. Depending on the flight condition and engine power, the fan-face Mach number M_2 will in general differ considerably from the corresponding local M'_∞, The nacelle is therefore effectively a loaded ring airfoil, which can be represented by a ring vortex sheet whose resulting external nacelle-surface velocity is approximately

$$V_{{\rm n}_{LE}} \simeq 2V_{\rm nace} - V_2 \tag{A.365}$$

$$\frac{V_{\rm nace}}{V_\infty} = r_{V_{\rm nace}} \tag{A.366}$$

$$\frac{V_{{\rm n}_{LE}}}{V_\infty} = 2\frac{V_{\rm nace}}{V_\infty} - \frac{V_2}{V_\infty} \simeq \max\left(2r_{V_{\rm nace}} - \frac{M_2}{M_\infty}\ ,\ 0\right) \tag{A.367}$$

at the lip, as sketched in Figure A.16. Limiting $V_{{\rm n}_{LE}}$ above zero avoids unrealistic results for low airspeed, high-power operation situations.

Assuming a linear acceleration or deceleration from $V_{{\rm n}_{LE}}$ to $V_{\rm nace}$ at the nacelle nozzle gives the following mean-cube velocity ratio on the nacelle surface.

$$r^3_{V_{\rm nsurf}} \equiv \frac{1}{V^3_\infty}\int_0^1 \left[V_{\rm nace} + (V_{{\rm n}_{LE}} - V_{\rm nace})\,(1-\xi)\right]^3 d\xi \tag{A.368}$$

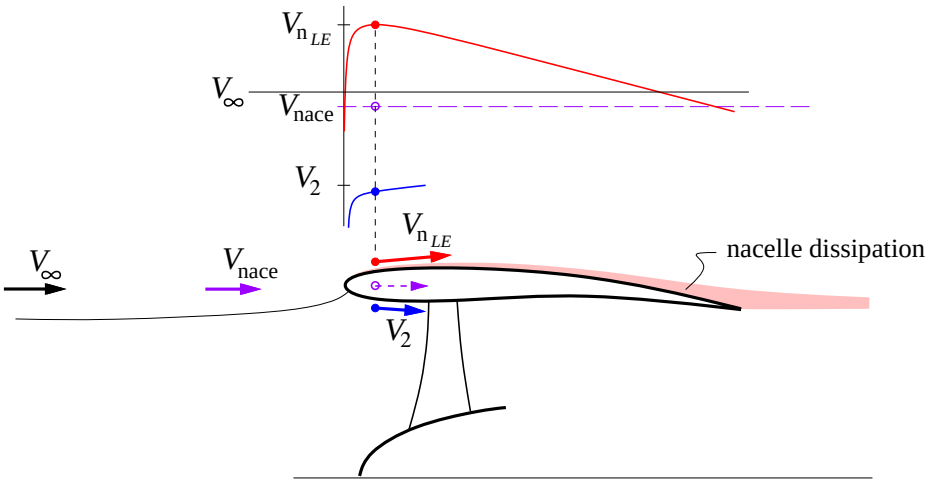

Figure A.16: Velocity distribution on inside and outside of engine nacelle. Outside velocity determines nacelle dissipation and implied nacelle drag. The $V_{n_{LE}} > V_2$ case shown is for a typical cruise condition, while $V_{n_{LE}} < V_2$ will occur at low speeds and high power.

$$= \frac{1}{4}\left[\frac{V_{n_{LE}}}{V_\infty} + r_{V_{nace}}\right]\left[\left(\frac{V_{n_{LE}}}{V_\infty}\right)^2 + r^2_{V_{nace}}\right] \tag{A.369}$$

The nacelle-surface dissipation, expressed as the equivalent nacelle drag coefficient, is now estimated using a turbulent wetted-area skin-friction coefficient, weighted by the mean-cube velocity ratio.

$$C_{D_{nace}} = f_{Snace}\, C_{f_{nace}}\, r^3_{V_{nsurf}} \tag{A.370}$$

Induced Drag

The induced drag is calculated using a discrete vortex Trefftz-Plane analysis. The circulation of the wing wake immediately behind the trailing edge is

$$\Gamma_{wing(\eta)} = \frac{\tilde{p}(\eta)}{\rho V_\infty} \simeq \frac{p(\eta)}{\rho V_\infty}\sqrt{1-\eta^{k_t}} \tag{A.371}$$

$$k_t \simeq 16 \tag{A.372}$$

where the approximation realistically represents the tip lift rolloff for typical taper ratios, and is consistent with the assumed $f_{L_t} \simeq -0.05$ value for the tip lift loss factor. This circulation is convected into the wake along streamlines which will typically constrict behind the fuselage by continuity. Figure A.17 shows two possible aft fuselage taper shapes, giving two different wake constrictions.

An annular streamtube at the wing contracts to another annular streamtube in the wake with the same cross-sectional area. The y and y' locations on the wing and wake which are connected by a streamline are therefore related by the correspondence function.

$$y'_{(y)} = \sqrt{y^2 - y_o^2 + y_o'^2} \tag{A.373}$$

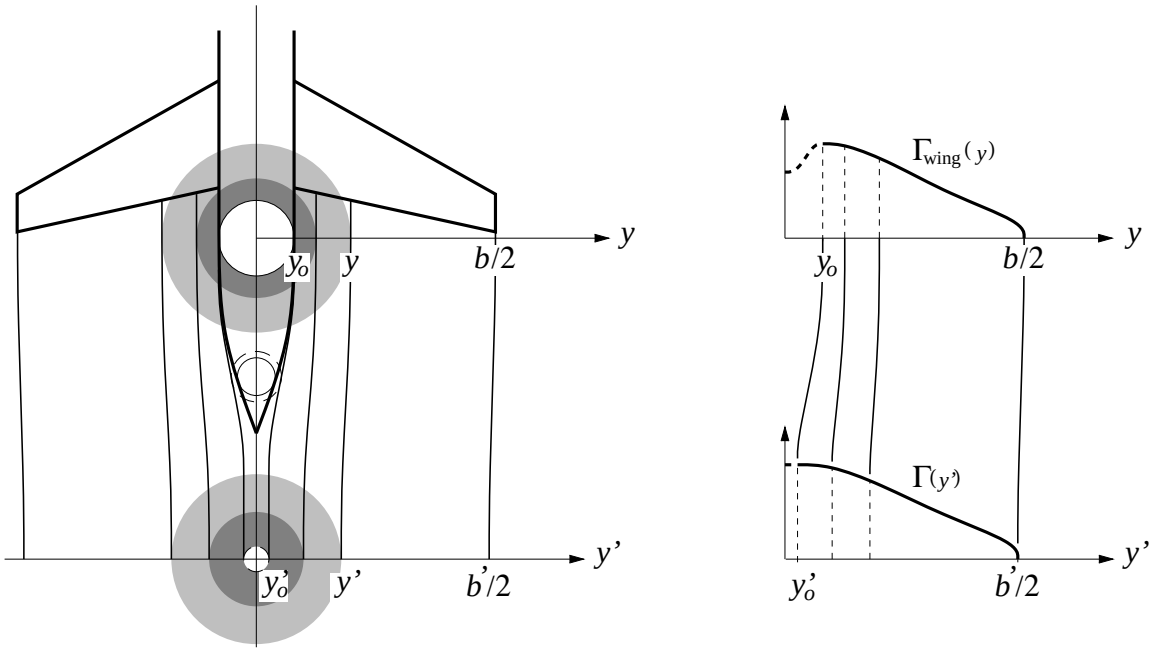

Figure A.17: Wake streamline contraction due to fuselage thickness, carrying wing circulation into the wake. Two shaded streamtubes are shown. Wake center radius y'_o is nonzero due to the fuselage viscous wake displacement area.

The Trefftz Plane circulation $\Gamma_{(y')}$ is then given by the coordinate shift. The mapping function $y'_{(y)}$ is not defined for $y < y_o$, so the circulation there is simply set from the y_o value.

$$\Gamma_{\text{wake}(y')} = \begin{cases} \Gamma_{\text{wing}}\left(y_{(y')}\right) & , \quad y > y_o \\ \Gamma_{\text{wing}}\left(y_o\right) \end{cases} \tag{A.374}$$

The Trefftz Plane analysis uses point vortices. The circulation (A.374) is evaluated at the midpoints of n intervals along the wake trace, spaced more or less evenly in the Glauert angle to give a cosine distribution in physical space. The wake's vertical z positions are simply taken directly from the wing.

$$\theta_{i+1/2} = \frac{\pi}{2}\,\frac{i-1/2}{n} \quad , \quad i = 1 \ldots n \tag{A.375}$$

$$y_{i+1/2} = \frac{b}{2}\,\cos\theta_{i+1/2} \tag{A.376}$$

$$y'_{i+1/2} = \sqrt{y_{i+1/2}^2 - y_o^2 + {y'_o}^2} \tag{A.377}$$

$$z'_{i+1/2} = z_{i+1/2} \tag{A.378}$$

$$\Gamma_{i+1/2} = \Gamma_{\text{wing}}(y_{i+1/2}) \tag{A.379}$$

The locations of $n+1$ trailing vortices are computed similarly.

$$\theta_i = \frac{\pi}{2}\,\frac{i-1}{n} \quad , \quad i = 1 \ldots n+1 \tag{A.380}$$

$$y_i = \frac{b}{2}\,\cos\theta_i \tag{A.381}$$

$$y'_i = \sqrt{y_i^2 - y_o^2 + {y'_o}^2} \tag{A.382}$$

$$z'_i = z_i \tag{A.383}$$

The circulations of these trailing vortices are the differences of the adjacent bound circulations, with the circulation beyond the tips effectively zero.

$$\bar{\Gamma}_i = \begin{cases} -\Gamma_{i-1/2} & , \quad i = 1 \qquad \text{(left tip)} \\ \Gamma_{i+1/2} - \Gamma_{i-1/2} & , \quad i = 2 \ldots n \\ \Gamma_{i+1/2} & , \quad i = n{+}1 \qquad \text{(right tip)} \end{cases} \tag{A.384}$$

The above definitions are also applied to the horizontal tail, with its discrete points simply appended to the list and n increased accordingly.

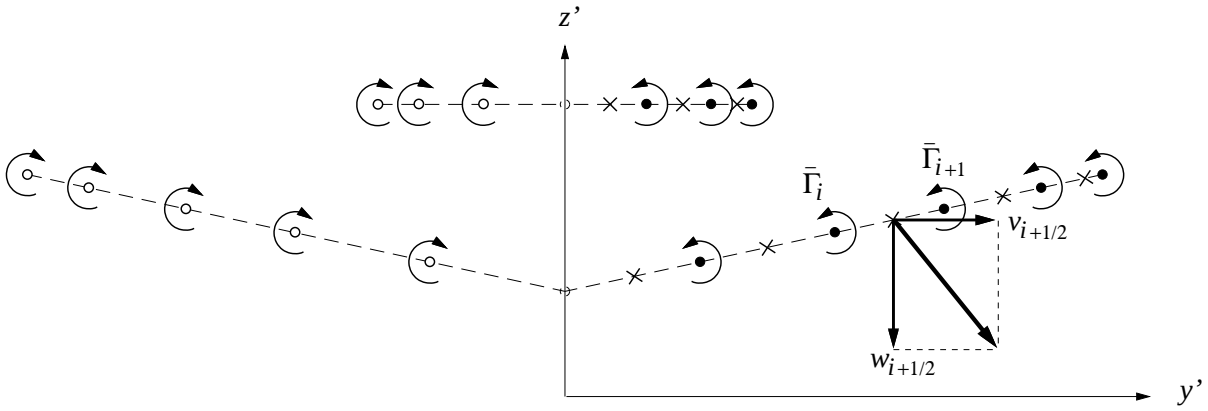

Figure A.18: Trefftz Plane vortices $i, i{+}1 \ldots$ and collocation points $i{+}1/2$ used for velocity, impulse, and kinetic energy calculations. Left/right symmetry is exploited.

The Trefftz plane calculation proceeds by first calculating the y-z wake velocity components at the $y'_{i+1/2}, z'_{i+1/2}$ interval midpoints, induced by all the trailing vortices and their left-side images.

$$v_{i+1/2} = \sum_{j=1}^{n+1} \frac{\bar{\Gamma}_j}{2\pi} \left[\frac{-(z'_{i+1/2} - z'_j)}{(y'_{i+1/2} - y'_j)^2 + (z'_{i+1/2} - z'_j)^2} - \frac{-(z'_{i+1/2} - z'_j)}{(y'_{i+1/2} + y'_j)^2 + (z'_{i+1/2} - z'_j)^2} \right] \tag{A.385}$$

$$w_{i+1/2} = \sum_{j=1}^{n+1} \frac{\bar{\Gamma}_j}{2\pi} \left[\frac{y'_{i+1/2} - y'_j}{(y'_{i+1/2} - y'_j)^2 + (z'_{i+1/2} - z'_j)^2} - \frac{y'_{i+1/2} + y'_j}{(y'_{i+1/2} + y'_j)^2 + (z'_{i+1/2} - z'_j)^2} \right] \tag{A.386}$$

The overall lift and induced drag are then computed using the Trefftz Plane vertical impulse and kinetic energy. The sums are doubled to account for the left side image.

$$C_{L_{TP}} = \frac{2}{\frac{1}{2}\rho V_\infty^2 S} \sum_{i=1}^{n} \rho V_\infty \, \Gamma_{i+1/2} \, (y'_{i+1} - y'_i) \tag{A.387}$$

$$C_{D_{TP}} = \frac{2}{\frac{1}{2}\rho V_\infty^2 S} \sum_{i=1}^{n} -\frac{\rho}{2} \, \Gamma_{i+1/2} \left[w_{i+1/2} \, (y'_{i+1} - y'_i) \; - \; v_{i+1/2} \, (z'_{i+1} - z'_i) \right] \tag{A.388}$$

To minimize any modeling and numerical errors incurred in the wake contraction model and the point-vortex summations, the final induced drag value is scaled by the square of the

surface-integral and Trefftz-Plane drag values.

$$C_{D_i} \;=\; C_{D_{TP}} \left(\frac{C_L}{C_{L_{TP}}} \right)^2 \tag{A.389}$$

This is equivalent to using the Trefftz Plane analysis to calculate the span efficiency rather than the actual induced drag coefficient.

Total Drag

The total effective aircraft dissipation coefficient is obtained by summing all the contributions.

$$C'_D \;=\; C_{D_i} + C'_{D_{\rm fuse}} + C'_{D_{\rm wing}} + C_{D_{\rm htail}} + C_{D_{\rm vtail}} + C_{D_{\rm strut}} + C_{D_{\rm nace}} \tag{A.390}$$

A.2.14 Engine Performance Model and Sizing

Engine model summary

The extensive details of the engine calculations are given in the separate documents "Turbofan Sizing and Analysis with Variable $c_{p(T)}$" and "Film Cooling Flow Loss Model". The treatment of the inlet kinetic energy defect $K_{\rm inl}$ is described in the document "Power Accounting with Boundary Layer Ingestion". In brief, $K_{\rm inl}$ reduces the fan inlet total pressure, and also adds to the net effective thrust by the amount $K_{\rm inl}/V_\infty$, which in engine parlance can be interpreted as a reduction in inlet "ram drag".

The engine model can be run in one of three modes:

1) Design sizing mode. The net thrust F'_e and combustor exit temperature $T_{t\,4}$ are specified along with a number of other component and operating parameters, and the engine flow areas $A_2, A_5 \ldots$ are computed.

2) Off-design analysis mode. The areas and $T_{t\,4}$ are prescribed, and thrust F'_e is computed.

3) Off-design analysis mode. The areas and F'_e are prescribed, and $T_{t\,4}$ is computed.

For all three modes, the specific fuel consumption $TSFC'$ and all other engine operating parameters which are not specified are also computed.

$$\{A_2, A_{5\cdots}\,;\, TSFC'_{\cdots}\} \;=\; \mathcal{F}_{\rm eng_1}(F'_e, T_{t_4}, OPR_{\rm D}, BPR_{\rm D\cdots}\,;\, M_\infty, p_\infty, T_\infty, K_{\rm inl\cdots}) \tag{A.391}$$

$$\{F'_e\,;\, TSFC', OPR, BPR_{\cdots}\} \;=\; \mathcal{F}_{\rm eng_2}(T_{t_4}, A_2, A_{5\cdots}\,;\, M_\infty, p_\infty, T_\infty, K_{\rm inl\cdots}) \tag{A.392}$$

$$\{T_{t_4}\,;\, TSFC', OPR, BPR_{\cdots}\} \;=\; \mathcal{F}_{\rm eng_3}(F'_e, A_2, A_{5\cdots}\,;\, M_\infty, p_\infty, T_\infty, K_{\rm inl\cdots}) \tag{A.393}$$

$$\text{where} \qquad TSFC' \;\equiv\; \frac{F'_e}{\dot{m}_{\rm fuel}\, g} \tag{A.394}$$

$$K_{\rm inl} \;\equiv\; \left(\tfrac{1}{2}\rho_e V_e^3 \Theta^*\right)_{\rm inl} \;=\; \frac{f_{\rm BLI\,f}}{n_{\rm eng}} \left(\tfrac{1}{2}\rho_e V_e^3 \Theta^*\right)_{TE} \tag{A.395}$$

In these calculations, the fan inlet total pressure $p_{t\,2}$ is reduced as a result of the BLI. A reasonable estimate is

$$p_{t\,2} = p_{t\,\infty} - \frac{K_{\rm inl}}{\dot{\mathcal{V}}_{\rm inl}} \tag{A.396}$$

$$\dot{\mathcal{V}}_{\rm inl} = \iint_{\rm inl} V\, dA \tag{A.397}$$

where $\dot{\mathcal{V}}_{\rm inl}$ is the fan face volume flow.

Engine Sizing

In the design mode 1), the specified thrust is obtained is determined from the start-of-cruise weight W_c, lift/drag ratio, and the slight cruise-climb angle $\gamma_{\rm CR}$.

$$F'_{\rm D} = r_{B_c}\, W_c \left(\frac{C'_D}{C_L} + \gamma_{\rm CR}\right)_c \tag{A.398}$$

$$F'_{e_{\rm D}} = \frac{F'_{\rm D}}{n_{\rm eng}} \tag{A.399}$$

The engine calculations determine the specific thrust

$$F_{\rm sp_D} \equiv \frac{F'_{e_{\rm D}}}{a_\infty\, \dot{m}_{\rm core}(1+BPR_{\rm D})} \tag{A.400}$$

which then determines the core mass flow $\dot{m}_{\rm core}$ and the associated fan flow area A_2 and fan diameter $d_{\rm f}$.

$$A_2 = \frac{\dot{m}_{\rm core}(1+BPR_{\rm D})}{\rho_2 u_2} = \frac{1}{F_{\rm sp_D}}\, \frac{F'_{e_{\rm D}}}{\gamma p_\infty}\, \frac{1}{M_{2_{\rm D}}} \left(\frac{1+\frac{\gamma-1}{2}M^2_{2_{\rm D}}}{1+\frac{\gamma-1}{2}M^2_\infty}\right)^{\frac{\gamma+1}{2(\gamma-1)}} \tag{A.401}$$

$$d_{\rm f} = \sqrt{\frac{4A_2}{\pi(1-HTR^2_{\rm f})}} \tag{A.402}$$

Similar calculations are used for the other component and nozzle areas.

A.2.15 Mission Performance and Fuel Burn Analysis

Mission profiles

The altitude, weight, and thrust profiles versus range are schematically shown in Figure A.19.

At any profile point these are related via the following normal force and axial force relations.

$$W\, \sin\gamma = F' - D' - \frac{W}{g}\, \frac{dV}{dt} \tag{A.403}$$

$$W\, \cos\gamma = L \tag{A.404}$$

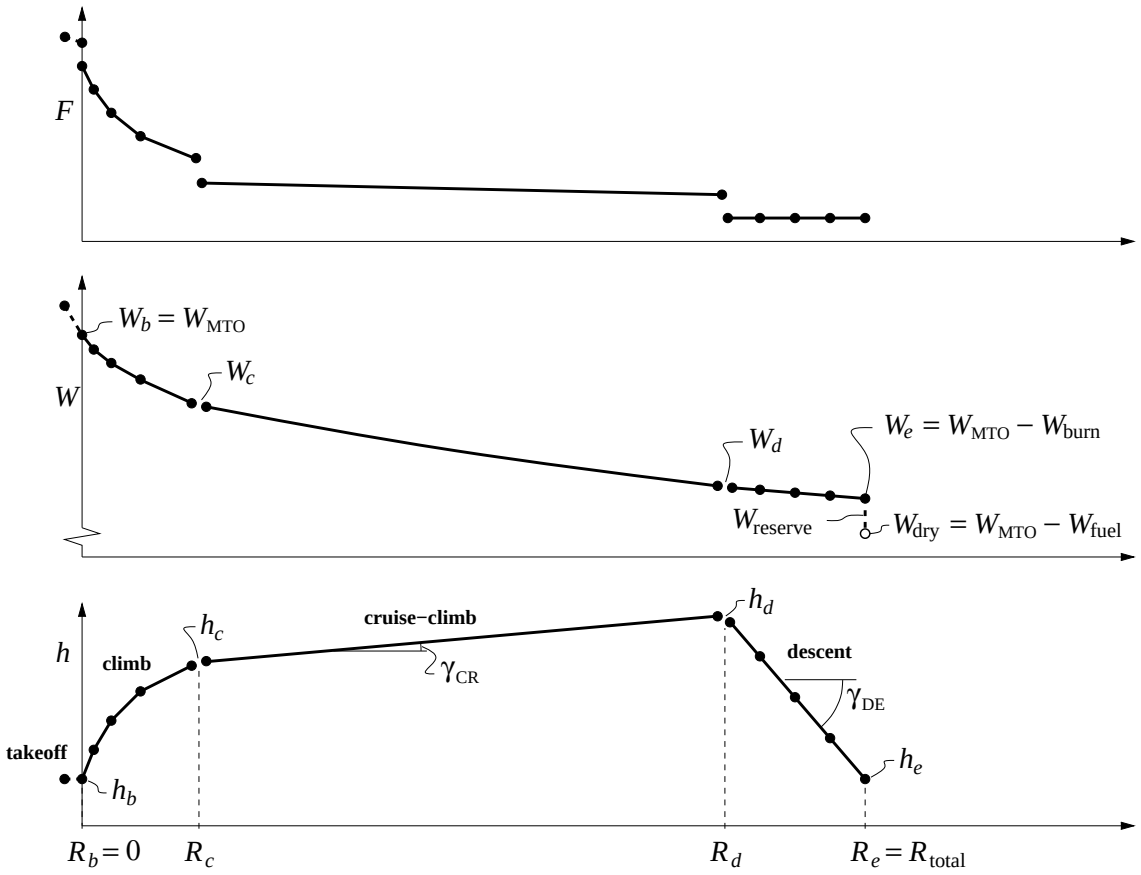

Figure A.19: Design-mission profiles of altitude, weight, thrust, versus range.

Equation (A.403) is merely a recast form of the power-balance equation (A.307), with the added last acceleration term. The subscript has also been dropped from V_∞ for convenience.

The flight speed at any profile point is obtained from a specified C_L and ambient density using equation (A.404).

$$V \;=\; \sqrt{\frac{2W\cos\gamma}{\rho\, S\, C_L}} \tag{A.405}$$

Some iteration is required with the thrust/drag relations below to determine the climb angle γ needed in (A.405).

Dividing (A.403) by (A.404), and using the kinematic ground-speed relation

$$\frac{dR}{dt} \;=\; V\cos\gamma \tag{A.406}$$

together with the fuel-burn to thrust relation

$$\frac{dW}{dt} \;=\; -\dot{m}_{\rm fuel}\, g \;=\; -F'\, TSFC' \tag{A.407}$$

gives an expression for the climb angle γ or the equivalent climb gradient dh/dR, and also the weight-loss gradient dW/dR.

$$\tan\gamma \;=\; \frac{dh}{dR} \;=\; \frac{F'}{W}\frac{1}{\cos\gamma} \;-\; \frac{D'}{L} \;-\; \frac{1}{2g}\,\frac{d(V^2)}{dR} \tag{A.408}$$

$$\frac{dW}{dR} = -F' \frac{TSFC'}{V \cos\gamma} \tag{A.409}$$

These will be suitably integrated over the mission segments to obtain the altitude and weight profiles $h_{(R)}$ and $W_{(R)}$.

The instantaneous climb or descent angle γ in the above expressions can be computed by combining (A.403) and (A.404), and solving for the resulting quadratic equation for $\sin\gamma$.

$$\phi = \frac{F'}{W} - \frac{\dot{V}}{g} \tag{A.410}$$

$$\epsilon = \frac{C'_D}{C_L} \tag{A.411}$$

$$\sin\gamma = \frac{\phi - \epsilon\sqrt{1 - \phi^2 + \epsilon^2}}{1 + \epsilon^2} \tag{A.412}$$

The $\dot{V}$ acceleration term in the excess thrust-to-weight ratio ϕ can be neglected for most transport aircraft. The corresponding integrated $d(V^2)$ differential in (A.408) is also typically small, but there's little reason to exclude it in calculations.

Mission profile integration

The fuel weight required for a given mission range is determined by integration of the trajectory equations (A.408) and (A.409), which are first put in the following equivalent differential forms.

$$dR = \left(dh + \frac{d(V^2)}{2g}\right)\left(\frac{F'}{W}\frac{1}{\cos\gamma} - \frac{C'_D}{C_L}\right)^{-1} \tag{A.413}$$

$$d(\ln W) = -\frac{F'}{W}\frac{TSFC'}{V\cos\gamma}\, dR \tag{A.414}$$

The various terms are then approximated with 2-point finite differences or averages, and marched forward using a predictor/corrector scheme, over the climb, cruise, and descent segments of the mission. The details will be given in the Calculation Procedures section.

The following segment endpoint values are inputs to the integration, and are either specified externally, or obtained from the weight-sizing calculations:

W_b	takeoff weight
C_L	lift coefficient for all points
$M_{\rm CR}$	cruise Mach number
h_b	takeoff altitude
h_c	start-of-cruise altitude
h_e	landing altitude

Climb distance

The climb-segment range R_c is computed by integrating equations (A.413) and (A.414) from the takeoff range $R_b = 0$, over the prescribed climb altitude change $h_b \ldots h_c$. The start-of-climb weight W_c is also computed in the process.

Cruise and descent angles, distances

Before the cruise and descent segments are integrated, it is first necessary to determine the end-of-cruise range R_d and altitude h_d.

The first step is to calculate the slight cruise-climb angle γ_{CR}, so as to preserve a constant flight Mach number M and flight C_L as the aircraft loses weight from fuel burn. These are related to the current weight W at any point in the cruise by the lift equation.

$$\frac{1}{2}\rho V^2 \;=\; \frac{\gamma}{2} p M^2 \;=\; \frac{W}{S C_L} \tag{A.415}$$

This assumes that $\cos\gamma \simeq 1$ which is appropriate for the extremely small climb angles ocurring during a typical cruise-climb segment. With M and C_L held at their prescribed cruise values, this then gives the atmospheric pressure as a function of weight.

$$p \;=\; \frac{2}{\gamma M^2\, S\, C_L}\, W \tag{A.416}$$

$$\frac{dp}{dW} \;=\; \frac{p}{W} \tag{A.417}$$

The very small change in W_{buoy} over the cruise-climb is neglected here. Using the atmospheric hydrostatic pressure gradient $dp/dh = -\rho g$, and the fuel-burn weight gradient (A.409), equation (A.417) is used to explicitly obtain the small climb angle during the cruise.

$$\gamma \;\simeq\; \tan\gamma \;=\; \frac{dh}{dR} \;=\; \frac{dh}{dp}\,\frac{dp}{dW}\,\frac{dW}{dR} \tag{A.418}$$

$$= \left[-\frac{1}{\rho g}\right]\left[\frac{p}{W}\right]\left[-W\frac{TSFC'}{V}\left(\frac{C_D'}{C_L}+\gamma\right)\right] \tag{A.419}$$

$$\gamma_{\text{CR}} \;=\; \left(\frac{C_D'}{C_L}\,\frac{p\,TSFC'}{\rho g V - p\,TSFC'}\right)_c \tag{A.420}$$

With the calculated cruise-climb angle γ_{CR}, the prescribed descent angle γ_{DE}, and the total cruise+descent remaining range $R_{\text{total}} - R_c$, the end-of-cruise range and altitude is the intersection of the straight cruise-climb and descent paths, calculated as follows.

$$R_d \;=\; R_c \;+\; \frac{h_e - h_c - \gamma_{\text{DE}}(R_{\text{total}} - R_c)}{\gamma_{\text{CR}} - \gamma_{\text{DE}}} \tag{A.421}$$

$$h_d \;=\; h_c \;+\; \gamma_{\text{CR}}(R_d - R_c) \tag{A.422}$$

Cruise-Climb

Because the cruise-climb segment proceeds at a fixed Mach number, the integrand in equation (A.414) can be assumed to be constant and equal to its value at start of cruise, so that an analytic integration is possible. The result is of course a form of the Breguet equation.

$$\frac{W_d}{W_c} \;=\; \exp\left[-\left(\frac{F'}{W}\,\frac{TSFC'}{V}\right)_c (R_d - R_c)\right] \tag{A.423}$$

$$t_d \;=\; t_c \;+\; \frac{R_d - R_c}{V} \tag{A.424}$$

Descent

The descent integration proceeds in much the same way as the climb, except that the descent angle is now prescribed, and the necessary thrust at each integration point i is computed from equation (A.413). The corresponding $T_{t\,4}$ and all the other engine operating variables are the calculated via the engine model run in prescribed-thrust off-design mode 3.

$$F'_e = \frac{W}{n_{\text{eng}}}\left(\sin\gamma_{\text{DE}} + \frac{C'_D}{C_L}\cos\gamma_{\text{DE}}\right) \tag{A.425}$$

$$\{T_{t_4}\,;\,TSFC', OPR, BPR\ldots\} = \mathcal{F}_{\text{eng}_3}(F'_e, A_2, A_{5\ldots}\,;\,M_\infty, p_\infty, T_\infty, K_{\text{inl}\cdots}) \tag{A.426}$$

The end result of the integration is the final weight W_e and flight time t_e.

A.2.16 Mission fuel

From the final landing weight W_e, the fuel burn and takeoff fuel weight can then be obtained.

$$W_{\text{burn}} = W_b - W_e \tag{A.427}$$

$$W_{\text{fuel}} = W_{\text{burn}}\,(1+f_{\text{reserve}}) \tag{A.428}$$

$$f_{\text{fuel}} = \frac{W_{\text{fuel}}}{W_{\text{MTO}}} \tag{A.429}$$

Appendix B

Turbofan Sizing and Analysis with Variable $c_p(T)$

B.1 Summary

The turbofan model described here is used for two purposes:
1) Sizing of a turbofan engine to obtain a specified thrust at design conditions, and
2) Calculations for a given engine at off-design conditions, with a specified thrust or burner outlet temperature.

It is largely based on the formulation of Kerrebrock [11], with a number of modifications. Turbine cooling flow which bypasses the combustor is introduced, and a multi-constituent gas model with variable $c_{p(T)}$ is used for all the flowpath calculations.

B.2 Nomenclature

A	flowpath area
a	speed of sound ($= \sqrt{TRc_p/(c_p - R)}$)
F	thrust force
f	fuel mass flow fraction ($= \dot{m}_{\text{fuel}}/\dot{m}_{\text{core}}$)
M	Mach number ($= u/a$)
$\bar{m}$	component corrected mass flow ($= \dot{m}\sqrt{T_t/T_{\text{ref}}}/(p_t/p_{\text{ref}})$)
$\bar{N}$	component corrected rotation speed ($= N/\sqrt{T_t/T_{\text{ref}}}$)
h, h_t	static and total complete enthalpy
p, p_t	static and total pressure
T, T_t	static and total temperature
u	velocity
α	bypass ratio ($= \dot{m}_{\text{fan}}/\dot{m}_{\text{core}}$)
α_c	turbine-cooling bypass ratio ($= \dot{m}_{\text{cool}}/\dot{m}_{\text{core}}$)
$\Delta h_{()}$	total enthalpy jump across component ()
$\pi_{()}$	total pressure ratio across component ()
$\eta_{\text{pol}_{()}}$	polytropic efficiency of component ()
$\eta_{()}$	overall total-to-total efficiency of component ()
$c_{p_i(T)}$	specific heat of gas constituent i
$h_{i(T)}$	complete enthalpy of gas constituent i
$\sigma_{i(T)}$	entropy-complement function of gas constituent i ($= \int (c_{p_i}/T)dT$)
R_i	ideal-gas constant of constituent i
$\alpha_i, \beta_i, \lambda_i$	constituent i mass fractions for air, fuel vapor, combustion product
$(\,)_{\text{f}}$	fan quantity
$(\,)_{\text{lc}}$	low pressure compressor (LPC) quantity
$(\,)_{\text{hc}}$	high pressure compressor (HPC) quantity
$(\,)_{\text{ht}}$	high pressure turbine (HPT) quantity
$(\,)_{\text{lt}}$	low pressure turbine (LPT) quantity
$(\,)_{\text{fn}}$	fan nozzle quantity
$(\,)_{\text{tn}}$	turbine nozzle quantity
$(\,)_{\ldots\text{D}}$	design-case quantity

The constituent property values and the mass fractions will also be denoted as a vector, e.g.

$$\begin{aligned} h_i &= \vec{h} \\ \alpha_i &= \vec{\alpha} \\ &\vdots \end{aligned}$$

B.2.1 Gas mixture properties

Overall gas-mixture functions $c_{p(T)}$, $h_{(T)}$, $\sigma_{(T)}$, R are computed using the individual $c_{p_i(T)}$, $h_{i(T)}$, $\sigma_{i(T)}$, R_i constituent functions and the mass fractions α_i, β_i, λ_i. For air we have the following.

$$c_{p(T)} = \sum_i \alpha_i \, c_{p_i(T)} = \vec{\alpha} \cdot \vec{c}_{p(T)} \tag{B.1}$$

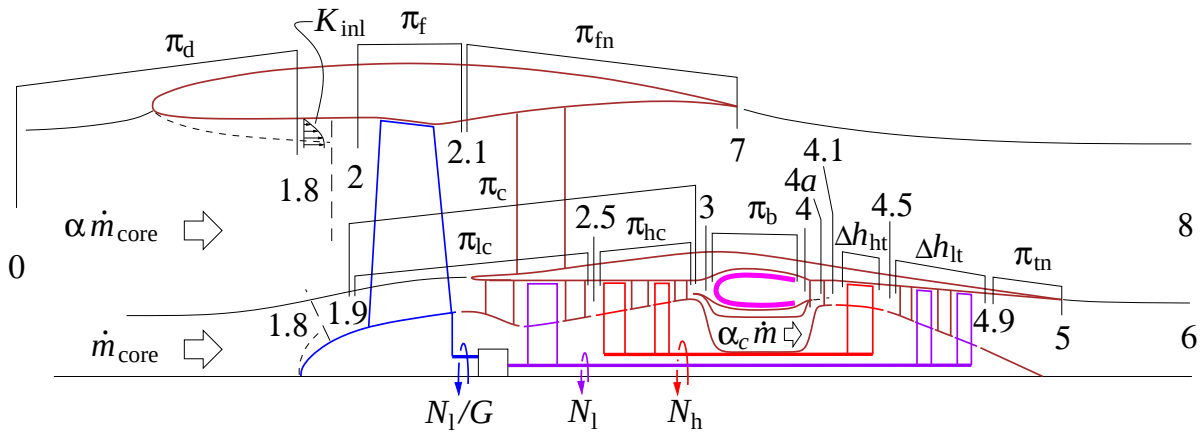

Figure B.1: Engine station numbers, total-pressure ratios, mass flows, and spool speeds.

$$h_{(T)} = \sum_i \alpha_i\, h_{i(T)} = \vec{\alpha} \cdot \vec{h}_{(T)} \tag{B.2}$$

$$\sigma_{(T)} = \sum_i \alpha_i\, \sigma_{i(T)} = \vec{\alpha} \cdot \vec{\sigma}_{(T)} \tag{B.3}$$

$$R = \sum_i \alpha_i\, R_i = \vec{\alpha} \cdot \vec{R} \tag{B.4}$$

For fuel vapor β_i is used instead of α_i, and for the combustion products λ_i is used instead of α_i. The combustion relations and the calculation of λ_i are described in detail in the related document "Thermally-Perfect Gas Calculations".

B.3 Pressure, Temperature, Enthalpy Calculations

B.3.1 Relations to be replaced

The standard constant–c_p equations connecting a baseline state T_o, h_o, p_o to some other state T, h, p are the familiar caloric and isentropic relations, with the latter possibly having a polytropic efficiency η_{pol} included to account for a non-isentropic process.

$$\Delta h \equiv h - h_o = c_p\,(T - T_o) \tag{B.5}$$

$$\pi \equiv \frac{p}{p_o} = \left(\frac{T}{T_o}\right)^{\eta_{\text{pol}}{}^{\pm 1} c_p/R} \tag{B.6}$$

The $+1/-1$ exponent on η_{pol} indicates a compression/expansion process, respectively. For a gas or gas mixture with a temperature-dependent $c_{p(T)}$, these relations are no longer valid, and will not be used here. The replacement relations described in the subsequent sections will be used instead.

The function Jacobian derivatives $\partial(\text{output})/\partial(\text{input})$ will also be derived for each case. These are required for off-design performance calculations via the Newton method.

B.3.2 Enthalpy prescribed

Occasionally it is necessary to obtain the temperature from a specified enthalpy. This is performed by simply inverting the $h_{(T)}$ function via the Newton method.

$$\text{initial guess:} \quad T = T_{\text{guess}} \quad \text{(e.g. standard temperature)} \tag{B.7}$$

$$\text{solve:} \quad h_{(T)} - h_{\text{spec}} = 0 \quad \rightarrow \quad T \tag{B.8}$$

The overall calculation will be denoted by

$$T = \mathcal{F}_T\left(\vec{\alpha}, h_{\text{spec}}\,;\, T_{\text{guess}}\right) \tag{B.9}$$

where the $\vec{\alpha}$ argument is required to evaluate the $h_{(T)}$ function in (B.8), via (B.2).

The derivative of the calculated temperature is simply the inverse of the specific heat.

$$\frac{dT}{dh} = \frac{1}{c_{p(T)}} \tag{B.10}$$

B.3.3 Pressure ratio prescribed

For prescribed $p_o, T_o, \pi, \eta_{\text{pol}}$, the new state p, T, h after a compression/expansion process is computed as follows.

$$\sigma_o = \sigma_{(T_o)} \tag{B.11}$$

$$c_{p_o} = c_{p(T_o)} \tag{B.12}$$

$$\text{initial guess:} \quad T = T_o\, \pi^{R_o/(c_{p_o}\, \eta_{\text{pol}}{}^{\pm 1})} \tag{B.13}$$

$$\text{solve:} \quad \frac{\sigma_{(T)} - \sigma_o}{R} - \frac{\ln \pi}{\eta_{\text{pol}}{}^{\pm 1}} = 0 \quad \rightarrow \quad T \tag{B.14}$$

$$p = p_o\, \pi \tag{B.15}$$

$$h = h_{(T)} \tag{B.16}$$

The solution for T is via Newton iteration. The overall calculation will be denoted by

$$\{p, T, h\} = \mathcal{F}_p\left(\vec{\alpha}, p_o, T_o, \pi, \eta_{\text{pol}}{}^{\pm 1}\right) \tag{B.17}$$

The function Jacobian derivatives $\partial\{p, T, h\}/\partial\{p_o, T_o, \pi\}$ are obtained by first implicitly differentiating (B.14) with respect to the specified p_o, T_o, π.

$$\frac{1}{R}\frac{d\sigma}{dT}\frac{\partial T}{\partial p_o} = 0 \tag{B.18}$$

$$\frac{1}{R}\left(\frac{d\sigma}{dT}\frac{\partial T}{\partial T_o} - \frac{d\sigma_o}{dT_o}\right) = 0 \tag{B.19}$$

$$\frac{1}{R}\frac{d\sigma}{dT}\frac{\partial T}{\partial \pi} - \frac{1}{\eta_{\text{pol}}{}^{\pm 1}}\frac{1}{\pi} = 0 \tag{B.20}$$

Using $d\sigma/dT = c_{p(T)}/T$ these then give $\partial T/\partial(\ )$, and also the remaining p and h derivatives via the chain rule.

$$\frac{\partial T}{\partial p_o} = 0 \tag{B.21}$$

$$\frac{\partial T}{\partial T_o} = \frac{c_{p_o}}{T_o}\frac{T}{c_{p(T)}} \tag{B.22}$$

$$\frac{\partial T}{\partial \pi} = \frac{R}{\pi\,{\eta_{\rm pol}}^{\pm 1}}\,\frac{T}{c_{p(T)}} \tag{B.23}$$

$$\frac{\partial p}{\partial p_o} = \pi \tag{B.24}$$

$$\frac{\partial p}{\partial T_o} = 0 \tag{B.25}$$

$$\frac{\partial p}{\partial \pi} = p_o \tag{B.26}$$

$$\frac{\partial h}{\partial p_o} = \frac{dh}{dT}\frac{\partial T}{\partial p_o} = 0 \tag{B.27}$$

$$\frac{\partial h}{\partial T_o} = \frac{dh}{dT}\frac{\partial T}{\partial T_o} = c_{p(T)}\,\frac{c_{p_o}}{T_o}\frac{T}{c_{p(T)}} = \frac{c_{p_o}}{T_o}\,T \tag{B.28}$$

$$\frac{\partial h}{\partial \pi} = \frac{dh}{dT}\frac{\partial T}{\partial \pi} = c_{p(T)}\,\frac{R}{\pi}\,\frac{T}{c_{p(T)}} = \frac{R}{\pi\,{\eta_{\rm pol}}^{\pm 1}}\,T \tag{B.29}$$

B.3.4 Pure loss prescribed

A pure loss with no work or heat addition is the limiting case of a prescribed pressure ratio $\pi < 1$, with $\eta_{\rm pol} = 0$. The relations above then greatly simplify to the following.

$$p = p_o\,\pi \tag{B.30}$$

$$T = T_o \tag{B.31}$$

$$h = h_o \tag{B.32}$$

B.3.5 Enthalpy difference prescribed

For prescribed $p_o, T_o, \Delta h, \eta_{\rm pol}$, the new state p, T, h after a compression/expansion process is computed as follows.

$$h_o = h_{(T_o)} \tag{B.33}$$

$$\sigma_o = \sigma_{(T_o)} \tag{B.34}$$

$$c_{p_o} = c_{p(T_o)} \tag{B.35}$$

$$\text{initial guess:} \quad T = T_o + \Delta h/c_{p_o} \tag{B.36}$$

$$\text{solve:} \quad h_{(T)} - h_o - \Delta h = 0 \quad \rightarrow \quad T \tag{B.37}$$

$$p = p_o\,\exp\!\left({\eta_{\rm pol}}^{\pm 1}\,\frac{\sigma_{(T)} - \sigma_o}{R}\right) \tag{B.38}$$

$$h = h_{(T)} \tag{B.39}$$

The solution for T is via Newton iteration. The overall calculation will be denoted by

$$\{p, T, h\} \;=\; \mathcal{F}_h\left(\vec{\alpha}, p_o, T_o, \Delta h, {\eta_{\rm pol}}^{\pm 1}\right) \tag{B.40}$$

The function Jacobian derivatives $\partial\{p, T, h\}/\partial\{p_o, T_o, \Delta h\}$ are obtained by first implicitly differentiating (B.37) with respect to the specified $p_o, T_o, \Delta h$.

$$\frac{dh}{dT}\frac{\partial T}{\partial p_o} \;=\; 0 \tag{B.41}$$

$$\frac{dh}{dT}\frac{\partial T}{\partial T_o} - \frac{dh_o}{dT_o} \;=\; 0 \tag{B.42}$$

$$\frac{dh}{dT}\frac{\partial T}{\partial \Delta h} - 1 \;=\; 0 \tag{B.43}$$

Using $dh/dT = c_{p(T)}$ these then give $\partial T/\partial(\,)$, and also the remaining p and h derivatives via the chain rule.

$$\frac{\partial T}{\partial p_o} \;=\; 0 \tag{B.44}$$

$$\frac{\partial T}{\partial T_o} \;=\; \frac{c_{p_o}}{c_{p(T)}} \tag{B.45}$$

$$\frac{\partial T}{\partial \Delta h} \;=\; \frac{1}{c_{p(T)}} \tag{B.46}$$

$$\frac{\partial p}{\partial p_o} \;=\; \frac{p}{p_o} + p\,\frac{{\eta_{\rm pol}}^{\pm 1}}{R}\left(\frac{d\sigma}{dT}\frac{\partial T}{\partial p_o}\right) \;=\; \frac{p}{p_o} \tag{B.47}$$

$$\frac{\partial p}{\partial T_o} \;=\; p\,\frac{{\eta_{\rm pol}}^{\pm 1}}{R}\left(\frac{d\sigma}{dT}\frac{\partial T}{\partial T_o} - \frac{d\sigma_o}{dT_o}\right) \;=\; p\,\frac{{\eta_{\rm pol}}^{\pm 1}}{R}\left(\frac{c_{p(T)}}{T} - \frac{c_{p_o}}{T_o}\right) \tag{B.48}$$

$$\frac{\partial p}{\partial \Delta h} \;=\; p\,\frac{{\eta_{\rm pol}}^{\pm 1}}{R}\frac{d\sigma}{dT}\frac{\partial T}{\partial \Delta h} \;=\; p\,\frac{{\eta_{\rm pol}}^{\pm 1}}{R}\frac{1}{T} \tag{B.49}$$

$$\frac{\partial h}{\partial p_o} \;=\; \frac{dh}{dT}\frac{\partial T}{\partial p_o} \;=\; 0 \tag{B.50}$$

$$\frac{\partial h}{\partial T_o} \;=\; \frac{dh}{dT}\frac{\partial T}{\partial T_o} \;=\; c_{p(T)}\,\frac{c_{p_o}}{c_{p(T)}} \;=\; c_{p_o} \tag{B.51}$$

$$\frac{\partial h}{\partial \Delta h} \;=\; \frac{dh}{dT}\frac{\partial T}{\partial \Delta h} \;=\; c_{p(T)}\,\frac{1}{c_{p(T)}} \;=\; 1 \tag{B.52}$$

B.3.6 Composition change prescribed

A composition change, such as due to combustion, is specified by the following mass fractions and input properties:

- α_i constituent i mass fraction for air
- β_i constituent i mass fraction for fuel vapor (assumed all burned)
- γ_i constituent i mass fraction change in air due to combustion
- T_o air temperature before combustion
- $T_{\rm f}$ fuel vapor temperature before combustion
- T temperature after combustion

The following quantities are computed:

f	fuel/air mass ratio
λ_i	constituent i mass fraction for combustion products

$$\vec{h}_o = h_{i(T_o)} \tag{B.53}$$
$$\vec{h} = h_{i(T)} \tag{B.54}$$
$$\vec{h}_{\rm f} = h_{i(T_{\rm f})} \tag{B.55}$$

The enthalpy balance across the combustor is

$$\dot{m}\,\vec{\alpha}\cdot\vec{h}_o + \dot{m}_{\rm fuel}\,\vec{\beta}\cdot\vec{h}_{\rm f} = \dot{m}\,\vec{\alpha}\cdot\vec{h} + \dot{m}_{\rm fuel}\,\vec{\gamma}\cdot\vec{h} \tag{B.56}$$

which can be solved for the fuel/air mass ratio.

$$f \equiv \frac{\dot{m}_{\rm fuel}}{\dot{m}_{\rm core}} = \frac{\vec{\alpha}\cdot\vec{h} - \vec{\alpha}\cdot\vec{h}_o}{\vec{\beta}\cdot\vec{h}_{\rm f} - \vec{\gamma}\cdot\vec{h}} \tag{B.57}$$

The mass fraction vector $\vec{\lambda}$ of the combustion products is obtained from the mass balance across the combustor.

$$\left[\,\dot{m}_{\rm core} + \dot{m}_{\rm fuel}\,\right]\vec{\lambda} = \dot{m}_{\rm core}\,\vec{\alpha} + \dot{m}_{\rm fuel}\,\vec{\gamma} \tag{B.58}$$
$$\vec{\lambda} = \frac{\vec{\alpha} + f\vec{\gamma}}{1+f} \tag{B.59}$$

The overall combustion-change calculation will be denoted by

$$\left\{f, \vec{\lambda}\right\} = \mathcal{F}_b\left(\vec{\alpha}, \vec{\beta}, \vec{\gamma}, T_o, T_{\rm f}, T\right) \tag{B.60}$$

The Jacobian derivatives of f and $\vec{\lambda}$ are obtained by direct differentiation of their definitions (B.57) and (B.59).

$$\frac{\partial f}{\partial T_o} = -\frac{\vec{\alpha}\cdot\vec{c}_{p_o}}{\vec{\beta}\cdot\vec{h}_{\rm f} - \vec{\gamma}\cdot\vec{h}} \tag{B.61}$$
$$\frac{\partial f}{\partial T_f} = -f\,\frac{\vec{\beta}\cdot\vec{c}_{p_{\rm f}}}{\vec{\beta}\cdot\vec{h}_{\rm f} - \vec{\gamma}\cdot\vec{h}} \tag{B.62}$$
$$\frac{\partial f}{\partial T} = \frac{\vec{\alpha}\cdot\vec{c}_p}{\vec{\beta}\cdot\vec{h}_{\rm f} - \vec{\gamma}\cdot\vec{h}} \tag{B.63}$$
$$\frac{\partial \vec{\lambda}}{\partial f} = \frac{\vec{\gamma} - \vec{\lambda}}{1+f} \tag{B.64}$$
$$\frac{\partial \vec{\lambda}}{\partial T_o} = \frac{\partial \vec{\lambda}}{\partial f}\,\frac{\partial f}{\partial T_o} \tag{B.65}$$
$$\frac{\partial \vec{\lambda}}{\partial T_{\rm f}} = \frac{\partial \vec{\lambda}}{\partial f}\,\frac{\partial f}{\partial T_{\rm f}} \tag{B.66}$$
$$\frac{\partial \vec{\lambda}}{\partial T} = \frac{\partial \vec{\lambda}}{\partial f}\,\frac{\partial f}{\partial T} \tag{B.67}$$

B.3.7 Mixing

Mixing between two streams is a simplified version of the combustion case above. No chemical reaction is assumed, so that $\vec{\gamma} = 0$. However, in general the two streams will have two different chemical compositions specified by their mass fraction vectors $\vec{\lambda}_a$ and $\vec{\lambda}_b$, two different temperatures T_a and T_b, and two different enthalpies $\vec{h}_a = h_{i(T_a)}$ and $\vec{h}_b = h_{i(T_b)}$. The species mass flow balance gives the composition mass fraction vector $\vec{\lambda}$ of the mixed gas, in terms of the convenient relative mass fractions f_a, f_b of the two streams.

$$f_a = \frac{\dot{m}_a}{\dot{m}_a + \dot{m}_b} \tag{B.68}$$

$$f_b = \frac{\dot{m}_b}{\dot{m}_a + \dot{m}_b} \tag{B.69}$$

$$\vec{\lambda} = f_a \vec{\lambda}_a + f_b \vec{\lambda}_b \tag{B.70}$$

Without any chemical reaction change term, the mixed enthalpy is

$$\vec{\lambda} \cdot \vec{h}_{(T)} \equiv h_{\rm mix} = f_a \vec{\lambda}_a \cdot \vec{h}_a + f_b \vec{\lambda}_b \cdot \vec{h}_b \tag{B.71}$$

which can be numerically inverted for the mixed temperature T, using the previously-defined $\mathcal{F}_T$ function.

$$T_{\rm guess} = f_a T_a + f_b T_b \tag{B.72}$$

$$T = \mathcal{F}_T \left(\vec{\lambda}, h_{\rm mix} \,;\, T_{\rm guess} \right) \tag{B.73}$$

B.3.8 Mach number prescribed

For prescribed $p_o, T_o, M_o, M, \eta_{\rm pol}$, the new adiabatic-change state p, T, h corresponding to M is computed as follows.

$$\sigma_o = \sigma_{(T_o)} \tag{B.74}$$

$$c_{p_o} = c_{p(T_o)} \tag{B.75}$$

$$h_o = h_{(T_o)} \tag{B.76}$$

$$u_o^2 = M_o^2 \, \frac{c_{p_o} R_o}{c_{p_o} - R_o} \, T_o \tag{B.77}$$

$$\text{initial guess:} \quad T = T_o \, \frac{1 + \frac{R_o}{2(c_{p_o} - R_o)} M_o^2}{1 + \frac{R_o}{2(c_{p_o} - R_o)} M^2} \tag{B.78}$$

$$\text{solve:} \quad h_{(T)} + \frac{1}{2} M^2 \frac{c_{p(T)} R}{c_{p(T)} - R} T - h_o - \frac{1}{2} u_o^2 = 0 \quad \rightarrow \quad T \tag{B.79}$$

$$p = p_o \, \exp\left({\eta_{\rm pol}}^{\pm 1} \, \frac{\sigma_{(T)} - \sigma_o}{R} \right) \tag{B.80}$$

$$h = h_{(T)} \tag{B.81}$$

The solution for T is via Newton iteration. The overall calculation will be denoted by

$$\{p, T, h\} = \mathcal{F}_M \left(\vec{\alpha}, p_o, T_o, M_o, M, {\eta_{\rm pol}}^{\pm 1} \right) \tag{B.82}$$

The convenient u^2 and u_o^2 derivatives are defined next.

$$u^2 = M^2 \frac{c_{p(T)}\, R}{c_{p(T)} - R} T \tag{B.83}$$

$$\frac{\partial u^2}{\partial M} = 2M \frac{c_{p(T)}\, R}{c_{p(T)} - R} T \tag{B.84}$$

$$\frac{\partial u^2}{\partial T} = M^2 \frac{R}{c_{p(T)} - R} \left(c_{p(T)} - \frac{R}{c_{p(T)} - R}\, c'_{p(T)}\, T \right) \tag{B.85}$$

$$\frac{\partial u_o^2}{\partial M_o} = 2M_o \frac{c_{p_o}\, R_o}{c_{p_o} - R_o} T_o \tag{B.86}$$

$$\frac{\partial u_o^2}{\partial T_o} = M_o^2 \frac{R_o}{c_{p_o} - R_o} \left(c_{p_o} - \frac{R_o}{c_{p_o} - R_o}\, c'_{p_o}\, T_o \right) \tag{B.87}$$

The function Jacobian derivatives $\partial \{p, T, h\} / \partial \{p_o, T_o, Mo, M\}$ are then obtained by first implicitly differentiating (B.79) with respect to the specified p_o, T_o, M_o, M.

$$\frac{dh}{dT}\frac{\partial T}{\partial p_o} + \frac{1}{2}\frac{\partial u^2}{\partial T}\frac{\partial T}{\partial p_o} = 0 \tag{B.88}$$

$$\frac{dh}{dT}\frac{\partial T}{\partial T_o} + \frac{1}{2}\frac{\partial u^2}{\partial T}\frac{\partial T}{\partial T_o} - \frac{\partial h_o}{\partial T_o} - \frac{\partial u_o^2}{\partial T_o} = 0 \tag{B.89}$$

$$\frac{dh}{dT}\frac{\partial T}{\partial M_o} + \frac{1}{2}\frac{\partial u^2}{\partial T}\frac{\partial T}{\partial M_o} - \frac{\partial u_o^2}{\partial M_o} = 0 \tag{B.90}$$

$$\frac{dh}{dT}\frac{\partial T}{\partial M} + \frac{1}{2}\frac{\partial u^2}{\partial T}\frac{\partial T}{\partial M} = 0 \tag{B.91}$$

Using $dh/dT = c_{p(T)}$ these then give $\partial T / \partial(\,)$, and also the remaining p and h derivatives via the chain rule.

$$\frac{\partial T}{\partial p_o} = 0 \tag{B.92}$$

$$\frac{\partial T}{\partial T_o} = \frac{c_{p_o}}{c_{p(T)}} \tag{B.93}$$

$$\frac{\partial T}{\partial \Delta h} = \frac{1}{c_{p(T)}} \tag{B.94}$$

$$\frac{\partial p}{\partial p_o} = \frac{p}{p_o} + p\, \frac{{\eta_{\rm pol}}^{\pm 1}}{R} \left(\frac{d\sigma}{dT}\frac{\partial T}{\partial p_o} \right) = \frac{p}{p_o} \tag{B.95}$$

$$\frac{\partial p}{\partial T_o} = p\, \frac{{\eta_{\rm pol}}^{\pm 1}}{R} \left(\frac{d\sigma}{dT}\frac{\partial T}{\partial T_o} - \frac{d\sigma_o}{dT_o} \right) = p\, \frac{{\eta_{\rm pol}}^{\pm 1}}{R} \left(\frac{c_{p(T)}}{T} - \frac{c_{p_o}}{T_o} \right) \tag{B.96}$$

$$\frac{\partial p}{\partial \Delta h} = p\, \frac{{\eta_{\rm pol}}^{\pm 1}}{R}\frac{d\sigma}{dT}\frac{\partial T}{\partial \Delta h} = p\, \frac{{\eta_{\rm pol}}^{\pm 1}}{R}\frac{1}{T} \tag{B.97}$$

$$\frac{\partial h}{\partial p_o} = \frac{dh}{dT}\frac{\partial T}{\partial p_o} = 0 \tag{B.98}$$

$$\frac{\partial h}{\partial T_o} = \frac{dh}{dT}\frac{\partial T}{\partial T_o} = c_{p(T)}\, \frac{c_{p_o}}{c_{p(T)}} = c_{p_o} \tag{B.99}$$

$$\frac{\partial h}{\partial \Delta h} = \frac{dh}{dT}\frac{\partial T}{\partial \Delta h} = c_{p(T)}\, \frac{1}{c_{p(T)}} = 1 \tag{B.100}$$

B.3.9 Mass flux prescribed

It is occasionally useful to calculate the static quantities p, T, h corresponding to a specified stagnation state p_o, T_o, h_o, and a specified mass flux $\rho u = \dot{m}/A \equiv m'$. This is computed as follows, starting from some given initial guess specified by the Mach number M_{guess}, which also selects the subsonic or supersonic branch.

$$\sigma_o = \sigma_{(T_o)} \tag{B.101}$$

$$h_o = h_{(T_o)} \tag{B.102}$$

$$\text{initial guess:} \quad T = T_o \Big/ \left(1 + \frac{R_o}{2(c_{p_o} - R_o)} M_{\text{guess}}^2\right) \tag{B.103}$$

$$\text{solve:} \qquad \left(\frac{p_{(T)}}{RT}\right)^2 2\left(h_o - h_{(T)}\right) - (m')^2 = 0 \qquad \rightarrow \qquad T \tag{B.104}$$

$$p = p_o \exp\left(\frac{\sigma_{(T)} - \sigma_o}{R}\right) \tag{B.105}$$

$$h = h_{(T)} \tag{B.106}$$

The solution for T is via Newton iteration. The overall calculation will be denoted by

$$\{p, T, h\} = \mathcal{F}_m\left(\vec{\alpha}, p_o, T_o, m' \,;\, M_{\text{guess}}\right) \tag{B.107}$$

This function's Jacobian derivatives can be calculated by the same procedures used for the other functions.

B.4 Turbofan Component Calculations

Most of the calculations described in this section are common to both the design and the off-design cases. The design case requires only a single calculation pass, with the mass flow and component dimensions determined only at the end. In contrast, the off-design case requires multiple Newton-iteration passes to converge the component pressure ratios and mass flows.

B.4.1 Design case inputs

The following quantities are assumed to be known for the design-case calculation.

T_0, p_0	atmospheric properties
M_0	flight Mach number
$T_{t\,4}$	burner exit total temperature
π_{f}	fan pressure ratio
π_{lc}	LPC pressure ratio
π_{hc}	HPC pressure ratio
α	fan bypass ratio
π_{d}	diffuser pressure ratio
π_{b}	burner pressure ratio
π_{fn}	fan duct loss pressure ratio
M_{4a}	representative Mach number at start of HPT cooling-flow mixing zone
T_{m}	HPT design metal temperature (if α_c is to be sized)
α_c	cooling-flow bypass ratio (if previously sized)

B.4.2 Freestream properties

From the specified freestream static temperature, pressure, and Mach number, T_0, p_0, M_0, we can obtain the freesteam speed of sound and velocity.

$$c_{p_0} = c_{p(T_0)} \tag{B.108}$$

$$a_0 = \sqrt{\frac{c_{p_0}}{c_{p_0} - R_0}\, R_0 T_0} \tag{B.109}$$

$$u_0 = M_0\, a_0 \tag{B.110}$$

B.4.3 Freestream-stagnation properties

The freestream stagnation quantities are computed using the specified enthalpy change procedure, with $\eta_{\mathrm{pol}} = 1$.

$$\Delta h = \tfrac{1}{2}\, u_0^2 \tag{B.111}$$

$$\{p_{t\,0}, T_{t\,0}, h_{t\,0}\} = \mathcal{F}_h\left(\vec{\alpha}, p_0, T_0, \Delta h, 1\right) \tag{B.112}$$

The standard fixed-c_p relations could also be used here, since the stagnation-static temperature difference is sufficiently small for any non-hypersonic flight Mach number.

B.4.4 Fan and compressor quantities

Inlet conditions

The stagnation conditions $()_{t\,1.8}$ in the inlet inviscid flow (excluding the inlet BLs) are computed as the pure-loss case with a diffuser total/total pressure ratio π_{d}.

$$p_{t\,1.8} = p_{t\,0}\, \pi_{\mathrm{d}} \tag{B.113}$$

$$T_{t\,1.8} = T_{t\,0} \tag{B.114}$$

$$h_{t\,1.8} = h_{t\,0} \tag{B.115}$$

Normally $\pi_{\mathrm{d}} \simeq 1$, unless an inlet screen or other losses are present upstream.

Fan and LPC inlet conditions

The inlet BL is characterized by a kinetic energy defect $K_{\rm inl}$.

$$K_{\rm inl} \;=\; \iint \frac{1}{2}(u_e^2 - u^2)\,\rho u\; dA \tag{B.116}$$

A low-speed approximation for the equivalent reduced total pressure $p_{t\,2}$ is obtained by a simple volume-flow average of p_t.

$$\dot{\mathcal{V}}_{\rm inl} \;\equiv\; \iint_{\rm inl} u\; dA \tag{B.117}$$

$$\begin{aligned}
(p_{t\,2} - p_{t\,1.8})\;\dot{\mathcal{V}}_{\rm inl} \;&=\; \iint_{\rm inl} (p_t - p_{t\,1.8})\,u\; dA \\
&\simeq\; \iint_{\rm inl} \left(p + \tfrac{1}{2}\rho u^2 \;-\; p_e + \tfrac{1}{2}\rho_e u_e^2\right) u\; dA \\
&=\; -\tfrac{1}{2}\rho_e u_e^3\,(\Theta^* + \Delta^{**})_{\rm inl} \;\simeq\; -\tfrac{1}{2}\rho_e u_e^3\,\Theta^*_{\rm inl} \;=\; -K_{\rm inl}
\end{aligned} \tag{B.118}$$

$$p_{t\,2} \;=\; p_{t\,1.8} \;-\; \frac{K_{\rm inl}}{\dot{\mathcal{V}}_{\rm inl}} \tag{B.119}$$

$$T_{t\,2} \;=\; T_{t\,1.8} \tag{B.120}$$

$$h_{t\,2} \;=\; h_{t\,1.8} \tag{B.121}$$

A similar calculation is carried out for the LPC inlet state $()_{t\,1.9}$. Possible limiting cases are:

$$(\,)_{t\,1.9} \;=\; \begin{cases} (\,)_{t\,1.8} \;, & \text{(no significant BL ingestion)} \\ (\,)_{t\,2} \;, & \text{(nacelle BL fills inlet flow)} \end{cases} \tag{B.122}$$

Fan exit conditions

The fan exit stagnation conditions are computed from the fan pressure ratio $\pi_{\rm f}$. The polytropic efficiency is computed first using the appropriate assumed fan efficiency map.

$$\eta_{\rm pol_f} \;=\; \begin{cases} \mathcal{F}_\eta(\pi_{\rm f}\,,\;\pi_{\rm f}\;,\;1\;,\;1\;) & , \text{(design case)} \\ \mathcal{F}_\eta(\pi_{\rm f}\,,\pi_{\rm f\,D}\,,\;\bar{m}_{\rm f}, \bar{m}_{\rm f\,D}) & , \text{(off-design case)} \end{cases} \tag{B.123}$$

$$\{p_{t\,2.1}, T_{t\,2.1}, h_{t\,2.1}\} \;=\; \mathcal{F}_p\left(\vec{\alpha}, p_{t\,2}, T_{t\,2}, \pi_{\rm f}, \eta_{\rm pol_f}\right) \tag{B.124}$$

Fan nozzle exit conditions

Fan duct and fan nozzle losses are represented by the total pressure-drop ratio $\pi_{\rm fn}$ with no total enthalpy change.

$$p_{t\,7} \;=\; p_{t\,2.1}\,\pi_{\rm fn} \tag{B.125}$$

$$T_{t\,7} \;=\; T_{t\,2.1} \tag{B.126}$$

$$h_{t\,7} \;=\; h_{t\,2.1} \tag{B.127}$$

LPC exit conditions

The LPC calculation is the same as for the fan. But the inlet state can be either 2 or 1.8, depending on whether the LPC does or does not ingest the inlet BL fluid.

$$\eta_{\mathrm{pol_{lc}}} = \begin{cases} \mathcal{F}_\eta(\pi_{\mathrm{lc}}\,,\ \pi_{\mathrm{lc}}\ ,\ 1\ ,\ 1\ ) & ,\ \text{(design case)} \\ \mathcal{F}_\eta(\pi_{\mathrm{lc}}, \pi_{\mathrm{lcD}}\,,\ \bar{m}_{\mathrm{lc}}, \bar{m}_{\mathrm{lcD}}) & ,\ \text{(off-design case)} \end{cases} \tag{B.128}$$

$$\{p_{t\,2.5}, T_{t\,2.5}, h_{t\,2.5}\} = \mathcal{F}_p\left(\vec{\alpha}, p_{t\,1.9}, T_{t\,1.9}, \pi_{\mathrm{lc}}, \eta_{\mathrm{pol_{lc}}}\right) \tag{B.129}$$

HPC exit conditions

The HPC calculation procedure is the same as for the LPC and fan, except that the 2.5 station quantities from the LPC calculation above are used for the HPC inlet.

$$\eta_{\mathrm{pol_{hc}}} = \begin{cases} \mathcal{F}_\eta(\pi_{\mathrm{hc}}\,,\ \pi_{\mathrm{hc}}\ ,\ 1\ ,\ 1\ ) & ,\ \text{(design case)} \\ \mathcal{F}_\eta(\pi_{\mathrm{hc}}, \pi_{\mathrm{hcD}}\,,\ \bar{m}_{\mathrm{hc}}, \bar{m}_{\mathrm{hcD}}) & ,\ \text{(off-design case)} \end{cases} \tag{B.130}$$

$$\{p_{t\,3}, T_{t\,3}, h_{t\,3}\} = \mathcal{F}_p\left(\vec{\alpha}, p_{t\,2.5}, T_{t\,2.5}, \pi_{\mathrm{hc}}, \eta_{\mathrm{pol_{hc}}}\right) \tag{B.131}$$

Fan and compressor efficiencies

The equivalent isentropic states and overall efficiencies can be computed for the fan and compressors out of interest, although these are not required for any subsequent calculations.

$$\{p_{t\,2.1}, (T_{t\,2.1})_{is}, (h_{t\,2.1})_{is}\} = \mathcal{F}_p\left(\vec{\alpha}, p_{t\,2}, T_{t\,2}, \pi_{\mathrm{f}}, 1\right) \tag{B.132}$$

$$\{p_{t\,2.5}, (T_{t\,2.5})_{is}, (h_{t\,2.5})_{is}\} = \mathcal{F}_p\left(\vec{\alpha}, p_{t\,1.9}, T_{t\,1.9}, \pi_{\mathrm{lc}}, 1\right) \tag{B.133}$$

$$\{p_{t\,3}, (T_{t\,3})_{is}, (h_{t\,3})_{is}\} = \mathcal{F}_p\left(\vec{\alpha}, p_{t\,2.5}, T_{t\,2.5}, \pi_{\mathrm{hc}}, 1\right) \tag{B.134}$$

$$\eta_{\mathrm{f}} = \frac{(h_{t\,2.1})_{is} - h_{t\,2}}{h_{t\,2.1} - h_{t\,2}} \tag{B.135}$$

$$\eta_{\mathrm{lc}} = \frac{(h_{t\,2.5})_{is} - h_{t\,1.9}}{h_{t\,2.5} - h_{t\,1.9}} \tag{B.136}$$

$$\eta_{\mathrm{hc}} = \frac{(h_{t\,3})_{is} - h_{t\,2.5}}{h_{t\,3} - h_{t\,2.5}} \tag{B.137}$$

B.4.5 Cooling Mass Flow or Metal Temperature Calculations

Cooling-flow calculations consist of either

1) Determination of cooling mass flow ratio (cooling sizing), or
2) Determination of metal temperature (cooling analysis).

It should be noted that the cooling sizing case 1) may be performed for any operating point, and not necessarily the engine-sizing design point. For example, an engine whose design sizing case is the cruise condition will typically have its cooling flow ratio sized at the off-design takeoff condition.

Cooling Mass Flow Ratio Sizing

For the cooling-sizing case, the cooling mass flow ratios ε_1, $\varepsilon_2 \ldots$ for the hot-section blade rows are determined to obtain required blade-row metal temperatures $T_{\mathrm{m}_1}, T_{\mathrm{m}_2} \ldots$ as described in the document "Film Cooling Flow Loss Model". The function has the form

$$\{\varepsilon_1, \varepsilon_2, \ldots\} \;=\; \mathcal{F}_\varepsilon \left(T_{t3}, T_{t4}, T_{\mathrm{m}_1}, T_{\mathrm{m}_2} \ldots ;\, M_{\mathrm{exit}}, \Delta T_{\mathrm{streak}}, St_A, \theta_f, \eta\right) \qquad \text{(B.138)}$$

where $M_{\mathrm{exit}} \ldots \eta$ are the various parameters in the cooling model. The overall cooling mass flow is the sum of the individual blade-row cooling mass flows.

$$\alpha_c \;=\; \varepsilon_1 + \varepsilon_2 + \ldots \qquad \text{(B.139)}$$

Metal Temperature Calculation

In this case the individual blade-row cooling mass flow ratios $\varepsilon_1, \varepsilon_2 \ldots$ and and the overall cooling mass flow ratio α_c are assumed to be known. The blade-row metal temperatures can then be determined from the cooling model relations, which are now recast into the following form.

$$\{T_{\mathrm{m}_1}, T_{\mathrm{m}_2}, \ldots\} \;=\; \mathcal{F}_{T_{\mathrm{m}}} \left(T_{t3}, T_{t4}, \varepsilon_1, \varepsilon_2 \ldots ;\, M_{\mathrm{exit}}, \Delta T_{\mathrm{streak}}, St_A, \theta_f, \eta\right) \qquad \text{(B.140)}$$

These metal temperatures are not required for any subsequent calculations.

B.4.6 Combustor quantities

The combustor/IGV section possibly has cooling air flow which bypasses the combustor. The mass flows and control volumes are detailed in Figure B.2.

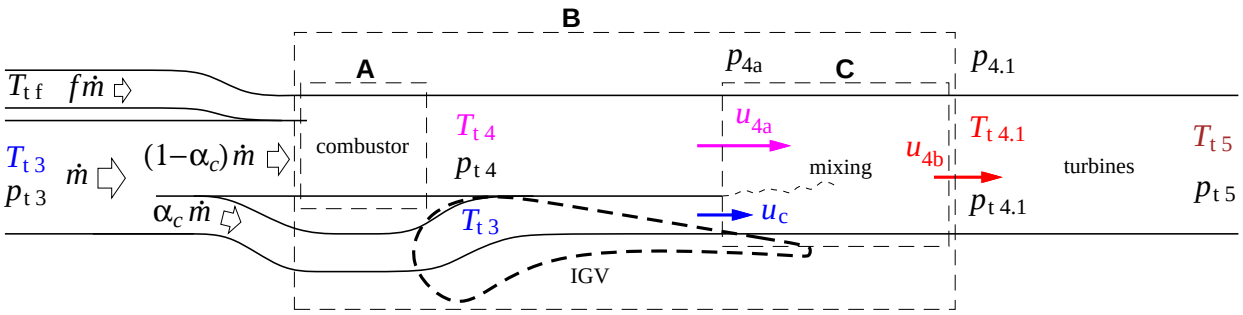

6.5in1.5in

Figure B.2: Combustor and film-cooling flows, with mixing over and downstream of IGV. Dashed rectangles are control volumes.

Using control volume A in Figure B.2, the fuel/combustor-air mass flow fraction f_b and the combustion-product constituent mass fraction vector $\vec{\lambda}$ are obtained by using the compressor exit condition $()_{t3}$, together with the specified combustor exit total temperature T_{t4}. The fuel/core-air fraction f then follows.

$$\left\{f_b, \vec{\lambda}\right\} \;=\; \mathcal{F}_b \left(\vec{\alpha}, \vec{\beta}, \vec{\gamma}, T_{t3}, T_{t_f}, T_{t4}\right) \qquad \text{(B.141)}$$

$$f \;=\; f_b \left(1 - \alpha_c\right) \qquad \text{(B.142)}$$

The combustor exit conditions are then obtained using this $\vec{\lambda}$, together with the specified $T_{t\,4}$ and the assumed combustor pressure ratio $\pi_{\rm b}$.

$$h_{t\,4} = \vec{\lambda} \cdot \vec{h}_{(T_{t\,4})} \tag{B.143}$$

$$\sigma_{t\,4} = \vec{\lambda} \cdot \vec{\sigma}_{(T_{t\,4})} \tag{B.144}$$

$$p_{t\,4} = p_{t\,3}\,\pi_{\rm b} \tag{B.145}$$

B.4.7 Station 4.1 without IGV Cooling Flow

Without cooling flow ($\alpha_c = 0$), the 4.1 station quantities and constituent mass fraction at the first turbine rotor inlet are the same as the 4 station quantities at the combustor exit.

$$T_{t\,4.1} = T_{t\,4} \tag{B.146}$$

$$p_{t\,4.1} = p_{t\,4} \tag{B.147}$$

$$\vec{\lambda}' = \vec{\lambda} \tag{B.148}$$

The analysis can then skip the cooling flow mixing calculations below, and proceed directly to the **Turbine Quantities** section.

B.4.8 Station 4.1 with IGV Cooling Flow

The IGV pressure at the cooling flow exit is specified indirectly via the cooling-exit Mach M_{4a} at the combustor-exit stagnation conditions. The corresponding static conditions and velocity are calculated using the $\mathcal{F}_M$ function.

$$\{\, p_{4a}, T_{4a}, h_{4a} \,\} = \mathcal{F}_M\left(\vec{\lambda}, p_{t\,4}, T_{t\,4}, 0, M_{4a}, 1\right) \tag{B.149}$$

$$u_{4a} = \sqrt{2(h_{t\,4} - h_{4a})} \tag{B.150}$$

The cooling flow is assumed to exit the IGV at some fraction r_{u_c} of this u_{4a}.

$$u_{\rm c} = r_{u_c}\, u_{4a} \tag{B.151}$$

The combustor and cooling flows are assumed to be fully mixed at station 4.1. The mixed-out mass fraction vector $\vec{\lambda}'$ is calculated by the mass flow balance,

$$\vec{\lambda}' = \frac{1 - \alpha_c + f}{1 + f}\,\vec{\lambda} + \frac{\alpha_c}{1 + f}\,\vec{\alpha} \tag{B.152}$$

and is used for the downstream turbine and core exhaust calculations. Assuming a constant static pressure over the mixing region, a simple momentum balance gives the mixed-out velocity $u_{4.1}$.

$$p_{4.1} = p_{4a} \tag{B.153}$$

$$u_{4.1} = \frac{1 - \alpha_c + f}{1 + f}\,u_{4a} + \frac{\alpha_c}{1 + f}\,u_c \tag{B.154}$$

The enthalpy balance across control volume B in Figure B.2 gives the mixed-out total temperature $T_{t\,4.1}$ via the $\mathcal{F}_h$ function.

$$h_{(T_{t\,4.1})} \equiv h_{t\,4.1} = \frac{1-\alpha_c+f}{1+f}\,h_{t\,4} + \frac{\alpha_c}{1+f}\,h_{t\,3} \tag{B.155}$$

$$T_{\text{guess}} = \frac{1-\alpha_c+f}{1+f}\,T_{t\,4} + \frac{\alpha_c}{1+f}\,T_{t\,3} \tag{B.156}$$

$$T_{t\,4.1} = \mathcal{F}_T\left(\vec{\lambda}', h_{t\,4.1}\,;\,T_{\text{guess}}\right) \tag{B.157}$$

The total pressure is then obtained using the mixed-out velocity $u_{4.1}$, together with the $\mathcal{F}_h$ function.

$$h_{4.1} = h_{t\,4.1} - \frac{1}{2}\,u_{4.1}^2 \tag{B.158}$$

$$\Delta h = \frac{1}{2}\,u_{4.1}^2 \tag{B.159}$$

$$\{\,p_{t\,4.1}, T_{t\,4.1}, h_{t\,4.1}\,\} = \mathcal{F}_h\left(\vec{\lambda}', p_{4.1}, T_{4.1}, \Delta h, 1\right) \tag{B.160}$$

B.4.9 Turbine quantities

High Pressure Turbine

The HPT enthalpy drop is obtained by equating the turbine work with the HPC work.

$$\dot{m}_{\text{hc}}(1+f)\,(h_{t\,4.1}-h_{t\,4.5}) = \dot{m}_{\text{hc}}\,(h_{t\,3}-h_{t\,2.5}) \tag{B.161}$$

$$h_{t\,4.5}-h_{t\,4.1} \equiv \Delta h_{\text{ht}} = \frac{-1}{1+f}\left[h_{t\,3}-h_{t\,2.5}\right] \tag{B.162}$$

This enthalpy drop, together with an assumed polytropic efficiency, is then used to determine the HPT exit stagnation conditions.

$$\{p_{t\,4.5}, T_{t\,4.5}, h_{t\,4.5}\} = \mathcal{F}_h\left(\vec{\lambda}', p_{t\,4.1}, T_{t\,4.1}, \Delta h_{\text{ht}}, {\eta_{\text{pol}_{\text{t}}}}^{-1}\right) \tag{B.163}$$

Low Pressure Turbine (Design case)

The LPT enthalpy drop for the design case is obtained by equating the turbine work with the LPC plus fan work.

$$\dot{m}_{\text{hc}}(1+f)\,(h_{t\,4.5}-h_{t\,4.9}) = \dot{m}_{\text{lc}}\,(h_{t\,2.5}-h_{t\,1.9}) + \dot{m}_{\text{fan}}\,(h_{t\,2.1}-h_{t\,2}) \tag{B.164}$$

$$h_{t\,4.9}-h_{t\,4.5} \equiv \Delta h_{\text{lt}} = \frac{-1}{1+f}\,\frac{\dot{m}_{\text{lc}}}{\dot{m}_{\text{hc}}}\left[(h_{t\,2.5}-h_{t\,1.9}) + \alpha\,(h_{t\,2.1}-h_{t\,2})\right] \tag{B.165}$$

The $\dot{m}_{\text{lc}}/\dot{m}_{\text{hc}}$ mass flow ratio is known, and is unity if there's no bleed at the 2.5 station. The enthalpy drop calculated above, together with an assumed turbine polytropic efficiency,

is then used to determine all the station 4.9 LPT exit conditions. The turbine nozzle total pressure ratio $\pi_{\rm tn}$ then give the station 5 nozzle conditions.

$$\{p_{t\,4.9}, T_{t\,4.9}, h_{t\,4.9}\} = \mathcal{F}_h\left(\vec{\lambda}', p_{t\,4.5}, T_{t\,4.5}, \Delta h_{\rm lt}, \eta_{\rm pol_t}{}^{-1}\right) \quad \text{(B.166)}$$

$$p_{t\,5} = p_{t\,4.9}\,\pi_{\rm tn} \quad \text{(B.167)}$$

$$T_{t\,5} = T_{t\,4.9} \quad \text{(B.168)}$$

$$h_{t\,5} = h_{t\,4.9} \quad \text{(B.169)}$$

Low Pressure Turbine (Off-Design case)

The relations above could be used to determine the $()_{t\,5}$ core exit quantities for the off-design case. However, this opens the possibility of $p_{t\,5}$ falling below the nozzle static pressure $p_5 = p_0$ during one Newton iteration. A common cause is the fan's enthalpy extraction term $\alpha(h_{t\,2.1} - h_{t\,2})$ in (B.165) being too large because of a momentarily excessive $\pi_{\rm f}$ and/or $\bar{m}_{\rm f}$ values, so that $\Delta h_{\rm lt}$ is too negative which gives a small $p_{t\,5}$ in calculations (B.166) and (B.167).

Regardless of the cause, if $p_{t\,5} < p_5$ is a result then the nozzle velocity u_5 cannot be computed, and the subsequent nozzle mass flow and thrust relations cannot be imposed. This causes failure of the overall Newton iteration process. One solution is to underrelax an "excessive" Newton update so that $p_{t\,5}$ never falls below p_5. However, this is rather impractical since a very long calculation chain is required to reach the $p_{t\,5}$ evaluation operations (B.166) and (B.167), so the necessary underrelaxation factor cannot be determined without in effect performing and possibly discarding the calculations for one whole Newton iteration.

The solution taken here is to introduce $p_{t\,5}$ as a Newton variable, so that during the Newton update it can be easily monitored to ensure that it never falls below p_5. It also means that so that the $()_{t\,5}$ quantities are now computed by the alternative procedure of a specified pressure ratio as used for the compressors.

$$\pi_{\rm lt} = \frac{p_{t\,4.9}}{p_{t\,4.5}} = \frac{1}{\pi_{\rm tn}}\,\frac{p_{t\,5}}{p_{t\,4.5}} \quad \text{(B.170)}$$

$$\{p_{t\,4.9}, T_{t\,4.9}, h_{t\,4.9}\} = \mathcal{F}_p\left(\vec{\lambda}', p_{t\,4.5}, T_{t\,4.5}, \pi_{\rm lt}, \eta_{\rm pol_t}{}^{-1}\right) \quad \text{(B.171)}$$

$$p_{t\,5} = p_{t\,4.9}\,\pi_{\rm tn} \quad \text{(B.172)}$$

$$T_{t\,5} = T_{t\,4.9} \quad \text{(B.173)}$$

$$h_{t\,5} = h_{t\,4.9} \quad \text{(B.174)}$$

The LPT work relation (B.165) will now play the role as a Newton equation which constrains $p_{t\,5}$. This overall procedure will of course produce the same final result as if $p_{t\,5}$ was calculated from (B.165), but its Newton iteration behavior is far more stable and reliable.

Turbine efficiencies

The turbine efficiencies (including cooling-air losses) can also be computed out of interest.

$$\{p_{t\,4.5}, (T_{t\,4.5})_{is}, (h_{t\,4.5})_{is}\} = \mathcal{F}_p\left(\vec{\lambda}', p_{t\,4}, T_{t\,4}, p_{t\,4.5}/p_{t\,4}, 1\right) \quad \text{(B.175)}$$

$$\{p_{t\,4.9}, (T_{t\,4.9})_{is}, (h_{t\,4.9})_{is}\} = \mathcal{F}_p\left(\vec{\lambda}', p_{t\,4.5}, T_{t\,4.5}, p_{t\,5}/p_{t\,4.5}, 1\right) \quad \text{(B.176)}$$

$$\eta_{\rm ht} = \frac{h_{t\,4.5} - h_{t\,4}}{(h_{t\,4.5})_{is} - h_{t\,4}} \quad \text{(B.177)}$$

$$\eta_{\rm lt} = \frac{h_{t\,4.9} - h_{t\,4.5}}{(h_{t\,4.9})_{is} - h_{t\,4.5}} \quad \text{(B.178)}$$

B.4.10 Fan exhaust quantities

The fan exhaust velocity is computed from the known $()_{t\,8}$ fan plume stagnation conditions, and the requirement of ambient exhaust pressure, $p_8 = p_0$.

$$p_{t\,8} = p_{t\,7} \quad \text{(B.179)}$$

$$T_{t\,8} = T_{t\,7} \quad \text{(B.180)}$$

$$\{p_8, T_8, h_8\} = \mathcal{F}_p\left(\vec{\alpha}, p_{t\,8}, T_{t\,8}, p_0/p_{t\,8}, 1\right) \quad \text{(B.181)}$$

$$u_8 = \sqrt{2(h_{t\,8} - h_8)} \quad \text{(B.182)}$$

B.4.11 Core exhaust quantities

The core exhaust velocity is computed from the known $()_{t\,6}$ core plume conditions and the requirement of ambient exhaust pressure, $p_6 = p_0$.

$$p_{t\,6} = p_{t\,5} \quad \text{(B.183)}$$

$$T_{t\,6} = T_{t\,5} \quad \text{(B.184)}$$

$$\{p_6, T_6, h_6\} = \mathcal{F}_p\left(\vec{\lambda}', p_{t\,6}, T_{t\,6}, p_0/p_{t\,6}, 1\right) \quad \text{(B.185)}$$

$$u_6 = \sqrt{2(h_{t\,6} - h_6)} \quad \text{(B.186)}$$

B.4.12 Overall engine quantities

The overall specific thrust is obtained from the total fan and core thrust forces.

$$\dot{m}_{\rm core} \equiv \bar{m}_{\rm lc} \frac{p_{t\,2}/p_{\rm ref}}{\sqrt{T_{t\,2}/T_{\rm ref}}} \quad \text{(B.187)}$$

$$F_8 = \alpha \dot{m}_{\rm core}\left[u_8 - u_0\right] \quad \text{(B.188)}$$

$$F_6 = \dot{m}_{\rm core}\left[(1+f)u_6 - u_0\right] \quad \text{(B.189)}$$

$$F = F_6 + F_8 \quad \text{(B.190)}$$

$$F_{\rm sp} \equiv \frac{F}{(1+\alpha)\,\dot{m}_{\rm core}\,a_0} = \frac{(1+f)u_6 - u_0 + \alpha(u_8 - u_0)}{(1+\alpha)\,a_0} \quad \text{(B.191)}$$

The overall specific impulse and thrust specific fuel consumption then follow.

$$I_{\rm sp} \equiv \frac{F}{\dot{m}_{\rm fuel}\,g} = \frac{F_{\rm sp}}{f}\frac{a_0}{g}(1+\alpha) \quad \text{(B.192)}$$

$$TSFC = \frac{1}{I_{\rm sp}} \quad \text{(B.193)}$$

B.5 Design Sizing Calculation

For the design case, the following quantities are specified.

$F_{\rm D}$	design thrust
M_2	fan-face, LPC-face axial Mach number
$M_{2.5}$	HPC-face axial Mach number

B.5.1 Mass Flow Sizing

This consists of finding the core mass flow to achieve the required thrust at at the design operating conditions p_0, a_0, M_0. This design core mass flow $\dot{m}_{\rm core}$ is obtained directly from relation (B.191), using the specified design thrust $F_{\rm D}$.

$$\dot{m}_{\rm core} = \frac{F_{\rm D}}{F_{\rm sp}\, a_0\, (1+\alpha)} \tag{B.194}$$

B.5.2 Component Area Sizing

Fan area

The fan-face static ρ_2 and a_2 are obtained from the specified-Mach procedure, with some specified fan-face Mach number M_2, and some $\eta_{\rm pol} = \eta_{\rm pol_d}$.

$$\{p_2, T_2, h_2\} = \mathcal{F}_M\left(\vec{\alpha}, p_0, T_0, M_0, M_2, \eta_{\rm pol_d}\right) \tag{B.195}$$

The fan area A_2 can then be computed from the design mass flow.

$$\rho_2 = \frac{p_2}{R_2 T_2} \tag{B.196}$$

$$u_2 = M_2\sqrt{\frac{c_{p_2}\, R_2}{c_{p_2} - R_2}\, T_2} \tag{B.197}$$

$$A_2 = \frac{(1+\alpha)\, \dot{m}_{\rm core}}{\rho_2 u_2} \tag{B.198}$$

A specified hub/tip ratio $HTR_{\rm f}$ then also gives the fan diameter,

$$d_{\rm f} = \sqrt{\frac{4}{\pi}\frac{A_2}{1 - HTR_{\rm f}^2}} \tag{B.199}$$

although this is not required for any subsequent off-design analysis.

The HP compressor fan area $A_{2.5}$ is obtained in this same manner from a specified compressor-face Mach number $M_{2.5}$.

$$\{p_{2.5}, T_{2.5}, h_{2.5}\} = \mathcal{F}_M\left(\vec{\alpha}, p_{t\,2.5}, T_{t\,2.5}, 0, M_{2.5}, \eta_{\rm pol_d}\right) \tag{B.200}$$

$$\rho_{2.5} = \frac{p_{2.5}}{R_{2.5} T_{2.5}} \tag{B.201}$$

$$u_{2.5} = M_{2.5}\sqrt{\frac{c_{p_{2.5}}\,R_{2.5}}{c_{p_{2.5}}-R_{2.5}}\,T_{2.5}} \tag{B.202}$$

$$A_{2.5} = \frac{(1+\alpha)\,\dot{m}_{\rm core}}{\rho_{2.5}u_{2.5}} \tag{B.203}$$

A specified hub/tip ratio $HTR_{\rm f}$ then also gives the HPC face diameter.

$$d_{\rm hc} = \sqrt{\frac{4}{\pi}\frac{A_{2.5}}{1-HTR_{\rm hc}^2}} \tag{B.204}$$

Fan nozzle area

The fan nozzle flow type can be determined from the fan-plume Mach number.

$$M_8 = u_8/\sqrt{\frac{c_{p_8}\,R_8}{c_{p_8}-R_8}\,T_8} \tag{B.205}$$

If $M_8 < 1$ then the fan nozzle is assumed to be unchoked, and the nozzle conditions are obtained by using the specified pressure ratio function. The nozzle is assumed here to be at ambient static pressure, although any other pressure can be specified instead.

$$p_7 = p_0 \tag{B.206}$$

$$\{p_7, T_7, h_7\} = \mathcal{F}_p\left(\vec{\alpha}, p_{t\,7}, T_{t\,7}, p_7/p_{t\,7}, 1\right) \tag{B.207}$$

If $M_8 \geq 1$ the the fan nozzle is choked, and the nozzle conditions are obtained using the specified Mach function.

$$M_7 = 1 \tag{B.208}$$

$$\{p_7, T_7, h_7\} = \mathcal{F}_M\left(\vec{\alpha}, p_{t\,7}, T_{t\,7}, 0, M_7, 1\right) \tag{B.209}$$

In either case, the fan area follows directly.

$$u_7 = \sqrt{2(h_{t\,7} - h_7)} \tag{B.210}$$

$$\rho_7 = \frac{p_7}{R_7 T_7} \tag{B.211}$$

$$A_7 = \frac{\alpha\,\dot{m}_{\rm core}}{\rho_7 u_7} \tag{B.212}$$

Core nozzle area

The core nozzle flow type is determined from the core-plume Mach number.

$$M_6 = u_6/\sqrt{\frac{c_{p_6}\,R_6}{c_{p_6}-R_6}\,T_6} \tag{B.213}$$

If $M_6 < 1$ then the core nozzle is unchoked, and the nozzle conditions are obtained by using the specified pressure ratio function.

$$p_5 = p_0 \tag{B.214}$$

$$\{p_5, T_5, h_5\} = \mathcal{F}_p\left(\vec{\alpha}, p_{t\,5}, T_{t\,5}, p_5/p_{t\,5}, 1\right) \tag{B.215}$$

If $M_6 \geq 1$ the the fan nozzle is choked, and the nozzle conditions are obtained using the specified Mach function.

$$M_5 = 1 \tag{B.216}$$

$$\{p_5, T_5, h_5\} = \mathcal{F}_M\left(\vec{\alpha}, p_{t\,5}, T_{t\,5}, 0, M_5, 1\right) \tag{B.217}$$

The core nozzle area follows.

$$u_5 = \sqrt{2(h_{t\,5} - h_5)} \tag{B.218}$$

$$\rho_5 = \frac{p_5}{R_5 T_5} \tag{B.219}$$

$$A_5 = \frac{\dot{m}_{\text{core}}}{\rho_5 u_5} \tag{B.220}$$

B.5.3 Design corrected speeds and mass flows

Since only speed ratios will be considered in the off-design calculation, the LPC and HPC design spool speeds can be arbitrarily set to unity.

$$N_{\text{lcD}} = 1 \tag{B.221}$$

$$N_{\text{hcD}} = 1 \tag{B.222}$$

The design corrected spool speeds and high-pressure and low-pressure turbine corrected mass flows are defined in the usual manner.

$$\bar{N}_{\text{lD}} = N_{\text{lD}} \frac{1}{\sqrt{T_{t\,1.9}/T_{\text{ref}}}} \tag{B.223}$$

$$\bar{N}_{\text{hD}} = N_{\text{hD}} \frac{1}{\sqrt{T_{t\,2.5}/T_{\text{ref}}}} \tag{B.224}$$

$$\bar{m}_{\text{htD}} = (1+f)\,\dot{m}_{\text{core}} \frac{\sqrt{T_{t\,4.1}/T_{\text{ref}}}}{p_{t\,4.1}/p_{\text{ref}}} \tag{B.225}$$

$$\bar{m}_{\text{ltD}} = (1+f)\,\dot{m}_{\text{core}} \frac{\sqrt{T_{t\,4.5}/T_{\text{ref}}}}{p_{t\,4.5}/p_{\text{ref}}} \tag{B.226}$$

B.6 Off-Design Operation Calculation

For an off-design case, the following eight quantities which were assumed known at the start of the calculation pass are really unknowns, and must be updated.

π_{f}	fan pressure ratio
π_{lc}	LPC pressure ratio
π_{hc}	HPC pressure ratio
$\bar{m}_{\text{f}}$	fan corrected mass flow
$\bar{m}_{\text{lc}}$	LPC corrected mass flow
$\bar{m}_{\text{hc}}$	HPC corrected mass flow
$T_{t\,4}$	burner exit total temperature
$p_{t\,5}$	core nozzle total pressure

The necessary eight constraining equations involve the spool speeds, which are calculated as described in the next section. The speed calculation is based on an assumed fan or compressor map, and has the following functional form.

$$\bar{N} \;=\; \mathcal{F}_N\,(\pi\,,\,\bar{m}) \tag{B.227}$$

This is used to compute the fan, LPC, and HPC speed from each component's current pressure ratio and corrected mass flows. The current station 1.9, 2, 2.5 stagnation conditions are also used, to compute the necessary $\bar{m}$ arguments for the $\mathcal{F}_N$ functions.

$$N_\mathrm{f} \;=\; \sqrt{T_{t\,2}/T_\mathrm{ref}}\;\mathcal{F}_N(\pi_\mathrm{f}\,,\;\bar{m}_\mathrm{f}) \tag{B.228}$$

$$N_\mathrm{l} \;=\; \sqrt{T_{t\,1.9}/T_\mathrm{ref}}\;\mathcal{F}_N(\pi_\mathrm{lc}\,,\;\bar{m}_\mathrm{lc}) \tag{B.229}$$

$$N_\mathrm{h} \;=\; \sqrt{T_{t\,2.5}/T_\mathrm{ref}}\;\mathcal{F}_N(\pi_\mathrm{hc}\,,\;\bar{m}_\mathrm{hc}) \tag{B.230}$$

Each of these three functions uses the appropriate map constants for that component, given in the component-map section.

The off-design fan face Mach number M_2 can be calculated from the fan-face mass flow relation.

$$\rho_2 u_2 A_2 \;=\; \bar{m}_\mathrm{f}\sqrt{\frac{T_\mathrm{ref}}{T_{t\,2}}}\,\frac{p_{t\,2}}{p_\mathrm{ref}} \;+\; \bar{m}_\mathrm{lc}\sqrt{\frac{T_\mathrm{ref}}{T_{t\,1.9}}}\,\frac{p_{t\,1.9}}{p_\mathrm{ref}} \;=\; (1{+}\alpha)\dot{m}_\mathrm{core} \tag{B.231}$$

This is solved for the implied M_2 (subsonic branch) using the $\mathcal{F}_m$ specified-mass function. The design M_2 value is a suitable initial guess.

$$M_\mathrm{guess} \;=\; (M_2)_\mathrm{D} \tag{B.232}$$

$$m' \;=\; (1{+}\alpha)\,\dot{m}_\mathrm{core}/A_2 \tag{B.233}$$

$$\{p_2, T_2, h_2\} \;=\; \mathcal{F}_m\,(\vec{\alpha}, p_{t\,2}, T_{t\,2}, h_{t\,2}, m'\,;\,M_\mathrm{guess}) \tag{B.234}$$

$$u_2 \;=\; \sqrt{2(h_{t\,2} - h_2)} \tag{B.235}$$

$$M_2 \;=\; u_2/\sqrt{\frac{c_{p_2}\,R_2}{c_{p_2}{-}R_2}\,T_2} \tag{B.236}$$

B.6.1 Constraint residuals

The eight residuals for constraining the eight operating unknowns are listed below.

Fan/LPC speed constraint

Equating the fan and LPC speeds, with some specified gear ratio G_f, defines the constraining equation residual.

$$\mathcal{R}_1 \;\equiv\; N_\mathrm{f}\,G_\mathrm{f} \;-\; N_\mathrm{l} \;=\; 0 \tag{B.237}$$

HPT mass flow

In lieu of a full turbine map, it is reasonable to assume that the high-pressure turbine IGV is always choked. The appropriate constraining residual is therefore a fixed corrected mass flow at station 4.1, equal to the design value.

$$\mathcal{R}_2 \;\equiv\; (1+f)\bar{m}_{\rm hc}\sqrt{\frac{T_{t\,4.1}}{T_{t\,2.5}}}\frac{p_{t\,2.5}}{p_{t\,4.1}} \;-\; \bar{m}_{\rm htD} \;=\; 0 \tag{B.238}$$

Note that this approximation means that the high spool speed $N_{\rm h}$ is not required in any of the calculations.

LPT mass flow

The low-pressure turbine IGV is also assumed to be choked. Again, the appropriate constraining residual is therefore a fixed corrected mass flow at station 4.5, equal to the design value.

$$\mathcal{R}_3 \;\equiv\; (1+f)\bar{m}_{\rm hc}\sqrt{\frac{T_{t\,4.5}}{T_{t\,2.5}}}\frac{p_{t\,2.5}}{p_{t\,4.5}} \;-\; \bar{m}_{\rm ltD} \;=\; 0 \tag{B.239}$$

Fan nozzle mass flow

The type of constraint imposed at the fan nozzle depends on whether or not the nozzle is choked. The fan nozzle trial static conditions and trial Mach number $\tilde{M}_7$ are first computed assuming a specified nozzle static pressure, equal to the freestream pressure.

$$\tilde{p}_7 \;=\; p_0 \tag{B.240}$$

$$\left\{\tilde{p}_7, \tilde{T}_7, \tilde{h}_7\right\} \;=\; \mathcal{F}_p\left(\vec{\alpha}, p_{t\,7}, T_{t\,7}, p_7/p_{t\,7}, 1\right) \tag{B.241}$$

$$\tilde{u}_7 \;=\; \sqrt{2(h_{t\,7}-\tilde{h}_7)} \tag{B.242}$$

$$\tilde{M}_7 \;=\; \tilde{u}_7/\sqrt{\frac{\tilde{c}_{p_7}\,R_7}{\tilde{c}_{p_7}-R_7}\,\tilde{T}_7} \tag{B.243}$$

If $\tilde{M}_7 \leq 1$, then the trial state is the actual state.

$$p_7 \;=\; \tilde{p}_7 \tag{B.244}$$

$$T_7 \;=\; \tilde{T}_7 \tag{B.245}$$

$$h_7 \;=\; \tilde{h}_7 \tag{B.246}$$

If $\tilde{M}_7 > 1$, then the trial state is incorrect, and a unity Mach number is imposed instead.

$$M_7 \;=\; 1 \tag{B.247}$$

$$\{p_7, T_7, h_7\} \;=\; \mathcal{F}_M\left(\vec{\alpha}, p_{t\,7}, T_{t\,7}, 0, M_7, 1\right) \tag{B.248}$$

For either case, the velocity, density, and mass flow constraint residual is formulated the same way.

$$u_7 = \sqrt{2(h_{t\,7} - h_7)} \tag{B.249}$$

$$\rho_7 = \frac{p_7}{R_7 T_7} \tag{B.250}$$

$$\mathcal{R}_4 \equiv \bar{m}_{\rm f} \sqrt{\frac{T_{\rm ref}}{T_{t\,2}}} \frac{p_{t\,2}}{p_{\rm ref}} - \rho_7 u_7 A_7 = 0 \tag{B.251}$$

Core nozzle mass flow

The type of constraint imposed at the core nozzle depends on whether or not the nozzle is choked. The core nozzle trial static conditions and trial Mach number $\tilde{M}_5$ are first computed assuming a specified nozzle static pressure, equal to the freestream pressure.

$$\tilde{p}_5 = p_0 \tag{B.252}$$

$$\left\{\tilde{p}_5, \tilde{T}_5, \tilde{h}_5\right\} = \mathcal{F}_p\left(\vec{\alpha}, p_{t\,5}, T_{t\,5}, p_5/p_{t\,5}, 1\right) \tag{B.253}$$

$$\tilde{u}_5 = \sqrt{2(h_{t\,5} - \tilde{h}_5)} \tag{B.254}$$

$$\tilde{M}_5 = \tilde{u}_5 / \sqrt{\frac{\tilde{c}_{p_5} R_5}{\tilde{c}_{p_5} - R_5} \tilde{T}_5} \tag{B.255}$$

If $\tilde{M}_5 \leq 1$, then the trial state is the actual state.

$$p_5 = \tilde{p}_5 \tag{B.256}$$

$$T_5 = \tilde{T}_5 \tag{B.257}$$

$$h_5 = \tilde{h}_5 \tag{B.258}$$

If $\tilde{M}_5 > 1$, then the trial state is incorrect, and a unity Mach number is imposed instead.

$$M_5 = 1 \tag{B.259}$$

$$\{p_5, T_5, h_5\} = \mathcal{F}_M\left(\vec{\alpha}, p_{t\,5}, T_{t\,5}, 0, M_5, 1\right) \tag{B.260}$$

For either case, the velocity, density, and mass flow constraint residual is formulated the same way.

$$u_5 = \sqrt{2(h_{t\,5} - h_5)} \tag{B.261}$$

$$\rho_5 = \frac{p_5}{R_5 T_5} \tag{B.262}$$

$$\mathcal{R}_5 \equiv (1+f)\bar{m}_{\rm hc} \sqrt{\frac{T_{\rm ref}}{T_{t\,2.5}}} \frac{p_{t\,2.5}}{p_{\rm ref}} - \rho_5 u_5 A_5 = 0 \tag{B.263}$$

LPC/HPC mass flow constraint

Equating the LPC and HPC mass flows defines the sixth constraining equation residual.

$$\mathcal{R}_6 \equiv \bar{m}_{\rm lc} \sqrt{\frac{T_{\rm ref}}{T_{t\,1.9}}} \frac{p_{t\,1.9}}{p_{\rm ref}} - \bar{m}_{\rm hc} \sqrt{\frac{T_{\rm ref}}{T_{t\,2.5}}} \frac{p_{t\,2.5}}{p_{\rm ref}} = 0 \tag{B.264}$$

An offset term could be included here to model any bleed upstream of the 2.5 station.

Burner exit temperature constraint

One of two possible constraints on $T_{t\,4}$ can be used.

$$\mathcal{R}_7 \;\equiv\; T_{t\,4} \;-\; (T_{t\,4})_{\rm spec} \;=\; 0 \qquad (T_{t\,4} \text{ specified}) \tag{B.265}$$

$$\mathcal{R}_7 \;\equiv\; F \;-\; F_{\rm spec} \;=\; 0 \qquad (\text{thrust specified}) \tag{B.266}$$

The thrust F is defined by relation (B.190), and is ultimately a function of the eight Newton variables.

Core exit total pressure constraint

The constraint on $p_{t\,5}$ is obtained from the LPT work relations (B.165) and (B.166), which have not been used yet for the off-design case.

$$\Delta h_{\rm lt} \;=\; \frac{-1}{1+f}\,\frac{\dot{m}_{\rm lc}}{\dot{m}_{\rm hc}}\Big[\,(h_{t\,2.5} - h_{t\,1.9}) \;+\; \alpha\;(h_{t\,2.1} - h_{t\,2})\Big] \tag{B.267}$$

$$p_{t\,4.9} \;=\; \mathcal{F}_h\left(\vec{\lambda}', p_{t\,4.5}, T_{t\,4.5}, \Delta h_{\rm lt}, {\eta_{\rm pol_t}}^{-1}\right) \tag{B.268}$$

$$\mathcal{R}_8 \;\equiv\; p_{t\,5} \;-\; p_{t\,4.9}\,\pi_{\rm tn} \;=\; 0 \tag{B.269}$$

The enthalpy drop $\Delta h_{\rm lt}$ is computed using (B.165).

B.6.2 Newton update

The eight residuals depend explicitly or implicitly on the eight unknowns. Newton changes are computed by forming and solving the 8×8 linear Newton system.

$$\left[\frac{\partial(\mathcal{R}_1,\mathcal{R}_2,\mathcal{R}_3,\mathcal{R}_4,\mathcal{R}_5,\mathcal{R}_6,\mathcal{R}_7,\mathcal{R}_8)}{\partial(\pi_{\rm f},\pi_{\rm lc},\pi_{\rm hc},\bar{m}_{\rm f},\bar{m}_{\rm lc},\bar{m}_{\rm hc},T_{t\,4},p_{t\,5})}\right]\left\{\begin{array}{c}\delta\pi_{\rm f}\\ \delta\pi_{\rm lc}\\ \delta\pi_{\rm hc}\\ \delta\bar{m}_{\rm f}\\ \delta\bar{m}_{\rm lc}\\ \delta\bar{m}_{\rm hc}\\ \delta T_{t\,4}\\ \delta p_{t\,5}\end{array}\right\} \;=\; -\left\{\begin{array}{c}\mathcal{R}_1\\ \mathcal{R}_2\\ \mathcal{R}_3\\ \mathcal{R}_4\\ \mathcal{R}_5\\ \mathcal{R}_6\\ \mathcal{R}_7\\ \mathcal{R}_8\end{array}\right\} \tag{B.270}$$

The Newton changes are then used to update the variables,

$$\pi_{\rm f} \;\leftarrow\; \pi_{\rm f} \;+\; \omega\,\delta\pi_{\rm f} \tag{B.271}$$

$$\pi_{\rm lc} \;\leftarrow\; \pi_{\rm lc} \;+\; \omega\,\delta\pi_{\rm lc} \tag{B.272}$$

$$\pi_{\rm hc} \;\leftarrow\; \pi_{\rm hc} \;+\; \omega\,\delta\pi_{\rm hc} \tag{B.273}$$

$$\bar{m}_{\rm f} \;\leftarrow\; \bar{m}_{\rm f} \;+\; \omega\,\delta\bar{m}_{\rm f} \tag{B.274}$$

$$\bar{m}_{\rm lc} \;\leftarrow\; \bar{m}_{\rm lc} \;+\; \omega\,\delta\bar{m}_{\rm lc} \tag{B.275}$$

$$\bar{m}_{\rm hc} \;\leftarrow\; \bar{m}_{\rm hc} \;+\; \omega\,\delta\bar{m}_{\rm hc} \tag{B.276}$$

$$T_{t\,4} \;\leftarrow\; T_{t\,4} \;+\; \omega\,\delta T_{t\,4} \tag{B.277}$$

$$p_{t\,5} \;\leftarrow\; p_{t\,5} \;+\; \omega\,\delta p_{t\,5} \tag{B.278}$$

where $\omega \leq 1$ is possible underrelaxation factor set so that the resulting new variables stay within physically-dictated limits, e.g. $\pi > 1$, $p_{t\,5} > p_0$, etc. This is usually required only for the first few iterations where the Newton changes are large. Once the solution is approached and the changes become small, $\omega = 1$ is used.

After the update, all calculations are repeated for the next Newton iteration. Typically, 4–10 iterations are required for convergence to machine zero.

B.7 Fan and Compressor Maps

To enforce the fan/compressor speed matching requirement, the fan and compressor speeds are determined from their pressure ratios and mass flows. Also, it is desirable to obtain realistic degraded efficiencies away from the design point. These are implemented here using approximate canonincal compressor pressure-ratio maps and efficiency maps.

B.7.1 Pressure ratio map

The corrected speed and mass flow is defined in the usual way,

$$\bar{N} = N \frac{1}{\sqrt{T_{ti}/T_{\rm ref}}} \tag{B.279}$$

$$\bar{m} = \dot{m} \frac{\sqrt{T_{ti}/T_{\rm ref}}}{p_{ti}/p_{\rm ref}} \tag{B.280}$$

where T_{ti}, p_{ti} are the face quantities, either $T_{t\,2}, p_{t\,2}$ for the fan and the LPC, or $T_{t\,2.5}, p_{t\,2.5}$ for the HPC.

The fan and compressor maps are in turn defined in terms of these corrected values normalized by their design values.

$$\tilde{p} = \frac{\pi - 1}{\pi_{\rm D} - 1} \tag{B.281}$$

$$\tilde{m} = \frac{\bar{m}}{\bar{m}_{\rm D}} \tag{B.282}$$

$$\tilde{N} = \frac{\bar{N}}{\bar{N}_{\rm D}} \tag{B.283}$$

The "spine" $\tilde{p}_s(\tilde{m}_s)$ on which the speed lines are threaded is parameterized by the corrected speed in the form

$$\tilde{m}_{s(\tilde{N})} = \tilde{N}^b \tag{B.284}$$

$$\tilde{p}_{s(\tilde{N})} = \tilde{m}_s^a = \tilde{N}^{ab} \tag{B.285}$$

where a controls the shape of the spine, and b controls the positioning of the speed lines along the spine.

The "knee" shape of each speed line is assumed to be a simple logarithmic function, translated to the $\tilde{m}_s, \tilde{p}_s$ position along the spine.

$$\tilde{p} - \tilde{p}_s \;=\; 2\tilde{N}\,k\;\ln\!\left(1 - \frac{\tilde{m} - \tilde{m}_s}{k}\right) \tag{B.286}$$

The constant k controls the sharpness of the logarithmic knee. Function (B.286) can be recast into an explicit form of a usual compressor map.

$$\pi\left(\bar{m}, \bar{N}\right) \;=\; 1 \;+\; (\pi_{\rm D} - 1)\left[\tilde{N}^{ab} \;+\; 2\tilde{N}\,k\;\ln\!\left(1 - \frac{\tilde{m} - \tilde{N}^{b}}{k}\right)\right] \tag{B.287}$$

Equation (B.287) is actually used here in inverse form, giving the fan or compressor corrected speed as a function of the pressure ratio and corrected mass flow.

$$\bar{N} \;=\; \mathcal{F}_N\left(\pi, \pi_{\rm D}, \bar{m}, \bar{m}_{\rm D}\right) \tag{B.288}$$

This is implemented by inverting the map (B.286) using the Newton method. To avoid problems with the extremely nonlinear logarithmic shape of each speed line curve, the Newton residual of (B.287) is formulated in one of two equivalent ways, depending on whether the specified $\tilde{m}, \tilde{p}$ point is above or below the spine curve (see Figure B.3).

$$\mathcal{R}_{(\tilde{N})} \;=\; \tilde{p}_{s(\tilde{N})} \;+\; 2\tilde{N}\,k\;\ln\!\left(1 - \frac{\tilde{m} - \tilde{m}_{s(\tilde{N})}}{k}\right) \;-\; \tilde{p} \qquad (\text{if } \tilde{p} \geq \tilde{m}^a) \tag{B.289}$$

$$\mathcal{R}_{(\tilde{N})} \;=\; \tilde{m}_{s(\tilde{N})} \;+\; k\left[1 \;-\; \exp\!\left(\frac{\tilde{p} - \tilde{p}_{s(\tilde{N})}}{2\tilde{N}k}\right)\right] \;-\; \tilde{m} \qquad (\text{if } \tilde{p} < \tilde{m}^a) \tag{B.290}$$

Residual (B.289), used above the spine curve, drives to the intersection of a speed line curve with a vertical constant-$\tilde{m}$ line. Residual (B.290), used below the spine curve, drives to the intersection of a speed line curve with a horizontal constant-$\tilde{p}$ line. In each case the intersection is nearly orthogonal, giving an extremely stable Newton iteration with rapid convergence in all cases.

B.7.2 Polytropic efficiency

The polytropic efficiency function is assumed to have the following form.

$$\eta_{\rm pol} \;=\; \mathcal{F}_\eta(\pi, \pi_{\rm D}, \bar{m}, \bar{m}_{\rm D}) \;=\; \eta_{{\rm pol}_o}\left(1 \;-\; C\left|\frac{\tilde{p}}{\tilde{m}^{a+\Delta a-1}} \;-\; \tilde{m}\right|^{c} \;-\; D\left|\frac{\tilde{m}}{\tilde{m}_o} \;-\; 1\right|^{d}\right) \tag{B.291}$$

The maximum efficiency is $\eta_{{\rm pol}_o}$, located at $\tilde{m}_o, \tilde{p}_o = \tilde{m}_o^{(a+\Delta a)}$ along the spine of the efficiency map. The exponent of the spine is $a+\Delta a$, which differs from the exponent of the pressure-map spine by the small amount Δa. Typically, Δa is slightly negative for single-stage fans, and slightly positive for multi-stage compressors. The c, d, C, D constants control the decrease of $\eta_{\rm pol}$ as $\tilde{m}, \tilde{p}$ move away from the $\tilde{m}_o, \tilde{p}_o$ point.

Table B.1: Pressure-ratio-map and efficiency-map constants for the E^3 fan.

π_D	a	b	k	η_{pol_o}	$\tilde{m}_o$	Δa	c	d	C	D
1.7	3.0	0.85	0.03	0.90	0.75	-0.5	3	6	2.5	15.0

B.7.3 Map calibration

The constants in Table B.1 give a realistic fan map, which is compared to the E^3 fan data. The resulting pressure-ratio contours are shown in Figure B.3, along with experimental data. The efficiency contours are shown in Figure B.4.

The constants in Table B.2 give a realistic high-pressure compressor map, which is compared to the E^3 compressor data. The resulting pressure-ratio contours are shown in Figure B.5,

Table B.2: Pressure-ratio-map and efficiency-map constants for the E^3 compressor.

π_D	a	b	k	η_{pol_o}	$\tilde{m}_o$	Δa	c	d	C	D
26.0	1.5	5	0.03	0.887	0.80	0.5	3	4	15.0	1.0

along with experimental data. The efficiency contours are shown in Figure B.6.

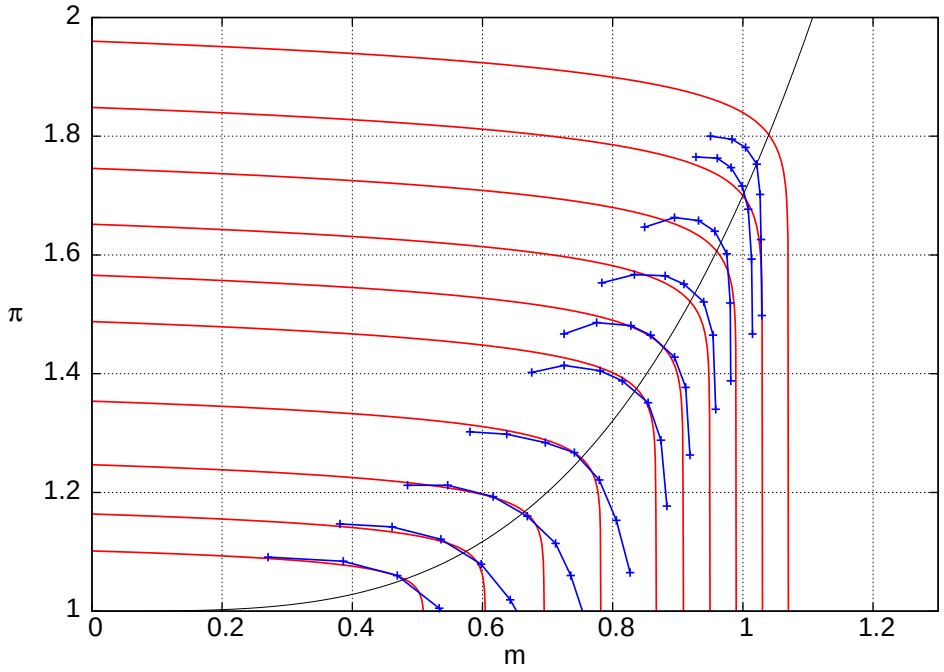

Figure B.3: Pressure ratio versus normalized corrected mass flow and corrected speed, for E^3 fan. Each red line is equation (B.287) with E^3 fan-model constants in Table B.1, and a specified experimental $\bar{N}$ value. Blue lines with symbols are measured data. Single black line is the "spine" curve $\tilde{p} = \tilde{m}^a$.

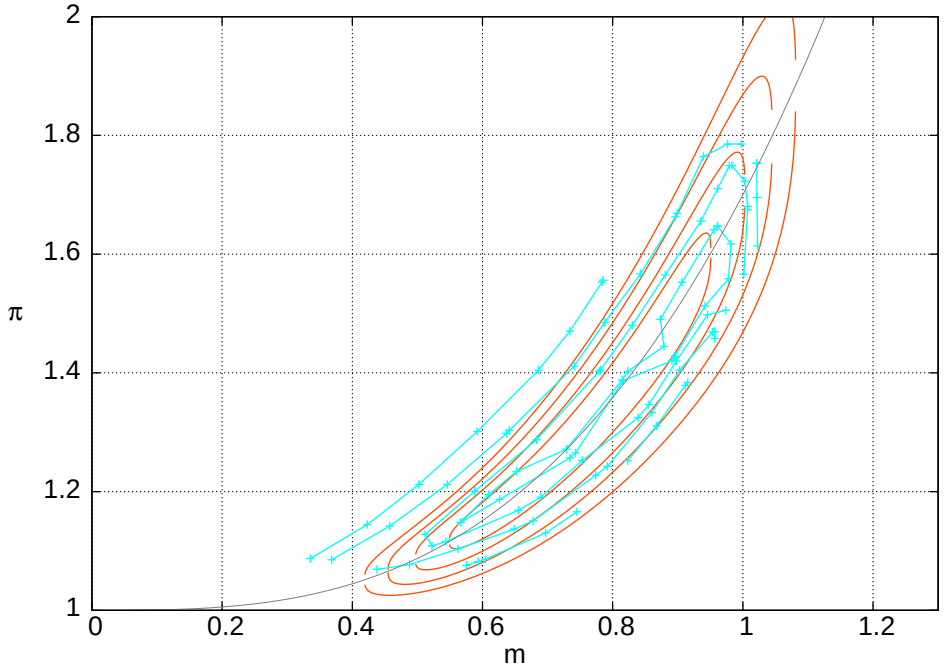

Figure B.4: Polytropic efficiency contours versus corrected mass flow and pressure ratio for E^3 fan. Red lines are isocontours of equation (B.291) with E^3 fan-model constants in Table B.1. Cyan lines with symbols are measured data. Single black line is the "spine" curve $\tilde{p} = \tilde{m}^{a+\Delta a}$.

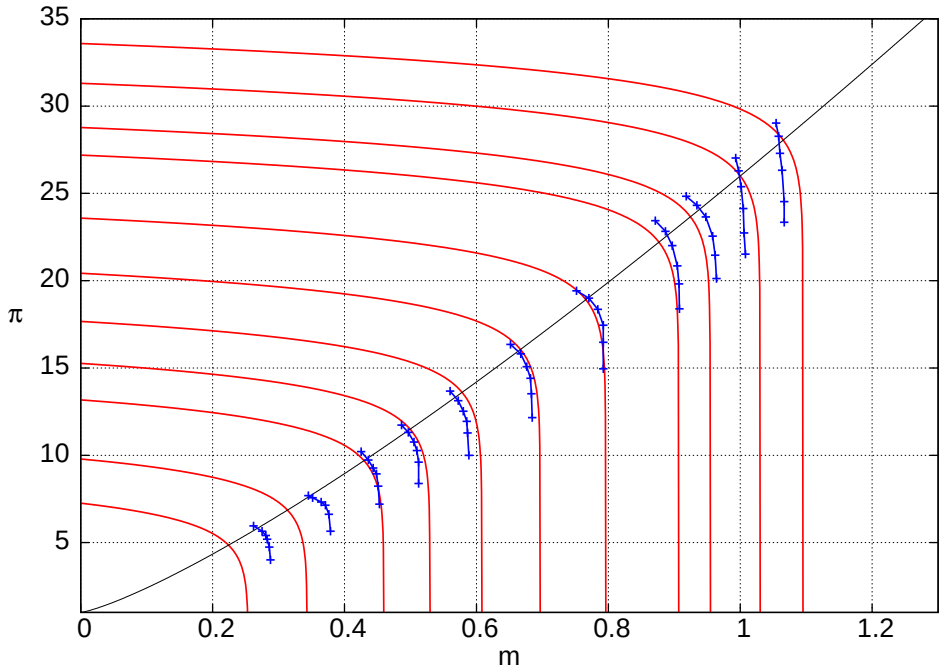

Figure B.5: Pressure ratio versus normalized corrected mass flow and corrected speed for E^3 compressor. Blue lines with symbols are measured data.

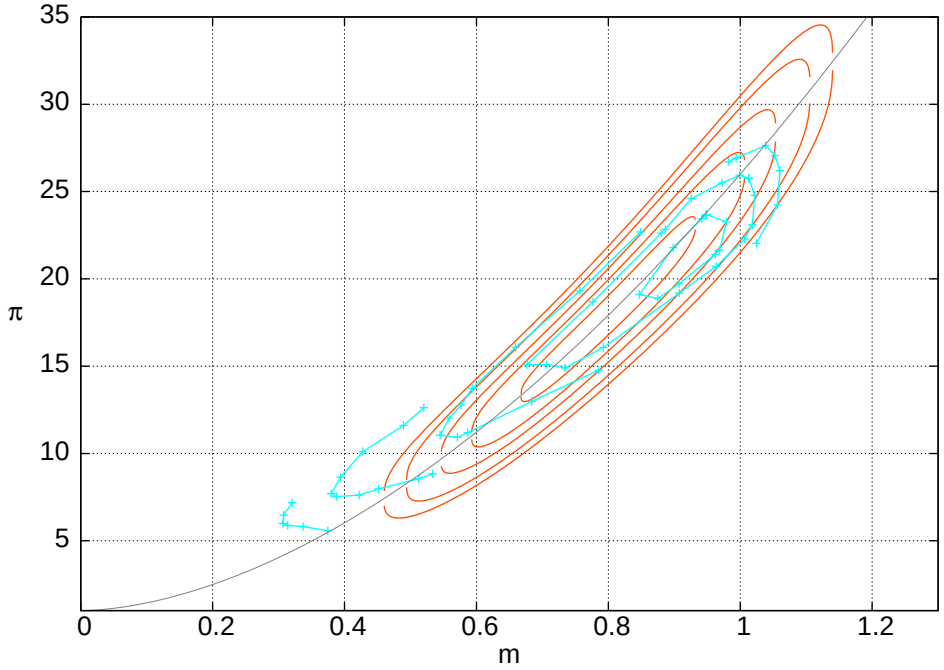

Figure B.6: Polytropic efficiency contours versus corrected mass flow and pressure ratio for E^3 compressor, for compressor-model constants in Table B.2. Cyan lines with symbols are measured data.

Appendix C

Film Cooling Flow Loss Model

C.1 Cooling mass flow calculation for one blade row

Figure C.1 shows the film-cooling model at the blade surface. The cooling gas flows into the blade at T_{ci}, and gets heated internally before issuing from the blade holes at T_{co}. The incoming hot gas at total temperature T_g is entrained into the film, and loses heat into the blade.

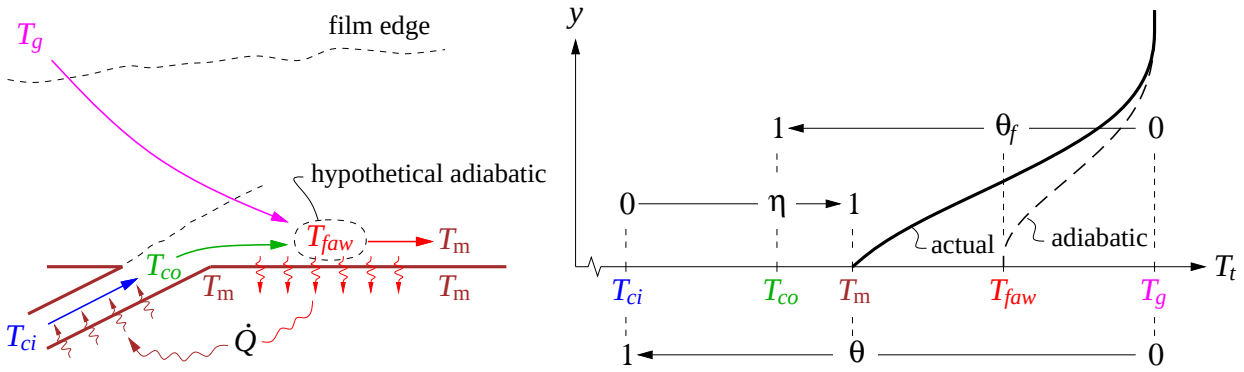

Figure C.1: Stream mixing, heat flow, and temperature profiles in film-cooling flow.

As analyzed by Horlock et al [19], the metal temperature $T_{\rm m}$ is characterized by the cooling effectiveness ratio θ,

$$\theta \;=\; \frac{T_r - T_{\rm m}}{T_g - T_{ci}} \;\simeq\; \frac{T_g - T_{\rm m}}{T_g - T_{ci}} \tag{C.1}$$

where T_r is the hot gas recovery temperature, $T_{\rm m}$ is the metal temperature, T_g is the hot gas inflow total temperature, and T_{ci} is the cooling-air inflow total temperature. The second approximate form in (C.1) makes the conservative assumption of full temperature recovery.

Since the cooling outlet holes cover only a fraction of the blade surface, the film fluid is a mixture of the cooling-fluid jets issuing at T_{co} and the entrained hot gas at T_g. In the

adiabatic (insulated wall) case, this temperature would be some T_{faw}, which is defined in terms of a film-effectiveness factor.

$$\theta_f \;=\; \frac{T_g - T_{faw}}{T_g - T_{co}} \;\simeq\; 0.4 \tag{C.2}$$

The limiting cases would be

i) $\theta_f = 0$ or $T_{faw} = T_g$ if the cooling-fluid holes are absent, and

ii) $\theta_f = 1$ or $T_{faw} = T_{co}$ if the cooling-fluid holes completely cover the blade.

The experiments of Sargison et al [20] show that the $\theta_f \simeq 0.4$ value is a reasonable surface average for a typical blade.

The cooling efficiency

$$\eta \;=\; \frac{T_{co} - T_{ci}}{T_{\rm m} - T_{ci}} \;=\; 1 \;-\; \exp\!\Big(-\frac{A_{cs}}{A_c}\,St_c\Big) \;\simeq\; 0.7 \tag{C.3}$$

indicates how much heat the cooling air has absorbed relative to the maximum possible amount before exiting the blade at temperature T_{co}. Horlock et al [19] indicate that for common internal heat transfer/flow area ratios A_{cs}/A_c and Stanton numbers St_c, the $\eta \simeq 0.7$ value is typical. This can be increased somewhat to reflect better cooling flowpath technology (e.g. improved pins, impingement, etc). However, increasing η closer to unity will also incur more total-pressure losses in the cooling flow, so $\eta < 1$ is clearly optimum from overall engine performance.

As indicated by Figure C.1, the outer-surface heat inflow from the film must be balanced by the internal heat outflow into the cooling flow. Equating these gives

$$\dot{Q} \;=\; A_{sg}\,St_g\,\rho_g V_g\,c_{p_g}(T_{faw} - T_{\rm m}) \;=\; \dot{m}_{c_1}\,c_{p_c}\,(T_{co} - T_{ci}) \tag{C.4}$$

$$A_{sg}\,St_g\,\frac{\dot{m}_g}{A_g}\,c_{p_g}(T_{faw} - T_{\rm m}) \;=\; \dot{m}_{c_1}\,c_{p_c}\,(T_{co} - T_{ci}) \tag{C.5}$$

where A_{sg} is the heat-transfer area of the hot gas, A_g is the flow area of the hot gas, and St_g is the external Stanton number. We now define the cooling/total mass flow ratio for one blade row,

$$\varepsilon \;=\; \frac{\dot{m}_{c_1}}{\dot{m}} \;=\; \frac{\dot{m}_{c_1}}{\dot{m}_g + \dot{m}_{c_1}} \tag{C.6}$$

so that equation (C.4) becomes

$$\frac{\dot{m}_{c_1}}{\dot{m}_g} \;=\; \frac{\varepsilon}{1-\varepsilon} \;=\; St_{_A}\,\frac{T_{faw} - T_{\rm m}}{T_{co} - T_{ci}} \tag{C.7}$$

$$\text{where} \qquad St_{_A} \;\equiv\; \frac{c_{p_g}}{c_{p_c}}\,\frac{A_{sg}}{A_g}\,St_g \;\simeq\; 0.035 \tag{C.8}$$

Horlock et al [19] argue that for typical blade solidities and aspect ratios, the assumed value for the weighted Stanton number $St_{_A} \simeq 0.035$ is reasonable. This will typically need to be increased by a substantial safety factor of 2 or more to allow for parameter uncertainties, hotspots, etc. Improved cooling design would be represented by a decreased safety factor.

Using θ, θ_f, and η to eliminate $T_{\rm m}$, T_{faw}, and T_{co} from (C.7) gives the following relation between all the dimensionless parameters.

$$\frac{\dot{m}_{c_1}}{\dot{m}_g} \;=\; \frac{\varepsilon}{1-\varepsilon} \;=\; St_{_A}\,\frac{\theta(1-\eta\,\theta_f)-\theta_f(1-\eta)}{\eta\,(1-\theta)} \tag{C.9}$$

Design case

The design problem is to determine the cooling flow required to achieve a specified $T_{\rm m}$ at the maximum design T_g (e.g. $T_g = T_{t\,4}$ at the takeoff case). Since T_{ci} is also known for any operating point (e.g. $T_{ci} = T_{t\,3}$), then θ is fully determined from its definition (C.1). Equation (C.9) can then be solved for the required design cooling flow ratio for the engine.

$$\varepsilon \;=\; \left[\,1 \,+\, \frac{1}{St_{_A}}\,\frac{\eta\,(1-\theta)}{\theta(1-\eta\,\theta_f)-\theta_f(1-\eta)}\right]^{-1} \tag{C.10}$$

Figure C.2 shows ε versus θ for three scaled Stanton numbers.

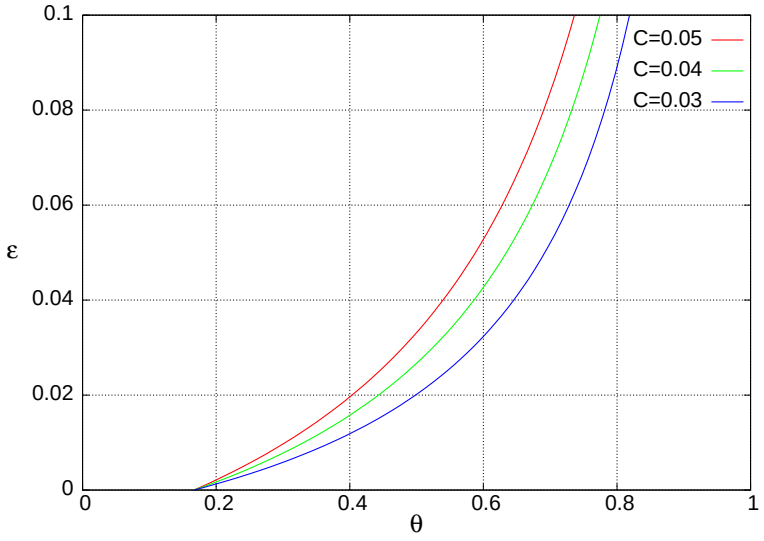

Figure C.2: Cooling mass flow ratio ε for one blade row, versus cooling effectiveness θ and Stanton number parameter C. Fixed parameters: $\eta = 0.7$, $\theta_f = 0.4$.

Off-design case

If the cooling mass flow is unregulated, it's reasonable to assume that ε will not change at off-design operation if the pressure ratios in the engine do not change appreciably. In that case, θ will not change either, and $T_{\rm m}$ can then be obtained from (C.1) for any specified T_g and T_{ci}. If the cooling flow ratio ε does change for whatever reason, it's then of interest to determine the resulting metal temperature. Hence, we now solve equation (C.9) for the new resulting θ in terms of a specified new ε.

$$\theta \;=\; \frac{\varepsilon\,\eta \,+\, St_{_A}\,\theta_f(1-\eta)(1-\varepsilon)}{\varepsilon\,\eta \,+\, St_{_A}\,(1-\eta\,\theta_f)(1-\varepsilon)} \tag{C.11}$$

C.2 Total Cooling Flow Calculation

The turbine cooling-flow bypass ratio is defined as follows.

$$\alpha_c \;=\; \frac{\dot{m}_{\rm cool}}{\dot{m}} \tag{C.12}$$

This represents the total cooling mass flow of all the blade rows which receive cooling flow. The calculations will assume the following quantities are specified, or known from other (e.g. compressor, combustor) calculations:

$h_{\rm fuel}$	fuel heating value
$T_{t\,\rm f}$	fuel total temperature
$T_{t\,3}$	compressor exit total temperature
$p_{t\,3}$	compressor exit total pressure
$T_{t\,4}$	turbine inlet total temperature
$p_{t\,4}$	turbine inlet total pressure ($= p_{t\,3}\pi_{\rm b}$)
$T_{\rm m}$	metal temperature (for design case)
α_c	total cooling-flow bypass ratio (for off-design case)
$St_{_A}$	area-weighted external Stanton number
$M_{\rm exit}$	turbine blade-row exit Mach number
M_{4a}	representative Mach number at start of mixing zone
r_{u_c}	cooling-flow velocity ratio ($= u_c/u_{4a}$)

To estimate the blade-relative hot-gas total temperature T_g incoming into each blade row, it is assumed that the inlet Mach number for that blade row is neglible. Hence, the inlet total temperature for a blade row is the same as the static exit temperature of the upstream blade row.

$$T_g \;\simeq\; (T_{\rm exit})_{\rm upstream} \tag{C.13}$$

Specifying the burner exit temperature $T_{t\,4}$ and a typical blade-relative exit Mach number $M_{\rm exit}$ is then sufficient to determine the blade-relative hot-gas temperatures $T_{g1}, T_{g2}, T_{g3}\ldots$ for all downstream blade rows.

$$T_{g1} \;=\; T_{t\,4} \,+\, \Delta T_{\rm streak} \tag{C.14}$$

$$T_{g2} \;=\; T_{t\,4}\left(1+\frac{\gamma_t-1}{2}M_{\rm exit}^2\right)^{-1} \tag{C.15}$$

$$T_{g3} \;=\; T_{t\,4}\left(1+\frac{\gamma_t-1}{2}M_{\rm exit}^2\right)^{-2} \tag{C.16}$$

$$\vdots$$

The added $\Delta T_{\rm streak}$ for T_{g1} is a hot-streak temperature allowance for the first IGV row. According to Koff [21], assuming $\Delta T_{\rm streak} \simeq 200°$K is realistic.

With the row T_g's defined, relation (C.1) gives the required cooling effectiveness ratio for each blade row,

$$\theta_1 \;=\; \frac{T_{g1}-T_{\rm m}}{T_{g1}-T_{ci}} \tag{C.17}$$

$$\theta_2 = \frac{T_{g2} - T_{\rm m}}{T_{g2} - T_{ci}} \tag{C.18}$$

$$\vdots$$

and relation (C.11) gives the corresponding cooling mass flow $\varepsilon_1, \varepsilon_2, \varepsilon_3 \ldots$ for each blade row. These are computed until $\varepsilon_{(\,)} < 0$ is reached, indicating that cooling is no longer required. The total cooling mass flow ratio is then the sum of the individual blade-row mass flow ratios.

$$\alpha_c = \varepsilon_1 + \varepsilon_2 + \varepsilon_3 \ldots \tag{C.19}$$

C.3 Mixed-out Flow and Loss Calculation

C.3.1 Loss Model Assumptions

The introduction of cooling air into the flowpath reduces the total pressure seen by the turbine. Strictly speaking, it is necessary to perform separate cooling-flow, mixing-loss, and rotor-work calculations separately for each cooled stator and rotor blade row.

To avoid this complication, a much simpler model will be used: The cooling air for all blade rows is assumed to be discharged entirely over the first IGV, and to fully mix out before flow enters the first turbine rotor. This seems to be a reasonable simplification given that the first IGV blade row typically requires the bulk of the cooling flow. The main motivation is that this model does not require work calculations to be performed for individual turbine stages, greatly simplifying the matching of overall compressor+fan and turbine work.

C.3.2 Loss Calculation

Figure C.3 shows the core and cooling mass flow paths assumed for the mixed-out state calculation. The cooling air is assumed to be bled off at the compressor exit, which defines the cooling-flow total temperature.

$$T_{ci} = T_{t3} \tag{C.20}$$

The cooling air is assumed to re-enter the flowpath over the first IGV.

The heat flow $\dot{Q}$ from the core flow to the metal and then to the cooling flow does not need to be considered here, since this heat flow is purely internal to the control volume spanning stations 4 and 4.1, for example.

The cooling flow is assumed to remain unmixed until some representative station 4a (e.g. somewhere between stagnation and IGV exit Mach), where it has velocity $u_c = r_{u_c} u_{4a}$, and the local static pressure p_{4a}. The mixing then occurs between 4a and 4.1, producing a total-pressure drop and ultimately resulting in a reduced core-flow exhaust velocity at station 6.

For clarity and convenience, the equations shown assume a constant c_p. In practice, the calculations would be performed using their equivalent variable-c_p forms.

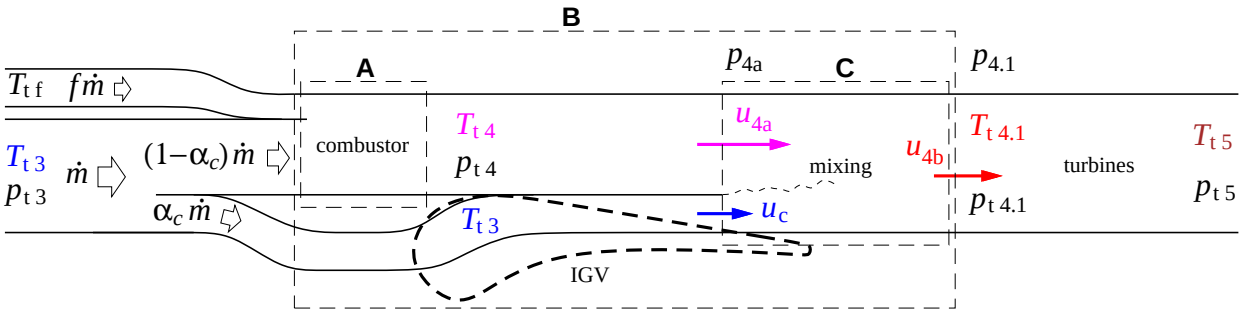

Figure C.3: Combustor and film-cooling flows, with mixing over and downstream of IGV. Dashed rectangles are control volumes.

Using control volume A, the heat-balance equation for the fuel/core mass flow ratio $f = \dot{m}_{\rm fuel}/\dot{m}$ is as follows.

$$h_{\rm fuel}\, f\dot{m} \;=\; \bar{c}_p\,(T_{t\,4} - T_{t\,3})\,(1-\alpha_c)\dot{m} \;+\; \bar{c}_p\,(T_{t\,4} - T_{t\,f})\,f\dot{m} \tag{C.21}$$

$$f \;=\; \frac{\bar{c}_p\,(T_{t\,4} - T_{t\,3})\,(1-\alpha_c)}{h_{\rm fuel} \;-\; \bar{c}_p\,(T_{t\,4} - T_{t\,f})} \tag{C.22}$$

Using control volume B, the heat-balance equation for the mixed-out total temperature $T_{t\,4.1}$ is as follows.

$$h_{\rm fuel}\, f\dot{m} \;=\; \bar{c}_p\,(T_{t\,4.1} - T_{t\,3})\,\dot{m} \;+\; \bar{c}_p\,(T_{t\,4.1} - T_{t\,f})\,f\dot{m} \tag{C.23}$$

$$T_{t\,4.1} \;=\; \frac{h_{\rm fuel}\, f/\bar{c}_p + T_{t\,3} + T_{t\,f} f}{1+f} \tag{C.24}$$

The core and cooling flow velocities u_{4a}, u_c are obtained from the specified M_{4a} and the velocity ratio r_{u_c}.

$$u_{4a} \;=\; \frac{M_{4a}}{\sqrt{1 + \frac{\gamma-1}{2} M_{4a}^2}}\,\sqrt{\gamma R T_{t\,4}} \tag{C.25}$$

$$u_c \;=\; r_{u_c} u_{4a} \tag{C.26}$$

Neglecting the mixing pressure rise over control volume C, a momentum balance gives the mixed-out velocity $u_{4.1}$.

$$p_{4.1} \;\simeq\; p_{4a} \;=\; p_{t\,4}\left(1 + \frac{\gamma-1}{2} M_{4a}^2\right)^{-\gamma/(\gamma-1)} \tag{C.27}$$

$$(1+f)\,\dot{m}\,u_{4.1} \;=\; (1-\alpha_c+f)\,\dot{m}\,u_{4a} \;+\; \alpha_c\,\dot{m}\,u_c \tag{C.28}$$

$$u_{4.1} \;=\; u_{4a}\,\frac{(1-\alpha_c+f)u_{4a} \;+\; \alpha_c\,u_c}{1+f} \tag{C.29}$$

The mixed-out static temperature and total pressure then follow.

$$T_{4.1} \;=\; T_{t\,4.1} \;-\; \frac{1}{2}\frac{u_{4.1}^2}{c_p} \tag{C.30}$$

$$p_{t\,4.1} \;=\; p_{4.1}\left(\frac{T_{t\,4.1}}{T_{4.1}}\right)^{\gamma/(\gamma-1)} \tag{C.31}$$

These can now be used as effective turbine inlet conditions for turbine-work and pressure-drop calculations.

Appendix D

Thermally-Perfect Gas Calculations

D.1 Governing equations

Starting equations, with some assumed known $c_{p(T)}$:

$$dh - v\,dp = T\,ds \tag{D.1}$$
$$pv = RT \tag{D.2}$$
$$dh = c_{p(T)}\,dT \tag{D.3}$$

D.2 Complete enthalpy calculation

The complete enthalpy function is obtained by integration of the known $c_{p(T)}$ function,

$$h_{(T)} \equiv \Delta h_f + \int_{T_s}^{T} c_{p(T)}\,dT \tag{D.4}$$

where Δh_f is the heat of formation, and T_s is the standard condition at which Δh_f is defined, typically $T_s = 298\,\mathrm{K}$.

D.3 Pressure calculation

For an adiabatic compressor or turbine, the entropy change is specified via a polytropic efficiency

$$T\,ds = \left(1 - {\eta_{\mathrm{pol}}}^{\pm 1}\right) c_p\,dT \tag{D.5}$$

with ${\eta_{\mathrm{pol}}}^{+1}$ used when $dT > 0$ as in a compressor, and ${\eta_{\mathrm{pol}}}^{-1}$ used when $dT < 0$ as in a turbine, so that ds is always positive. All the above relations above are combined into the definition of an entropy-complement variable $\sigma_{(T)}$, which then defines $p_{(T)}$.

$$\frac{dp}{p} = {\eta_{\mathrm{pol}}}^{\pm 1} \frac{c_p}{R} \frac{dT}{T} = {\eta_{\mathrm{pol}}}^{\pm 1} \frac{d\sigma}{R} \tag{D.6}$$

$$\sigma_{(T)} \equiv \int_{T_s}^{T} c_{p(T)} \frac{dT}{T} = \int_{\ln T_s}^{\ln T} c_{p(\ln T)}\, d(\ln T) \tag{D.7}$$

$$p_{(T)} = p_0 \exp\left(\eta_{\rm pol}{}^{\pm 1} \frac{\sigma_{(T)} - \sigma_{(T_0)}}{R}\right) \tag{D.8}$$

The compression or expansion process is assumed to occur over $p_0 \ldots p$ and $T_0 \ldots T$.

D.4 Properties of a gas mixture

A gas mixture is specified with the mass fraction vector $\vec{\alpha}$, whose components are the mass fractions of the mixture constituents. Similarly, the components of $\vec{R}$, $\vec{c}_p$, $\vec{h}$, $\vec{\sigma}$ are gas properties of the constituents. The overall properties are then

$$R = \vec{\alpha} \cdot \vec{R} \tag{D.9}$$

$$c_{p(T)} = \vec{\alpha} \cdot \vec{c}_{p(T)} \tag{D.10}$$

$$h_{(T)} = \vec{\alpha} \cdot \vec{h}_{(T)} \tag{D.11}$$

$$\sigma_{(T)} = \vec{\alpha} \cdot \vec{\sigma}_{(T)} \tag{D.12}$$

D.5 Calculations for turbomachine components

The $()_t$ total-quantity subscript will be omitted here for convenience.

D.5.1 Compressor

In a compressor, the total-pressure ratio

$$\pi_{\rm c} = \frac{p_3}{p_2}$$

is typically specified. The inlet conditions p_2 and T_2 are also assumed known. The objective here is to determine the corresponding exit total temperature T_3.

We first recast the specified pressure ratio definition in residual form.

$$\ln \pi_{\rm c} = \ln \frac{p_3}{p_2} = \frac{\eta_{\rm pol}}{R} (\sigma_3 - \sigma_2) \tag{D.13}$$

$$\mathcal{R}_{(T_3)} \equiv \frac{\sigma_{(T_3)}}{R} - \frac{\sigma_2}{R} - \frac{\ln \pi_{\rm c}}{\eta_{\rm pol}} = 0 \tag{D.14}$$

$$\mathcal{R}'_{(T_3)} \equiv \frac{d\mathcal{R}}{dT}_{(T_3)} = \frac{c_{p(T_3)}}{RT_3} \tag{D.15}$$

This is then solved for the unknown T_3 by the standard Newton method, with the sequence of progressively better iterates $T_3^1, T_3^2 \ldots T_3^n$. A good initial guess T_3^0 is obtained by assuming

a fixed isentropic exponent $(\gamma-1)/\gamma = R/c_p$ taken from the known $()_2$ condition.

$$c_{p_2} = c_{p(T_2)} \tag{D.16}$$

$$T_3^0 = T_2\ \pi_c^{R/(c_{p_2}\eta_{\rm pol})} \tag{D.17}$$

$$T_3^{n+1} = T_3^n - \frac{\mathcal{R}_{(T_3^n)}}{\mathcal{R}'_{(T_3^n)}} \tag{D.18}$$

After convergence, the exit h_3 is evaluated directly.

$$h_3 = h_{(T_3)} \tag{D.19}$$

D.5.2 Combustor

In a combustor, both the inlet and outlet temperatures T_3, T_4 are typically specified. The objective is to determine the fuel mass fraction.

It will be assumed that the fuel has the chemical form

$$C_{x_C}\, H_{x_H}\, O_{x_O}\, N_{x_N}$$

and the combustion reaction is limited to the fuel and atmospheric oxygen, and is complete (i.e. nitrogen oxide and carbon monoxide production is neglected).

$$\mathrm{C}_{x_C}\,\mathrm{H}_{x_H}\,\mathrm{O}_{x_O}\,\mathrm{N}_{x_N} + n_{O_2}\,\mathrm{O}_2 \rightarrow n_{CO_2}\,\mathrm{CO}_2 + n_{H_2O}\,\mathrm{H_2O} + n_{N_2}\,\mathrm{N}_2 \tag{D.20}$$

Equating the atom numbers gives the reaction mole numbers.

$$n_{O_2} = x_C + x_H/4 - x_O/2 \tag{D.21}$$

$$n_{CO_2} = x_C \tag{D.22}$$

$$n_{H_2O} = x_H/2 \tag{D.23}$$

$$n_{N_2} = x_N/2 \tag{D.24}$$

Using mole numbers together with the atomic masses

$$\begin{aligned} m_C &= 12.01 \\ m_H &= 1.01 \\ m_O &= 16.00 \\ m_N &= 14.01 \end{aligned}$$

gives the reactant masses.

$$M_{O_2} = n_{O_2}\,(2m_O) \tag{D.25}$$

$$M_{CO_2} = n_{CO_2}\,(m_C + 2m_O) \tag{D.26}$$

$$M_{H_2O} = n_{H_2O}\,(2m_H + m_O) \tag{D.27}$$

$$M_{N_2} = n_{N_2}\,(2m_N) \tag{D.28}$$

$$M_{\rm fuel} = x_C\, m_C + x_H\, m_H + x_O\, m_O + x_N\, m_N \tag{D.29}$$

The following mass fraction vector components are then calculated.

	i	α_i	β_i	γ_i
N_2	1	0.781	0	M_{N_2}/M_{fuel}
O_2	2	0.209	0	$-M_{O_2}/M_{\text{fuel}}$
CO_2	3	0.0004	0	M_{CO_2}/M_{fuel}
H_2O	4	0	0	M_{H_2O}/M_{fuel}
Ar	5	0.0096	0	0
fuel	6	0	1	0

Here, β_i gives the composition of the fuel, while γ_i gives the air constituent fractional changes over the reaction. The fraction vector component sums are all exactly $\sum \alpha_i = 1$, $\sum \beta_i = 1$, $\sum \gamma_i = 1$.

The total enthalpies of all the constituents are known from the specified T_3 and T_4, and also at the known fuel temperature T_{f}.

$$\vec{h}_3 = h_{i(T_3)} \tag{D.30}$$
$$\vec{h}_4 = h_{i(T_4)} \tag{D.31}$$
$$\vec{h}_{\text{f}} = h_{i(T_{\text{f}})} \tag{D.32}$$

The enthalpy balance across the combustor is

$$\dot{m}_{\text{air}}\,\vec{\alpha}\cdot\vec{h}_3 \;+\; \dot{m}_{\text{fuel}}\,\vec{\beta}\cdot\vec{h}_{\text{f}} \;=\; \dot{m}_{\text{air}}\,\vec{\alpha}\cdot\vec{h}_4 \;+\; \dot{m}_{\text{fuel}}\,\vec{\gamma}\cdot\vec{h}_4 \tag{D.33}$$

so that the fuel mass fraction is obtained directly.

$$f \;\equiv\; \frac{\dot{m}_{\text{fuel}}}{\dot{m}_{\text{air}}} \;=\; \frac{\vec{\alpha}\cdot\vec{h}_4 \;-\; \vec{\alpha}\cdot\vec{h}_3}{\vec{\beta}\cdot\vec{h}_{\text{f}} \;-\; \vec{\gamma}\cdot\vec{h}_4} \tag{D.34}$$

The mass fraction vector $\vec{\lambda}$ of the combustion products is obtained from the mass balance across the combustor,

$$(\dot{m}_{\text{air}} + \dot{m}_{\text{fuel}})\,\vec{\lambda} \;=\; \dot{m}_{\text{air}}\,\vec{\alpha} \;+\; \dot{m}_{\text{fuel}}\,\vec{\gamma} \tag{D.35}$$
$$\vec{\lambda} \;=\; \frac{\vec{\alpha} + f\vec{\gamma}}{1+f} \tag{D.36}$$

which can then be used to obtain the net properties of the combustion products.

$$R_4 = \vec{\lambda}\cdot\vec{R}_4 \tag{D.37}$$
$$c_{p_4} = \vec{\lambda}\cdot\vec{c}_{p_4} \tag{D.38}$$

D.5.3 Mixer

Mixing will typically occur between the combustor discharge flow and the turbine cooling flow. In general, the two streams will have two different chemical compositions specified by their mass fraction vectors $\vec{\lambda}_a$ and $\vec{\lambda}_b$, two different temperatures T_a and T_b, and two different

enthalpies $\vec{h}_a = h_{i(T_a)}$ and $\vec{h}_b = h_{i(T_b)}$. The species mass flow balance gives the composition mass fraction vector $\vec{\lambda}$ of the mixed gas.

$$(\dot{m}_a + \dot{m}_b)\,\vec{\lambda} \;=\; \dot{m}_a\,\vec{\lambda}_a \;+\; \dot{m}_b\,\vec{\lambda}_b \tag{D.39}$$

$$\vec{\lambda} \;=\; \frac{\dot{m}_a\,\vec{\lambda}_a \;+\; \dot{m}_b\,\vec{\lambda}_b}{\dot{m}_a + \dot{m}_b} \tag{D.40}$$

Assuming no chemical reaction takes place, the enthalpy balance equation is

$$(\dot{m}_a + \dot{m}_b)\,\vec{\lambda}\cdot\vec{h}_{(T)} \;=\; \dot{m}_a\,\vec{\lambda}_a\cdot\vec{h}_a \;+\; \dot{m}_b\,\vec{\lambda}_b\cdot\vec{h}_b \tag{D.41}$$

which can be numerically inverted for the mixed temperature T.

D.5.4 Turbine

In a turbine, the total-enthalpy difference is typically known from the compressor–turbine work balance.

$$(\dot{m}_{\text{air}} + \dot{m}_{\text{fuel}})(h_5 - h_4) \;=\; \dot{m}_{\text{air}}(h_2 - h_3) \tag{D.42}$$

$$\Delta h \;\equiv\; h_5 - h_4 \;=\; \frac{h_2 - h_3}{1+f} \tag{D.43}$$

The objective here is to determine the corresponding total-pressure ratio.

$$\pi_{\text{t}} \;=\; \frac{p_5}{p_4} \tag{D.44}$$

The procedure is similar to that for the compressor, except that $h_{(T)}$ is used in the Newton residual.

$$\mathcal{R}_{(T_5)} \;\equiv\; h_{(T_5)} \;-\; h_4 \;-\; \Delta h \;=\; 0 \tag{D.45}$$

$$\mathcal{R}'_{(T_5)} \;\equiv\; \frac{d\mathcal{R}}{dT}_{(T_5)} \;=\; c_{p(T_5)} \tag{D.46}$$

The Newton method is started by assuming a fixed c_p taken from the known $()_4$ condition.

$$c_{p_4} \;=\; c_{p(T_4)} \tag{D.47}$$

$$T_5^0 \;=\; T_4 \;+\; \Delta h / c_{p_4} \tag{D.48}$$

$$T_5^{n+1} \;=\; T_5^n \;-\; \frac{\mathcal{R}_{(T_5^n)}}{\mathcal{R}'_{(T_5^n)}} \tag{D.49}$$

After convergence, the total-pressure ratio and p_5 are evaluated directly.

$$\pi_{\text{t}} \;=\; \exp\left(\frac{1}{\eta_{\text{pol}}}\,\frac{\sigma_{(T_5)} - \sigma_{(T_4)}}{R}\right) \tag{D.50}$$

$$p_5 \;=\; p_4\,\pi_{\text{t}} \tag{D.51}$$

D.5.5 Inlet or Nozzle

An inlet or nozzle with losses can be considered as a turbine with zero efficiency, and is typically specified via a total-pressure drop ratio.

$$\pi_i = \frac{p_2}{p_0} \tag{D.52}$$

In the limit $\eta_{\rm pol} \rightarrow 0$, the turbine case above then reduces to the trivial relations

$$p_2 = p_0 \, \pi_i \tag{D.53}$$
$$T_2 = T_0 \tag{D.54}$$
$$h_2 = h_{(T_2)} = h_0 \tag{D.55}$$

with no need for Newton iteration.

Appendix: Spline representations

General

A cubic spline representation of a function $y_{(x)}$ requires the following discrete values at $i = 1, 2 \ldots N$ nodes:

x_i	spline parameter values
y_i	function values
y'_i	function derivative values, $(dy/dx)_i$

On each interval $i-1 \ldots i$, the four end values $y_{i-1}, y_i, y'_{i-1}, y'_i$ uniquely define a cubic-polynomial $y_{(x)}$ over that interval. The union of all intervals then defines the overall $y_{(x)}$ function.

The derivative values y'_i are obtained from x_i, y_i by solving a linear system of equations expressing 2nd-derivative continuity across all the interior nodes $i = 2, 3 \ldots N-1$, together with two zero 3rd-derivative end conditions at $i = 1, N$. This system of equations produces a tridiagonal matrix which is very rapidly solved in $\mathcal{O}(N)$ arithmetic operations.

Current application

Two splines are first generated using the tabulated values T_i, c_{p_i}:

1) $c_{p(T)}$ spline:

$$\begin{array}{rcll} x_i & = & T_i & \text{(table values)} \\ y_i & = & c_{p_i} & \text{(table values)} \\ y'_i & = & (dc_p/dT)_i & \text{(via spline system solution)} \end{array}$$

2) $c_{p(\ln T)}$ spline:

$$\begin{array}{rcll} x_i & = & \ln(T_i) & \text{(table values)} \\ y_i & = & c_{p_i} & \text{(table values)} \\ y'_i & = & (dc_p/d\ln T)_i & \text{(via spline system solution)} \end{array}$$

Then two related splines $h_{(T)}$, $\sigma_{(\ln T)}$ are constructed as follows, with Δh_f being the heat of formation.

3) $h_{(T)}$ spline:

$$\begin{aligned} x_i &= T_i \\ y'_i &= c_{p_i} \\ y_i &= \Delta h_f + \int_{T_s}^{T_i} c_{p(T)}\, dT \end{aligned}$$

4) $\sigma_{(\ln T)}$ spline:

$$\begin{aligned} x_i &= \ln(T_i) \\ y'_i &= c_{p_i} \\ y_i &= \int_{\ln T_s}^{\ln T_i} c_{p(\ln T)}\, d(\ln T) \end{aligned}$$

Since the splined $c_{p(T)}$ and $c_{p(\ln T)}$ are piecewise-cubic, exact integrations can be used here to give perfect consistency between the related splines.

Appendix E

Simplified Viscous/Inviscid Analysis for Nearly-Axisymmetric Bodies

E.1 Summary

The method described here uses a compressible extension of the old Von Karman airship method [22] to describe the potential flow, and an axisymmetric version of the integral boundary layer formulation of XFOIL [23] to describe the surface boundary layer and trailing wake. The two formulations are strongly coupled and solved simultaneously using the XFOIL methodology. Effects such as flow separation can thus be captured. The intent of this strongly-coupled viscous/inviscid method is to obtain reasonable drag prediction accuracy together with extreme computational speed.

E.2 Geometry

The body geometry is described by the area $A_{(x)}$ and perimeter $b_{0(x)}$ distributions, as shown in Figure E.1, with x being the axial coordinate. For a body of circular cross-section these are related by

$$4\pi A \;=\; b_0^2 \qquad\qquad \text{(round body)} \tag{E.1}$$

but considering them to be independent allows reasonably accurate drag calculation of bodies which are slender but not axisymmetric.

E.3 Potential Flow Calculation

To compute the potential flow, an equivalent axisymmetric body of radius $R_{(x)}$ is first defined.

$$R_{(x)} \;=\; \sqrt{\frac{A_{(x)}}{\pi}} \tag{E.2}$$

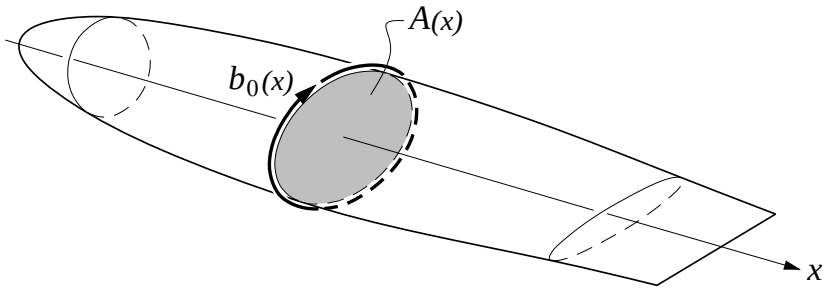

Figure E.1: Slender body with cross-sectional area $A_{(x)}$ and perimeter $b_{0(x)}$.

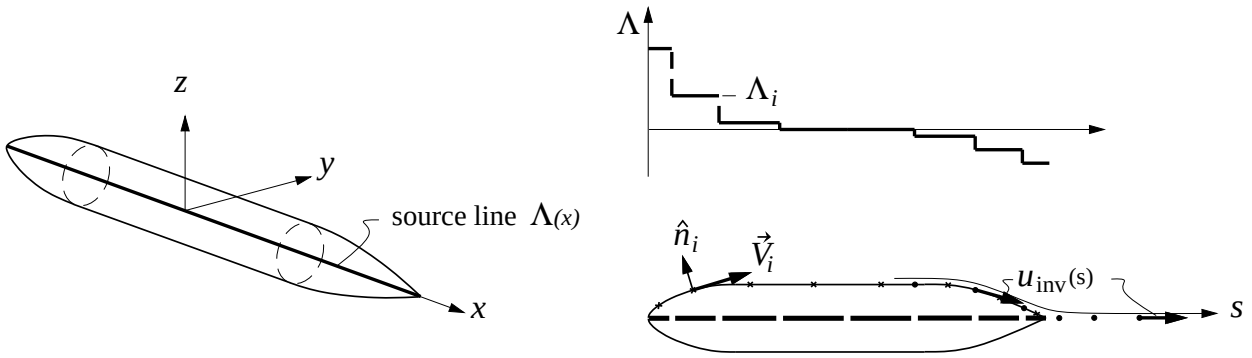

Figure E.2: Fuselage potential flow model using compressible source line on axis.

The compressible potential flow about this body is represented with piecewise-constant line sources placed on the axis, as sketched in Figure E.2.

The cartesian perturbation velocities of $i = 1, 2 \ldots n$ such segments located between points $x_1, x_2, \ldots x_{n+1}$ are

$$u(x,y,z) = \sum_{i=1}^{n} \frac{\Lambda_i}{4\pi\,\beta^2} \left(\frac{1}{r_{i+1}} - \frac{1}{r_i} \right) \tag{E.3}$$

$$v(x,y,z) = \sum_{i=1}^{n} \frac{\Lambda_i}{4\pi\,\beta} \left(\frac{x_{i+1}-x}{r_{i+1}} - \frac{x_i-x}{r_i} \right) \frac{\beta y}{(\beta y)^2 + (\beta z)^2} \tag{E.4}$$

$$w(x,y,z) = \sum_{i=1}^{n} \frac{\Lambda_i}{4\pi\,\beta} \left(\frac{x_{i+1}-x}{r_{i+1}} - \frac{x_i-x}{r_i} \right) \frac{\beta z}{(\beta y)^2 + (\beta z)^2} \tag{E.5}$$

where $$\beta^2 \equiv 1 - M_\infty^2 \tag{E.6}$$

$$r_i(x,y,z) \equiv \sqrt{(x-x_i)^2 + (\beta y)^2 + (\beta z)^2} \tag{E.7}$$

$$r_{i+1}(x,y,z) \equiv \sqrt{(x-x_{i+1})^2 + (\beta y)^2 + (\beta z)^2} \tag{E.8}$$

Setting flow tangency at each of the n control points on the actual body surface with normal vectors $\hat{n}_i$

$$\left[(V_\infty + u)\,\hat{\imath} + v\,\hat{\jmath} + w\,\hat{k} \right]_i \cdot \hat{n}_i = 0 \tag{E.9}$$

gives a $n \times n$ linear system for the source strengths Λ_i. Because the control points are not immediately adjacent to the source elements, this system becomes increasingly ill-conditioned

as n is increased, especially with non-slender bodies. However, with the cosine spacing sketched in Figure E.2, essentially converged results are obtained for $n = 25$ or less, with very great computational economy.

A proper axisymmetric panel method is of course an alternative to the present approach, but would greatly increase the code complexity, and also the system setup time which would dominate the system solution time for these small number of unknowns. These additional drawbacks favor the simple present approach.

E.4 Viscous Flow Calculation

E.4.1 Axisymmetric boundary layer and wake equations

All viscous calculations are performed in the meridional arc length coordinate s, defined from the equivalent $R_{(x)}$ distribution.

$$s_{(x)} \;=\; \int^{x} \sqrt{1 + (dR/dx)^2}\; dx \tag{E.10}$$

This is continued into the wake where $R{=}0$ is specified.

The axisymmetric momentum and kinetic energy boundary layer equations governing the viscous boundary layers and wake are as follows.

$$\frac{d\left(\rho_e u_e^2 \Theta\right)}{ds} \;=\; b\,\frac{\tau_w}{2} \;-\; \rho_e u_e \Delta^* \frac{du_e}{ds} \tag{E.11}$$

$$\frac{d\left(\frac{1}{2}\rho_e u_e^3 \Theta^*\right)}{ds} \;=\; (b\mathcal{D}) \;-\; \rho_e u_e^2 \Delta^{**} \frac{du_e}{ds} \tag{E.12}$$

Here, b is an effective perimeter shown in Figure E.3 which arises when the various areas Δ^*, Θ etc. in the equations above are approximated with their 2D equivalents.

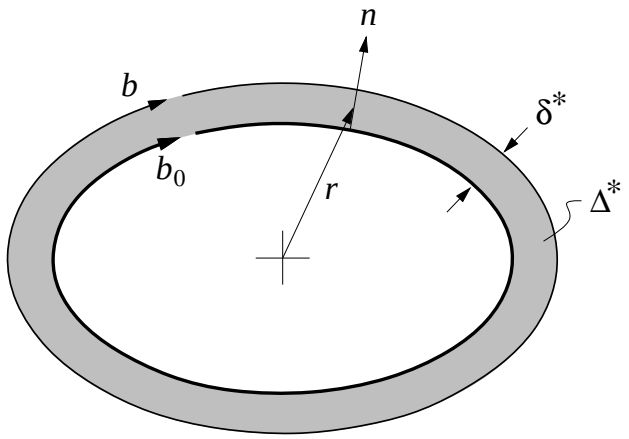

Figure E.3: Body perimeter b_0, displacement area Δ^*, and effective perimeter b.

For example, the definition of the displacement area is

$$\Delta^* \;=\; \int_0^{n_e} \left(1 - \frac{\rho u}{\rho_e u_e}\right) 2\pi r\; dn \tag{E.13}$$

which has the somewhat awkward radius r inside the integral. This is suitably approximated by its average value over the layer thickness, by using the 2D displacement thickness itself,

$$2\pi r \;\simeq\; b_0 \,+\, 2\pi\delta^* \;\equiv\; b \tag{E.14}$$

so that the modified perimeter b is taken as a suitable approximate value for the local perimeter $2\pi r_{(n)}$ over the integral. This allows all the viscous areas to be expressed in terms of the more familar 2D integral thicknesses as follows.

$$\delta^* \;=\; \int_0^{n_e} \left(1 - \frac{\rho u}{\rho_e u_e}\right) dn \tag{E.15}$$

$$\theta \;=\; \int_0^{n_e} \left(1 - \frac{u}{u_e}\right) \frac{\rho u}{\rho_e u_e}\, dn \tag{E.16}$$

$$\theta^* \;=\; \int_0^{n_e} \left(1 - \frac{u^2}{u_e^2}\right) \frac{\rho u}{\rho_e u_e}\, dn \tag{E.17}$$

$$\delta^{**} \;=\; \int_0^{n_e} \left(1 - \frac{u^2}{u_e^2}\right) \frac{\rho u}{\rho_e u_e}\, dn \tag{E.18}$$

$$\Delta^* \;=\; \int_0^{n_e} \left(1 - \frac{\rho u}{\rho_e u_e}\right) 2\pi r\, dn \;\simeq\; b\,\delta^* \tag{E.19}$$

$$\Theta \;=\; \int_0^{n_e} \left(1 - \frac{u}{u_e}\right) \frac{\rho u}{\rho_e u_e}\, 2\pi r\, dn \;\simeq\; b\,\theta \tag{E.20}$$

$$\Theta^* \;=\; \int_0^{n_e} \left(1 - \frac{u^2}{u_e^2}\right) \frac{\rho u}{\rho_e u_e}\, 2\pi r\, dn \;\simeq\; b\,\theta^* \tag{E.21}$$

$$\Delta^{**} \;=\; \int_0^{n_e} \left(1 - \frac{\rho}{\rho_e}\right) \frac{u}{u_e}\, 2\pi r\, dn \;\simeq\; b\,\delta^{**} \tag{E.22}$$

The dissipation integral is also defined in terms of its 2D form.

$$\mathcal{D} \;=\; \int_0^{n_e} \tau\, \frac{\partial u}{\partial n}\, dn \tag{E.23}$$

$$(b\mathcal{D}) \;=\; \int_0^{n_e} \tau\, \frac{\partial u}{\partial n}\, 2\pi r\, dn \;\simeq\; b\,\mathcal{D} \tag{E.24}$$

Using the approximate area definitions above, equations (E.11) and (E.12) are put in their equivalent logarithmic differential forms.

$$d\,\ln\theta \,+\, d\,\ln b \;=\; \frac{s}{\theta}\frac{C_f}{2}\, d\,\ln s \,-\, \left(H + 2 - M_e^2\right)\, d\,\ln u_e \tag{E.25}$$

$$d\,\ln H^* \;=\; \left(\frac{s}{\theta}\frac{2C_{\mathcal{D}}}{H^*} \,-\, \frac{s}{\theta}\frac{C_f}{2}\right) d\,\ln s \,-\, \left(\frac{2H^{**}}{H^*} + 1 - H\right) d\,\ln u_e \tag{E.26}$$

Equation (E.26) is actually the difference between the logarithmic forms of equations (E.12) and (E.11). The usual 2D shape parameter is defined as

$$H \;=\; \frac{\delta^*}{\theta} \tag{E.27}$$

and the 2D integral relations

$$\frac{\tau_w}{\frac{1}{2}\rho_e u_e^2} = C_f(H, Re_\theta, M_e^2) \quad \text{(E.28)}$$

$$\frac{\mathcal{D}}{\rho_e u_e^3} = C_{\mathcal{D}}(H, Re_\theta, M_e^2) \quad \text{(E.29)}$$

$$\frac{\theta^*}{\theta} = H^*(H, Re_\theta, M_e^2) \quad \text{(E.30)}$$

$$\frac{\delta^{**}}{\theta} = H^{**}(H, Re_\theta, M_e^2) \quad \text{(E.31)}$$

are used to close the equations. Except for the trivial additional term $d \ln b$ in (E.25), all these relations are identical to their 2D forms, so that an existing 2D implementation can be used with only minimal modification.

E.4.2 Direct BL solution

In the classical BL formulation, $u_{e(s)}$ is prescribed to be the inviscid velocity, e.g.

$$u_e = u_{\text{inv}} \quad \text{(E.32)}$$

This can be obtained from the Λ_i strengths computed above, by using them in the u, v, w summations (E.3,E.4,E.5) to compute the inviscid surface tangential velocities $u_{\text{inv}(s)}$ along the surface and also into the wake.

$$u_{\text{inv}(s)} = \sqrt{u^2 + v^2 + w^2} \quad \text{(E.33)}$$

Once $u_{e(s)}$ is specified, then equations (E.25) and (E.26) can in principle be solved for the boundary layer variables $\theta_{(s)}, \delta^*_{(s)}$ by usual downstream ODE integration. However, if separation is encountered this integration will fail, since $dH^*/dH \simeq 0$ at separation, and equation (E.26) cannot then be used to obtain the necessary $d\delta^*/ds$ form for integration.

E.4.3 Viscous/Inviscid interacted solution

The present method eliminates the separation problem by the usual viscous/inviscid interaction formulation. Using the wall-blowing concept, the actual viscous edge velocities $u_{e(s)}$ seen by the boundary layer and wake are modified by adding contributions from the apparent wall-blowing sources, assumed to be axisymmetric point sources at the $j \ldots j{+}1$ interval midpoints.

$$u_{e_i} = u_{\text{inv}_i} + \frac{1}{\rho_{e_i}} \sum_j \frac{1}{4\pi} \frac{m_{j+1} - m_j}{\left| s_i - \frac{1}{2}(s_{j+1}+s_j) \right| \left(s_i - \frac{1}{2}(s_{j+1}+s_j) \right)} \quad \text{(E.34)}$$

Here, m is the axisymmetric mass defect, defined by

$$m = \rho_e u_e \Delta^* = \int_0^{n_e} (\rho_e u_e - \rho u)\, 2\pi r \, dn \simeq \rho_e u_e \delta^* (b_0 + 2\pi\delta^*) \quad \text{(E.35)}$$

which is a quadratic equation giving δ^* in terms of m and u_e.

$$\delta^* = \frac{1}{4\pi}\left(-b_0 + \sqrt{b_0^2 + \frac{8\pi\, m}{\rho_e u_e}}\right) \tag{E.36}$$

The summation (E.34) can be put into a more concise form by precomputation of the mass-influence matrix d_{ij} which depends only on the geometry.

$$u_{e_i} = u_{\mathrm{inv}_i} + \frac{1}{\rho_{e_i}} \sum_j d_{ij}\, m_j \tag{E.37}$$

$$d_{ij} = \frac{1}{4\pi}\left[\frac{1}{\left|s_i - \frac{1}{2}(s_j + s_{j-1})\right| \left(s_i - \frac{1}{2}(s_j + s_{j-1})\right)} - \frac{1}{\left|s_i - \frac{1}{2}(s_{j+1} + s_j)\right| \left(s_i - \frac{1}{2}(s_{j+1} + s_j)\right)} \right] \tag{E.38}$$

In the viscous/inviscid solution scheme, the boundary layer equations (E.25) and (E.26) are solved together with the u_e definition equation (E.37), to obtain the overall solution $\theta_{(s)}$, $\delta^*_{(s)}$, $u_{e(s)}$. Only the inviscid velocity $u_{\mathrm{inv}(s)}$ is prescribed. Because equation (E.37) has global influence, the equations are not solved by marching, but instead are solved "everywhere" at once by a global Newton iteration. An initial maching calculation with $u_e = u_{\mathrm{inv}}$ prescribed (and necessarily modified at separation) is still used to obtain a good initial guess to start the Newton cycle.

E.4.4 Drag and dissipation calculation

In the absence of any boundary layer ingestion, the body profile drag is simply the momentum defect at the end of the wake.

$$D = (\rho_e u_e^2 \Theta)_{\mathrm{wake}} \tag{E.39}$$

$$C_D = \frac{2\Theta_{\mathrm{wake}}}{S_{\mathrm{ref}}} \tag{E.40}$$

The overall surface + wake viscous dissipation is the kinetic energy defect at the end of the wake, with a density-flux thickness correction.

$$\Phi_{\mathrm{surf}} + \Phi_{\mathrm{wake}} = \int_0^\infty b\mathcal{D}\, ds = (\rho_e u_e^3 \Theta^*)_{\mathrm{wake}} + \int_0^\infty b\rho_e u_e^2 \Delta^{**} \frac{du_e}{ds}\, ds \tag{E.41}$$

$$= DV_\infty \tag{E.42}$$

The overall calculation gives reliable fuselage drag and dissipation predictions for any reasonable fuselage shape, without the need to rely on effective wetted area correlations, closure-angle correlations, or effective fineness-ratio correlations. For example, if the rear closure of the body is too rapid, the present method will simply predict separation off the back and into the wake, together with the increased dissipation leading to an increase in the downstream wake defect which reflects the larger drag.

It's useful to note that the individual 2D thicknesses θ, δ^* significantly depend on exactly how the effective perimeter b is defined. For example, in the wake where $b_0 = 0$, the momentum and kinetic energy area breakdowns become

$$\Theta = b\,\theta = 2\pi\delta^*\,\theta \tag{E.43}$$

$$\Theta^* = b\,\theta^* = 2\pi\delta^*\,\theta^* \tag{E.44}$$

So for example if the factor of 2π in the b definition (E.14) is modified somewhat because of a non-circular body cross section, then the θ, θ^* and δ^* values will change somewhat. However, because equations (E.11) and (E.12) evolve the full momentum and K.E. defects, these defects are extremely insensitive to how they are broken down into the θ, θ^*, and δ^* components in (E.43) and (E.44). So the computed drag and dissipation are also insensitive to such modeling ambiguities, since they depends only on the overall Θ and Θ^*. This justifies the somewhat ad-hoc definitions of b in the various integral area approximations.

For related reasons, the present drag and dissipation calculation method is surprisingly accurate for bodies which are not quite axisymmetric. If the flow is slender but not quite axisymmetric, the local 2D momentum defect $\rho_e u_e^2\,\theta$ might vary considerably at any given x location. In Figure E.3, for example, the corresponding δ^* might be very nonuniform around the perimeter. A typical cause is redistribution of the viscous fluid via crossflow, from a small angle of attack, for instance. However, the circumferential integral of $\rho_e u_e^2\theta$ will average out this redistribution, and since this integral is simply the total momentum defect,

$$\int \rho_e u_e^2\,\theta\; db = \rho_e u_e^2\,\Theta \tag{E.45}$$

the overall drag will also be very insensitive to such redistribution. The same argument follows for the kinetic energy thicknesses. Hence, accurate drag and dissipation predictions are still expected for weakly non-axisymmetric flows.

Appendix F

Power Accounting with Boundary Layer Ingestion

F.1 General Power Balance

The general power balance relation for an aircraft is written as follows.

$$(P_{K_{\text{inl}}} + P_V) \; + \; (P_{K_{\text{out}}} - \Phi_{\text{jet}}) \;\; = \;\; \Phi_{\text{surf}} \; + \; \Phi_{\text{wake}} \; + \; \dot{E}_{\text{v}} \; + \; W\dot{h} \tag{F.1}$$

F.2 Isolated–Propulsor Case

For an isolated-propulsion case without Boundary Layer Ingestion (BLI) all the terms above reduce as follows.

$$P_{K_{\text{inl}}} + P_V \;\; = \;\; 0 \tag{F.2}$$

$$P_{K_{\text{out}}} - \Phi_{\text{jet}} \;\; = \;\; \iint_{\text{out}} \rho V_\infty u \, (V_\infty + u) \, dA \;\; = \;\; \iint_{\text{out}} V_\infty u \, d\dot{m} \;\; = \;\; F V_\infty \tag{F.3}$$

$$\Phi_{\text{surf}} \; + \; \Phi_{\text{wake}} \;\; = \;\; D_p V_\infty \tag{F.4}$$

$$\dot{E}_{\text{v}} \;\; = \;\; D_i V_\infty \tag{F.5}$$

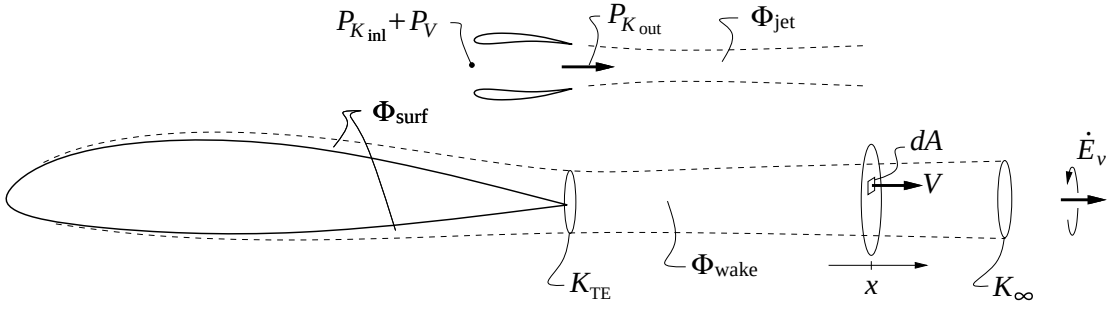

Figure F.1: Power terms in non-ingesting airframe and propulsion system.

As expected for this case, the above can then be combined into the usual force-balance relation.

$$\boxed{FV_\infty \;=\; D_pV_\infty \;+\; D_iV_\infty \;+\; W\dot{h}} \tag{F.6}$$

which is compared term-by-term with (F.1) in the top half of Figure F.2. Equation (F.6) can be considered as a formula for the thrust F necessary to achieve a required climb rate $\dot{h}$, or as a formula for the climb rate $\dot{h}$ which results from a given thrust and total drag, at a given flight speed. Corresponding interpretations will be made for the equivalent equation in the BL-ingesting case, considered next.

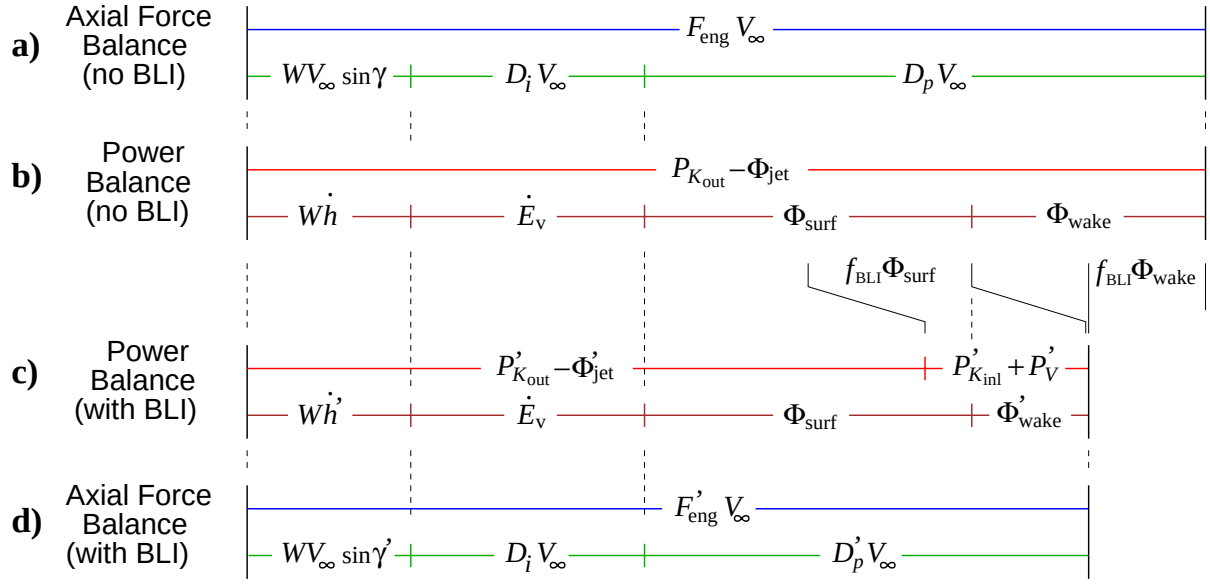

Figure F.2: Force balance compared to power balance (top half of figure). Power balance readily addresses the BLI case, and can be interpreted as equivalent forces (bottom half of figure). Primes $(\,)'$ denote quantities which are significantly modified by the BLI.

It's useful to first define the viscous kinetic energy defect K, and the density-flux defect Q,

$$K_{(x)} \;\equiv\; \iint \tfrac{1}{2}\left(V_e^2 - V^2\right)\rho V\, dA \;=\; \tfrac{1}{2}\,\rho_e V_e^3 \Theta^* \tag{F.7}$$

$$Q_{(x)} \;\equiv\; \iint \left(\rho_e - \rho\right) V\, dA \;=\; \rho_e V_e \Delta^{**} \tag{F.8}$$

where Θ^* is the kinetic energy area and Δ^{**} is the density-flux area. The integrals are over a plane in the viscous layer, normal to the flow at some x location, shown in Figure F.1.

For the incompressible case, where $Q = \Delta^{**} = 0$, K is simply related to the various terms in (F.1) as follows.

$$\Phi_{surf} \;=\; K_{TE} \tag{F.9}$$

$$\Phi_{wake} \;=\; K_\infty \;-\; K_{TE} \tag{F.10}$$

$$D_pV_\infty \;=\; K_\infty \tag{F.11}$$

If density variations and hence Q are significant, then surface integrals of Q must be included:

$$\Phi_{surf} \;=\; K_{TE} \;+\; \int_{surf} Q\, V_e \frac{\partial V_e}{\partial x}\, dx \tag{F.12}$$

$$\Phi_{\rm wake} \;=\; K_\infty \,-\, K_{TE} \,+\, \int_{\rm wake} Q\, V_e \frac{\partial V_e}{\partial x}\, dx \tag{F.13}$$

The Q contributions scale as the local M_e^2, and for typical high subsonic flows contribute perhaps $\sim 5\%$ to the total $\Phi_{\rm surf}$ and $\Phi_{\rm wake}$. They will be omitted here for physical clarity.

F.3 Ingesting–Propulsor Case

Primes $(\,)'$ will now be used to denote ingestion-case quantities, which will be expressed in terms of the non-ingestion-case quantities above.

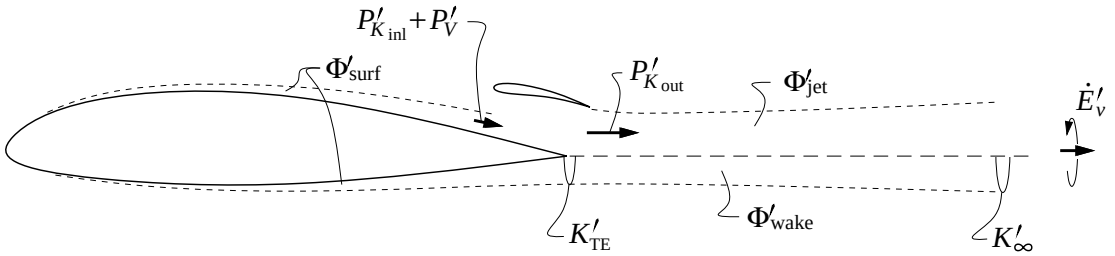

Figure F.3: Power terms in ingesting airframe and propulsion system.

The propulsor is assumed to ingest a fraction $f_{\rm BLI}$ of the body's kinetic energy defect at the trailing edge, so that the inlet P_K term is now no longer zero.

$$(P_{K_{\rm inl}} \,+\, P_V)' \;=\; f_{\rm BLI} K_{TE} \;=\; f_{\rm BLI}\, \Phi_{\rm surf} \tag{F.14}$$

Furthermore, the defect flowing into the wake is reduced by the same amount, so that the amount of rotational fluid flowing into the wake, and the associated wake dissipation are reduced correspondingly.

$$K'_{TE} \;=\; (1-f_{\rm BLI}) K_{TE} \tag{F.15}$$

$$\Phi'_{\rm wake} \;=\; (1-f_{\rm BLI})\, \Phi_{\rm wake} \tag{F.16}$$

In contrast, the surface dissipation occurs upstream of the propulsor and hence is largely unaffected. The trailing vortex system and hence the induced power are also unaffected.

$$\Phi'_{\rm surf} \;=\; \Phi_{\rm surf} \tag{F.17}$$

$$\dot{E}'_{\rm v} \;=\; \dot{E}_{\rm v} \tag{F.18}$$

Inserting all these primed quantities into the general power balance relation (F.1) gives

$$\boxed{(P_{K_{\rm inl}} + P_V)' \,+\, (P_{K_{\rm out}} - \Phi_{\rm jet})' \;=\; \Phi'_{\rm surf} \,+\, \Phi'_{\rm wake} \,+\, \dot{E}'_{\rm v} \,+\, W\dot{h}'} \tag{F.19}$$

$$\text{or} \qquad (P_{K_{\rm inl}} + P_V)' \,+\, (P_{K_{\rm out}} - \Phi_{\rm jet})' \;=\; \Phi_{\rm surf} \,+\, (1-f_{\rm BLI})\Phi_{\rm wake} \,+\, \dot{E}_{\rm v} \,+\, W\dot{h}' \tag{F.20}$$

Replacing these Φ and $\dot{E}_{\rm v}$ in terms of the more familiar drag quantities (all defined for the non-ingesting case), we have the following force-balance equation.

$$\boxed{F'V_\infty \;=\; D_p V_\infty \,-\, f_{\rm BLI}\Phi_{\rm wake} \,+\, D_i V_\infty \,+\, W\dot{h}'} \tag{F.21}$$

Although the equivalent-force relation (F.21) is usable, it has a potential problem in that D_p and Φ_{wake} are both hypothetical for the BLI case, in that they correspond to the non-BLI case which really does not exist. Hence, it would be difficult to apply to high-fidelity calculations since both the BLI and non-BLI cases would then need to be computed, even though the non-BLI case is geometrically different and may be unrealizable. In contrast, the power-balance relation (F.19) is given only in term of the BLI-case quantities which really exist.

Setting aside such interpretation or computability issues, equation (F.21) can be treated as a formula for either F' or $\dot{h}'$. However, the modified thrust F' needs more careful consideration. By definition, it is credited with the normally positive inlet defect $f_{\text{BLI}}K_{TE}$.

$$\begin{aligned} F'V_\infty &\equiv (P_{K_{\text{inl}}} + P_V)' + (P_{K_{\text{out}}} - \Phi_{\text{jet}})' \\ &\simeq f_{\text{BLI}}K_{TE} + \iint_{\text{out}} \rho V_\infty u' \,(V_\infty + u')\, dA \\ &= f_{\text{BLI}}K_{TE} + \iint_{\text{out}} V_\infty u' \, d\dot{m}' \end{aligned} \tag{F.22}$$

This is consistent with a basic momentum argument, that as the velocity into a propulsor is reduced with the power input fixed, the "ram drag" is reduced and the net thrust will naturally increase.

However, when u' and $\dot{m}'$ in (F.22) are computed with an engine-cycle calculation, it is necessary to account for the ingested defect $f_{\text{BLI}}K_{TE}$, via a reduced inlet total pressure for example. The resulting engine parameters will then be different from the non-ingesting case, hence the primes on u' and $\dot{m}'$ above. Additional distortion-related component losses may also be included if deemed appropriate. In any case, this inlet defect will definitely have a fuel-burn penalty which can more than offset the otherwise large gain of the $f_{\text{BLI}}K_{TE}$ credit term in the final thrust power $F'V_\infty$ in (F.22). If this cancellation is perfect, then the only gain of ingestion is the $-f_{\text{BLI}}\Phi_{\text{wake}}$ term in the overall power-balance equation (F.21).

F.4 Incorporation into Range Equation

Starting from the general power balance equation (F.1), with $\dot{h} = 0$, the corresponding Breguet-type equation is obtained as follows. First we define the total dissipation and vortex energy-rate coefficients $C_\Phi, C_{E_{\text{v}}}$, the usual lift coefficient C_L, and the net effective propulsive power P and associated power-specific fuel consumption *PSFC*.

$$C_\Phi \equiv \frac{\Phi_{\text{surf}} + \Phi_{\text{wake}}}{\frac{1}{2}\rho V_\infty^3 S} \tag{F.23}$$

$$C_{E_{\text{v}}} \equiv \frac{\dot{E}_{\text{v}}}{\frac{1}{2}\rho V_\infty^3 S} \tag{F.24}$$

$$C_L \equiv \frac{L}{\frac{1}{2}\rho V_\infty^2 S} \tag{F.25}$$

$$P \equiv (P_{K_{\text{inl}}} + P_V) + (P_{K_{\text{out}}} - \Phi_{\text{jet}}) = \Phi_{\text{surf}} + \Phi_{\text{wake}} + \dot{E}_{\text{v}} \tag{F.26}$$

$$P = \tfrac{1}{2}\rho V_\infty^3 S\,(C_\Phi + C_{E_{\text{v}}}) \tag{F.27}$$

$$PSFC \equiv \frac{\dot{m}_{\text{fuel}}\, g}{P} \tag{F.28}$$

The weight rate of change can be related to the fuel flow rate and hence the power, and also to the weight/range gradient via the velocity for nearly-level flight.

$$\frac{dW}{dt} = -\dot{m}_{\text{fuel}}\, g = -P\ PSFC \tag{F.29}$$

$$\frac{dW}{dt} = \frac{dW}{dR}\frac{dR}{dt} = \frac{dW}{dR}\, V_\infty \tag{F.30}$$

Equating these two weight rate relations, inserting $W/L = 1$ for level flight, and invoking the coefficient definitions above gives

$$\frac{dW}{dR} = -\frac{P}{V_\infty}\, PSFC = -W\frac{P}{V_\infty L}\, PSFC \tag{F.31}$$

$$\frac{dW}{dR} = -W\, \frac{C_\Phi + C_{E_{\text{v}}}}{C_L}\, PSFC \tag{F.32}$$

This is then integrated over the mission to give the mission range in terms of the fuel-burned weight W_{f}, and the final aircraft weight W_{e}.

$$R = \frac{C_L}{C_\Phi + C_{E_{\text{v}}}}\, \frac{1}{PSFC}\, \ln\!\left(\frac{W_{\text{e}} + W_{\text{f}}}{W_{\text{e}}}\right) \tag{F.33}$$

F.4.1 Non-ingesting case

For the non-BLI isolated propulsion case, the following relations hold.

$$P = FV_\infty \tag{F.34}$$

$$PSFC = TSFC/V_\infty \tag{F.35}$$

$$C_\Phi = C_{D_p} \tag{F.36}$$

$$C_{E_{\text{v}}} = C_{D_i} \tag{F.37}$$

$$C_\Phi + C_{E_{\text{v}}} = C_D \tag{F.38}$$

The power-based Breguet equation (F.33) is then exactly equivalent to its usual thrust-based form as expected:

$$R = \frac{C_L}{C_D}\, \frac{V_\infty}{TSFC}\, \ln\!\left(\frac{W_{\text{e}} + W_{\text{f}}}{W_{\text{e}}}\right) \tag{F.39}$$

F.4.2 Ingesting case

For the ingesting case, the corresponding derivations above give

$$P' \equiv (P_{K_{\text{inl}}} + P_V) + (P_{K_{\text{out}}} - \Phi_{\text{jet}})' = \Phi'_{\text{surf}} + \Phi'_{\text{wake}} + \dot{E}_{\text{v}} \tag{F.40}$$

$$R = \frac{C_L}{C'_\Phi + C_{E_{\text{v}}}}\, \frac{1}{PSFC'}\, \ln\!\left(\frac{W_{\text{e}} + W_{\text{f}}}{W_{\text{e}}}\right) \tag{F.41}$$

where the BLI-case dissipation coefficient is defined as before in (F.23),

$$C'_{\Phi} \equiv \frac{\Phi'_{\text{surf}} + \Phi'_{\text{wake}}}{\frac{1}{2}\rho V_\infty^3 S} \tag{F.42}$$

$$\simeq C_{D_p} - \frac{f_{\text{BLI}}\Phi_{\text{wake}}}{\frac{1}{2}\rho_\infty V_\infty^3 S}$$

$$= C_{D_p} - f_{\text{BLI}}\frac{K_\infty - K_{TE}}{\rho_\infty V_\infty^3 S} \tag{F.43}$$

with the second approximate form using values from the non-ingesting case and may be useful in some applications. Similarly, $PSFC'$ is defined as

$$PSFC' = \frac{\dot{m}'_{\text{fuel}}\, g}{P'} \tag{F.44}$$

where it's essential to remember that P' and corresponding $\dot{m}'_{\text{fuel}}$ must be computed in the presence of the implied inlet kinetic energy defect $f_{\text{BLI}}K_{TE}$ and equivalent inlet total pressure loss. The range for the BLI case is then given simply by the power-based Breguet equation using the primed parameters.

$$R' = \frac{C_L}{C'_{\Phi} + C_{E_{\text{v}}}} \frac{1}{PSFC'} \ln\left(\frac{W_{\text{e}} + W_{\text{f}}}{W_{\text{e}}}\right) \tag{F.45}$$

F.5 Thrust and Drag Accounting

The presence of boundary layer ingestion makes the definition of "thrust" and "drag" somewhat ambiguous. However, the above definitions of F' and C'_{Φ} are reasonable choices for comparing against non-ingesting alternatives, since they reduce to the usual F and C_{D_p} definitions in the non-ingesting case. Furthermore, these choices closely reflect what really happens to the flowfield when boundary layer ingestion is introduced, and can be explained using common engine terminology.

- The dissipation of the removed wake is excluded from C'_{Φ}
- The reduced velocities into the engine inlet are both beneficial (from a "ram drag" argument), and detrimental (from a cycle efficiency argument). The net benefit can be either positive or negative, depending on a number of secondary factors.

F.6 Inlet Total Pressure Calculation

For engine-cycle calculations, it is necessary to define a suitably-averaged inlet total pressure $p_{t\,2}$ from the inlet boundary layer properties.

F.6.1 Low speed flow case

For low speed flow, a suitable method is to perform a volume-flow weighted average of the total pressure.

$$\dot{\mathcal{V}}_{\rm inl} \equiv \iint_{\rm inl} V\, dA \tag{F.46}$$

$$\begin{aligned}(p_{t\,2} - p_{t\,\infty})\ \dot{\mathcal{V}}_{\rm inl} &= \iint_{\rm inl} (p_t - p_{t\,\infty})\, V\, dA \\ &\simeq \iint_{\rm inl} \left(p + \tfrac{1}{2}\rho V^2 \ - \ p_e + \tfrac{1}{2}\rho_e V_e^2\right) V\, dA \\ &= -\tfrac{1}{2}\rho_e V_e^3 \left(\Theta^* + \Delta^{**}\right)_{\rm inl} \\ &= -f_{\rm BLI}\left(K_{TE} + \tfrac{1}{2}V_e^2 Q_{TE}\right) \ \simeq \ -f_{\rm BLI} K_{TE} \end{aligned} \tag{F.47}$$

$$p_{t\,2} = p_{t\,\infty} \ - \ \frac{f_{\rm BLI} K_{TE}}{\dot{\mathcal{V}}_{\rm inl}} \tag{F.48}$$

F.6.2 High speed flow case

An alternative approach, more justifiable for the high speed case, is to employ a mass weighted average of the entropy. The adiabatic boundary layer is assumed to have some known velocity profile a constant total temperature $T_t = T_{t_e} = T_{t_\infty}$, and the usual assumption of a constant profile static pressure $p = p_e$ is also made. This gives the following temperature and entropy profiles in terms of the velocity profile $V_{(y)}$.

$$T_{(y)} = T_{t_e} \ - \ \frac{{V_{(y)}}^2}{2\, c_p} \tag{F.49}$$

$$s_{(y)} = \ln \frac{(T_{(y)}/T_{t_\infty})^{\frac{\gamma}{\gamma-1}}}{p_{(y)}/p_{t_\infty}} \ = \ \ln \frac{(T_{(y)}/T_e)^{\frac{\gamma}{\gamma-1}}}{p_{(y)}/p_e} \ = \ \frac{\gamma}{\gamma-1}\ \ln \frac{T_{(y)}}{T_e} \tag{F.50}$$

For modest heat transfer and near-unity Prandtl numbers, the Stewartson temperature profile is quite accurate.

$$\frac{V_{(y)}}{V_e} \equiv U_{(y)} \tag{F.51}$$

$$\frac{T_{(y)}}{T_e} = 1 \ + \ \frac{T_w - T_{aw}}{T_e}\,(1-U) \ + \ r\,\frac{\gamma-1}{2}\,M_e^2\,\left(1-U^2\right) \tag{F.52}$$

$$= 1 \ + \ r\,\frac{\gamma-1}{2}\,M_e^2\,\left(1-U^2\right) \qquad \text{(for adiabatic flow)} \tag{F.53}$$

$$r \ \simeq \ Pr^{1/2} \ \simeq \ 0.9 \qquad \text{(for air)} \tag{F.54}$$

For a typical fan, $M_e \simeq 0.6$, so that the compressibility factor is quite small compared to unity.

$$r\,\frac{\gamma-1}{2}\,M_e^2 \ \simeq \ 0.065 \ \ll \ 1 \qquad (\text{for } M_e = 0.6) \tag{F.55}$$

The entropy profile can then be simplified using the logarithm's Taylor series,

$$\ln(1+\epsilon) \;=\; \epsilon \;-\; \frac{1}{2}\epsilon^2 \;+\; \frac{1}{3}\epsilon^3 \;-\; \ldots \qquad \text{(F.56)}$$

$$\frac{s(y)}{c_p} \;=\; \frac{\gamma}{\gamma-1}\,\ln\!\Big[1 \;+\; r\,\frac{\gamma-1}{2}\,M_e^2\,\Big(1-U^2\Big)\Big] \;\simeq\; r\,\frac{\gamma}{2}\,M_e^2\,\Big(1-U^2\Big) \qquad \text{(F.57)}$$

which is accurate to roughly 3% for the $M_e = 0.6$ case.

The mass-weighted entropy flux and the associated average entropy $\bar{s}$ are then computed as follows.

$$\dot{m}_{\rm inl} \;\equiv\; \iint_{\rm inl} \rho V\, dA \qquad \text{(F.58)}$$

$$\bar{s}\,\dot{m}_{\rm inl} \;=\; \iint s\; d\dot{m} \;=\; \iint s\;\rho V\, dA \;=\; \rho_e V_e\, r\,\frac{\gamma}{2} M_e^2 \iint \Big(1-U^2\Big)\; RU\; dA \qquad \text{(F.59)}$$

$$\bar{s} \;=\; \frac{\rho_e V_e \Theta^*_{\rm inl}}{\dot{m}_{\rm inl}}\; r\,\frac{\gamma}{2} M_e^2 \qquad \text{(F.60)}$$

Substituting $\gamma M_e^2 = \rho_e V_e^2 / p_e$ and for $\Theta^*_{\rm inl}$ in terms of $K_{\rm inl}$ gives

$$\bar{s} \;=\; \frac{K_{\rm inl}}{\dot{m}_{\rm inl}}\; r\,\frac{\rho_e}{p_e} \qquad \text{(F.61)}$$

Finally, the equivalent average total pressure is computed from this $\bar{s}$ via the entropy definition (F.50).

$$p_{t\,2} \;=\; p_{t\,\infty}\,\exp(-\bar{s}) \qquad \text{(F.62)}$$

Bibliography

[1] J. Roskam. *Airplane Design*. DAR Corporation, Lawrence, Kansas, 2000.

[2] E. Torrenbeek. *Synthesis of Subsonic Airplane Design*. Delft University Press, 1988.

[3] D.P. Raymer. *Aircraft Design: A Conceptual Approach*. AIAA Education Series. AIAA, 1992.

[4] S. Jayaram, A. Myklebust, and P. Gelhausen. ACSYNT — A standards-based system for parametric computer aided conceptual design of aircraft. AIAA Paper 92-1268, Feb 1992.

[5] W.H. Mason and T.K. Arledge. ACSYNT aerodynamic estimation — An examination and validation for use in conceptual design. AIAA Paper 93-0973, Feb 1993.

[6] M.D. Ardema, M.C. Chambers, A.P. Patron, A.S. Hahn, M. Hirokazu, and M.D. Moore. Analytical fuselage and wing weight estimation of transport aircraft. NASA TM 110392, May 1996.

[7] B. Knapp, Matt. Applications of a nonlinear wing planform design program. Master's thesis, MIT, Aug 1996.

[8] S. Wakayama. *Lifting Surface Design Using Multidisciplinary Optimization*. PhD thesis, Stanford, June 1994.

[9] S. Wakayama. Blended-wing-body optimization setup. AIAA Paper 00-4740, Sept 2000.

[10] I. Kroo. PASS, program for aircraft synthesis studies. Software Package, Desktop Aeronautics, Palo Alto, CA, 2005.

[11] J.L. Kerrebrock. *Aircraft Engines and Gas Turbines, 2nd Ed.* The MIT Press, Cambridge, 1996.

[12] M. Drela. Power balance in aerodynamic flows. *AIAA Journal*, 47(7):1761–1771, July 2009. Also AIAA Paper 09-3762, San Antonio Conference, June 2009.

[13] J.K.C. Low. Ultra-high bypass ratio jet noise. NASA Contractor Report NASA CR-195394, NASA, 1994.

[14] J.R. Stone, D.E. Groesbeck, and C.L. Zola. Conventional profile coaxial jet noise prediction. *AIAA Journal*, 21(3), Mar 1983.

[15] M.R. Fink. Airframe noise prediction method. Report FAA-RD-77-29, FAA, 1977.

[16] J. Wolkovitch. The joined wing: An overview. *Journal of Aircraft*, 23(3), Mar 1986.

[17] R. Liebeck. Design of the blended wing body subsonic transport. *Journal of Aircraft*, 41(1), Jan 2004.

[18] M. Drela and M.B. Giles. Viscous-inviscid analysis of transonic and low Reynolds number airfoils. *AIAA Journal*, 25(10):1347–1355, Oct 1987.

[19] J.H. Horlock, D.T. Watson, and T.V. Jones. Limitations on gas turbine performance imposed by large turbine cooling flows. *Journal of Engineering for Gas Turbines and Power*, 123:487–494, Jul 2001.

[20] J.E. Sargison, S.M. Guo, M.L.G. Oldfield, G.D. Lock, and A.J. Rawlinson. A converging slot-hole film-cooling geometry — part 2: Transonic nozzle guide vane heat transfer and loss. *Journal of Turbomachinery*, 124:461–471, July 2002.

[21] B.L. Koff. Gas turbine technology evolution: A designer's perspective. *Journal of Propusion and Power*, 20(4):577–595, Jul–Aug 2004.

[22] T. Von Karman. Calculation of pressure distribution on airship hulls. Technical Memorandum 574, NACA, 1930.

[23] M. Drela. XFOIL: An analysis and design system for low Reynolds number airfoils. In T.J. Mueller, editor, *Low Reynolds Number Aerodynamics*. Springer-Verlag, Jun 1989. Lecture Notes in Engineering, No. 54, http://raphael.mit.edu/xfoil/.

Appendix G: Advanced Materials and Design Load Reduction

G.1 Advanced Materials

New materials beyond metallics offer the potential for high-strength/high-stiffness lightweight structures. In addition, advanced materials can offer increased fatigue life and damage tolerant structures. Tailoring the materials based on specific structural requirements can offer significant weight advantages.

G.1.1 Fiber

Currently, fiber manufacturers are developing new carbon fibers to replace the industry standards, IM7 and T800 intermediate modulus fibers. Fiber manufacturers are targeting the 1000 ksi strength and 50 ksi stiffness range (~25% improvement) and developing the fiber-matrix interface technologies required to translate these high fiber properties into high lamina and laminate properties. Because these fibers are already in development 20 years before the service entry date of the N+3 aircraft, it is reasonable to assume that these fibers will be available with robust allowables, vendor qualification and manufacturing data to give designers confidence to use them on large commercial airframe structures.

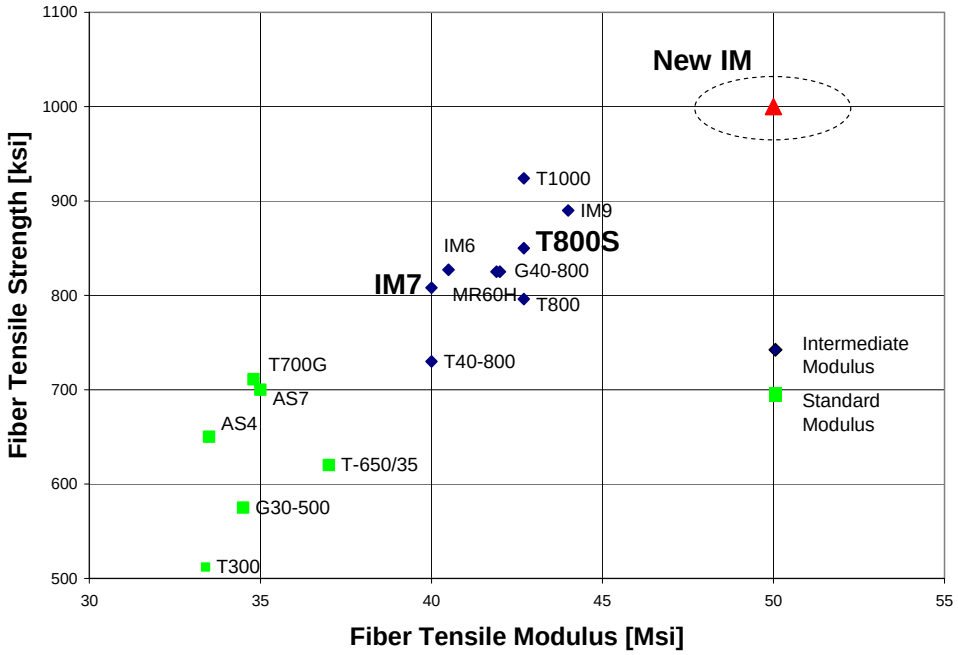

Figure G.1: Strength-stiffness progression of fiber reinforcement materials.

A discussion of future fibers is not complete without an assessment of Carbon Nanotube Technology (CNT). In the timeframe of this study, it is certainly possible that long CNTs will be used for structural fibers; however, their challenges are significant. While long CNTs provide outstanding tensile properties and will see applications in bulletproofing, CNTs suffer in compression properties because of the inability to make long, aligned and uniformly dispersed fibers that resist buckling from compression loads. As a further challenge, individual CNT fibers are so narrow that the spaces between fibers in a CNT lamina are relatively large, which exacerbates the fiber buckling problem. Instead, CNTs will provide their primary advantages by enhancing the matrix through the use of short CNTs in an aligned and dispersed manner.

G.1.2 Matrix

The baseline matrices for autoclaved carbon composites today are Cytec 977-3, Hexcel 8552 and Toray 3900-2 because they provide damage tolerance and the required laminate properties for a given service temperature. The 977-3 and 8552 are considered mid-toughened systems while the 3900-2 is considered a highly toughened system. The Airbus Next Generation Composite Wing (NGCW) program is developing a resin system with both high toughness and high service temperature. A natural trade off exists between the level of toughening and service temperature as shown in Figure G.2.

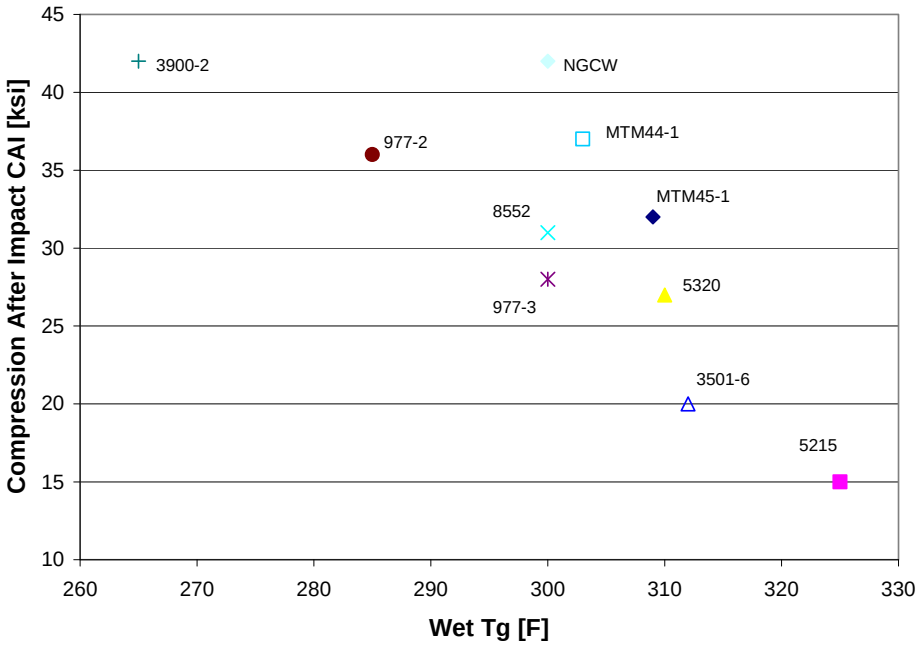

Figure G.2: Compression after impact (CAI) - transition temperature progression of matrix materials.

Compression after impact (CAI) is a measure of toughness and damage tolerance while service temperature correlates to the wet glass transition temperature (wet Tg). High toughening is desirable but comes at the expense of high service temperature. Typically, commercial aircraft do not require the high service temperature of their military counterparts, and therefore can use higher toughened systems to extract a weight savings. In addition, military aircraft typically use Open Hole Compression (OHC) as a sizing parameter which puts toughened materials at a weight disadvantage because the damage is simulated with a 0.25" diameter hole. In order to optimize the design for lowest weight in a military environment, OHC will be used as the basic sizing parameter with a hot wet service temperature of 200F.

G.1.3 Future Systems

Several underlying technology trends will shape matrix systems used in the 2030-2050 timeframe, chief among them is the use of nanotube technology to enhance matrix properties. Many methods have emerged to use short CNTs as listed in Figure G.3.

1. Nanotube dispersion by mixing methods
2. Low-concentration approaches to impact Z direction properties
3. New resin formulation for hybrid polymer formation.
4. Polymer approaches such as forming interpenetrating network polymers
5. Fuller integration that yields paradigm changes in the ways composites are made.

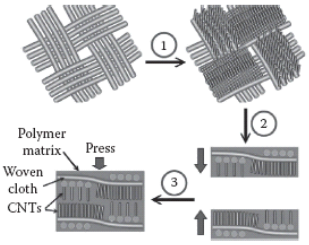

Method 2: Z-direction reinforcement

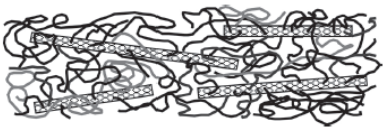
Method 2: Side wall cross-linked nanotube

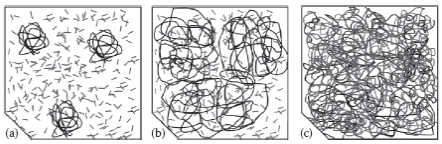

Method 4: Interpenetrating networks

Figure G.3: Short Carbon Nanotube (CNT) infusion methods.

The MIT team has surveyed many manufacturers and universities who are actively involved in this research to improve fracture toughness and compression properties. MIT's NESCT has shown promising work to improve matrix properties with aligned, unfunctionalized CNTs using a proprietary process of depositing CNTs on prepreg as shown in Figure G.4.

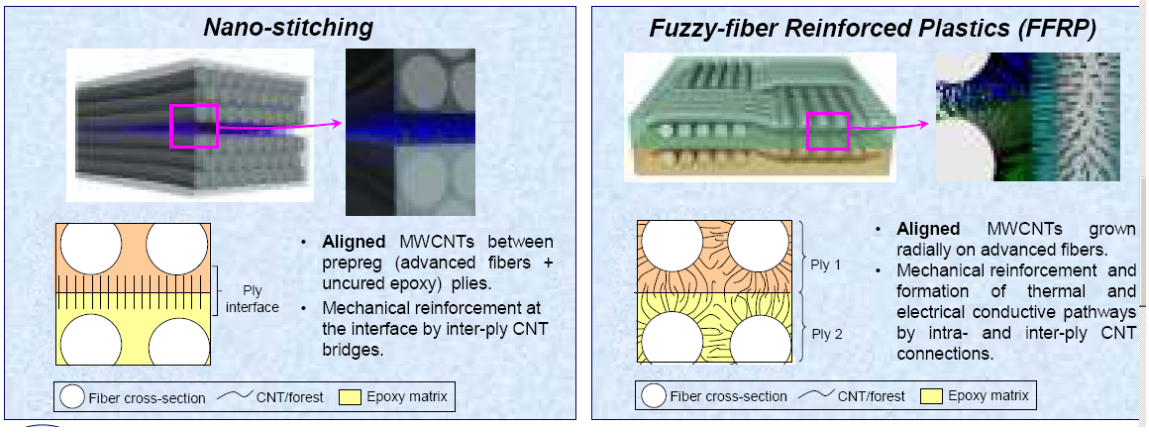

Figure G.4: MIT NESCT short CNT deposits on prepreg.

However, while gains in interlaminar properties have been achieved (fracture toughness) as above, these have yet to be translated into properties such as compression strength. As in the early stages of any new technology, time will be necessary to filter out true performers from methods that do not provide significant performance benefits. The MIT team predicts the nanotube resin enhancements will translate into a 15% to 20% improvement in CAI strength and modulus over current materials [zyvexpro].

G.1.4 Composite Lamina

Given the fiber reinforcement and matrix advancements, the following chart lists design values for the material properties. These design values are based on the rule and inverse rule of mixtures using a fiber volume fraction of 62%, which is consistent with volume fractions of other carbon-epoxy composite material systems.

Table G.1: Composite Lamina Properties (Unidirectional Tape)

Fiber Volume Fraction (Vf) [%]	62
Density (ρ) [lbs/in3]	0.056
Elastic Modulus (E1) [Msi]	31.4
Elastic Modulus (E2) [Msi]	2.5
Strength (σ1) [ksi]	623.8
Strength (σ2) [ksi]	25.9

G.1.5 Composite Laminate

It is assumed that various biased laminate ply layups will be used to design the airframe structure. While the particular layup will be tailored to the component loading, a nominal bias of 50%/40%/10% 0°/±45°/90° is used to determine bulk laminate properties for the conceptual sizing of the aircraft. The bulk laminate properties are shown in the table below. The unnotched strength was calculated using Tsai-Hill criteria for uniaxial loading conditions. Additionally, the CAI and OHC properties are shown as they are assumed to be sizing strengths for the aircraft based on survivability and damage tolerance requirements.

Table G.2: Composite Laminate Properties

Elastic Modulus (E1) [Msi]	18.2
Elastic Modulus (E2) [Msi]	7.5
Shear Modulus (G) [Msi]	3.7
Unnotched Strength (σ1) [ksi]	198
Unnotched Strength (σ2) [ksi]	64.0
Compression After Impact (σCAI) [ksi]	59.6
Open Hole Compression (σOHC) [ksi]	53.5

These properties take into account the effects of temperature, moisture, and damage on the material properties. Currently, composite material properties are extremely conservative with regard to conditional environmental impacts on strength due to the following combined criteria:

- Worst case temperature and moisture
- Worst case damage, undetected
- Reduced design allowables

The conservatism is illustrated in Figure G.5. The goal of future material allowable development is to ultimately create material properties as safe as the metallic counterparts, which are in general derived from variability unconditional on environments and damage[1].

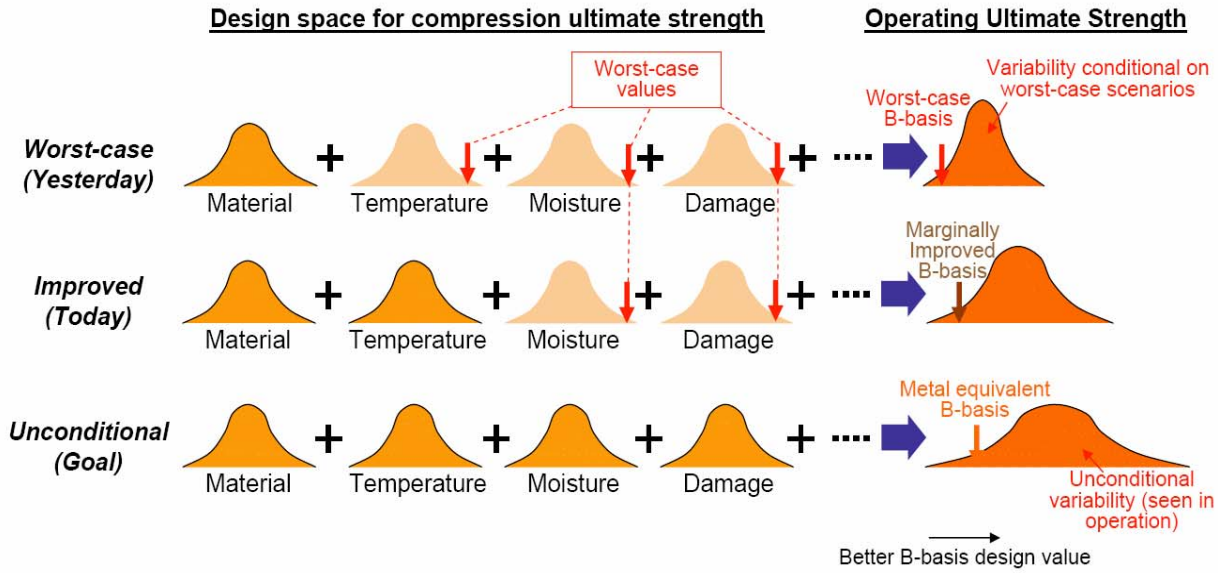

Figure G.5: Current and unconditional design strength process of composite materials.

G.1.6 Advanced Processes

Advanced processes are also used in the vehicle concepts for further reduction in weight. This is projected to be achieved by primarily using the unitized structure manufacturing and assembly techniques. The vehicle concepts will have a reduced part count due to the ability to layup complex parts as a co-cured structure requiring fewer fasteners and fittings. Out-of-Autoclave (OOA) resins enable larger components to be cured without the size restriction of an autoclave. Processes like Resin Transfer Modling (RTM) and Vacuum-assisted Resin Transfer Molding (VaRTM) allow increased out-time for complex layups prior to curing. Pultruded Rod Stitched Efficient Unitized Structure (PRSEUS) and similar processes allow for the combination of skin, stringer, and frame elements into a common structure. These techniques and others allow for weight savings at details and interfaces to match weight savings in the structure itself.

[1] Renton, J. and C. Chen. "The Potential Power of Non-Deterministic Analysis Methods in the Aircraft Design/Build/Test Process," 46th AIAA/ASME/ASCE/AHS/ASC Structures, 19 April 2005.

G.2 Design Load Reduction

The airframe structure for the concept vehicle is sized to withstand ultimate loading corresponding to a 2.5g pull-up limit load. This represents a small reduction from the sizing load of the B737 comparative baseline (3g pull-up). This value was chosen as it is the minimum value achievable with Gust Load Alleviation (GLA). When GLA is used as a mission critical system, the sizing load is no longer vertical gusts but the maneuvering envelope specified by the FAA. When GLA is used in conjunction with other load reduction technologies (envelope protection, predictive path planning, and others), this value becomes increasingly achievable, as it may be incrementally approached through small contributions to ultimate loading reduction from each of the supporting technologies. Through a study done by the University of Dayton that measured 11,721 flights of a B737-400 (compared to a design life of 75,000 flight cycles), both maneuver and gust loads have been measured to be less than 2.5g's, as shown in Figure G.6.

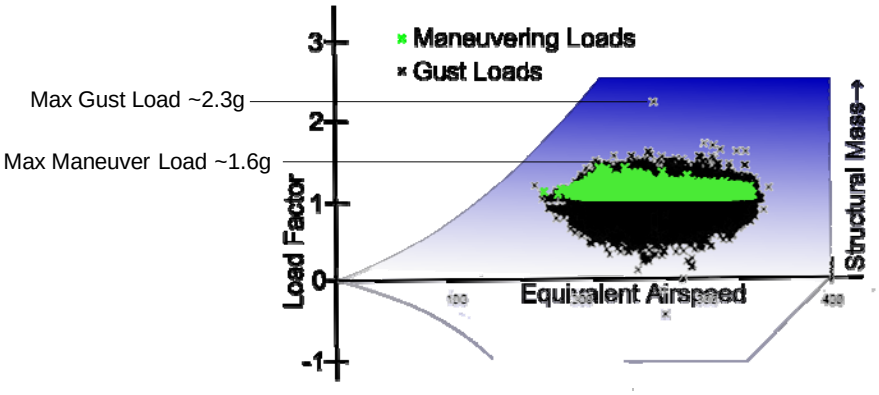

Figure G.6: University of Dayton study on B737-400 maneuver and gust flight loads.

Historically, the factor of safety from limit loading to ultimate loading is 1.5. The pressurized fuselage tends to use a factor of safety of 2.0. Additionally, the main landing gear structures use a factor of safety of 1.25. The following two strength criteria control the design of aircraft to the loading:

1. The structure must not detrimentally deform at limit loading (i.e. plastic deformation)

2. The structure must not fail at ultimate loading.

Although there is some difference of opinion on where the factor originated, one theory is that 1.5 was initially chosen as it represented the rough ratio of an early aluminum ultimate strength to yield strength, and therefore represented a scenario whereby both criteria would be met. Advanced materials such as composites have increasingly smaller ultimate to yield strength ratios, which causes the ultimate factor of safety to dominate the strength criteria.

Today, the factor of safety represents a confidence of the material reliability, the certainty of the load determination, tolerances and manufacturing workmanship of the parts, eccentricity of loading, etc. This confidence level is illustrated in Figure G.7, with a probability function of the loading and material strength shown. The design limit loading (DLL) represents the design load point, while the A- or B-Basis strength represents the design strength point, with a minimum factor of safety defining the spread between the two.

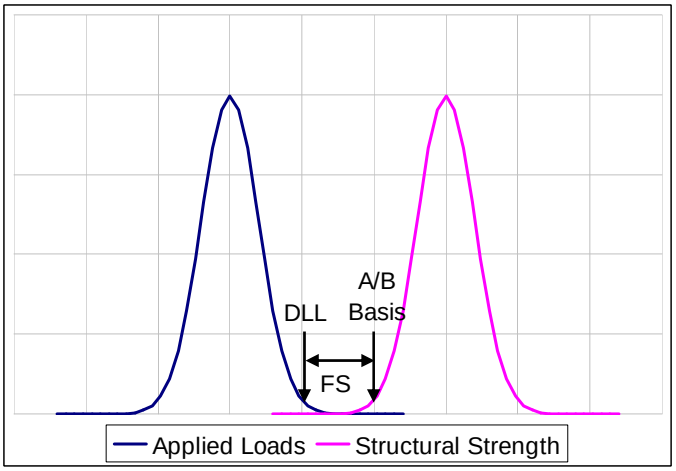

Figure G.7: Typical factor of safety separation between loading and strength.

Reductions in either the limit loading or ultimate loading result in corresponding design load factors. The following technologies are used to achieve the overall reduction calculated above.

G.2.1 Gust Load Alleviation

Effectiveness of gust load alleviation can be greatly enhanced if knowledge of the gust field[2] can be obtained earlier ideally with sufficient time to reduce speed down to best gust penetration speed. Aircraft response within the gust can also be improved by using modern sensors[3] providing better information about the instantaneous aeroservoelastic loads. Such sensors exist and can be applied using advanced mission and flight control laws to reduce the maximum in-flight loads and amplitude of the fatigue spectrum; thereby reducing the airplane structural mass. The long range gust detection sensor can also be used to select the best mission altitude accounting for wind speed.

Sections 25.337-341 of the Federal Aviation Regulations set structural strength requirements based on an aircraft's flight envelope and gust loads. In order to realize gains due to load factor reduction, Phase 2 proposed technologies that can maintain statistical reliability while pushing back on these strength requirements are investigated.

Gust Load Alleviation addresses the FAA 'severe vertical gust' requirement. Such a gust would increase the aircraft's angle of attack, and thus its overall lift coefficient. The additional force on the wing must be translated into acceleration of the fuselage without causing the wings to buckle. To mitigate the additional load, GLA senses the gust as it approaches or arrives at the wing and deflects the vehicle's control surfaces to maintain a constant lift coefficient. The new control surface configuration lowers wing bending moments and creates a smoother ride for passengers. This is illustrated in Figure G.8 below.

---

[2] Soreide, D., R. Bogue, L.J. Ehernberger, and H. Bagley. "Coherent Lidar Turbulence Measurement for Gust Load Alleviation." NASA TM-104318, August 1996.

[3] Mangalam, A. and T. Moes. "Real-Time Unsteady Loads Measurements Using Hot-Film Sensors." NASA TM-2004-212854, August 2004.

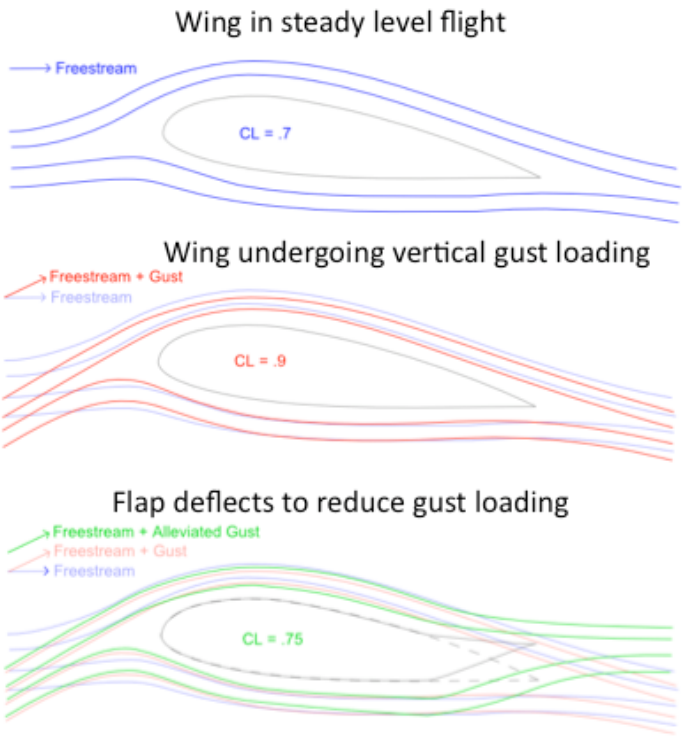

Figure G.8: Gust load alleviation.

G.2.2 Envelope Protection and Predictive Path Planning

Two other 'Fly Better' technologies that promise to provide the capability to maintain statistical reliability while pushing back on strength requirements are Envelope Protection (EP) and Predictive Path Planning (PPP), which address the flight envelope requirement. As is seen in Figure G.9 the required envelope vastly exceeds what is used for normal missions. For passenger comfort, commercial aircraft fly with maneuvering load factors below approximately 1.5 g's. The remaining envelope covers emergency maneuvering (terrain or collision avoidance) and gives the pilot confidence that he will not command the aircraft to states resulting in aircraft damage.

Envelope Protection removes the need for envelope margin by measuring the loads on the aircraft and limiting pilot commands to those which are safe to use. This frees the pilot to fly at the outer limits of the envelope when needed, without concern of damaging the aircraft. Envelope protection allows the designer to reduce structural overdesign, as the task of providing maneuvering confidence is now offloaded to an electronic system. Predictive Path Planning addresses the need for emergency maneuvering capabilities by calculating all possible paths available to a safe, stable state using only the normal maneuvering envelope. PPP can then guide the pilot through a path which maintains the largest number of safe alternatives, such that in an emergency situation the pilot is not forced to dip into the emergency envelope. As the ability of PPP to sense obstacles and prepare for possible aircraft failures improves, the design flight envelope can shrink back to what is absolutely necessary to fly the intended mission.

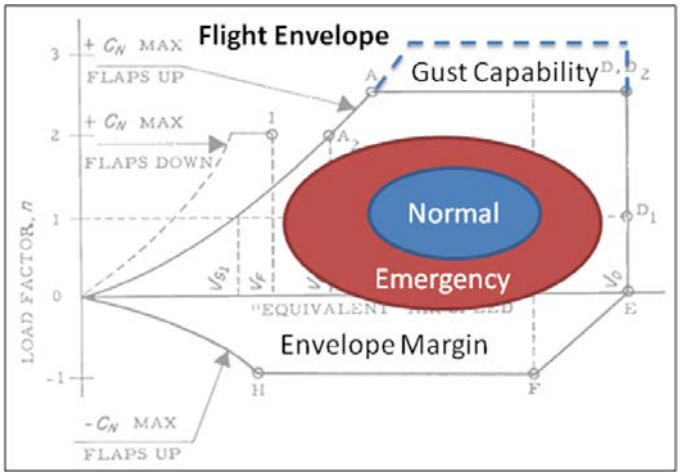

Figure G.9: The required flight envelope provides for normal and emergency maneuvering.

The minimal flight envelope necessary for a successful mission in the ideal case occurs where everything works perfectly: GLA removes all gusts, EP ensures that there are no pilot errors, and PPP ensures that there are no unplanned maneuvers. In this case the flight envelope is limited by the coordinated turn bank angle. A standard rate turn requires 3 degrees per second, or 1.5 degrees per second above 250 kts. In Figure G.10 we can see the load factor and bank angle for such a turn at various speeds. The largest required load factor for this ideal case is 1.2 g's.

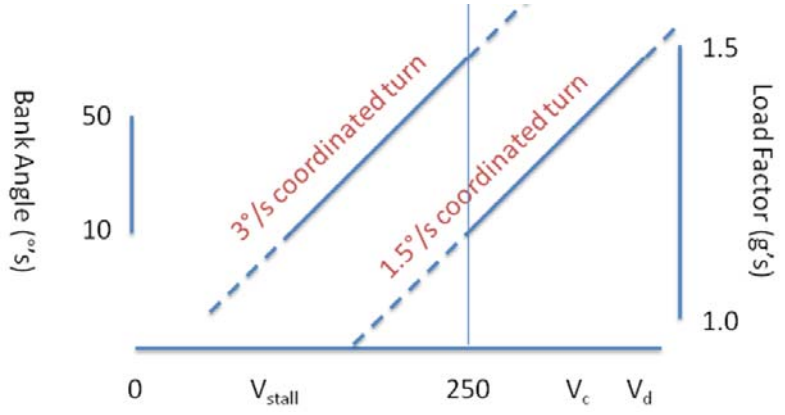

Figure G.10: Load factor required to complete a standard rate turn.

The maximal impact of these changes on aircraft performance occurs when the load factor is reduced to the ideal case. Figure G.11 shows the structural weight and performance benefit associated with N_{max} reduction between current values and the best case scenario. With the ideal case known, the extent of improvements possible can be determined.

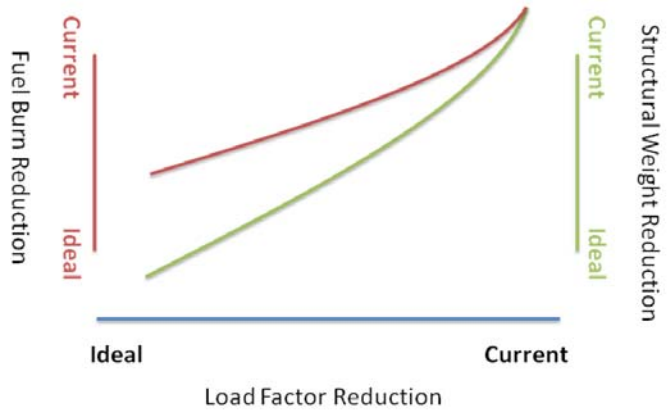

Figure G.11: Load factor reduction corresponds to reductions of structural weight and fuel burn.

To determine the place on the benefits curve the following must be determined. By how much can gusts be reduced? By how much can the flight envelope be reduced? How can the system maintain equivalent statistical reliability to current systems?

FAA regulations illustrate a cosine-shaped gust which is symmetrically distributed across the aircraft, as in Figure G.12. Making the assumption that there is no substantial vertical acceleration to reduce the gust velocity, we will find the worst case peak angle of attack, lift coefficient and load factor. Using simple aerodynamic tools we will determine the maximum ability of the aircraft to reduce its lift coefficient at these angles of attack, and determine a peak load factor when GLA operates instantly and flawlessly. By limiting the actuation rate and simulating imperfect knowledge of gust profiles, we can determine expected performance of the GLA system as a function of its sensing and actuation capability, and thereby understand the g-load reduction that GLA affords. We will then base our reliability calculation for the GLA system on the statistical reliability of both current actuation systems and anticipated gust sensing systems.

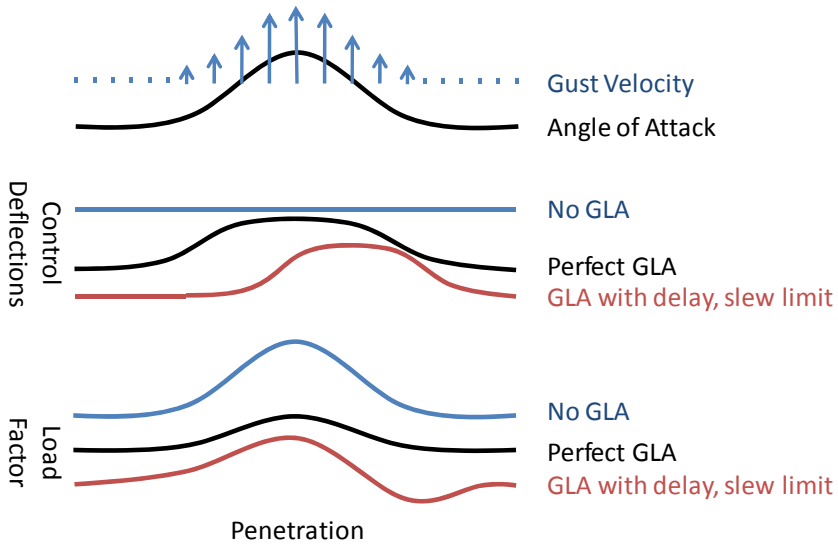

Figure G.12: Penetration through a gust with varying GLA.

The load factor reduction δ available through Envelope Protection and Predictive Path Planning is chosen to provide equal or better reliability than current designs. In this case wing system reliability is the probability that EP and PPP system will fail at the same time as the aircraft has cause to exceed the allowable load factor for its current weight.

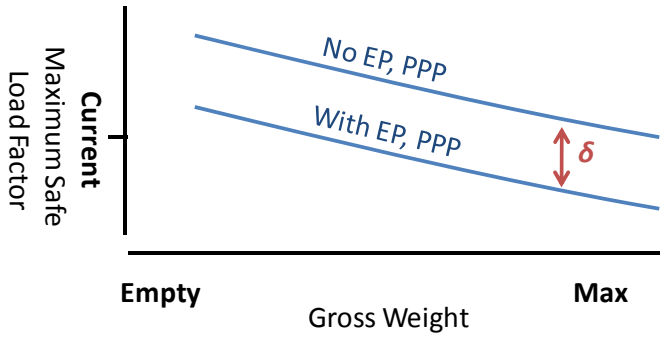

Figure G.13: Maximum safe load factor with and without envelope protection and predictive path planning.

The aircraft's maximum safe load factor is at any moment a function of its gross weight, as seen in Figure G.13. The FAA flight envelope defines the current MTOW safe load factor, and as the aircraft burns fuel and becomes lighter, higher load factors become available. As most flight hours are significantly below MTOW, we can take the statistical weight and corresponding load factors together to determine the fraction of fleet hours at which it is safe to fly at a given load factor. In Figure G.14 we combine this with a probability that the pilot will request of the aircraft each specific load factor, extrapolated from measured FAA maneuvering profiles. We now know the probability that the pilot will request a load factor above what is available for each value of δ. We can calculate for each EP and PPP reliability what the overall system reliability will be as a function of delta, as shown in figure K.

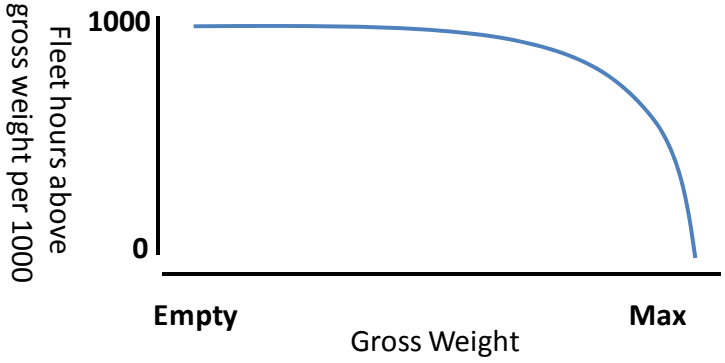

Figure G.14: Statistical observation of fleet gross weight.

With zero reliability (ie, no EP, PPP in place) and δ set to zero, we are reduced to the current case, and find our baseline for reliability. With perfect reliability, load factor reduction can occur all the way to the limit imposed by the pilot's normal maneuvering requirement. An optimum EP and EPP reliability is reached when the current level of wing system reliability can be reached with the maximum reduction in load factor. Any gains beyond this point will not provide further load factor reduction but will instead serve to increase overall wing system reliability. The expected case, however, is that possible EP and PPP reliability lies somewhere between nonexistent and optimal. We can then determine the value of δ possible due to EP and PPP by determining where this curve reaches current system reliability levels.

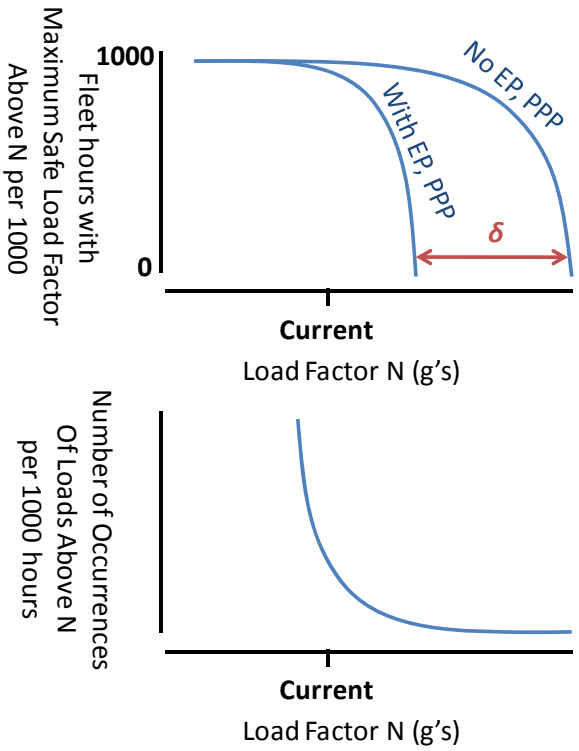

Figure G.15: Fleet hours with maximum safe load factor and number of occurrences above load factor.

When we have calculated the load factor enabled by GLA, EP, and PPP individually we need to determine how their influence together impacts our choice of N_{max}. For a conservative estimate we can choose the value which represents the smaller of the two reductions. Further gains can be made by determining the degree of correlation between GLA, EP and PPP systems, and calculating a probability of failure for all systems together, resulting in a similar plot to Figure G.11.

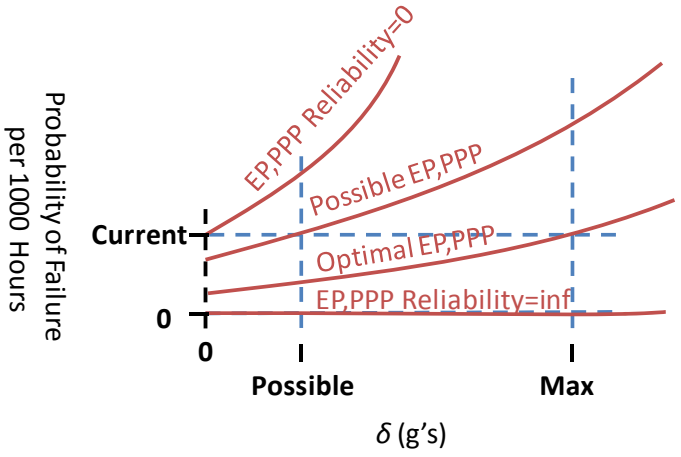

Figure G.16: Envelope protection and predictive path planning load factor trade space.

G.2.3 Structural Health Monitoring

Structural Health Monitoring (SHM) refers not just to detection of change to a material state, but to the broader field of material and load monitoring through the use of multiple sensor types. This encompasses current Health and Usage Monitoring Systems (HUMS) as well as additional flight data readers such as Inertial Measurement Units (IMUs), pressure transducers, Lift Reserve indicators, etc. The data set is used in unison to create an overall structural performance through the life of the aircraft. Using that knowledge, it is possible to create structures that are lighter-weight, with flight envelopes that are determined by the current aircraft capability and environment.

The implications of constant material and load state information can be determined by looking at the reduction in uncertainty in the loading and materials. Additionally, the vehicle can operate under different maintenance directives eschewing scheduled maintenance for condition based maintenance (CBM). This can allow for less stringent fatigue crack-growth minimum crack sizes based on the ability to address cracks in a timelier manner than scheduled maintenance, which means the time in which a crack is allowed to grow to critical size is reduced. Finally, areas that are inaccessible by technicians can be monitored with SHM sensors to reduce the sizing on the components for infinite life and maximum damage tolerance. While the benefits and uses of SHM and load-state monitoring are varied due to the cross-disciplinary nature of the technology, for the NASA N+3 concept vehicles the benefit is constrained to a confidence metric for benefit to the concept. It is expected that by adding SHM and other sensors, the benefits may in fact exceed what is proposed.

The weight of the sensor network will negatively impact the overall structure weight. It is estimated that a typical sensor would weight 0.25 ounces and that 600 sensors would be required to detect material health over the vehicle. Additionally, cabling would weigh 1 pound per 10 yards with a total of 255 yards estimated to run the length of the aircraft, for a total of 35.5 pounds. The load sensors are estimated to be equivalent in mass, making the entire network weight penalty roughly 71 pounds. Additionally, the power requirements of the sensors are estimated to be about 3W (instantaneous peak) per sensor with 750mW average power for a total of 450W (1800W peak).

The weight savings from a material and load monitoring system can be realized in several ways:

- Reduction of material weight in previously inaccessible areas that had previously been designed for safe-flight without inspection.
- Reduction of overall material weight from increased material design allowable strengths as a result of reduced initial and critical flaw sizes.
- Reduction of load environment (e.g. FAR) from increased awareness of actual usage compared with previous design usage.
- Reduction of safety factor due to increased state awareness resulting in less variability.

In order to characterize the weight savings in a more general way, a probabilistic study of the material and loads is devised below to estimate the equivalent reduction in design load factor from SHM.

While traditional design holds the factor of safety between maximum applied loads and minimum residual strength constant for design, the design point can instead be determined by a probabilistic approach, where failure is measured by the probability of the applied load exceeding the structural strength. In this case, the equivalent factor of safety becomes dependent upon the variability and confidence of the load and strength distributions. This methodology allows for technologies that reduce variance of the loads and

strength to reduce the equivalent factor of safety for conditions where current design methodology using a factor of safety of 1.5 is greater than the acceptable failure probability would allow. This shift and the measurement of the failure probability are illustrated below in Figure G.17.

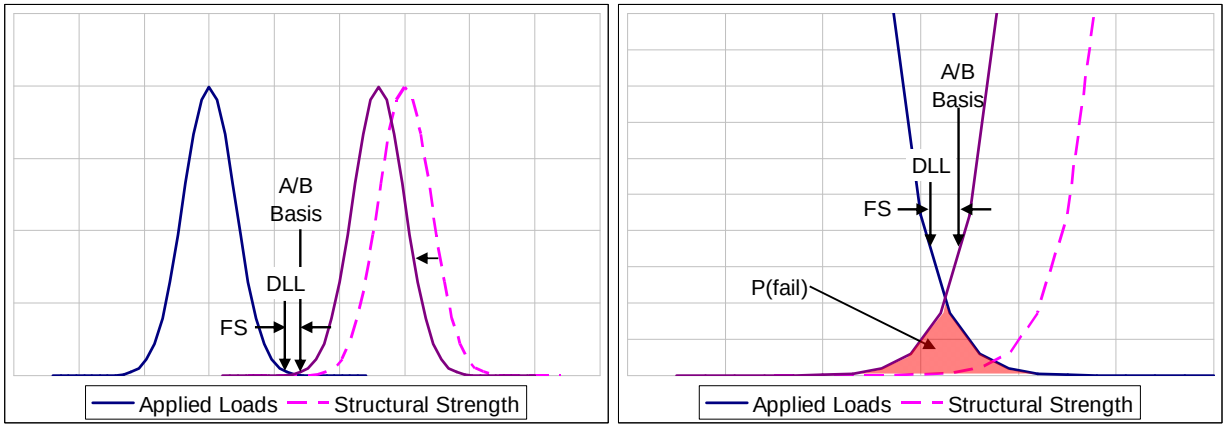

Figure G.17: Probabalistic equivalent factor of safety based on non-deterministic analysis.

If both the applied load and structural strength are assumed to be normal distributions, it is possible to equate the probability of failure to the strength and loads distributions. The probability density function (PDF, denoted ϕ_i) is defined by Equation G.1.

$$\phi_i = \frac{1}{\sqrt{2\pi\sigma_i^2}} e^{\left(-\frac{(x-\mu_i)^2}{2\sigma_i^2}\right)}$$

Equation G.1: Probability Density Function of a Normal Distribution

The PDF for the loading, φ_A, and strength, φ_B, are equal at the intersection of the two curves, which determines the intersection point, x, as shown in Equation G.2 below.

$$\frac{1}{\sqrt{2\pi\sigma_A^2}} e^{\left(-\frac{(x-\mu_A)^2}{2\sigma_A^2}\right)} = \frac{1}{\sqrt{2\pi\sigma_B^2}} e^{\left(-\frac{(x-\mu_B)^2}{2\sigma_B^2}\right)}$$

$$\frac{\sigma_B}{\sigma_A} e^{\left(-\frac{(x-\mu_A)^2}{2\sigma_A^2}\right)} = e^{\left(-\frac{(x-\mu_B)^2}{2\sigma_B^2}\right)}$$

$$\ln\left(\frac{\sigma_B}{\sigma_A}\right) - \frac{(x-\mu_A)^2}{2\sigma_A^2} = -\frac{(x-\mu_B)^2}{2\sigma_B^2}$$

Equation G.2: Intersection of Strength and Loading PDFs

This equation is a quadratic relationship shown in Equation G.3, which can be solved for the intersection point, x.

$$ax^2 + bx + c = 0$$

$$a = \sigma_A^2 - \sigma_B^2$$

$$b = 2\mu_A\sigma_B^2 - 2\mu_B\sigma_A^2$$

$$c = 2\sigma_A^2\sigma_B^2 \ln\left(\frac{\sigma_B}{\sigma_A}\right) + \mu_B^2\sigma_A^2 - \mu_A^2\sigma_B^2$$

$$x = \frac{-b \pm \sqrt{b^2 - 4ac}}{2a} \quad if \quad \sigma_A \neq \sigma_B$$

$$x = -\frac{c}{b} \quad if \quad \sigma_A = \sigma_B$$

Equation G.3: Quadratic Relationship of Strength and Loading PDF Intersection Point

The cumulative density function (CDF) can then be used to determine the probability of the loading exceeding the intersection point, *x*, as well as the probability the strength is less than the intersection point, as shown in Equation G.3. The probability of failure can then be calculated using Equation G.4.

$$\Phi_i = \frac{1}{2}\left[1 + erf\left(\frac{x - \mu_i}{\sigma_i\sqrt{2}}\right)\right]$$

Equation G.4: Cumulative Density Function of a Normal Distribution

$$P_{fail} = \left(1 - \Phi_A\right) + \Phi_B$$

$$P_{fail} = 1 + \frac{1}{2}\left[erf\left(\frac{x - \mu_B}{\sigma_B\sqrt{2}}\right) - erf\left(\frac{x - \mu_A}{\sigma_A\sqrt{2}}\right)\right]$$

Equation G.5: Probability of Failure

For an initial estimate of the equivalent factor of safety, we set the probability of failure to $1 \cdot 10^{-6}$. Also the standard deviations of both the strength and loading will be set equal to each other. This assumption greatly simplifies the relationship shown in Equation G.2, as shown in Equation G.6 below:

$$\sigma_A = \sigma_B = \sigma$$

$$x = -\frac{2\sigma_A^2\sigma_B^2 \ln\left(\frac{\sigma_B}{\sigma_A}\right) + \mu_B^2\sigma_A^2 - \mu_A^2\sigma_B^2}{2\mu_A\sigma_B^2 - 2\mu_B\sigma_A^2} = -\frac{2\sigma^2\sigma^2 \ln\left(\frac{\sigma}{\sigma}\right) + \mu_B^2\sigma^2 - \mu_A^2\sigma^2}{2\mu_A\sigma^2 - 2\mu_B\sigma^2}$$

$$x = -\frac{\mu_B^2 - \mu_A^2}{2\mu_A - 2\mu_B} = \frac{\mu_A^2 - \mu_B^2}{2\mu_A - 2\mu_B} = \frac{\left(\mu_A + \mu_B\right)\left(\mu_A - \mu_B\right)}{2\mu_A - 2\mu_B}$$

$$x = \frac{\mu_A + \mu_B}{2}$$

Equation G.6: Strength and Loading PDF Intersection Point with Equal Standard Deviations

The failure probability can then be further simplified as shown in Equation G.7. Since the current factor of safety is determined by the 3σ offset from the mean on the loading and strength, the equivalent factor of safety can be written using Equation G.8. Table G.3 lists some values of equivalent factor of safety using a unitized mean load and varying the standard deviation while keeping the probability of failure below $1 \cdot 10^{-6}$. The relationship between variance (standard deviation) and factor of safety is quite high, which means that minimizing the variance in both the material strength (e.g. better manufacturing processes) and loading (e.g. health and usage monitoring) becomes a prime way to reduce the safety factor and hence weight of the aircraft.

$$P_{fail} = 1 + \frac{1}{2}\left[erf\left(\frac{\mu_A - \mu_B}{\sigma 2\sqrt{2}} \right) - erf\left(\frac{\mu_B - \mu_A}{\sigma 2\sqrt{2}} \right) \right] \leq 0.0001$$

Equation G.7: Probability of Failure with Equal Standard Deviations

$$FS = \frac{\mu_B - 3\sigma_B}{\mu_A + 3\sigma_A}$$

$$FS = \frac{\mu_B - 3\sigma}{\mu_A + 3\sigma}$$

Equation G.8: Equivalent Factor of Safety

Table G.3: Specific Mean Load and Variance Impact on Failure Probability and Factor of Safety

μ_A	μ_B	σ	P_{fail}	Load	Strength	FS
1	3.94	0.3	0.000000899	1.900	3.040	1.60
1	2.96	0.2	0.000000899	1.600	2.360	1.48
1	2.47	0.15	0.000000899	1.450	2.020	1.39
1	1.98	0.1	0.000000899	1.300	1.680	1.29

A standard deviation of 0.2 coincides with a factor of roughly 1.5, representing the baseline design performed today. Better understanding and increased monitoring of loads and material health will increase the confidence in the loading and residual strength, which could lead to a standard deviation reduction of 0.15, which coincides with a factor of safety of roughly 1.4. This would be equivalent to a design load reduction corresponding to 2.8g from the initial 3.0g pull-up maneuver.

Appendix H: Gas Turbine Engine Weight Estimation

H.1 Introduction

The following appendix gives the methodology and substantiation for gas turbine bare engine weight estimation for the N+3 Phase 1 effort. It begins with an outline of the methodology used to generate weight correlations using the NASA NPSS/WATE++ software as a foundation. The validation procedure is described, followed by the extension of the model to geared fan drive configurations and to advanced materials estimation. The appendix concludes with a summary and recommendations for follow on work.

H.2 Methodology

As outlined in previous sections of this report, the MIT-led N+3 team has created a first-principles based aircraft sizing and performance code for simultaneous weight and performance optimization of potential new technologies. The goal was to build the aircraft weight from basic principles like allowable stress levels, then use an optimizer to choose the best combination of design parameters to minimize the overall fuel burn of the configuration over a given mission. The engine was characterized by a first principles performance model, similar to what is seen in reference texts[1]. However, from an aircraft fuel burn prospective, the engine will tend to want to optimize to the highest bypass ratio possible to maximize propulsive efficiency. In reality, the trend to high bypass ratio is limited by the weight penalty; high bypass ratio engines require large, heavy fans, as well as additional LPT stages to extract the necessary power. The weight modeling for N+3 must take into account the effect of engine design parameters on the weight of the system in order for the optimizer to come up with a reasonable answer.

Typically, the relationship between the weight and design parameters can be inferred from historical data from existing engines. However, this approach is not appropriate for new configurations that are not well represented in the existing fleet. This is the case with some of the concepts that needed to be analyzed in N+3, particularly geared turbofan engine configurations. Only one commercial geared turbofan engine exists in the world today, the Pratt & Whitney PW1000G series engine, which does not give an adequate database to infer the sensitivity of engine weight to the various engine design parameters.

In order to meet the needs of the N+3 program, a more first-principles based assessment of engine weight based on the thermodynamic design of the engine had to be developed. The approach was to use a version of the NASA WATE++ model, first described in a NASA technical document by Onat and Klees[2]. Given some empirical assumptions, WATE provides a framework with which to infer how the thermodynamic design affects the weight of the engine.

The calibrated WATE++ model forms the basis from which bare engine weight is estimated for direct drive and geared fan engine configurations at a variety of bypass ratios. This model also provides insight into the contributions of weight from various engine subcomponents. The subcomponent breakdown allows the effects of weight reduction technology for specific components to be assessed in relation to the engine as a whole.

To improve computational speed and robustness of the aircraft sizing and optimization code, analytic expressions for the weight of current and advanced (low weight) technology turbofans were derived by running the WATE++ model over a wide range of inputs and correlating the results.

---

[1] J.L. Kerrebrock. Aircraft Engines and Gas Turbines, 2nd Ed. The MIT Press, Cambridge, 1996.

[2] E. Onat and W. G. Klees. A method to estimate weight and dimensions of large and small gas turbine engines. NASA/CR 159481, January 1979

H.2.1 WATE++ Model

WATE++ is a software product that builds up the weight of an aircraft gas turbine engine from a combination of first principles based component sizing and historically based component correlations. The original documentation has the detailed description of the various components. Weight Analysis of Turbine Engines (WATE) in its most current implementation interfaces with the NASA NPSS performance simulation for thermodynamic performance computations. An example output of the WATE++ tool is shown in Figure H.1. This section will briefly describe some of the modeling assumption used in the framework.

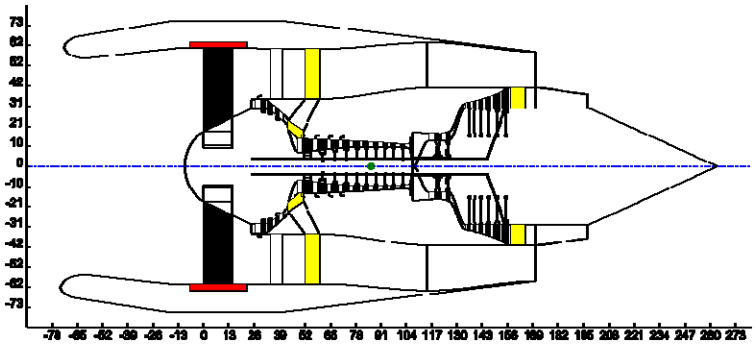

Figure H.1: Example output from WATE simulation.

The weight estimation begins with a detailed, station-by-station, thermodynamic description of the engine. By knowing the pressures, temperatures, and mass flows at each engine station, the cross-sectional area required to satisfy the mass flow continuity can be directly calculated. The weight implications of that cross section area requirement depend on the tip radius, or equivalently the hub-to-tip ratio, for the assumed axisymmetric flow path layout. Using the information, stage by stage weight of the fan, compressors, and turbines can be estimated by characterizing the blading requirements for the flow path, the number of stages, the disks required to support the blades at the max rotational speeds, cases required to support containment and pressure loads, as well as the connecting hardware that holds everything together. Shafts weights are estimated from the thickness required to support the torque load given the radial constraints imposed by the disks. With the exceptions of frames and combustors, most other engine components are treated as a percentage of some other engine components. This is how items like the variable stator vanes are handled. For most components, the weight is estimate by applying a density from a typical component material to a volume estimate for the part in question.

Given the thermodynamic requirements of an engine, the bare engine weight estimate using the WATE methodology is largely a function of the following items:

- Flowpath Mach Number: The thermodynamic state of an engine is described by the stagnation pressure and temperatures at each engine station. The mass flow then sets the dimensional scaling in terms of thrust. However, the Mach number is required in order to calculate the area required to accommodate the flow rate.
- Inlet Hub-to-Tip Ratio for the Fan and HPC: Given the cross-sectional area requirements specified by the mass flow and thermodynamics, this sets the tip radius and span of the initial blades of these machines. From there, the assumption of constant hub, constant tip, or constant meanline can be used to set the flow path shape for the remainder of the machine.
- Airfoil aspect ratio: With the passage height set by the hub-to-tip ratio and the mass flow requirement, the aspect ratio controls the axial length of each blade. WATE defines the aspect

ratio as the span divided by the axial projection of the chord. In WATE++, the user can set the inlet and exit aspect ratios of the rotors and stators of the compressors and turbines separately, and these settings have the largest impact to the estimated length of the engine.

- Blade Volume Factors: WATE uses what is essentially an average thickness to chord parameter to estimate the volume of each blade in a given bladerow, once the passage height and axial chord have been established. Thus, the volume of the blade is estimated as the product of the volume factor, aspect ratio, and the cube of the span, and the weight of each blade is then determined from the material density.
- Blade Solidity: Then given the other blade non-dimensional parameters, the solidity controls the number of blades in a given bladerow. As with the aspect ratio, WATE defines the solidity using the axial projection of the blade chord instead of the chord itself.
- Blade Loading: The enthalpy capability per blade row sets the stage count in the turbomachinery components.

Although actual engines have varying combinations of the aforementioned design parameters, the approach for the N+3 project was to assume that a single set of parameters could be used to define an "average" engine in terms of weight. Therefore, the task for the weight estimation became to find a set of the non-dimensional parameters that allowed the weight a set of known engines to be reasonably approximated. The inputs would all be the same, and the only difference would be the different thermodynamic conditions of the different engines.

H.2.2 WATE++ Model Calibration

The coefficients in the WATE++ were modified so that a common set of parameters could be used to describe a large number of engines. Table H.1 shows the sea level static performance for seven engines that were used to calibrate the WATE++ model. The engines range in bypass ratio from 4.6 to 8.5 and in takeoff thrust from 27000 lbs to 85000 lbs.

Table H.1: Existing Engine Configuration and Sea Level Static Performance

	CFM56-7B27	V2530-A5	PW2037	PW4462	PW4168	PW4090	GE90-85B
W2 (pps)	774	858	1207	1786	2010	2736	3100
BPR	5.0	4.6	5.77	4.6	5.0	6.1	8.5
FPR	1.72	1.77	1.61	1.76	1.75	1.71	1.51
OPR	27.8	32.1	26.4	31.6	32.5	38.6	37.5
CPR	10.3	12.3	10.5	11	9.9	9.9	20.4
N1 (rpm)	5380	5650	4575	4010	3600	3030	2465
N2 (rpm)	15183	14950	12250	10450	10450	10850	10705
Stage Count (FAN/LPC/HPC/HPT/LPT)	1/3/9/1/4	1/4/10/2/5	1/4/12/2/5	1/4/11/2/4	1/5/11/2/5	1/6/11/2/7	1/3/10/2/6
D_{fan} (in)	61	63.5	78.5	94	100	112	123

Weight	5291	5210	7300	9332	11400	15585	17250

Using these engines as baselines, the major calibration parameters for each component were varied until the data reasonably matched each case and the overall breakdown was consistent with the information provided by Pratt & Whitney. The main parameters used in the model are listed in Table H.2.

Table H.2: Calibration Parameters

	Fan	LPC	HPC	HPT	LPT
Mach Number In	0.63	0.4	0.46	0.092	0.2
Mach Number Out	0.4	0.41	0.27	0.27	0.31
1st Stage Hub/Tip Ratio	0.325		0.59		
Rotor Solidity	1.5	1.04	1.1	0.829	1.45
Stator Solidity	1	1.27	1.27	0.763	0.92
Rotor AR in	2.73	1.5 to 2.2*	1.5 to 2.2*	1.0 to 2.0*	1.0 to 8.0*
Stator AR in	4	2.3 to 3.1*	2.3 to 3.1*	rotor / 1.5	rotor / 1.2
Rotor Volume Factor	0.078 to 0.029*	0.06	0.12	0.195	0.045
Stator Volume Factor	0.685 to 0.253*	0.06	0.12	0.195	0.045
Loading (DH/U^2)	~0.25	0.19	0.31	~1.2	1.5
Materials	Ti-17 "Fan Blade Material"	Ti-17	Ti-17 Inconel 718	Hastelloy S Rene 95	Inconel 718 Hastelloy S Rene 95 Udimet 700

*Varies with engine

The two sets of numbers for aspect ratio represent a variation of aspect ratio with span. An attempt was made to calibrate the engine weight model assuming constant aspect ratios for all engines. However, with this approach it became difficult to match weights for both large and small engines. The physical reason for the bad fit is that assuming constant aspect ratio is equivalent to assuming that the blade chord based Reynolds number decreases as the engine size and mass flow decreases. Decreasing Reynolds number decreases engine efficiency, so real engines are designed to attempt to maintain Reynolds number even in the smaller size engines. This leads to smaller aspect ratios in smaller engines. An assumption of constant aspect ratio for both large and small engines leads to an underestimation of the weight of the small engines, or an over estimation of the weight of the large engines. Therefore a variation of aspect ratio with engine size had to be assumed.

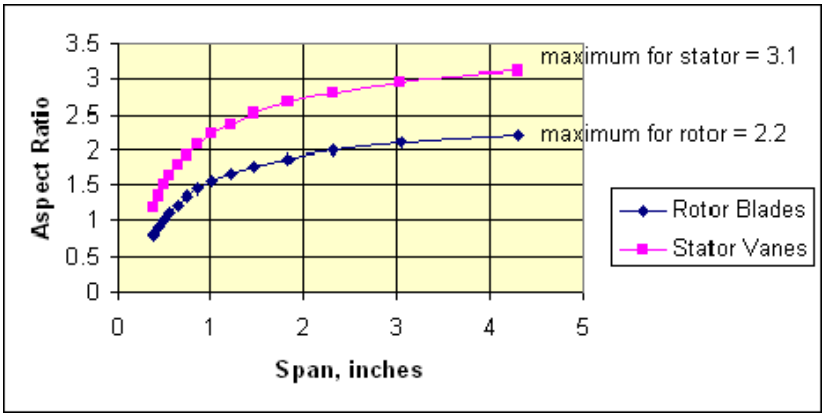

Figure H.2: Compressor aspect ratio variations with span.

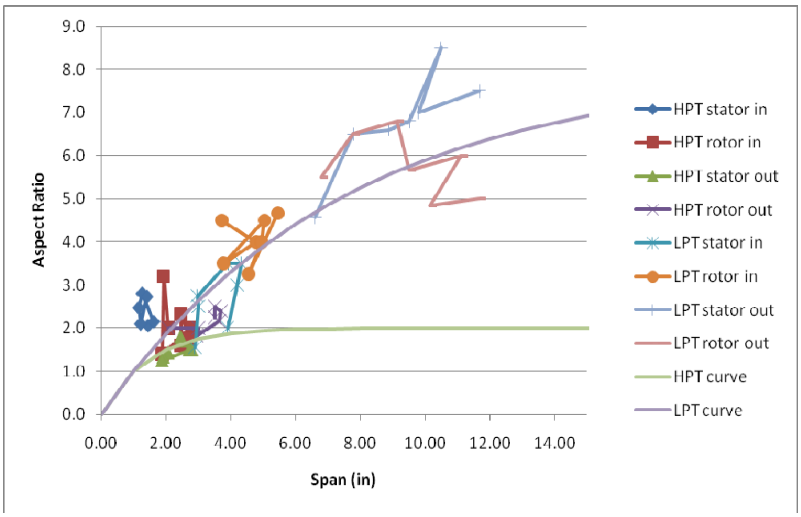

Figure H.3: Turbine aspect ratio from published engine cross-sections.

Figure H.2 and Figure H.3 show the variation of aspect ratio with blade span used in the N+3 implementation of WATE++. The compressor aspect ratio trend was adapted from a previous implementation of WATE, and the turbine trend was generated by examining the published cross-sectional drawings of the seven calibration engines. Both assume aspect ratio is a function of blade span, such that smaller blades tend toward smaller aspect ratios. Distinct correlations are assumed for compressor rotors and stators, HPT blades, and LPT blades.

Using the sea level static thrust performance from Table H.1, the calibration factors from Table H.2, and the aspect ratio variations from Figure H.2 and Figure H.3, the weight of the seven calibration engines was estimated. The comparison to published weight data is shown in Figure H.4 and Figure H.5, dimensionally in pounds and as a percentage of the published weight respectively. In these figures, the blue stars represent the published data and red squares represent the estimated output from the WATE++ based on the given inputs. The green triangles show estimates from a previous regression analysis of many existing engines, and the yellow triangles show the estimates from a correlation generated from WATE++ simulations. The later correlation is used by the TASOPT routine and its generation is described in detail in Section 0.

The WATE++ estimates are within +/- 10% of the published data for all engines examined with the exception of the CFM56-7B27. For that engine, the model under-predicts the weight by 18%. The published bare engine weight of the CFM56 is approximately 1.6% higher than the V2530-A5, but it has only 90% of the published mass flow. Scaling laws dictate that less airflow should correspond to less mass, but the data indicates that the CFM does not follow this trend. It is likely that other design factors such as maintainability and efficiency have made the CFM configuration sufficiently different that it cannot be categorized by the same set of parameters from Table H.2 as the other existing engines. The reasonable agreement of the WATE++ model with the remaining engines gives confidence that the model is sufficient for general turbine engine weight estimation.

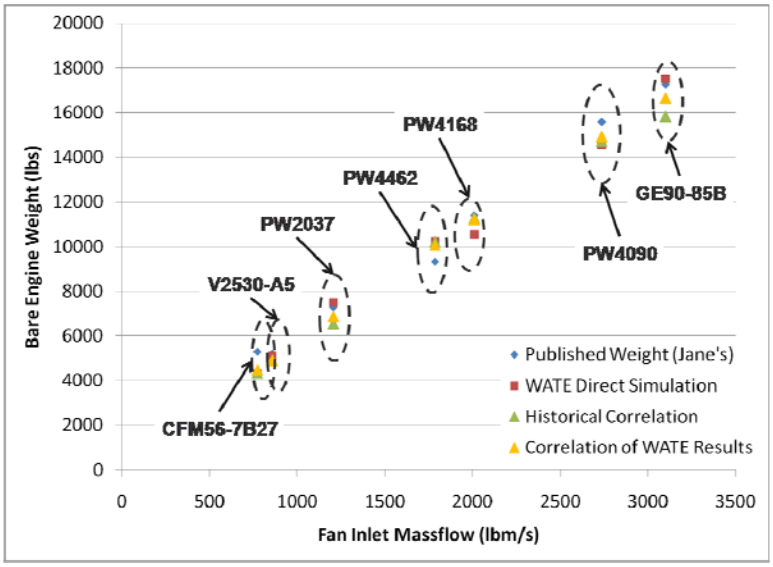

Figure H.4: Dimensional comparison of WATE model and correlations to published engine weights.

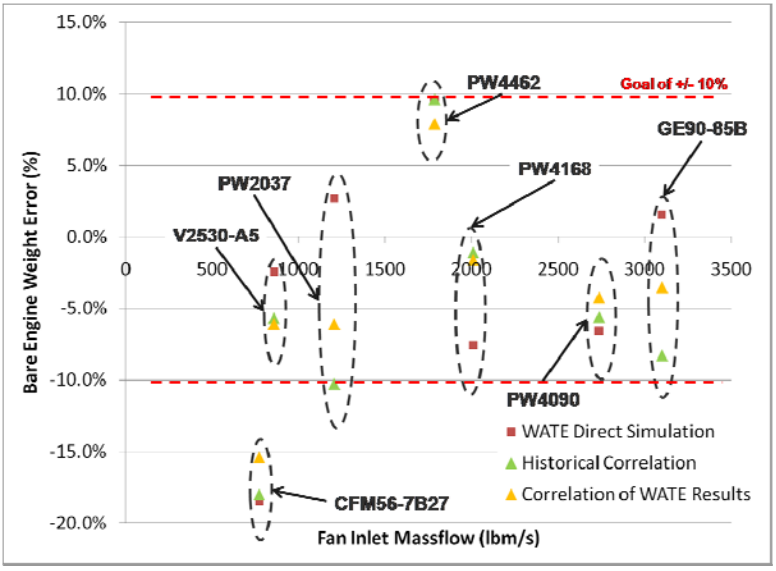

Figure H.5: Comparison of WATE model and correlations as a percentage of published engine weights.

Table H.3 and Table H.4 show the weight breakdowns estimated by WATE++ for each of the seven engines used in the model calibration. The composite breakdowns for the fan, core, LPC, LPT, and accessories are consistent with generic (i.e. not engine-specific) engine breakdowns provided by Pratt & Whitney.

Table H.3: Weight Breakdown Estimates from WATE++ Simulations (all values in lbs.)

	CFM56-7B27	V2530-A5	PW2037	PW4462 (94")	PW4168 (100")	PW4090 (112")	GE90-85B
FAN	**1188**	**1350**	**1925**	**2281**	**2658**	**3906**	**4630**
Rotor blades	337	380	504	541	623	870	996
Stator blades	286	295	534	422	516	811	1432
Containment	294	371	469	748	903	1401	1229
Disk	104	121	150	195	224	301	279
Case	57	63	91	131	148	204	240
DUCT	13	16	20	31	30	32	44
Frame	85	89	135	184	181	240	348
Other	13	14	21	29	33	47	61
LPC	**215**	**204**	**418**	**650**	**670**	**1108**	**1074**
Rotor blades	24	23	56	87	85	134	177
Stator blades	32	34	68	111	111	161	202
Disk	58	58	113	216	234	427	317
Case	57	51	103	134	134	215	217
Frame	0	0	0	0	0	0	0
Other	43	39	78	103	104	170	161
HPC	**419**	**573**	**797**	**1248**	**1161**	**1227**	**2000**
Rotor blades	36	48	82	144	139	137	181
Stator blades	48	63	96	172	163	162	244
Disk	188	275	352	548	484	548	1136
Case	91	115	167	234	227	226	267
DUCT	13	16	20	38	39	45	45
Frame	0	0	0	0	0	0	0
Other	43	55	81	113	109	109	127
Burner	**236**	**282**	**336**	**538**	**521**	**539**	**722**
HPT	**509**	**620**	**857**	**1331**	**1301**	**1299**	**1621**
Rotor blades	28	28	41	74	78	76	58
Stator blades	68	69	99	174	181	176	141
Disk	105	151	228	403	374	381	671
Case	48	51	66	95	96	95	94
Frame	131	175	237	305	298	301	358
Other	105	116	149	214	215	213	216
High Shaft	24	30	36	64	59	58	82
LPT	**969**	**1078**	**1606**	**2173**	**2438**	**3944**	**4701**
Rotor blades	77	86	136	175	189	315	439
Stator blades	79	89	141	183	199	332	462
Disk	179	200	295	358	400	685	873
Case	120	129	188	205	221	352	472
DUCT	41	45	67	93	107	151	185
Frame	103	119	155	304	355	549	477
Other	221	240	352	395	434	723	946
Low Shaft	148	169	271	460	533	836	847
Accessories	**699**	**800**	**1108**	**1532**	**1634**	**2217**	**2659**
Fan Drive Gearbox	**0**	**0**	**0**	**0**	**0**	**0**	**0**
Other	**88**	**100**	**139**	**192**	**205**	**277**	**331**
Grand Total	**4323**	**5008**	**7186**	**9945**	**10587**	**14517**	**17738**

Table H.4: Percentage Weight Breakdown from WATE Simulations

	CFM56-7B27	V2530-A5	PW2037	PW4462 (94”)	PW4168 (100”)	PW4090 (112”)	GE90-85B

FAN	**27.49%**	**26.95%**	**26.79%**	**22.94%**	**25.10%**	**26.91%**	**26.10%**
Rotor blades	7.79%	7.59%	7.02%	5.44%	5.89%	5.99%	5.62%
Stator blades	6.61%	5.89%	7.44%	4.24%	4.87%	5.59%	8.07%
Containment	6.80%	7.41%	6.53%	7.52%	8.53%	9.65%	6.93%
Disk	2.40%	2.42%	2.09%	1.96%	2.11%	2.08%	1.57%
Case	1.32%	1.26%	1.27%	1.32%	1.40%	1.41%	1.35%
DUCT	0.31%	0.32%	0.27%	0.32%	0.29%	0.22%	0.25%
Frame	1.96%	1.78%	1.88%	1.85%	1.71%	1.65%	1.96%
Other	0.30%	0.27%	0.30%	0.29%	0.31%	0.32%	0.35%
LPC	**4.97%**	**4.08%**	**5.81%**	**6.54%**	**6.32%**	**7.63%**	**6.06%**
Rotor blades	0.56%	0.46%	0.78%	0.87%	0.81%	0.93%	1.00%
Stator blades	0.75%	0.67%	0.95%	1.11%	1.05%	1.11%	1.14%
Disk	1.35%	1.17%	1.57%	2.18%	2.21%	2.94%	1.79%
Case	1.31%	1.01%	1.44%	1.34%	1.27%	1.48%	1.22%
Frame	0.00%	0.00%	0.00%	0.00%	0.00%	0.00%	0.00%
Other	1.00%	0.77%	1.08%	1.03%	0.99%	1.17%	0.91%
HPC	**9.70%**	**11.44%**	**11.09%**	**12.55%**	**10.97%**	**8.45%**	**11.28%**
Rotor blades	0.83%	0.96%	1.14%	1.45%	1.31%	0.95%	1.02%
Stator blades	1.11%	1.27%	1.34%	1.73%	1.54%	1.11%	1.38%
Disk	4.35%	5.50%	4.89%	5.51%	4.58%	3.78%	6.41%
Case	2.11%	2.30%	2.32%	2.36%	2.15%	1.56%	1.50%
DUCT	0.31%	0.32%	0.28%	0.38%	0.36%	0.31%	0.25%
Frame	0.00%	0.00%	0.00%	0.00%	0.00%	0.00%	0.00%
Other	1.00%	1.10%	1.13%	1.13%	1.03%	0.75%	0.72%
Burner	**5.45%**	**5.63%**	**4.67%**	**5.41%**	**4.92%**	**3.71%**	**4.07%**
HPT	**11.78%**	**12.38%**	**11.92%**	**13.38%**	**12.29%**	**8.94%**	**9.14%**
Rotor blades	0.65%	0.55%	0.58%	0.75%	0.74%	0.52%	0.33%
Stator blades	1.58%	1.38%	1.38%	1.75%	1.71%	1.21%	0.79%
Disk	2.43%	3.01%	3.17%	4.05%	3.53%	2.62%	3.78%
Case	1.10%	1.03%	0.92%	0.96%	0.91%	0.65%	0.53%
Frame	3.03%	3.50%	3.30%	3.07%	2.82%	2.07%	2.02%
Other	2.43%	2.31%	2.08%	2.16%	2.03%	1.47%	1.22%
High Shaft	0.55%	0.61%	0.49%	0.65%	0.56%	0.40%	0.46%
LPT	**22.41%**	**21.52%**	**22.35%**	**21.85%**	**23.02%**	**27.17%**	**26.50%**
Rotor blades	1.78%	1.72%	1.90%	1.76%	1.79%	2.17%	2.47%
Stator blades	1.83%	1.77%	1.96%	1.84%	1.88%	2.29%	2.61%
Disk	4.15%	4.00%	4.11%	3.60%	3.78%	4.72%	4.92%
Case	2.78%	2.58%	2.62%	2.06%	2.08%	2.42%	2.66%
DUCT	0.96%	0.89%	0.93%	0.94%	1.01%	1.04%	1.04%
Frame	2.38%	2.38%	2.16%	3.05%	3.35%	3.78%	2.69%
Other	5.10%	4.80%	4.89%	3.97%	4.10%	4.98%	5.33%
Low Shaft	3.43%	3.37%	3.77%	4.63%	5.03%	5.76%	4.78%
Accessories	**16.17%**	**15.99%**	**15.43%**	**15.40%**	**15.44%**	**15.27%**	**14.99%**
Fan Drive Gearbox	**0.00%**	**0.00%**	**0.00%**	**0.00%**	**0.00%**	**0.00%**	**0.00%**
Other	**2.04%**	**2.00%**	**1.93%**	**1.93%**	**1.94%**	**1.91%**	**1.87%**
Grand Total	**100.00%**	**100.00%**	**100.00%**	**100.00%**	**100.00%**	**100.00%**	**100.00%**

H.3 Weight Reduction

To estimate the impact of emerging technologies on engine weight, potential weight reductions for individual components were estimated and then recombined to form an estimate for the complete engine. Table H.5 compares current technologies used on different components with emerging technologies for weight reduction. The quantification of the weight impact comes from published papers and presentations from the MTU website, ASME and NASA publications, as well as from communication with Pratt & Whitney subject area experts. The estimates for engines with advanced materials for weight reduction were composed by modifying the WATE++ generated weight breakdowns, such as those seen in Table H.3, by these amounts, and then summing the modified component weights to estimate the bare engine weight of the complete engine.

Table H.5: Technologies for Weight Reduction

Component	Current Technology	Future Technology	Weight Reduction Potential (% of Baseline)	References	Challenges
Shafts	Steel Alloys	Metal Matrix Composites	30% compared to current designs	MTU: Steffens and Wihelm	
Fan Blades	Composite, Titanium	More incorporation of more PMC	40%-45% improvement over Ti forging	MTU: Steffens and Wihelm	FOD, Erosion, Quality Control
Fan Containment	Alloy. Emerging Composite	Composite/Kevlar	30% over alloy hardware	NASA CR-2005-213969	Definition of prime reliable components
Compressor Blades	Titanium, Nickel alloy rear stages, IBR or "blisk" construction	Titanium Aluminide components	30-40% weight reduction current Ti components	MTU: Smarsly 2006 revised from P&W communication	
Compressor Disk	Titanium, Nickel alloy rear stages	Titanium Matrix Composite Rings	20-30% over titanium disks	MTU: Smarsly 2008	Production Cost, Quality Assurance
HPT Blades	Nickel Alloy	CMC	30-40% compared to nickel alloys	P&W communication	Cooling the blades, FOD, creep, matrix fiber reactions
HPT Disk	Nickel Alloy	CMC	30-40% compared to nickel alloys	Pratt recommendation	Disk fracture, creep, matrix-fiber reactions
LPT Blades	Nickel Alloy, Present Day Stage Loading	50% stage loading increase, TiAl or CMC components	30% due to stage loading (non additive) 30% due to TiAl or CMC	ASME GT2003-38374 MTU: Steffens and Wihelm	Maintaining efficiency at higher loading, creep, matrix-fiber reactions
LPT Disk	Nickel Alloy	50% stage loading increase, TiAl or CMC components	30% due to stage loading (non additive) 30% due to TiAl or CMC	ASME GT2003-38374 MTU: Steffens and Wihelm	Creep, matrix-fiber reactions
Fan Drive Gearbox	Baseline	improved materials	25% according to NASA trend P&W suggests 10-15%	NASA/TM-2005-213800 P&W communication	Reliability in the presence of corrosive oil environment
Major frames	Aluminum, Titanium, Nickel	More composites for low temperature, ceramics for higher temperature	20-30% from current designs	P&W communication	
Accessories	Baseline	improved materials	10% over baseline	P&W communication	

H.4 Engine Weight Correlations

H.4.1 Methodology

Rather than run the WATE++ software integrally in the TASOPT routine, correlations were generated from WATE++ simulations to allow a quick weight assessment without the overhead of the larger computational model. Several hundred WATE++ simulations were performed by varying the input parameters to the model. The goal was to perform a regression of the simulation results to generate a simple parametric model of the results. Once complete for the direct drive configuration, the process was then repeated for the geared fan configuration. This allowed separate correlations to be generated for the two distinct transmission systems.

The incorporation of weight reduction technologies was performed by modifying the weight breakdowns for the several hundred WATE++ simulations generated for the direct-drive and fan-drive configurations. The modified breakdowns were re-summed to create the advanced weight estimates. Finally, a regression of those results was performed to generate another set of parametric correlations corresponding to advanced materials in each configuration.

A number of assumptions were made concerning the input performance parameters for the hundreds of WATE++ simulations. Sea level static bypass ratio, overall pressure ratio, and core inlet mass flow was varied over a range of values to generate a diverse set of input for the model. Other inputs were synthesized or assumed. Fan pressure ratio was set at the value that would equalize the jet velocities of the bypass and the cores streams at a 35,000 ft, Mach 0.8 cruise condition for the same bypass ratio. However, a maximum FPR of 1.8 was enforced to prevent the need for multiple fan stages. The split in pressure ratio between the LPC and the HPC was calculated by assuming that the HPT pressure ratio remained constant at 15. In other words, variation in OPR was assumed to be the result of varying LPC pressure ratio alone. Turbine inlet temperatures were held constant at 3000 deg-R for all case, and cooling flow requirements were calculated assuming a fixed function of turbine inlet temperature and compressor exit temperature. These set the thermodynamic inputs to the NPSS model providing the individual cycle details to WATE++.

H.4.2 Direct Drive Bare Engine Weight

To develop the correlations for direct drive bare engine weight, 432 WATE++ simulations were run. Bypass ratio was varied from 4 to 20, fan inlet corrected mass flow was varied from 500 to 3000, and overall pressure ratio was varied from 25 to 60. An acceptable correlation for weight was found when a power law regression for core flow and overall pressure ratio was performed at each bypass ratio. The correlation coefficients for each bypass ratio were then fit to a polynomial, and the polynomial coefficients were then optimized to ensure that the correlated coefficients worked well at all bypass ratios. This process was performed on both the current and advanced technology data sets. The resulting correlations are presented below.

$$W_{direct,lbs} = a\left(\frac{\dot{m}_{core}}{100lbs/s}\right)^{b}\left(\frac{OPR}{40}\right)^{c}$$

- Current technology (late 1990's through mid 2000s)

$$a = \left(1.809\times10^{1}\right)BPR^{2} + \left(4.769\times10^{2}\right)BPR + 701.3$$
$$b = \left(1.077\times10^{-3}\right)BPR^{2} - \left(3.716\times10^{-2}\right)BPR + 1.190$$
$$c = \left(-1.058\times10^{-2}\right)BPR + 0.326$$

- Advanced materials (including carbon composites, CMC, MMC, and TiAl)

$$a = \left(1.538\times10^{1}\right)BPR^{2} + \left(4.011\times10^{2}\right)BPR + 631.5$$
$$b = \left(1.057\times10^{-3}\right)BPR^{2} - \left(3.693\times10^{-2}\right)BPR + 1.171$$
$$c = \left(-1.022\times10^{-2}\right)BPR + 0.232$$

Figure H.6 shows the correlation error between the WATE++ simulation outputs and the above correlations. The correlations match the WATE++ results to within +/-10% for all conditions run.

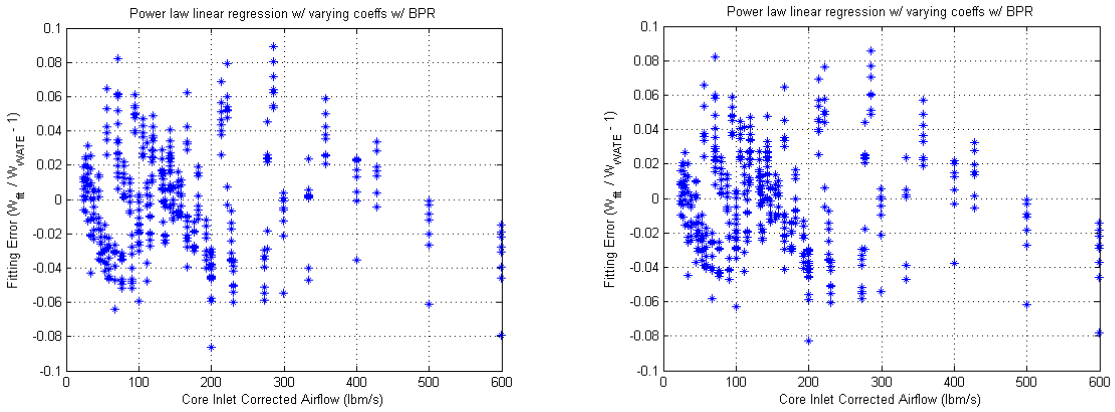

(a) Current Technology **(b) Advanced Materials**

Figure H.6: Regression fitting error for weight correlations based on direct drive WATE++ simulations.

H.4.3 Geared Fan Weight

To develop the correlations for geared turbofan engine weight, 1152 WATE++ simulations were run. Bypass ratio was varied from 4 to 50, and the mass flow and overall pressure variations were the same as for the direct drive case. Again, a power law regression for core flow and overall pressure ratio was performed at each bypass ratio and the correlation coefficients for each bypass ratio were then fit to a polynomial. As with the direct drive correlation, the polynomial coefficients were then optimized to ensure that the correlated coefficients worked well at all bypass ratios. This process was performed on both the current and advanced technology data sets. The resulting correlations are presented below.

$$W_{geared,lbs} = a\left(\frac{\dot{m}_{core}}{100lbs/s}\right)^{b}\left(\frac{OPR}{40}\right)^{c}$$

- Current technology (late 1990's through mid 2000s)

$$a = \left(-6.590\times10^{-1}\right)BPR^2 + \left(2.928\times10^{2}\right)BPR + 1915$$
$$b = \left(6.784\times10^{-5}\right)BPR^2 - \left(6.488\times10^{-3}\right)BPR + 1.061$$
$$c = \left(-1.969\times10^{-3}\right)BPR + 0.0711$$

- Advanced materials (including carbon composites, CMC, MMC, and TiAl)

$$a = \left(-6.204\times10^{-1}\right)BPR^2 + \left(2.373\times10^{2}\right)BPR + 1702$$
$$b = \left(5.845\times10^{-5}\right)BPR^2 - \left(5.866\times10^{-3}\right)BPR + 1.045$$
$$c = \left(-1.918\times10^{-3}\right)BPR + 0.0677$$

(a) Current Technology **(b) Advanced Materials**

Figure H.7 shows the correlation error between the WATE++ simulation outputs and the above correlations. The correlations match the WATE++ results to within +/-11% for all conditions run.

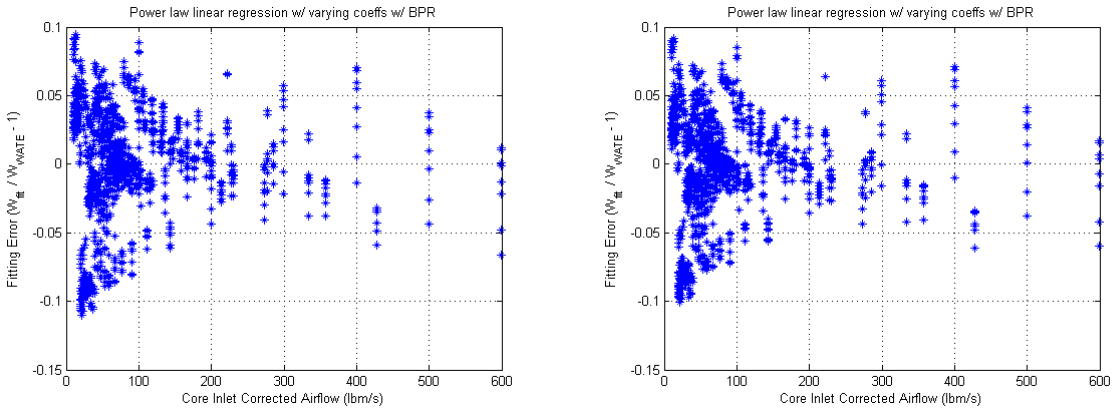

(a) Current Technology **(b) Advanced Materials**

Figure H.7: Regression fitting error for weight correlations based on geared fan drive WATE++ simulations.

As a check on the validity of the geared turbofan weight estimate, the current technology correlation above was compared to current estimates of the PW1000G turbofan engine. The engine provides 23,300 lbs thrust at sea level, has a 73 inch fan diameter, and the total propulsion system weight is expected to be approximately 7000 lbs. Based on this information, a basic cycle analysis, and a scaled weight estimate for nacelle and nozzle from an analysis presented by Benzakin[3], an estimate was made for bare engine weight of the PW1000G and compared to the WATE++ based correlation. The data and results are shown in Table H.6. The correlation weight matches the estimated bare engine weight to approximately 1%, giving confidence that the first-principles based weight buildup in the WATE++ simulation accurately reflected the key weight drivers for a geared fan configuration.

Table H.6: PW1000G Weight Estimate Compared to WATE++-Based Correlation

PW1000G Propulsion System Weight	7000 lbs
Estimated Nacelle and Nozzle Weight for 73” Fan Diameter	2394 lbs
Estimated PW1000G Bare Engine Weight	4606 lbs
WATE++ Based GTF Bare Engine Weight BPR = 12, OPR = 45, W2R = 1128	4659 lbs

H.4.4 Engine Length

As part of the first principles weight buildup in the WATE++ simulation, engine length is also estimated. The model was not specifically calibrated for length against existing engines, but the basic physics for flow cross sectional area and stage count should capture the variation of engine length with the key parameters. These correlations are not used in any part of the TASOPT routine, but rather are checked to provide a starting estimate for engine length in offline analyses. The correlations were formed in the same

[3] Benzakein, M. J., “Propulsion Strategy for the 21st Century: A Vision into the Future,” *Proceedings of International Symposium on Airbreathing Engines*, ISABE 2001-1005, AIAA, Reston, VA, 2001

manner as the direct drive and geared fan weight correlations, by fitting power law regressions to the length outputs from WATE++ at various bypass ratios and then fitting those correlations parameters to polynomials. No attempt was made to estimate the effect of future technology on the length of the engine. The resulting correlations are presented below.

$$L_{eng,in} = a\left(\frac{\dot{m}_{core}}{100lbs/s}\right)^{b}\left(\frac{OPR}{40}\right)^{c}$$

- Direct drive bare engine length

$$a = \left(6.156\times10^{2}\right)BPR^{2} + \left(1.357\times10^{1}\right)BPR + 27.51$$
$$b = \left(6.892\times10^{-4}\right)BPR^{2} - \left(2.714\times10^{-2}\right)BPR + 0.505$$
$$c = 0.129$$

- Geared fan drive bare engine length

$$a = \left(-1.956\times10^{-2}\right)BPR^{2} + \left(1.244\times10^{0}\right)BPR + 77.1$$
$$b = \left(7.354\times10^{-6}\right)BPR^{2} - \left(3.335\times10^{-3}\right)BPR + 0.388$$
$$c = -0.032$$

(a) Direct Drive **(b) Geared Fan Drive**

Figure H.8 shows the correlation error between the WATE++ simulation outputs and the above correlations. The correlations match the WATE++ results to within +/-15% for the direct drive and within +/-9% for the geared fan configuration.

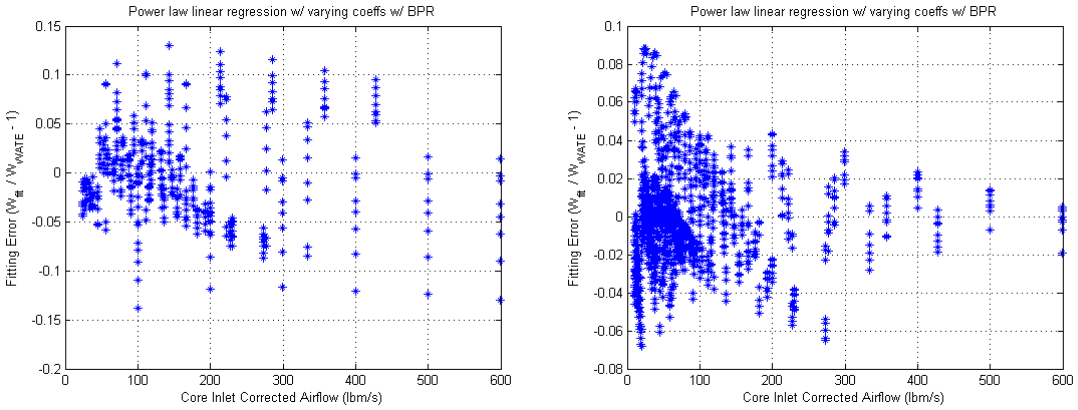

(a) Direct Drive **(b) Geared Fan Drive**

Figure H.8: Regression fitting error for length correlations based on WATE++ simulations

H.5 Summary

The goal of the bare engine weight modeling for the N+3 project was to incorporate the effects of key propulsion thermodynamic design parameters, particularly bypass ratio and mass flow, into the weight estimation for the engine. This was important to prevent the aircraft optimization routines (HWBOpt or TASOPT) from choosing unreasonable combinations of engine thermodynamic design parameters, and

was particularly required to understand the impact of the fan drive configuration on the optimum engine selection.

The approach was to conduct a first-principles weight build up based on flow area, staging, spool speed, and other requirements using the NASA NPSS/WATE++ software. This required several inputs to be estimated, in particular the blade solidities, aspect ratios, loading parameters, thickness to chord ratios, axial Mach numbers, and hub-to-tip radius ratios. The MIT N+3 team took the approach of calibrating these inputs to values that reasonably matched a set of existing engines. Weight estimates for various engines could then be created by leaving these input values fixed while varying the thermodynamic design parameters. A set of inputs to the WATE++ model were found that matched a selected set of seven engines ranging in thrust from 27,000 lbs to 90,000 lbs to within +/-10% with one noted exception.

Rather than using WATE++ directly in the TASOPT routine, the WATE++ model was used to generate analytic expressions for bare engine weight as functions of mass flow, overall pressure ratio, and bypass ratio. This choice was made to improve the speed and robustness of the aircraft optimization. The expressions were formed by running the WATE++ model over a range of the thermodynamic design conditions and then performing a regression to fit the data to power series law. This process was performed separately for direct drive and geared fan engine configurations, and the resulting regressions were accurate to approximately 11% compared to the WATE++ simulations. The analytic expression for geared turbofan weight was shown to agree well with estimates for the PW1000G, the only existing geared fan engine to date.

Estimates for the effect of using advanced materials on engine weight were created by modifying specific portions of the weight breakdown from the WATE++ simulations, re-summing the components, and performing another regression to develop a new analytical expression. Advanced material estimates derived from the available literature and communication Pratt & Whitney lead to correlations that show a 15%-20% improvement in weight for a given fan drive configuration over the next 25 years.

The correlations produced from the WATE++ simulations provide accurate weight estimates for the Phase 1 initial aircraft sizing and optimization. There are, however, some noted drawbacks to the approach that could be improved should further detail be required. In particular, engine tip speeds, aspect ratios, Mach numbers, and other parameters are typically designed to balance component efficiency and weight, and the current approach does not reflect design trades in those objectives. The WATE++ model was calibrated by assuming the sizing parameters of aspect ratio, Mach number, solidity, etc, are similar among engines, but in actuality they vary according to the balance with efficiency required for that particular engine design. Follow on work could include linking the component efficiency of the thermal model and the to the weight assessment for an even more integrated understanding of the effects on aircraft utility.

Appendix I: HWBOpt Optimization Model

I.1 Problem Definition

The general design optimization problem for objective function f can be written as:

$$\begin{aligned} &\text{minimize } f(\boldsymbol{x}) \\ &\text{subject to} \quad g_j(\boldsymbol{x}) \leq 0 \qquad j = 1, \ldots, m_1 \\ &\qquad\qquad h_k(\boldsymbol{x}) = 0 \qquad k = 1, \ldots, m_2 \\ &\qquad\qquad x_i^{min} \leq x_i \leq x_i^{max} \quad i = 1, \ldots, n \end{aligned}$$

where, $\boldsymbol{x} \in \mathbb{R}^n$ is the vector of design variables bounded by $\boldsymbol{x}^{min}, \boldsymbol{x}^{max} \in \mathbb{R}^n$. $g_j(\boldsymbol{x})$ and $h_k(\boldsymbol{x})$ are the set of $m\ (= m_1 + m_2)$ inequality and equality constraints.

I.2 Objective Function

The objective function for the HWB aircraft is the PFEI computed at the maximum design payload and range, which also partially addresses emissions implicitly. Noise analysis from all sources at all design segments is computationally prohibitive since it requires detailed off-design engine cycle analysis, aircraft trim computation and noise analysis. Instead, the airframe approach noise is computed and examined as a second objective. This improves design for reduced stall speed since approach speed is set as 1.23 x stall speed. Because decreased wing loading by increasing wing area (and consequently drag) can also be used to lower the aircraft stall speed there is a potential tradeoff between airframe noise and cruise performance. Designs are not explicitly optimized for NOx (or other emissions) and the goal is addressed at a higher level through architecture, fuel and technology selection.

$$f(\boldsymbol{x}) = \begin{bmatrix} \text{PFEI @ Max. Design Payload and Range} \\ \text{Approach Airframe Noise} \end{bmatrix}$$

I.3 Design Variables

The PFEI is a non-linear function of the airframe geometry, propulsion system and flight mission which form the optimized design variables. The approach noise is governed by the wing-loading and the approach profile, which are also governed by the same variables. Design variables that would be optimized to $\pm\infty$ or specified bounds (eg. material strength, density, etc.) are excluded. These only scale the objectives and are preset for the specified technology level and timeframe.

$$\boldsymbol{x}_{airframe} = \begin{bmatrix} \text{span} \\ \text{xle3} \\ \text{xle5} \\ \text{ale1} \\ \text{cho5} \\ \text{cho9} \\ \text{twst0} \\ \text{twst1} \\ \text{twst2} \end{bmatrix}$$

$$\boldsymbol{x}_{operation} = [h_{CBE}] \quad \text{Cruise Begin Altitude}$$

$$\boldsymbol{x}_{engine} = \begin{bmatrix} FPR \\ OPR \\ T_{t4}/T_{t2} \\ Prop \end{bmatrix} \begin{matrix} \text{Fan Pressure Ratio} \\ \text{Operating Pressure Ratio} \\ T_{t4}/T_{t2} \text{ Take-Off and Cruise} \\ \text{Propulsion System Configuration} \end{matrix}$$

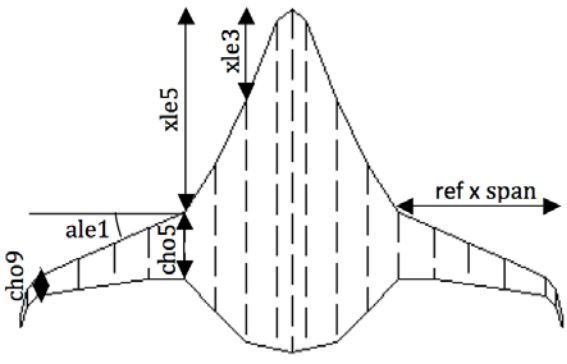

The HWB planform is specified here using 6 parameters that uniquely specify the outer-wing planform and allow partial modification of the centerbody. The scale of the centerbody is set by the fixed geometry of the cabin box. The 9% thick supercritical airfoil also evaluated for the D-series is used whereas centerbody and transitional airfoils from the Silent Aircraft Initiative are retained. The overall spanwise twist distribution is specified as piecewise linear and specified by 3 additional parameters. The twist distribution is scaled during the design process to achieve desired lift and static longitudinal stability characteristics. The engine cycle can be uniquely specified by 4 engine parameters at the design point (*OPR*, *FPR*, T_{t4}/T_{t2}, *Prop*) plus the BBR and cooling flow rate. *Prop* specifies the propulsion configuration from a list which includes all the permutations on number of fans, cores and transmission systems being considered. The *BPR* for minimum SFC is computed by solving an optimization sub-problem during the engine design process. T_{t4}/T_{t2} at takeoff is set to its cruise value assuming the use of variable area inlets and used to compute the required cooling flow rate. This assumption is relaxed post optimization to reduce takeoff noise. Since performance during the cruise flight segment has the largest impact on the PFEI, start of cruise altitude h_{CBN} is also parameterized. The end of cruise altitude h_{CBN} can then be computed for minimum fuel burn cruise-climb.

I.4 Design Parameters

The design parameters are the quantities that affect the objective function but are preset to the desired values based on design choices or *a priori* knowledge. The scale of the centerbody needs to be preset based on the cabin box design. The number of passengers is not a design variable since automated cabin design for the HWB airframe is complicated by the unconventional interior geometry. Range is set by the payload in order to compare to existing aircraft. The cruise Mach number is fixed based on a Boeing CFD study on the drag divergence Mach number of the Silent Aircraft. The fuel can be selected to be either conventional Jet A or Liquefied Natural Gas. The latter enables turboelectric propulsion options with cryogenic cycles and laminar flow on the bottom of the outer wing, however requires additional volume, additional insulation weight and risk. Another parameter is the overall technology level, which can be set to current or advanced. The former is based efficiency and weight estimation models for present day propulsion systems and airframe structures whereas the latter is based on predicted values for the N+3 timeframe.

I.5 Design Constraints

Since the airframe planform geometry and twist distribution are design variables, static stability of the aircraft is enforced through constraints on the static margin. The cruise angle of attack and consequently the cabin floor angle are also constrained for passenger comfort. The multiplex operational scenario requires utilization of existing secondary airports with runway length and taxiway width constraints that are also enforced based on ICAO standards. Additional constraints are incorporated to ensure valid planform geometries and computation within the permissible modeling fidelity.

$$g(x) = \begin{bmatrix} \text{Static Margin} \geq 5\% & \text{Static Stability} \\ -3 < \text{Cabin Floor Angle} < 3 & \text{Passenger Comfort} \\ -1 < \text{Root Twist} < 1 & \text{Passenger Comfort} \\ \text{Span} \leq 52m \text{ or } 65m & \text{Airport Requirements} \\ \text{Balanced Field Length} \leq 5000, 6000 \text{ or } 7000ft & \text{Airport Requirements} \\ \text{Maximum delta Pressure Coefficient} \leq 1 & \text{Modelling Fidelity} \end{bmatrix}$$

$$h(x) = [\ ]$$

I.6 Optimization Method

Manual exploration and gradient based optimization for the HWB design revealed extreme sensitivity of the objective function to the starting guess for the solution. Optimal solutions at different aircraft scales were also observed not to be within some local vicinity of each other. This indicated the problem to be highly non-linear, as expected for the multidisciplinary analysis, with gradient based optimization approaches yielding only local optima in a small neighborhood of the starting solution. Also, since the HWB design landscape including propulsion options is largely uncharted, the approach requires focuses on global optimization.

The vast design space is characterized with islands of feasibility created by imposing stability and sizing constraints on the airframe combined with the exploration of an exhaustive set of propulsion configurations and cycles. Infeasibility is also exaggerated by the inability of the individual design modules to run for all cases resulting in lack of convergence and no measure of the objective in those cases. Since the gradient/hessian information required for most deterministic approaches is not available as part of the design computation, the inability to converge several cases hinders its estimation in those regions. The inclusion of discrete propulsion configuration choices results in a mixed-integer programming problem that is also known to generally be NP-hard (non-deterministic polynomial-time hard). The lack of *a priori* knowledge of the target design space for the non-linear problem favored the use of a stochastic approach. The multi-objective nature favored a population-based search in order to better sample the design landscape and generate the Pareto front simultaneously. Based on these considerations, a hybrid multi-objective genetic algorithm is utilized with initial designs chosen using uniform Monte Carlo sampling of the design space.

The genetic algorithm (GA) is a particular class of Evolutionary Computation (EC) inspired by evolutionary biology. Though several optimization methods are ill-suited to this problem, it is also acknowledged that there is no theoretical basis for assuming that EC algorithms will have superior computational performance to other viable methods (eg. Multistart algorithms). However, GA's have in practice been successfully employed here and observed to perform robustly over different aircraft scales and the evolution of HWBOpt design modules. Additionally, the algorithm is easily parallelizable to compensate of for any undue computational burden.

The elitist single-objective GA optimizes a population of N individuals (containing N_e elites) over k successive generations of evolution, until fitness is optimized by meeting some ad-hoc convergence criteria. This process is illustrated through the simplified pseudo code below:

```
Initialization: Select initial population of N individuals
Evaluate fitness of each individual
for i = 1, 2, ..., k generations
  Elitism: Retain N_e fittest individuals from previous generation unaltered
  Selection: Stochastic fitness based picking of a portion of the population for breeding
  Crossover: Recombination of selected parents to generate children
  Mutation: Maintain genetic diversity by randomly altering some individuals
  Evaluate fitness of each individual in new population of size N
  Convergence criterion   overall fitness, time limit, etc.
```

The individuals in the population are represented by chromosome strings of fixed length. A common choice is encoding the design parameters into binary (0,1) strings of length B.

$$x = [x_1\ x_2\ \ldots\ x_n] \rightarrow \underbrace{011010\ \ldots\ 1010}_{\text{length } B}$$

The total number of unique populations attainable by a binary encoded population of size N is given by:

$$N_p = {}^{N+2^B-1}C_N = \frac{(N+2^B-1)!}{(2^B-1)!\,N!}$$

By discretizing the solution space to desired precision $\epsilon \gg \epsilon_{machine} \Rightarrow B \ll B_{single\ precision}$, the resulting solution subspace can be significantly smaller than if represented in single precision floating point. This subspace still contains the optimal solution (up to the desired accuracy) and can be more efficiently searched. Since the solutions of this problem are not required up to machine single precision, binary encoding is favored to alternative real-valued encodings.

Consider the Markov transition matrix $\mathcal{P} \in \mathbb{R}^{N_p \times N_p}$, where $\mathcal{P}_{ij}$ is the probability of transitioning from the ith population to the jth population. Proof of convergence by Markov chain analysis requires that the chain is ergodic and irreducible (any state is accessible from any state). Since N_p is typically large, $\mathcal{P}$ cannot be explicitly computed in practice. However, Rudolph[1] proved that in general, the canonical GA without elitism is provably non convergent, since the optimal solution, if found, could be lost through crossover and mutation. Hence an Elitist GA is used, with $N_e = 2$ for all single objective applications.

Though, global convergence is not guaranteed for the GA, the size of the population can be used to encourage global search and produce better results in practice. The minimum size of the initial binary encoded population required to make every point in the resulting subspace reachable with probability P $(= 99.99\%)$, by crossover alone, is given by Reeves[2] as:

$$N \approx \lceil 1 + \log(-B/\log P)/\log 2 \rceil$$

This population size grows as $\mathcal{O}(\log B)$, which implies lower computation cost compared to the general higher cardinality q-ary alphabet $(q > 2)$ encoding where the population size grows linearly with q. It is also noted that this estimate is typically significantly lower than the common rule of thumb where $N \approx 4B$. The algorithm implementation uses intermediate population sizes typically selected to balance computational cost per generation with the number of generations of evolution required for convergence.

Ideally, individuals in the initial population would be seeded with solutions in the vicinity of the global optimal or normal distributions of design variables based on apiori knowledge of optimal variable means and distributions. Since neither is typically available for most design cases, the initial population is created by constrained random search. This Monte Carlo approach random searches the design space, partially constrained for airframe geometric feasibility. Samples (feasible or infeasible) with converged solutions are retained and the population size is adjusted to maintain uniform sampling of each variable.

The non-linear constraints in the problem are incorporated using an exterior quadratic penalty method to penalize constraint violations through the objective function.

$$\text{minimize } \mathcal{J}(x) = f(x) + \sum_{j=1}^{m_g} M_{1j} g_j^2(x) + \sum_{k=1}^{m_h} M_{2k} h_k^2(x)$$

[1] Rudolph, G., "Convergence Analysis of Canonical Genetic Algorithms," IEEE Transactions on Neural Networks, vol. 5, pp. 96-101, 1994.

[2] Reeves, C.R. and Rowe, J.R., "Genetic Algorithms – Principles and Perspectives: A Guide to GA Theory," Kluwer Academic, Boston, 2003.

$$\text{subject to} \quad x_i^{min} \leq x_i \leq x_i^{max} \qquad i = 1,\ldots,n$$
$$M_{1f}\begin{cases} = 0, & g_f(x) \leq 0 \\ \gg 0, & g_f(x) > 0 \end{cases} \qquad f = 1,\ldots,m_1$$
$$M_{2k}\begin{cases} = 0, & h_k(x) = 0 \\ \gg 0, & h_k(x) \neq 0 \end{cases} \qquad k = 1,\ldots,m_2$$

In the limit $M \to \infty$, this approach converges to original formulation, however, it allows relative weighting of different constraints and relaxes strict enforcement of feasibility. This also allows quantification of relative fitness J of all individuals in the population, taking into account feasibility.

The procedure for picking individuals for crossover is tournament selection. Two individuals are selected at random and the fitter of the two is selected to be a parent. The deterministic outcome of the tournament favors fitter individuals while stochastic selection of competitors helps maintain genetic diversity. According to Spall[3], empirical evidence suggests tournament selection performs better than roulette selection, another popular option. The selected parents reproduce by single-point crossover, where genetic material is swapped at a randomly selected crossover point as illustrated below.

$$\underbrace{110|010110 \oplus 010|100100}_{\text{Parents}} \rightarrow \underbrace{110|100100 \text{ and } 010|010110}_{\text{Children}}$$

In order to expand the search beyond interpolations of the initial design, chromosomes are randomly mutated. This is done by flipping bits of the chromosome of a few individuals with a probability P_m. Using the Markov chain analysis Rudolph[4] proved convergence of the GA for $0 < P_m < 0.01$. Since the problem is highly non-linear, we select $P_m = 0.0099$ to allow more global search and be within the rule of thumb bound of $P_{max} = 0.05$.

The stopping criterion for the GA is not well defined since the KKT conditions are not applicable. Hence stagnation is typically considered convergence i.e. none or marginal improvement of objective over successive generations.

The multi-objective implementation is identical to the single objective formulation with the exception that designs are checked for local Pareto optimality. Additionally Pareto optimal designs are designated elite and retained until superseded. The hybrid nature of the algorithm incorporates gradient based Sequential Quadratic Programming (SQP) in the initial population sampling and also for refinement of the Pareto front to ensure thorough local search.

I.7 HWBOpt Aerodynamic Model Validation

The HWBOpt aerodynamic model consists of a quasi-3d approach, evolved from the model used to assess the Silent Aircraft[5,6] and N2A/N2B[7] airframes. The airframe lift distribution, induced drag and neutral

---

[3] Spall, J.C., "Introduction to Stochastic Search and Optimization: Estimation, Simulation, and Control," Wiley, Hoboken, NJ, 2003.

[4] Rudolp, G., "Convergence Properties of Evolutionary Algorithms," Verlag, Kovac, Hamburg, 1997.

[5] Hileman J., Spakovsky Z., Drela M. and Sargeant M., "Airframe design for "Silent Aircraft"," AIAA-2007-0453, 45th AIAA Aerospace Sciences Meeting and Exhibit, Reno, NV, 2007.

[6] Hileman J., Spakovsky Z., Drela M., Sargeant M. and Jones A., "Airframe Design for Silent Fuel-Efficient Aircraft," Journal of Aircraft (to be published)

point are computed for each lofted airframe (including twist and control surface deflection) using a vortex-lattice analysis performed using AVL[8]. AVL uses a Prandtl-Glauert correction which captures compressibility effects but is limited to wing-perpendicular Mach numbers below the transonic regime. Profile, viscous and wave drag for the outer wing supercritical airfoil is computed offline using MSES[9] at the cruise Mach number and a representative Reynolds number. The resulting polar is integrated as a lookup table with drag as a function of sectional lift and sweep. This 2-D approach is not applicable for the centerbody due to the 3-D nature of the flow field, where aerodynamic performance is estimated using Hoener[10]. The centerbody profile and viscous drag is computed using Hoerner correlations for bodies of revolution with lift coefficient dependence.

Boeing CFD study was performed on the untrimmed SAX40F[11] airframe with 7% thick outer wing supercritical airfoils without winglets, operating at Mach 0.8 at 40000 ft altitude. The N3H aircraft outer wings have a 9% thick supercritical airfoil with winglets and operate at Mach 0.83. Both the SAX40F airframe and cruise points are very similar to the N3H design models, providing relatively high confidence is applicability of these results to the N3H designs. The HWBOpt model was modified for the purpose of validation to include the untrimmed SAX40F airframe with no winglets and MSES lookup tables were updated to include the 7% thick outer wing airfoil. The drag polars are compared in the figure below.

---

[7] Tong, M., Jones S., and Haller J., "Engine Conceptual Design Studies for a Hybrid Wing Body Aircraft," NASA TM-2009-215680, Nov. 2009.

[8] Athena Vortex Lattice, Prof. Mark Drela, MIT, Cambridge, MA.

[9] Multi-Element Airfoil Design/Analysis Software, Prof. Mark Drela, MIT, Cambridge, MA.

[10] Hoerner S., "Fluid-Dynamic Drag," Hoerner Fluid Dynamics, 1965.

[11] Ng L., "Design and Acoustic Shielding Prediction of Hybrid Wing-Body Aircraft," M.S. Thesis, Department of Aeronautics and Astronautics, MIT, Cambridge, MA, 2009.

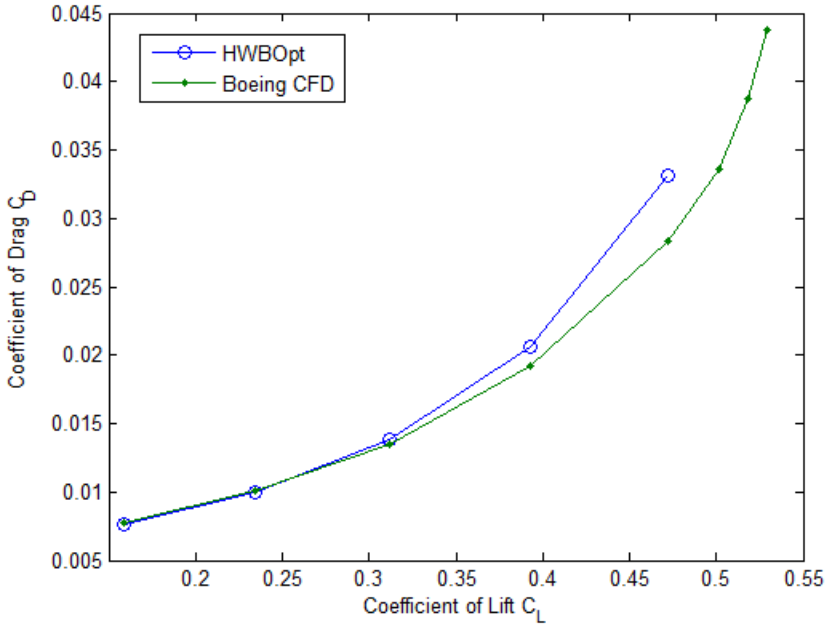

Figure I.1: Comparison of HWBOpt Aerodynamic Model to Boeing CFD analysis on SAX40F (untrimmed, no winglets).

The comparison shows that at lower C_L values both calculations are nearly identical with significant variation in HWBOpt results only at higher values of C_L. The disparity is explained using the plot below that shows the spanwise lift distribution and sectional CL distributions.

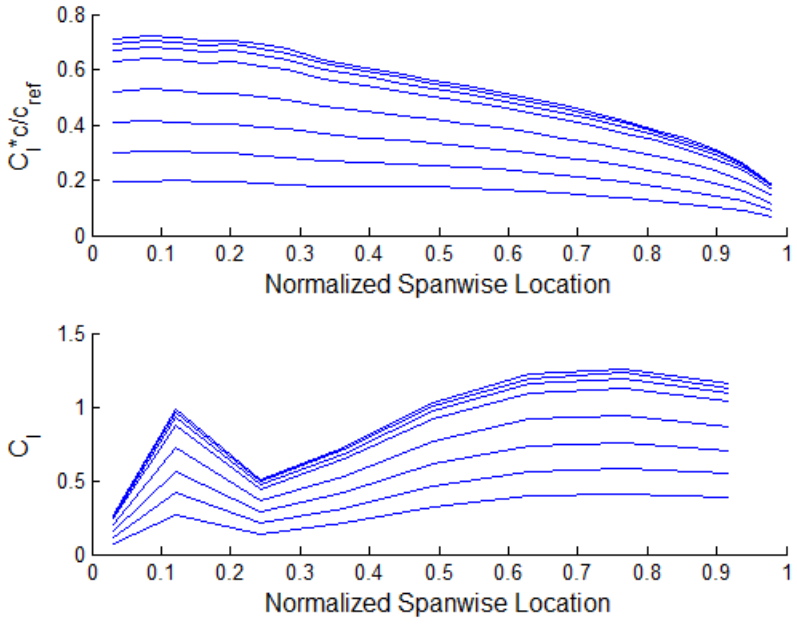

Figure I.2: HWBOpt span loading for SAX40F (untrimmed, no winglets).

The plot above shows that though the span loading is near elliptical, the sectional C_l needed on the outer wings is within the stall regime for the airfoil. The associated MSES analysis for separation is no longer reliable. By ignoring transition and assuming turbulent flow in the domain, CFD analysis encourages delayed separation and hence is not entirely applicable in that regime either. The SAX40F operates around C_L=0.2617 at start of cruise, where both methods are applicable and in agreement. Since the N+3 HWB designs also operate in a similar C_L range at cruise, the HWBOpt aerodynamic model is suitable for such analysis. Also, since MSES captures the effect of drag divergence, the wing sweep is optimized during the design process to limit the wing-perpendicular Mach numbers to the transonic regime, within the applicable range of the AVL analysis included in HWBOpt.

Appendix J: HWB Structural Weight Model

The following material properties are used in the design of the structural mass model. The material properties are used to estimate structural weight reductions for the H3.X Concept as the concept structural buildup is based upon the Boeing WingMOD program. The H3.X Concept will use carbon fiber reinforced polymer (CFRP) for the entire structure. Safety factors have been added to the material properties to account for ultimate loading and residual strength requirements.

Table J.1: N+3 Material Properties

Type	Location	Value	Units	Justification
Strength	Fuselage External Surfaces	59600	psi	compression after impact
	Fuselage Internal Surfaces	99000	psi	unnotched compression 50/40/10 layup
	Wing External Surfaces	59600	psi	compression after impact
	Wing Internal Surfaces	64000	psi	unnotched compression 10/40/50 layup

The material properties are applied to the structure at the locations shown in Figure J.1. The fuselage external surface is the wetted area around the cabin. The fuselage internal surface is the structure internal to the fuselage wetted area, as shown in Figure J.2. In the same manner, the wing surfaces and internal structures are defined by the wetted area and internal structure (e.g. spars, stringers, ribs).

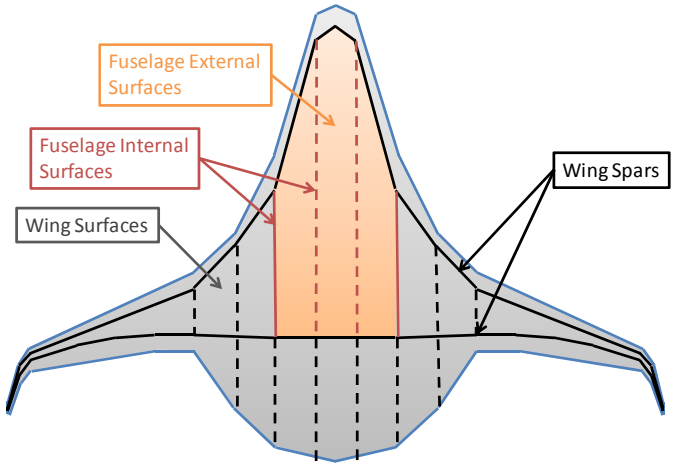

Figure J.1: General structural arrangement for material property areal projection.

Figure J.2: Concept fuselage external and internal surface cross-sections.

The estimated weight reduction is calculated using strength relationships of the current composite material properties, which are assumed to be a part of WingMOD, to the N+3 material properties above. Current composite materials are calculated in the same way as above, and are shown in TableJ.2 below. It is assumed that the component stiffness does not change between 2010 and N+3 components such that loading paths and fractions for components changes. It is also assumed that strength values indicate either the sizing property for the components or a representation of the material property advancement (e.g. N+3 material stiffness properties for stability calculations). Thus, this method represents a very rough estimation of the weight reduction due to advanced materials on the H3.1x Concept.

TableJ.2: 2010 Material Properties

Location	Value	Units	Justification
Fuselage External Surfaces	29800	psi	compression after impact
Fuselage Internal Surfaces	35900	psi	unnotched compression 50/40/10 layup
Wing External Surfaces	29800	psi	compression after impact
Wing Internal Surfaces	25000	psi	unnotched compression 10/40/50 layup

For unidirectional in-plane loading, the thickness of a plate is inversely proportional to the strength. For plate bending, the square of the thickness is inversely proportional to the strength. For similar concept component sizes, the thickness is proportional to the weight. Hybrid Wing Body aircraft have been shown to be sized by a combination of pressure and bending loads, which indicates that the weight reduction from strength will be between that of in-plane loading and bending. The average of the two is used to determine material property weight fractions, as shown in Table J.3.

Table J.3: 2010 to 2030 Material Weight Fractions

Location	In-Plane	Bending	In-Plane + Bending
Fuselage External Surfaces	0.50	0.71	0.60
Fuselage Internal Surfaces	0.36	0.60	0.48
Wing External Surfaces	0.50	0.71	0.60
Wing Internal Surfaces	0.39	0.63	0.51

The average weight fraction for combined in-plane and bending loading would be approximately 0.55, if each location were equal weight for the structure. The air vehicle structure contains components that would not benefit from the use of composites as well; for example the insulation would certainly not be made of composites and would not reduce in weight by 45%. Therefore, a fraction of the total weight must be determined that is applicable to the advanced material weight fraction. If 60% of the structure could realize this weight fraction while the other 40% of the air vehicle structure would be unchanged due to sizing not based on strength then the overall structural weight fraction would be approximately 0.7, representing an overall structure weight reduction of the H3.X Concept of 30%.

It should be noted that at interfaces of structural components are also reduced in weight using this weight reduction fraction (this reduction in weight is projected to be achieved by primarily using the unitized structure manufacturing and assembly techniques). The H3.X Concept will have a reduced part count due to the ability to layup complex parts as a co-cured structure requiring fewer fasteners and fittings.

A weight reduction of 30% compares to that of NASA estimates on Hybrid Wing Body Configurations. For an N+2 timeframe (2020 entry into service), a reduction in weight of the entire outboard wing was estimated to be 25% compared to a metal wing box[1] using the Boeing 777 as reference for model calibration. If we assume that the HWB metal wing uses a B777 technology level (1995 entry into service), a linear trend line shows a weight reduction of 35% by 2030, as shown in Figure J.3. The full aircraft structure would probably not be able to realize the full 35% that the outboard wing could, however a reduction of 30% in overall structure weight seems possible.

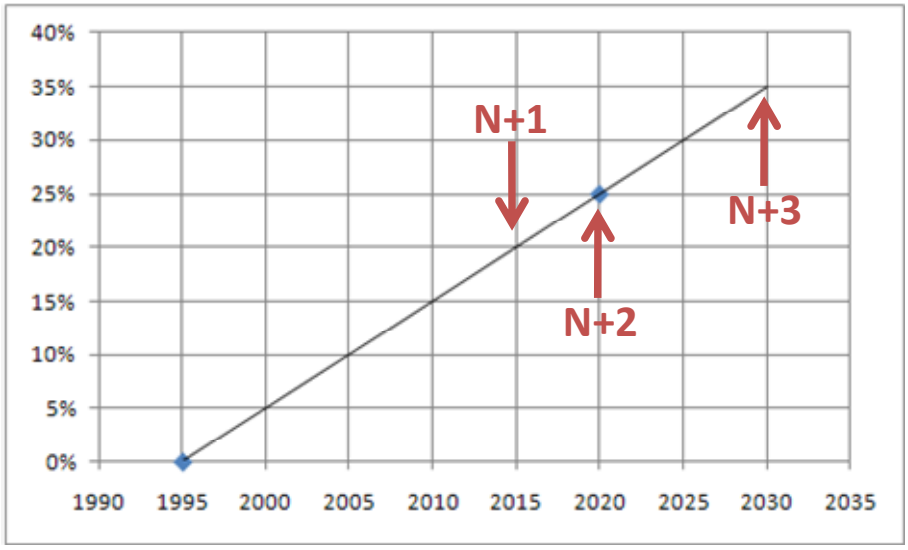

Figure J.3: Wing box weight reduction estimate.

[1] Nickol,C.L. and L.A. McCullers. "Hybrid Wing Body Configuration System Studies." AIAA 2009-931, 47th AIAA Aerospace Sciences Meeting Including The New Horizons Forum and Aerospace Exposition, Orlando, 5-8 January 2009.

Appendix K: Liquefied Natural Gas

K.1 LNG as a Fuel

K.1.1 Introduction

Natural gas (NG) is a fossil fuel containing mainly methane (about 90%), ethane, propane, butane, and trace amounts of nitrogen. When cooled at about atmospheric pressure to a liquid at -163 ^{o}C it is known as Liquefied Natural Gas (LNG) and is ~1/600th the volume of the NG. In 2007, NG contributed to 22% of the United States energy consumption[1] with 19.1% (0.77 trillion cubic feet) of the total net imports in the form of LNG[2] which serves as a cost-efficient transportation intermediary. NG consumption is expected to increase by 20% of 2003 levels by 2030[3] and the Energy Information Administration (EIA) estimates that LNG imports will peak in 2018 to 1.5 trillion cubic feet due to short term supply excesses created by a growth in world liquefaction capacity and return to 0.8 trillion cubic feet by 2030[4].

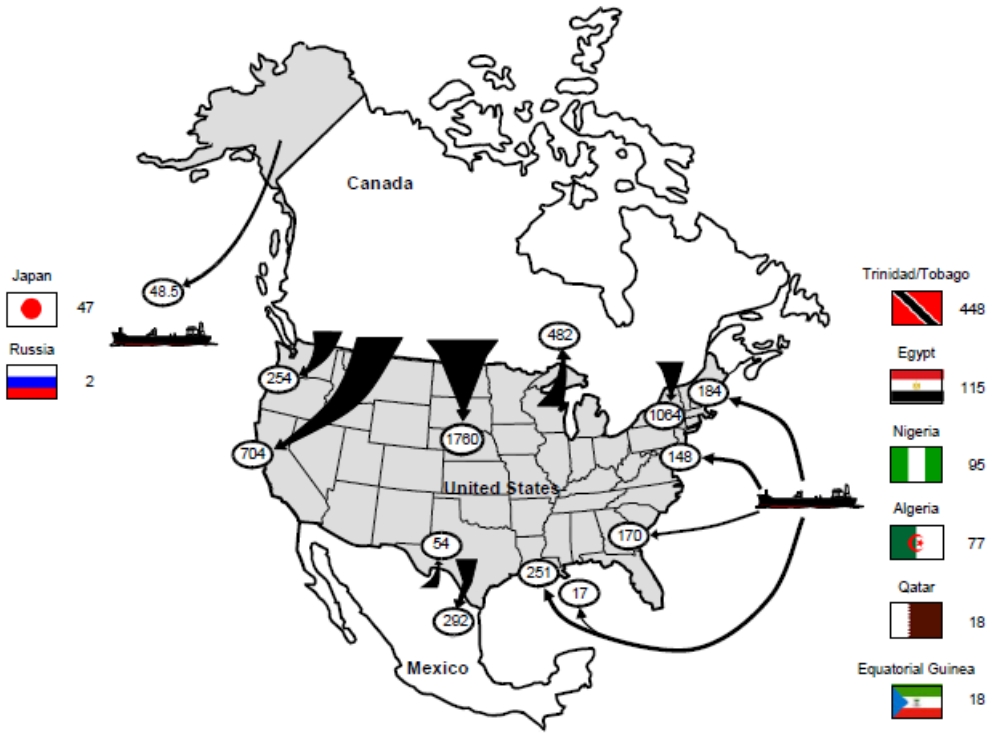

Figure K.1: NG (incl. LNG) imports and exports in 2007 (billion cubic feet)[2].

---

[1] Office of Global Warming, "Inventory of US Greenhouse Gas Emissions and Sinks: 1990-2007," U.S. EPA., 2009.

[2] Energy Information Administration, "Natural Gas Annual 2007," U.S. DOE., 2009.

[3] Jaramillo P., Griffin W. and Matthews H.**, "**Comparative Life-Cycle Air Emissions of Coal, Domestic Natural Gas, LNG, and SNG for Electricity Generation," Environmental Science and Technology, pp. 6290-6296, 2007.

[4] Energy Information Administration, "Annual Energy Outlook 2009," U.S. DOE., 2009.

Lifecycle Emissions

The life-cycle of LNG starts with the extraction of NG from wells which is sent to processing plants for the removal of water, carbon dioxide, sulfur and other hydrocarbons. It is then piped short distances to base-load liquefaction plants for cooling to obtain LNG. Non-North American (NNA) sourced LNG is then shipped using dedicated LNG ocean tankers to one of 5 LNG terminals in operation in the United States, where it is stored and then distributed within North America (NA) using trucks and rail.

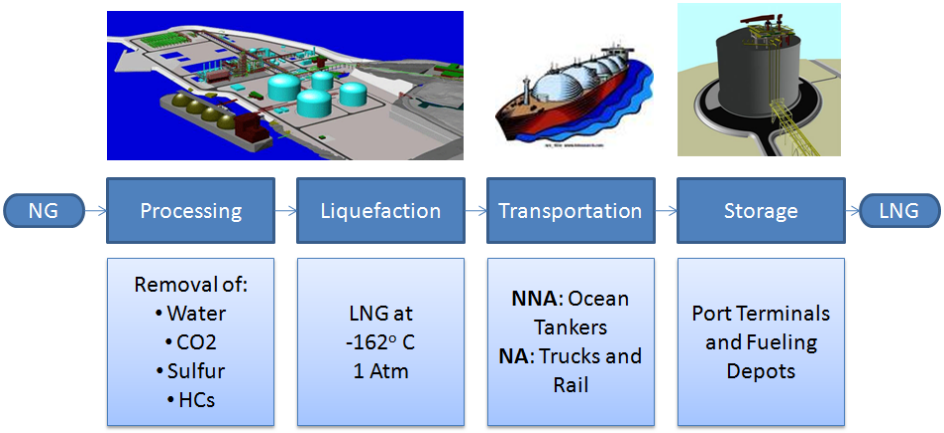

Figure K.2: LNG lifecycle.

The Greenhouse gases Regulated Emissions and Energy use in Transportation (GREET) framework developed by Argonne National Laboratory[5] was used as the primary tool for this analysis. Specifically, GREET version 1.8b was used with the inclusion of process fuel life-cycle updates made by the MIT PARTNER laboratory. This work analyzed the life-cycle green house gas (GHG) emissions of the production of LNG using conventional natural gas well sources in North America (NA) and non-North American (NNA) sources. Both pathways are available in GREET and account for different transportation and distribution requirements but with the assumption that process efficiencies remain the same.

The refrigeration compressors account for the majority of the LNG plant energy requirements[6] with liquefaction process energy efficiency estimated from literature to be between 88-92% (91% nominal)[5,7,8,9]. Extraction and processing process efficiencies were set at default GREET values of 97.2%[5]. For transportation via LNG tankers, the weighted average roundtrip distance to the U.S. of 7369 nautical miles[9] was used (comparable to the default GREET value). Boil-off rate during transport was estimated from literature to be between 0.1-0.25% (0.15% nominal) per day with 80% recovery[3,5]. The variations in different key parameters were used to create three scenarios for GHG analysis as shown below. Since the LNG is primarily used as a transport intermediary, the baseline scenario uses the 2007 export to import ratio for LNG[2].

---

[5] Wang, M., "The Greenhouse Gases, Regulated Emissions, and Energy Use in Transportation (GREET) Model," Argonne National Laboratory, 2009.

[6] Kikkawa, Y. and Aoki, I., "Gas to Liquid of 21st Century," Spring Meeting of American Institute of Chemical Engineers, Houston, TX, 1999.

[7] Tamura, I., et al., "Life Cycle CO2 Analysis of LNG and City Gas," Applied Energy, pp. 301-319, 2001.

[8] Chandra, V, "Fundamentals of Natural Gas: An International Perspective," PennWell Corp., Tulsa, OK, 2006.

[9] Center for Liquefied Natural Gas, "Life Cycle Assessment of GHG Emissions from LNG and Coal Fired Generation Scenarios: Assumptions and Results," PACE, Fairfax, VA, 2009.

Table K.1: LNG GHG Lifecycle Emissions Test Cases

	Low Emissions	Baseline	High Emissions
NG Source	100% NA / 0% NNA	20% NA / 80% NNA	0% NA / 100% NNA
Liquefaction Process Efficiency	92%	91%	88%
Tanker Boil-off Rate per Day	0.1%	0.15%	0.25%

The overall results are summarized in the table below. Other non- CO_2 emissions are not reported and excluded from the GHG emissions since they are dependent on the combustion mechanism.

Table K.2: LNG GHG Lifecycle Emissions Results

	Low Emissions	Baseline	High Emissions
WTT CO_2 emissions (gCO_2e/MJ)	11.2	12.6	15.3
WTT CH_4 emissions (gCO_2e/MJ)	4.6	6.0	7.6
WTT N_2O emissions (gCO_2e/MJ)	0.1	0.1	0.1
WTT GHG emissions (gCO_2e/MJ)	15.9	18.7	23.1
Combustion CO_2 (gCO_2e/MJ)	54.9	54.9	54.9
Total WTW GHG emissions (gCO_2e/MJ)	70.8	73.6	78.0
Total WTW GHG emissions relative to conventional jet fuel (87.5 gCO_2e/MJ)	0.81	0.84	0.89

The results obtained in this analysis are comparable to those reviewed in the literature and tabulated below. Emissions recovery/processing obtained here using GREET are higher than other literature sources but provide a conservative overestimate. Variations in transportation emissions are based on different scenario assumptions for location of NG sources.

Table K.3: LNG GHG Lifecycle Emissions Validation

GHG (gCO_2e/MJ)	Recovery	Processing	Liquefaction	Transportation
Literature	2.7-3.1[3] 0.94[10]	1.3[3] 1.7[10]	4.7-13.3[7] 6.05[10]	0.9-7.3[3] 1.05[10]
Current Analysis	3.5	4.0	6.5-10.0	1.0-4.6

[10] Ruether, J., Ramezan, M. and Grol, E., "Life Cycle Analysis of Greenhouse Gas Emissions from Hydrogen Fuel Production in the US from LNG and Coal," DOE/NETL-2006/1227, U.S. DOE., 2005.

It is also important to note that alternative paths, including NG obtained from methane hydrates, have not been quantified and may have significant impact on recovery and processing emissions. Methane hydrate is comprised of a cage-like lattice of bonded host water molecules enclosing gaseous methane guest molecules. The common form is $CH_4\ 5.75H_2O$ (Structure I Methane Hydrate), where 5.75 is the hydrate number and varies with the proportion of the guest methane molecule filled in the cages. These structures occur naturally but are known to be unstable under thermal stimulation, depressurization and chemical stimulation with brines and alcohols, reverting back to water and natural gas.

The Department of Energy estimates the worldwide methane hydrate potential to approach a staggering figure of 400 million trillion cubic feet making it an abundant source of energy, possibly exceeding the combined energy potential of all other known fossil fuels[11]. Despite their vast potential these deposits pose an enormous environmental threat[12] due to their thermal instability. The consequences of allowing spontaneous release combined with their energy potential makes the methane from hydrate a very attractive feedstock.

To meet the projected demands, net import of natural gas is forecast to grow from 16% of the total supply in 2005 to 21% in 2030. To help guard against potential supply interruptions, shortage and improve energy security, the United States has enacted the Methane Hydrate Research and Development Act of 2000. This has initiated an interagency effort to evaluate risk and demonstrate technical and economic viability of the methane recovery from arctic hydrate by 2015 and marine hydrate by 2025[13].

K.2 LNG Fuel Integration – Cryo Tanks and Laminar Wing Flow

In conventional aircraft, fuel is typically stored in the wing tanks and center body tanks (in the fuselage) using the existing wing box. The structure of fuel storage systems on the aircraft is subject to Federal Aviation Regulation (FAR) 25 and 29 tabulated below.

Table K.4: Fuel Tank Design Regulations

Design Loads	FAR 25.561 Emergency Landing	FAR 29.952 Fuel system crash resistance based on tank location		
		In cabin	Above /behind crew/passenger	Elsewhere
Upward	3.0 g	4.0 g	1.5 g	1.5 g
Forward	9.0 g	16.0 g	8.0 g	4.0 g
Sideways	3.0 g	8.0 g	2.0 g	2.0 g
Downward	6.0 g	20.0 g	4.0 g	4.0 g
Rearward	1.5 g	-	-	-

[11] U.S. DOE., "Methane Hydrate - Future Energy Within Our Grasp."

[12] Hendricks, R., "Methane Hydrates: More than a Viable Fuel Feedstock Option," NASA TM-214816 / AIAA–2007–4757, NASA Glenn Research Center, 2007.

[13] The Technical Coordination Team, National Methane Hydrate R&D Program, "An Interagency Roadmap for Methane Hydrate Research and Development," U.S. DOE, Office of Fossil Fuels, 2006.

K.2.1 Non-integral LNG Tank

Non-integral wing tanks are designed for both structural and thermal loads associated with LNG storage. Such architecture would maintain the LNG fuel at near atmospheric pressure in its cryogenic boiling liquid state and fuel would be supplied in its liquid state. Typical designs are dual walled with evacuated super insulation. Since minimizing heat loss favors designs with minimum surface area to volume, minimum weight designs are restricted to spheres, cylinders and other *rounded* geometries. The thermal design tradeoff lies between losses due to boil-off of fuel (assumed unusable) and insulation weight. The structural shells can be modeled as thin walled pressure vessels and sized based on regulation and safety margins[14].

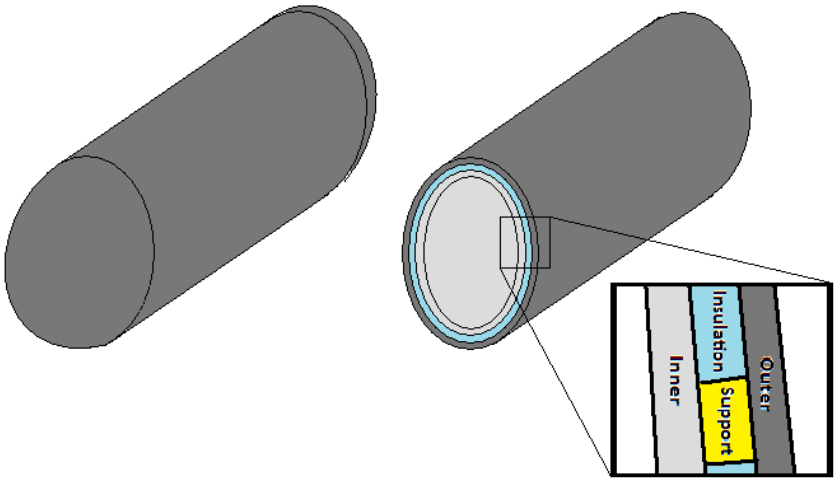

Figure K.3: Non-integral LNG fuel tank.

The coupled structural/heat transfer optimization problem can be solved analytically. Conductive heat flow Q through each surface can be computed by constructing simple thermal resistive circuits[15] combing the inner (i), outer (o), insulation (m) and support structures (s) as illustrated in the figure. The outside temperature is assumed to be ambient for fully insulated designs. For cylindrical portions of the tank of length L, with thickness' t, surface areas S, thermal conductivities k we have:

$$Q_{cyl} = Q_{cyl-1D}\, L; \quad Q_{cyl-1D} = \frac{\Delta T}{R_{cyl}}; \quad R_{cyl} = R_i + \left(\frac{1}{R_m} + \frac{1}{R_s}\right)^{-1} + R_o$$

$$R_i = \frac{t_i}{k_i S_i}; \quad R_m = \frac{t_m}{k_m S_m}; \quad R_s = \frac{t_m}{k_s S_s}; \quad R_o = \frac{t_o}{k_o S_o}$$

Steady heat conduction through the hemispherical ends of the tank is modeled as a multilayered sphere.

$$Q_{sph} = \frac{\Delta T}{R_{sph}}$$

---

[14] Carson L., Davis G., Versaw E., Cunnington Jr. G. and Daniels E., "Study of Methane Fuel For Subsonic Transport Aircraft," NASA CR 159320, NASA Langley Research Center, Sep. 1980.

[15] Chen Q., Wegrzyn J. and Prasad V., "Analysis of temperature and pressure changes in liquefied natural gas (LNG) cryogenic tanks," Cryogenics 44 701–709, Mar., 2004.

$$R_{sph} = \frac{t_i}{4\pi(r)(r+t_i)k_i} + \frac{t_m}{4\pi(r+t_i)(r+t_i+t_m)k_m} + \frac{t_o}{4\pi(r+t_i+t_m)(r+t_i+t_m+t_o)k_o}$$

The resulting steady rate of heat transfer through the fuel tank is given by:

$$Q_{tank} = Q_{cyl} + Q_{sph}$$

Results are shown below for a dual tanked system sized for fixed energy requirements assuming that the fuel is boiled off over a 12 hour cycle is unusable. These designs assume tank ullage of 10%, structural safety factor of 1.5, Al-Li Alloy 1460 structural material and Multi-Layer Insulation (MLI).

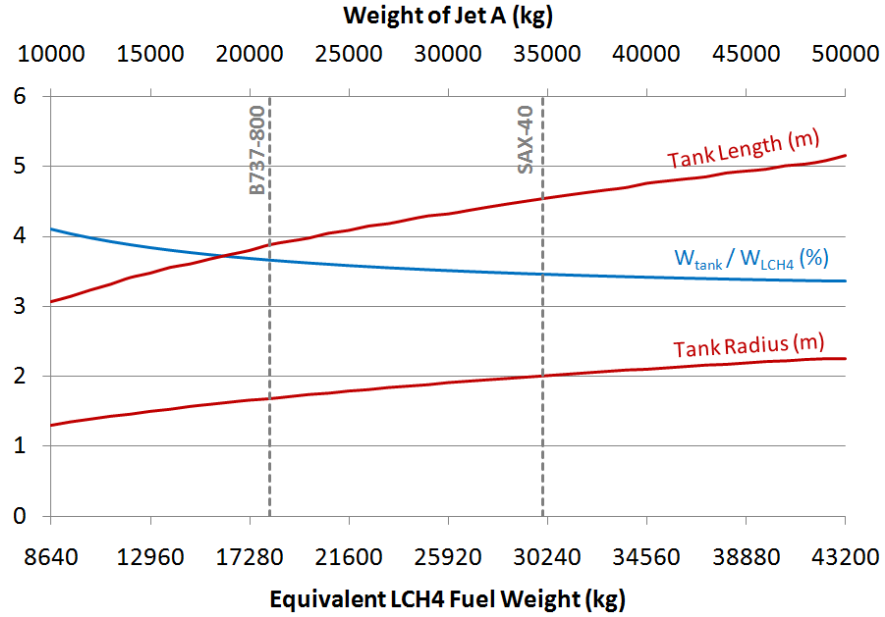

Figure K.4: Minimum weight non-integral tank sizing results.

The plot above has energy required on the x-axis with two reference points: the B737-800 and SAX 40. For most cases the tank/fuel weight penalty for such designs is 3-4%, however these results are for unconstrained geometries. The B737-800 is used as a representative example to elaborate on the issue. In the case of the B737-800 to achieve this minimum weight, the tank radius required is infeasible and constraints placed on the tank geometry result in significant increase in tank weight. This is compensated by LNG having 16% higher specific energy than Jet A and allows the B737-800 wing root and cargo compartments to be utilized for storage with same overall specific energy as Jet A alone. Usage of the outboard section of the wing adds excessive weight to the LNG storage due to the restrictive geometry. Since LNG has 33% lower energy density than Jet A, the issue is exaggerated by the need for additional volume for the same amount of fuel energy. If fuel is relocated out of the wing additional structural penalties are incurred due to increased wing bending moment. If the wing is oversized to incorporate the fuel, increased wetted area results in additional skin friction. These limitations are true for most aircraft configurations and make such tank designs unfavorable.

K.2.2 Integral LNG Tanks and Laminar Flow Promotion

Integral wing tanks designs use the existing wing box structure and were assessed briefly in the late 70's in the context of hydrogen fuel storage[16,17]. Since the boiling point of LNG (110K at 1atm) is better matched to promote laminar flow using wall cooling at cruise, insulation requirements are minimized. The fuel can be stored as a boiling liquid with heat additional from aerodynamic heating balanced by enthalpy sinked through vaporization. With the vaporized fuel piped for usage, the liquid fuel temperature can be assumed to remain constant.

The 2D boundary layer (BL) momentum equation near the wall using conventional nomenclature is:

$$\left(\rho v_w - \frac{d\mu}{dT}\frac{\partial T}{\partial y}\right)\frac{\partial u}{\partial y} + \frac{dp}{ds} = \mu_w \frac{\partial^2 u}{\partial y^2}$$

Suction $(v_w < 0)$ and wall cooling in air $(d\mu/dT > 0, \partial T/\partial y > 0)$ have the same effect as favorable pressure gradients $(dp/ds < 0)$ in increasing the boundary layer shape factor. In addition, wall cooling has been observed to diminish the range of linearly amplified frequencies and reduces the growth rate of frequencies[17]. The overall effect is an increase in the critical Reynolds number and delay of Tollmien-Schlichting (TS) wave instability dominated transition typically observed at cruise. This however does not apply to highly swept wings where cross-flow (CF) instabilities dominate or in flows with significant adverse pressure gradient as may be present on the upper surface of the wing. This limits the possibility of laminar flow promotion to the lower wing surface which remains in constant contact with the cryogenic fuel. The physics of the problem are complicated since they require modeling of transition and consideration of non-isothermal flows. A first estimate for the overall reduction in profile drag can be made using the e^N method. Increasing the Ncrit, a ~17% reduction in overall skin friction drag is expected based on this preliminary analysis using XFOIL.

Analyzing the inverse design problem, assuming laminar flow on the lower wing surface and turbulent flow on upper the wing surface, the insulation can be sized to match the fuel boil-off rate to the required fuel flow rate at cruise. Additional fuel flow can be supplied via a small heating element with minimal power consumption and without significant contribution to or weight and complexity. In contrast to the non-integral design that requires liquid fuel to be pumped or gravity fed, the fuel is supplied in its vaporized form through self pressurization as it boils off. Since the laminar flow promotion is expected primarily for 2D BLs, the problem can be solved numerically in 2D sections created at Gaussian quadrature points to allow spanwise integration as illustrated below.

---

[16] Theisen J., Brewer G. and Miranda L., "Laminar Flow Stabilization by Surface Cooling on Hydrogen Fueled Aircraft," AIAA-1979-1863, AIAA Aircraft Systems and Technology Meeting, New York, 1979.

[17] Reshotko E., "Drag Reduction by Cooling in Hydrogen-Fueled Aircraft," Journal of Aircraft, Vol. 16, No. 9, Article No. 79-4112, Feb. 1979.

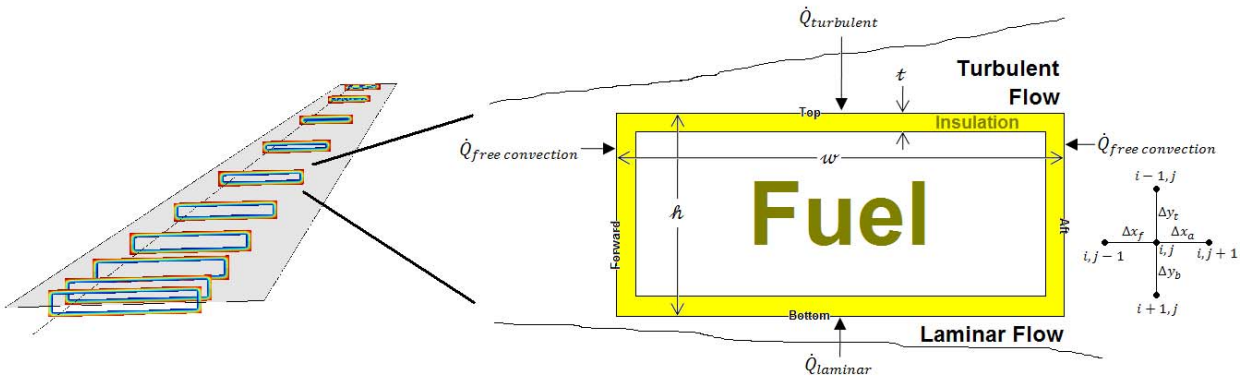

Figure K.5: Integral tank insulation sizing model.

The problem is addressed numerically to solve the steady heat equation for the temperature T on a domain $\Omega \subset \mathbb{R}^2$ with Dirichlet (D) and non-linear, solution dependent Neumann (N) boundary conditions, Γ_D and Γ_N respectively.

$$\begin{aligned} \nabla^2 T &= 0 \quad \text{on } \Omega \\ T &= T_D \quad \text{on } \Gamma_D \\ \frac{\partial T}{\partial n} &= T_N f(T_N) \quad \text{on } \Gamma_N \end{aligned}$$

The physical wing box is approximated as a hollow rectangular structure with a lining of insulation material. The thin insulation material is modeled as the computational domain Ω. The interior boundary is assumed to be at the fixed temperature of 110K, the boiling point of LNG. The thermal boundary conditions for the outer surfaces are derived from expected cruise flight flow conditions.

The upper outer surface thermal boundary condition $\in \Gamma_D$ is determined by forced convection for a flat plate with turbulent flow and an un-cooled starting length. The lower outer surface thermal boundary condition $\in \Gamma_D$ is determined by forced convection for a flat plate with laminar flow and an un-cooled starting length. Assuming uniform heat flux, solutions for the local Nusselt number on a flat plate with un-cooled starting length[18] are extended to the upper and lower outer surfaces:

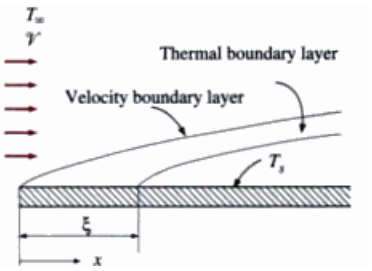

$$\text{Laminar: } Nu_x = \frac{h_x x}{k_{amb}} = \frac{0.453\ Re_x^{0.5}\ Pr^{\frac{1}{3}}}{[1-(\xi/x)^{3/4}]^{1/3}}$$

$$Turbulent: Nu_x = \frac{h_x x}{k_{amb}} = \frac{0.0308\ Re_x^{0.8}\ Pr^{1/3}}{[1-(\xi/x)^{9/10}]^{1/9}}$$

Where, h_x is the local convective heat transfer coefficient, k_{amb} is the thermal conductivity of the fluid, Re_x is the local Reynolds Number, Pr is the Prandtl for the fluid and ξ is the un-cooled starting length.

[18] Cengel, Y., "Heat and Mass Transfer - A Practical Approach," McGraw-Hill, New York, NY, 2007.

The average Nusselt number for free convection on a vertical flat plate (1) of height L is given by the following empirical correlation:

$$Nu = \frac{h(T_s)\,L}{k_{amb}} = \left(0.825 + \frac{0.387\,Ra_L^{1/6}}{(1 + (0.492/Pr)^{9/16})^{8/27}}\right)^2$$

Where, $h(T_s)$ is the convective heat transfer coefficient and Ra_L is the Rayleigh number given by the product of the Grashof and Prandtl numbers:

$$Ra_L = Gr_L Pr = \frac{g\,\beta\,(T_s - T_{amb})L^3}{\nu^2} Pr$$

Where, g is gravitational acceleration, β is the coefficient of volume expansion ($\beta = 1/T$ for ideal gases) and ν is the kinematic viscosity of the fluid. Since, the boundary value problem is ill-posed as formulated above with solution dependent, non-linear Neumann boundary conditions, an additional approximation assumes the forward/aft Neumann boundaries to be isothermal:

$$T_N = c \quad \text{on } \Gamma_N$$

where $c \in \mathbb{R}$ is a unique unknown constant for each Neumann boundary. This additional assumption is only enforced weakly since the problem is still ill-posed at the interface of the forward/aft and upper/lower interfaces.

The centertank is treated identically to the wing tank except the top surface of the centertank which is no longer exposed to the freestream. Heat transfer through this surface is estimated using free convection for a flat plate with the averaged Nusselt number[18] empirically given by:

$$Nu = \frac{h(T_s)\,\ell}{k_{amb}} = 0.27\,Ra_\ell^{1/4}$$

Unlike the vertical plate, the characteristic length ℓ for the horizontal flat plate is given by the ratio of the plate area to perimeter. Applying finite difference approximations, the system of governing equations and boundary conditions above can be converted to a non-linear matrix system of the form:

$$A(x)\,x = b$$

where, $x \in \mathbb{R}^{MN}$ is the solution vector of discretized temperatures $T_{i,j}$ given at nodes i, j of an $M \times N$ grid, $A(x) \in \mathbb{R}^{MN \times MN}$ is the discrete Laplacian operator matrix that is a function of x since it includes the solution dependent, non-linear Neumann boundary conditions, and $b \in \mathbb{R}^{MN}$ is a set of constants arising from Dirichlet boundary conditions.

Due to the non-linear nature of the boundary conditions, the Newton Rhapson method (NRM) is used to iteratively find the roots of the corresponding discrete residuals $r(x) = b - A(x)\,x = 0$.

Estimate $x^{(0)}$
for $k = 1, 2, \ldots$
  Compute $r^{(k)}$ and $J^{(k)}$
  Solve $J^{(k)}\delta x^{(k)} = -r^{(k)}$
  $x^{(k+1)} = x^{(k)} + \delta x^{(k)}$
Stopping criteria: $f(x^{(k)}) \cong f(x^{(k-1)})$

Each Newton step shown above requires solution of an $MN \times MN$ linear system $J\delta x = -r$, where $r \in \mathbb{R}^{MN}$ is the residual vector and $J \in \mathbb{R}^{MN \times MN}$ is Jacobian matrix with entries defined as:

$$J_{ij}(x^{(k)}) \equiv \frac{\partial \eta_i(x^{(k)})}{\partial x_j^{(k)}}, \qquad i,j = 1,\ldots,MN$$

J is different at each iteration since its includes the values of the residual derivatives evaluated at the current iterate. However, matrix J is always square and sparse (banded) since the residuals are based on finite difference discretization using a small local stencils. Hence, the sparse linear subsystem can be efficiently solved using Gaussian Elimination. NRM convergence is obtained when the net convective heat flow computed at the domain boundary matches the net conductive heat flow through the domain interior. Hence the method can converge despite the presence of large residuals near the interface of the forward/aft and upper/lower boundaries where the problem is ill-posed. Typical results for conventional foam insulation $(k = 0.033\ \mathrm{W/mK})$ shows insulation/fuel weight requirements of only ~1% since insulation requires are only $\mathcal{O}(\mathrm{mm})$.

K.2.3 Limitations

The true constraint for integral wing tanks is volume, since LNG requires 33% more volume than JetA for the same fuel energy. Hence maximum range of existing design would be limited if application as a retrofit is even viable. However, in the case of the HWB configuration, the wingbox is not volume limited due to the presence of a thick mid-wing section not suitable for cabin usage. Another serious issue not addressed here is the requirement to disable wall cooling at low altitudes due to icing concerns. Solutions to this problem have been proposed in other work[16], however additional consideration for the thermal management system is also required.

K.3 Alternative Engine Cycles

K.3.1 Introduction

Cryogenic fuels are attractive for aircraft use due to their energy density and low carbon content. However, the Brayton cycles used in traditional aircraft gas turbines have been optimized for the properties of Kerosene fuels. Cryogenic fuels have many different characteristics than kerosene based fuels and therefore may lead to a different optimum engine cycle.In particular the low storage temperature of cryogenic fuels such as LNG has a significant impact on the cycle efficiency. Simply utilizing cryogenic fuels in a traditional Brayton cycle leads to a major decrease in cycle efficiency as mixing the cold fuel chills the air entering the combustor, so for a given combustor exit temperature more fuel must be injected to create enough heat release to overcome this cooling.

A fair comparison of the impact of cryogenic fuels on aviation therefore requires an identification of engine cycles that appropriately utilize the characteristics of cryogenic fuels. Liquified Natural Gas, LNG, the cryogenic fuel selected for this study can be a good working fluid due to its high specific heat and thermal stability, therefore cycles which take advantage of this capability were selected for further inspection.

K.3.2 Analysis Approach

Engine cycles were constructed based on specifying compressor outlet and turbine inlet temperatures. Temperature limits are used to calculate pressure ratios, heat addition, and component work. Fuel flow and working fluid temperatures were calculated iteratively as heat transfer within the heat exchangers is interdependent with the amount of fuel used. Candidate cycles were analyzed over a range of different cycle parameters, summarized below.

Compressor Exit Temperature T_{t3}	500-1000 K
Turbine Inlet Temperature T_{t4}	1500-2230 K
Polytropic Efficiency (Turbine & Compressor)	90-100%
Compressor heat exchanger locations	Inlet to Exit

LNG candidate cycles were compared to a kerosene Brayton cycle baseline at the same cycle parameters using the following figures of merit:

Core Work: An expression of the work extracted from the cycle compared to the mass flow through the core. Engines with higher core work are smaller in size (inlet diameter), but not necessarily lighter.

$$\frac{W_{net}}{\dot{m}_{atr} C_p T_0}$$

Cycle Efficiency: The ratio of work out to heat input.

$$\frac{W_{net}}{Q_{in}}$$

Specific Cycle Work Ratio (SCWR): This term combines the thermal efficiency of the engine with the heating value of the fuel. SCWR is similar in concept to specific fuel consumption (SFC) but without any propulsive efficiency considerations, this allows direct comparisons of different engine cores without requiring detailed knowledge of the aircraft propulsors.

$$\frac{Cycle\ Power}{\dot{m}_{fuel}} = Fuel_{HV} * \eta_{cycle}$$

During analysis heat exchanger exit temperature was approximated by calculating the temperatures from mixing the two flows. Additional assumptions include locating any regenerator heat exchangers after the turbine and holding Cp and γ constant within components. Results are presented for the following conditions:

- 35,000 ft inlet conditions
- 95% polytropic component efficiency
- 1600K T_{t4} unless otherwise noted
- Compressor heat exchanger is located as a pre-cooler, unless otherwise noted

K.3.3 Cycles and Results

The following cycles were examined in this analysis:

- Brayton Cycle
- LNG/air pre and intercooling
- LNG/exhaust pre-heating (regenerator cycle)
- LNG to air cooling followed by fuel pre-heating (Chiller-Regenerator cycle)

K.3.3.1 Brayton Cycle Baseline

The Brayton cycle is the conventional aircraft gas turbine engine cycle and is well suited to kerosene fuel. A kerosene fueled Brayton cycle operating at the same cycle parameters was used as the baseline for all of the following analysis. As discussed previously simply replacing kereosene with LNG in a Brayton cycle leads to a large reduction in cycle efficiency. This effect is shown graphically in Figure K.7, where the inclusion of "c" in the cycle diagram requires more heat input without increasing the work output, represented by area enclosed by the cycle.

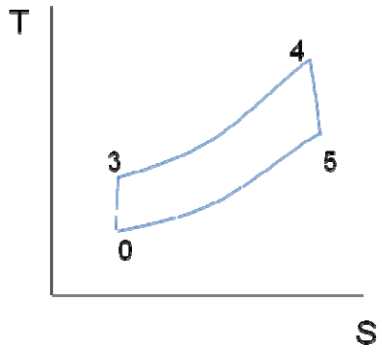

Figure K.6: Temperature (T) and Entropy (S) diagram of typical Brayton cycle.

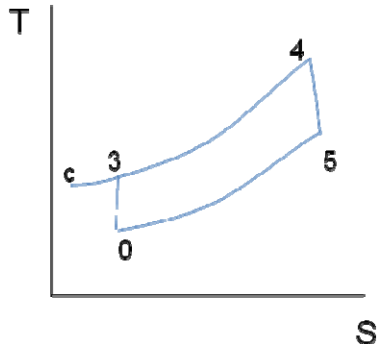

Figure K.7: T-S Diagram of Brayton cycle with cold fuel injection at "c".

Figure K.6 and Figure K.8 are used to graphically display the Brayton cycle and are included for reference as similar figures will be used to describe the candidate LNG cycles.

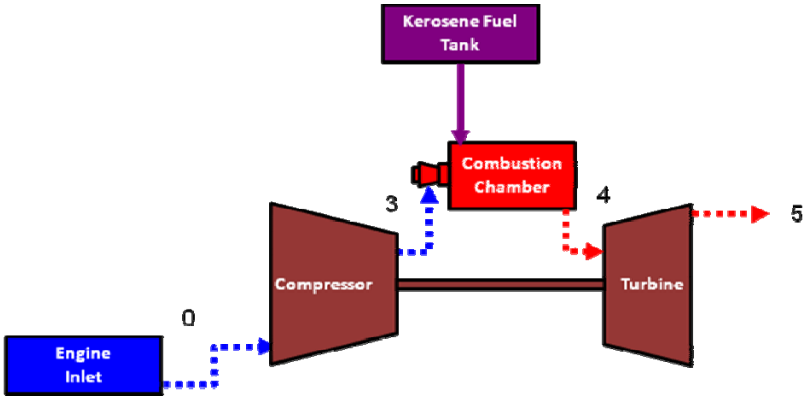

Figure K.8: Kerosene fuel Brayton cycle diagram.

K.3.3.2 LNG/Air pre- and intercooling

The cold temperature of the fuel can be used to pre- or intercool air in the compressor. This cooling has the effect of increasing the density of the air in the compressor, increasing the core power, and adding heat to the fuel. Bringing the fuel temperature closer to ambient reduces the negative efficiency impact of injecting the fuel.

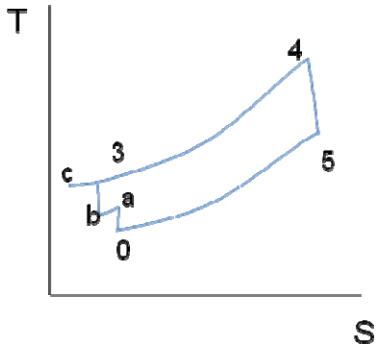

Figure K.9: T-S Diagram of LNG/Air Intercooled cycle.

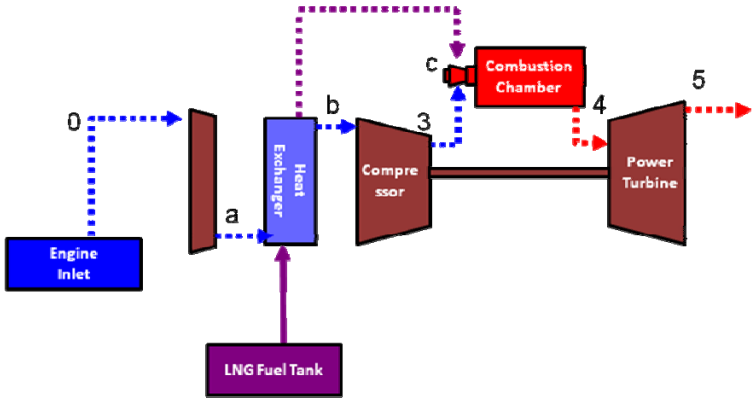

Figure K.10: LNG/Air intercooled cycle diagram.

Figure K.9 shows the cycle impact of intercooling the compressor flow, shown in the transition from point "a" to "b." As the intercooling moves closer to the engine inlet, "0", the cycle efficiency increases. Compared to the Brayton cycle baseline the pre- or intercooled cycles always have lower cycle efficiency, shown in Figure K.11 by having less than the inherent 16.8% increase in SCWR due to the heating value of the fuel. Pre-cooling the flow does produce a relative increase in core power, as shown in Figure K.12.

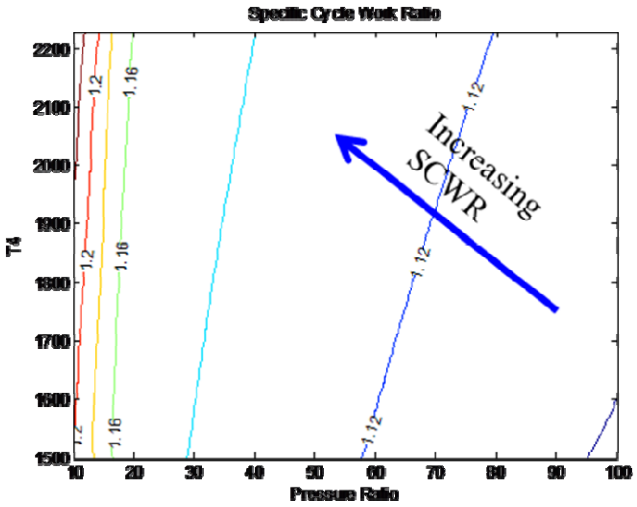

Figure K.11: LNG/Air pre-cooled cycle SCWR compared to baseline.

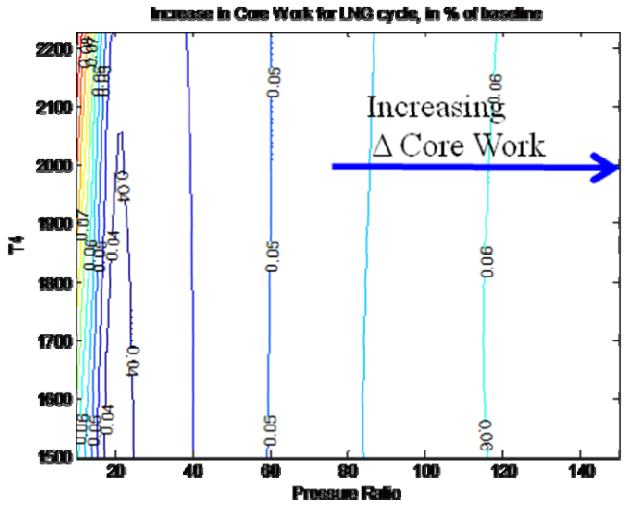

Figure K.12: LNG/air pre-cooled cycle core work compared to baseline.

Adding a heat exchanger to the compressor will lead to an increase in engine weight and compressor pressure loss not captured by this analysis.

K.3.3.3 Regenerator Cycle

Pre-heating the fuel in the engine exhaust can increase the engine's cycle efficiency compared to a Brayton cycle. Air to air regenerators are used to increase engine efficiency but typically have a large associated mass penalty. Utilizing the high specific heat and thermal stability of LNG allow for a much lighter solution. The attractiveness of this cycle let it to be used in the major two previous analysis of cryogenic aircraft[19][20].

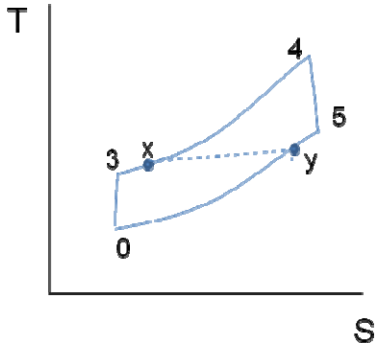

Figure K.13: T-S diagram of regenerator cycle.

[19]V. Sosounov, V. Orlov, *Experimental Turbofan Using Liquid Hydrogen and Liquid Natural Gas as Fuel*, AIAA paper # 90-2421, 26th Joint Propulsion Conference, Orlando ,FL 1990

[20]L.K. Carson, G.W. Davis, E.F Versaw, G.R. Cunnington, E.J. Daniels, *Study of Methane Fuel for Subsonic Transport Aircraft*, NASA CR-159320, 1980

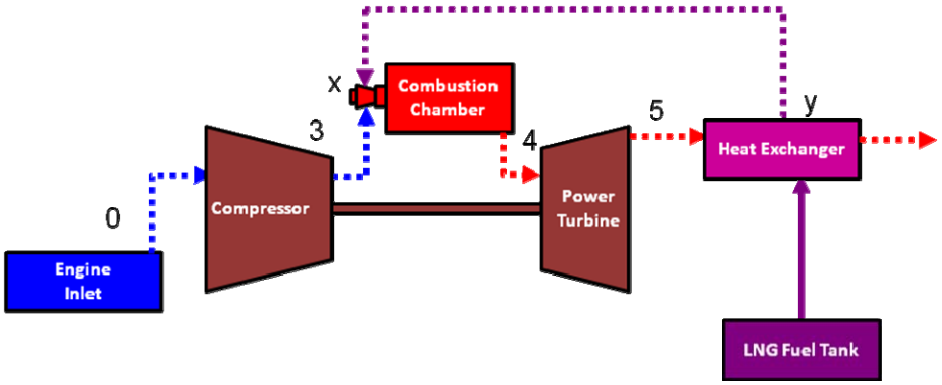

Figure K.14: LNG regenerator cycle diagram.

Pre-heating the fuel increases the cycle efficiency (2.5% increase at pressure ratio of 20) and the SCWR, as shown in Figure K.15. While the regenerator cycle always maintains an SCWR advantage, this benefit decreases as pressure ratio increases. Higher engine pressure ratios lead to decreasing the difference in temperature between the compressor exit and fuel leaving the exhaust heat exchanger, reducing the benefit of regeneration.

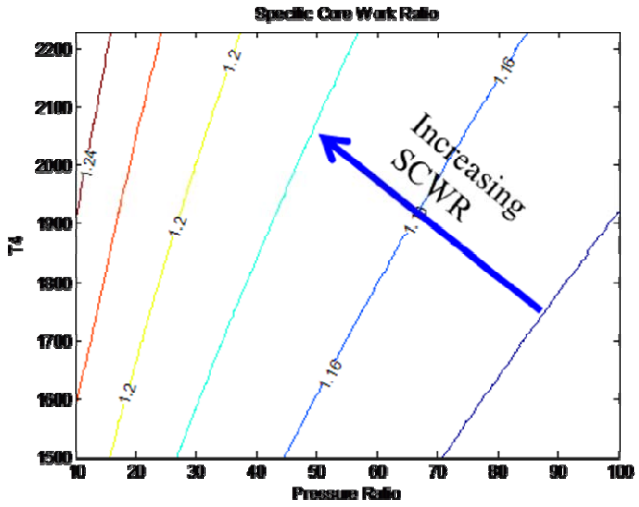

Figure K.15: Regenerator cycle SCWR compared to baseline.

The regenerator cycle has no impact on core work compared to the baseline cycle.

K.3.3.4 Chiller Regenerator Cycle

The chiller-regenerator cycle uses the LNG fuel to first, cool the inlet air, and second transfer waste heat from the exhaust to the combustor. This cycle combines the benefits of both the pre-cooled and regenerator cycles, leading to an increase in both core work and cycle efficiency compared to the Brayton cycle baseline.

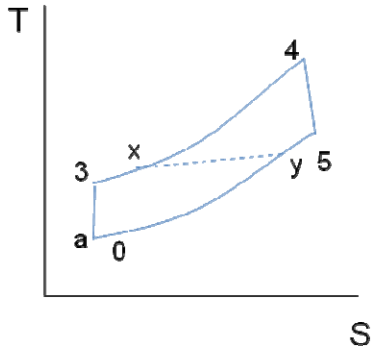

Figure K.16: T-S Diagram of chiller-regenerator cycle.

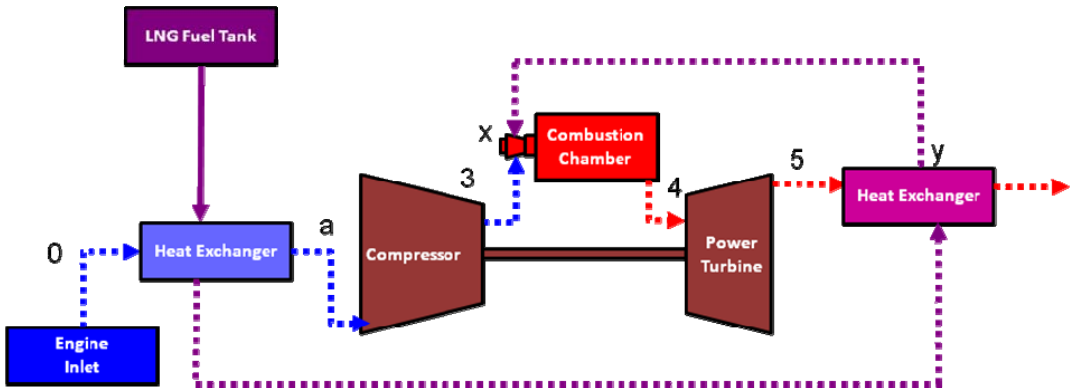

Figure K.17: Chiller-regenerator cycle diagram.

The chiller-regenerator cycle has a 2.2% increase in cycle efficiency, a 19% increase in SCWR, and a 4% increase in core power compared to the baseline cycle at a pressure ratio of 20. The increases in SCWR and core work, shown in Figure K.18 and Figure K.19, are similar to the regenerator and pre-cooled cycles respectively.

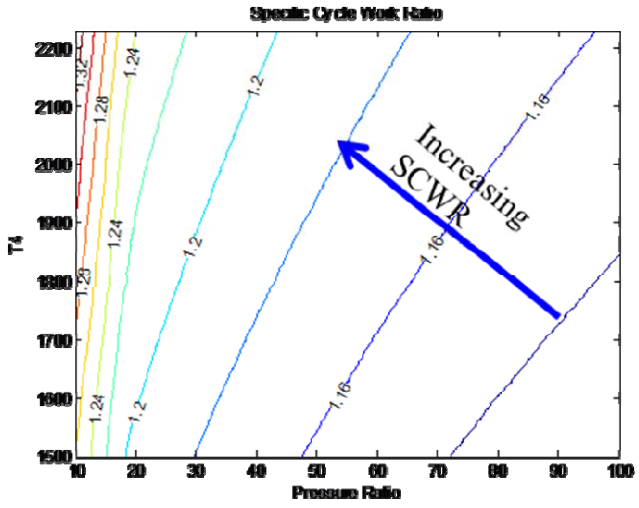

Figure K.18: Chiller-Regenerator SCWR compared to baseline.

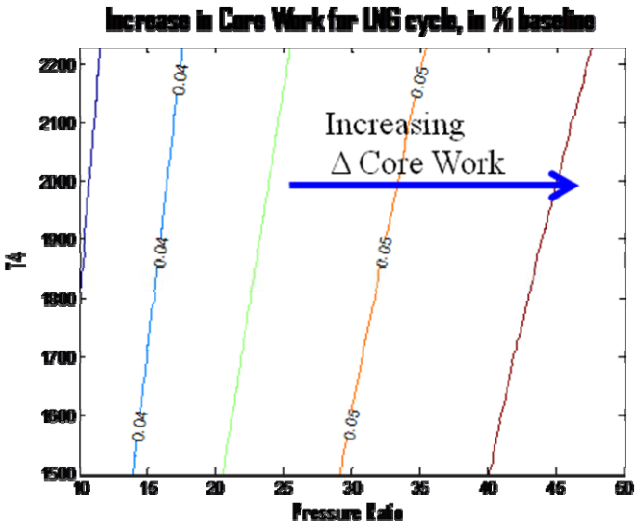

Figure K.19: Chiller regenerator core work compared to baseline.

While the chiller-regenerator cycle has a core-work advantage over the regenerator cycle there is likely to be a substantial mass penalty due to the extra heat exchanger and the gaseous state of fuel entering the exhaust heat exchanger.

K.3.3.5 Summary

Cycles that utilize the cryogenic fuel's properties as a working fluid have clear advantages over simply powering a Brayton cycle engine with cryogenic fuel. The chiller-regenerator cycle has an advantage in core power and SCWR over the Brayton cyle for all pressure ratios examined, therefore the properties of this cycle will be used to bound the potential impact of cryogenic fuels on the N+3 concepts. However, the lower potential mass of the regenerator cycle also makes it an attractive option, therefore if LNG fuel is carried forward a more detailed analysis will be required to determine which cycle has the most benefit to overall aircraft performance.

K.4 Electrical Transmission system

K.4.1 Introduction

One of the technologies that were explored in detail but finally not used in the H3.2 design was the use of a distributed turboelectric transmission system. This appendix summarizes the process followed for the design of this system.

Three electrical transmission systems were investigated in detail, and one of them was selected to be used in the optimization process that was conducted for the final design of the H3.2 configuration. The three evaluated electrical systems are: 1) Fully HTSC generators with fan tip driven permanent magnet motors and inverters, 2) Fully HTSC generators and motors with inverters and, 3) Fully HTSC generators and motors with no inverters. The electrical system that was finally selected is option number 2. The selection was based on an aircraft system level study that was performed, which took into account the effect of the efficiency and the weight of the electrical transmission systems on the aircraft performance. This study was presented by the team in the 6-month review conducted in NASA in March 2009.

K.4.2 Fan tip driven permanent magnet electrical motor model

Figure K.20 illustrates the motor configuration. The rotor consists of the containment hoop, the rotor core and the magnet. The stator consists of the field winding and the stator core. In order to maximize the winding conductivity to weight ratio of this motor, the fan tip driven permanent magnet electrical motor used aluminum conductors cooled to cryogenic temperature by the LNG fuel. To further improve its power density and efficiency, this design featured the rotor located outside the stator.

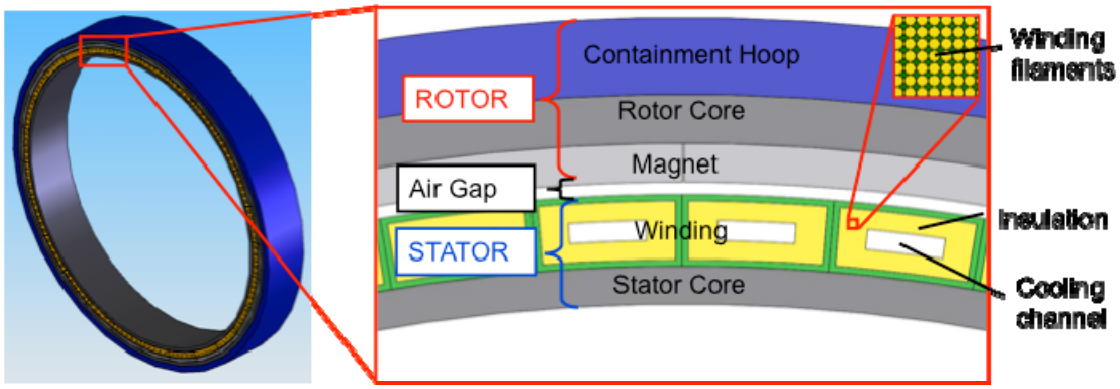

Figure K.20. Fan tip driven permanent magnet motor configuration

Figure K.21 shows a flow chart for the model developed to study the performance and weight of the fan tip driven permanent magnet motors[21]. The inputs to the model are the motor requirements at engine Sea Level Static conditions (operating rotational speed, the output shaft power and the fan diameters), the design variables (electrical frequency and current density) and the constraints (material properties). Given these inputs, the motor model generates the geometry, estimates the performance through the estimation of the losses such as resistive, eddy, core and windage losses. This model also estimates the weight of the motor, including the weight of the structure, the permanent magnet, and the windings, as well as thermal properties, such as winding temperature and cooling flow requirements. Finally, based on these geometry, performance and thermal properties of this design, this model sizes the motor for the required SLS conditions, while optimizing it to give maximum efficiency at cruise conditions. The outputs of the model are the geometry, the efficiency and the weight of the electrical motor.

[21] Sato, S., "Design and Characterization of Hover nano-Aerial Vehicle (HNAC) propulsion system", S.M. Massachusetts Institute of Technology, 2008

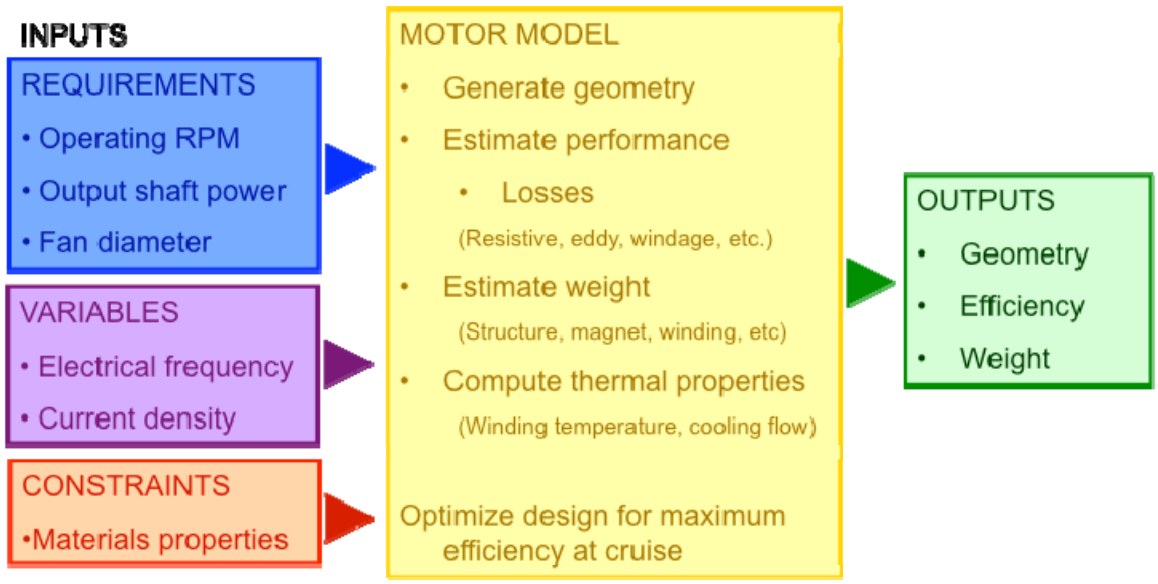

Figure K.21. Model flow chart

Figure K.22 shows a typical result of the optimization process for a specific set of the input parameters. The current density is varied between 10 and 100 A/mm^2 and the electrical frequency is modified between 0.8 and 1.6 kHz. The figure shows results for motor efficiency and weight. There are two lines that correspond to two current density limits: the state of the art operational motor limit and the experimental motor limit. The efficiency is independent of the electrical frequency below 1.6 kHz and the weight does not change significantly beyond 1.4 kHz. Based on the results and for the given input parameters, we would choose for this design an electrical frequency of 1.4 kHz and a

current density of 37 A/mm^2 with a weight estimation of 210 kg with the core being the heaviest component and an efficiency of 99.2% with the resistive and core losses being the highest followed closely by the windage losses.

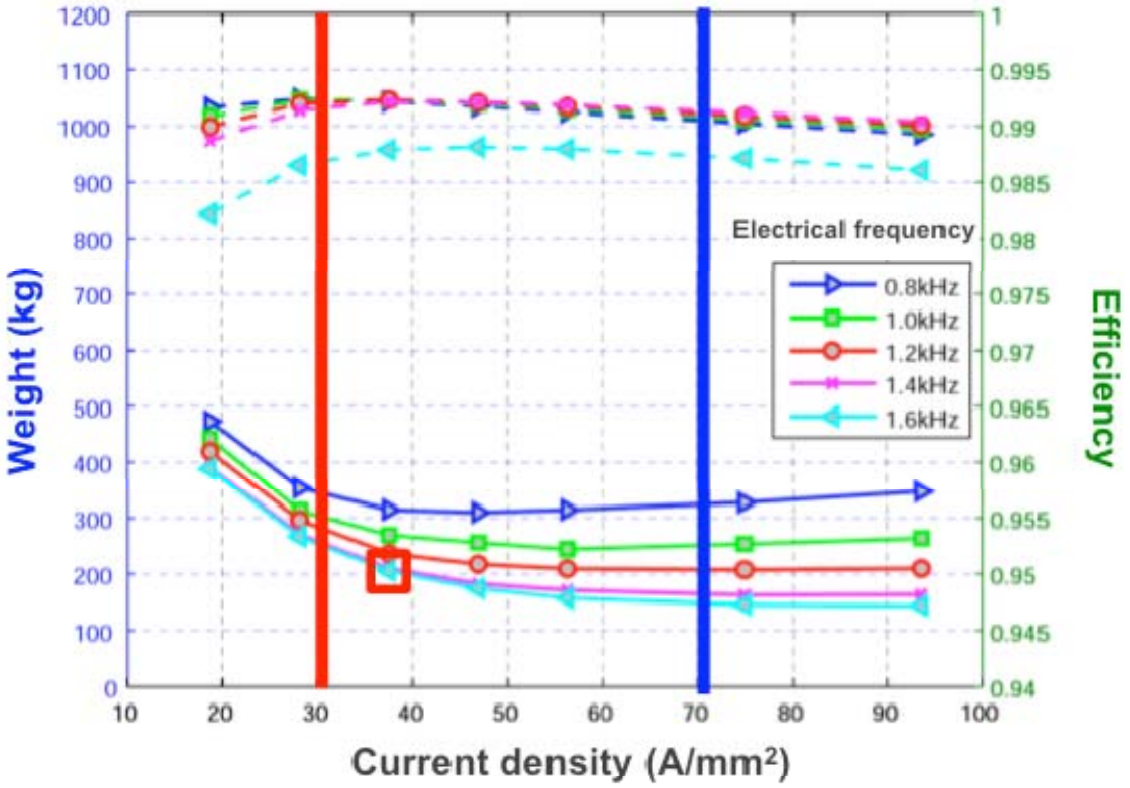

Figure K.22. Weight and efficiency of the electrical motor as a function of electrical frequency and current density

The described model was used to analyze a wide range of electrical motors so a correlation of efficiency and weight as a function of input power was generated to be used in the aircraft system level study that was performed, as explained in section K.4.1.

K 4.3 Fully HTSC generator and cryocooler model

The HTSC generators/motors were designed as fully HTSC machines as they show better performance and weight although they pose a harder technological challenge when compared with those with a resistive armature winding. The different components that were modeled are: the field and armature windings and the environmental shield that are considered the active components; the supporting components for the field winding and for the electromagnetic shield; and the housing and bearings. For these two components, no detailed design was performed and the weight was assumed to be 25% of the total weigh of the system. For the design of the fully HTSC machines, references 2 to 10 were used[222324252627282930]. Also, the team had frequent interactions with G. Brown from NASA, P.J. Masson from Magneto Lab and J.L. Kirtley from MIT. Their support is greatly appreciated by the team.

[22] Superconducting rotating electrical machines. Bumby, J.R., Oxford: Clarendon Press, 1983

The weight and efficiency of the cryocooler was also estimated[31]. A cryocooler is required to maintain the superconductivity state on the windings. To estimate the efficiency of the crycooloer, the loss due to the heat losses and the AC losses in the armature winding is required. The heat losses comprise the heat due to the conduction down the field winding, and the radiation heat from the warm region to the cryogenic region. The conductive heat is considered negligible as it is assumed that the HTSC winding is encased in vacuum. The AC losses comprise hysteretic, coupled losses, eddy current losses and transportation losses. The efficiency of the cryocooler is estimated based on the Carnot efficiency of a refrigeration process with a hot temperature of 110 K (LNG fuel) and a cold temperature given by the working temperature of the superconductor material. Then, the cryocooler efficiency will be a specified percent of this Carnot efficneiy that is based on the cryocooler capacity. Using the total loss and the cryocooler efficiency, the input power to the cryocooler can be estimated. Using this data with assumed power to weight ratio of 3 kg/kW for a 2035 time period, the weight of the cryocooler can be estimated.

For the HTSC performance model, the inputs are the requirements at engine Sea Level Static condition (operating rotational speed, the output shaft power and the fan diameters), the variables (electrical loading, the ratio of the internal radius of magnetic shield to mean armature radius, the number of pole pairs, the mean radius of armature winding, the air gap, and the aspect ratio of the machine) and the constrains (material properties, ratio of the rotor critical speed to maximum generator rotational speed and saturation magnetic field for environmental shield). The material considered for the windings is YBCO. Based on the literature, the current density for the armature and the field winding that were used are 120 A/mm^2 and 110 A/mm^2 respectively. Given those inputs, the generator/motor model generates the geometry, determines the relevant electromagnetic parameters, and estimates the performance through the estimation of the losses, mainly, the shield losses, the windage losses and the AC losses in the armature

---

[23] Smith, J.L. Jr, Kirtley, J.L., Keim, T.A., "Notes for Specila Summer Program on Application of Superconductivity to Rotatin Machines", 1974

[24] Philippe, J.M., Brown, G.V., Soban, D.S., Luongo C.A., "HTS machines as enambing techno

[25] Masson, P.J., Soban, D.S., Upton, E., Pienkos, J.E., Luongo, C.A., "HTS Motors in Aircraft Propulsion: Design considerations", IEEE Transactions on applied superconductivity, Vol.15, No.2, June 2005

[26] Masson, P.J., Soban, D.S., Upton, E., Pienkos, J.E., Luongo, C.A., "HTS Motors in Aircraft Propulsion: Design considerations", IEEE Transactions on applied superconductivity, Vol.15, No.2, June 2005

[27] Philippe, J.M., Luongo, C.A., "High Power Density Superconducting Motor for All-Electrical Aircraft Propulsion", IEEE Transactions on applied superconductivity, Vol.15, No.2, June 2005

[28] Barnes, P.N., Sumption, M.D., Rhoads, G.L., "Review of high power density superconducting generators: Present state and prospects for incorporating YBCO windings", Cryogenics, 45 (2005)

[29] Kalsi, S.S., "Development Status of Superconducting Rotating Machines", Ieee PES Meeting, New York, 27-31 January 2002

[30] Masson, P.J., Tixador, P., Ordoñez, J-C., Morega, A.M., Luong, C.A., "Electro-Thermal Model for HTSC Motor Design", IEEE Transactions on Applied Superconductivity, Vol.17, NO.2, June 2007

[31] Davis, T., Abhyankar, N., "Long Life Cryocoolers for Space Applications. A Database Update", Cryocoolers 13, edited by R.G. Ross, Jr. Speinger Science-Business media, Inc. New Yor, 2004

winding. This model also estimates the weight including the weight of the generator/motor and the cryocooler and, defines the design so it is properly sized with the required SLS conditions, while optimizing it to yield maximum power density of the entire electric transmission system. It is important to note that there is a tradeoff between the generator and the cryocooler weight with respect to the number of pole pairs. Thus, the generator/motor weight decreases when the number of pole pairs increases, while an opposite trend is shown by the cryocooler weight. The outputs of the model are the geometry, the efficiency and the weight of the system.

The described model was used to analyze a wide range of fully HTSC generators/motors+cryocoolers in order to generate a correlation of efficiency and weight as a function of input torque. This model was used in the aircraft system level study that was performed, as explained in section K.4.1. The correlation was finally used in the optimization process followed for the final design of the H3.2 configuration as explained in section 6.

REPORT DOCUMENTATION PAGE	Form Approved OMB No. 0704-0188

1. REPORT DATE *(DD-MM-YYYY)*	2. REPORT TYPE	3. DATES COVERED *(From - To)*
01-12-2010	Final Contractor Report	

4. TITLE AND SUBTITLE
N+3 Aircraft Concept Designs and Trade Studies, Final Report

Volume 2: Appendices--Design Methodologies for Aerodynamics, Structures, Weight, and Thermodynamic Cycles

5a. CONTRACT NUMBER

5b. GRANT NUMBER

5c. PROGRAM ELEMENT NUMBER

6. AUTHOR(S)
Greitzer, E., M.; Bonnefoy, P., A.; Blanco, E., de la Rosa; Dorbian, C., S.; Drela, M.; Hall, D., K.; Hansman, R., J.; Hileman, J., I.; Liebeck, R., H.; Lovegren, J.; Mody, P.; Pertuze, J., A.; Sato, S.; Spakovszky, Z., S.; Tan, C., S.; Hollman, J., S.; Duda, J., E.; Fitzgerald, N.; Houghton, J.; Kerrebrock, J., L.; Kiwada, G., F.; Kordonowy, D.; Parrish, J., C.; Tylko, J.; Wen, E., A.; Lord, W., K.

5d. PROJECT NUMBER
NNX08AW63A

5e. TASK NUMBER

5f. WORK UNIT NUMBER
WBS 561581.02.08.03.13.03

7. PERFORMING ORGANIZATION NAME(S) AND ADDRESS(ES)
Massachusetts Institute of Technology

8. PERFORMING ORGANIZATION REPORT NUMBER
E-17419-2

9. SPONSORING/MONITORING AGENCY NAME(S) AND ADDRESS(ES)
National Aeronautics and Space Administration
Washington, DC 20546-0001

10. SPONSORING/MONITOR'S ACRONYM(S)
NASA

11. SPONSORING/MONITORING REPORT NUMBER
NASA/CR-2010-216794-VOL2

12. DISTRIBUTION/AVAILABILITY STATEMENT
Unclassified-Unlimited
Subject Category: 05
Available electronically at http://gltrs.grc.nasa.gov
This publication is available from the NASA Center for AeroSpace Information, 443-757-5802

13. SUPPLEMENTARY NOTES

14. ABSTRACT
Appendices A to F present the theory behind the TASOPT methodology and code. Appendix A describes the bulk of the formulation, while Appendices B to F develop the major sub-models for the engine, fuselage drag, BLI accounting, etc.

15. SUBJECT TERMS
Jet propulsion; Subsonic aircraft

16. SECURITY CLASSIFICATION OF:			17. LIMITATION OF ABSTRACT	18. NUMBER OF PAGES	19a. NAME OF RESPONSIBLE PERSON
a. REPORT	b. ABSTRACT	c. THIS PAGE			STI Help Desk (email:help@sti.nasa.gov)
U	U	U	UU	191	19b. TELEPHONE NUMBER *(include area code)* 443-757-5802